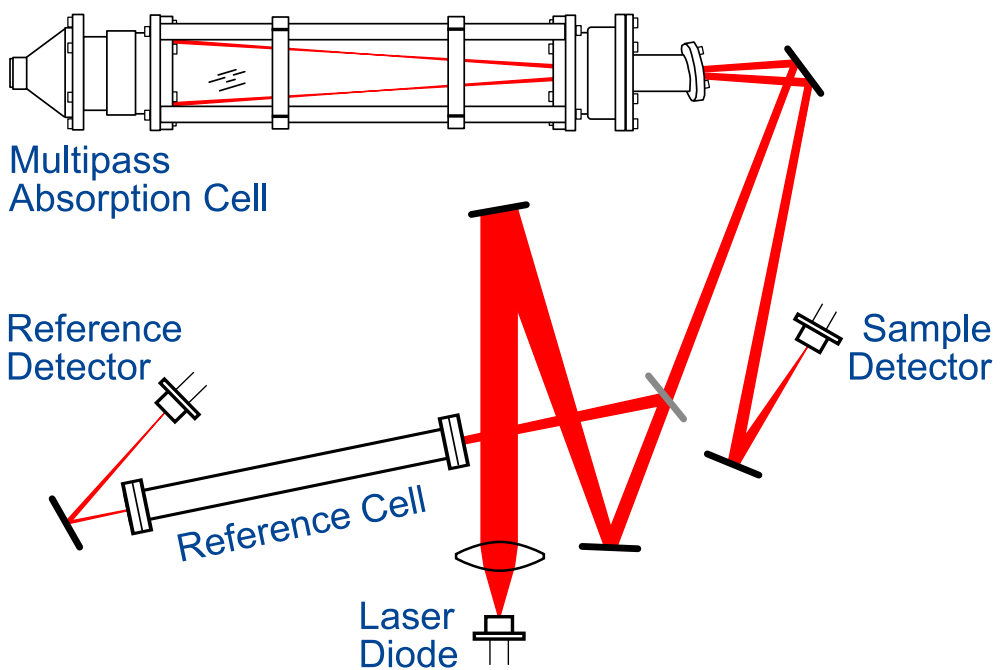


Christoph Dyroff

Tunable Diode-Laser Absorption Spectroscopy for Trace-Gas Measurements with High Sensitivity and Low Drift



Christoph Dyroff

Tunable Diode-Laser Absorption Spectroscopy for Trace-Gas Measurements with High Sensitivity and Low Drift

Karlsruhe Series in Photonics & Communications, Vol. 5
Edited by Prof. J. Leuthold and Prof. W. Freude

Universität Karlsruhe (TH), Institute of High-Frequency and Quantum Electronics (IHQ),
Germany

Tunable Diode-Laser Absorption Spectroscopy for Trace-Gas Measurements with High Sensitivity and Low Drift

by
Christoph Dyroff



universitätsverlag karlsruhe

Dissertation, Universität Karlsruhe (TH)
Fakultät für Elektrotechnik und Informationstechnik, 2008

Impressum

Universitätsverlag Karlsruhe
c/o Universitätsbibliothek
Straße am Forum 2
D-76131 Karlsruhe
www.uvka.de



Dieses Werk ist unter folgender Creative Commons-Lizenz
lizenziert: <http://creativecommons.org/licenses/by-nc-nd/2.0/de/>

Universitätsverlag Karlsruhe 2009
Print on Demand

ISSN: 1865-1100
ISBN: 978-3-86644-328-0

Tunable Diode-Laser Absorption Spectroscopy for Trace-Gas Measurements with High Sensitivity and Low Drift

Zur Erlangung des akademischen Grades eines

DOKTOR INGENIEURS

an der Fakultät für
Elektrotechnik und Informationstechnik
der Universität Fridericiana Karlsruhe

genehmigte

DISSERTATION

von

Dipl.-Ing. (FH) Christoph Dyroff

aus

Geislingen an der Steige

Tag der mündlichen Prüfung:

06.10.2008

Hauptreferent:

Prof. Dr.-Ing. Dr. h. c. Wolfgang Freude

1. Korreferent:

Prof. Dr. rer. nat. Herbert Fischer

2. Korreferent:

Prof. Dr. sc. nat. Jürg Leuthold

Abstract (German)

Die vorliegende Arbeit diskutiert einige wichtige Aspekte der Diodenlaserspektroskopie zum Nachweis atmosphärischer Spurengase bei der Anwendung an Bord von Forschungsflugzeugen. Es wird dabei insbesondere auf die Nachweisgrenze und deren Verbesserung eingegangen.

Die Nachweisgrenze ist ein Maß für die Messunsicherheit einer bestimmten Messung. Bei Konzentrationsmessungen stellt sie die minimal nachweisbare Konzentration eines Spurengases dar. Um die Nachweisgrenze zu optimieren, bedarf es der Auswahl rauscharmer Systemkomponenten. Dies gilt sowohl für die Laserquelle als auch für den Detektor. Bei sehr großen Anforderungen an die Nachweisgrenze kann die Messunsicherheit durch Mittelwertbildung verbessert werden. Für zahlreiche statistisch unabhängige Messungen gilt, dass Mittelwertbildung die Nachweisgrenze proportional zur Wurzel der Mittelungszeit verbessert.

Die Mittelwertbildung — und damit die Verbesserung der Nachweisgrenze — ist bei laserspektroskopischen Anwendungen jedoch in der Regel durch systematische Drift auf ca. 30 s bis 100 s limitiert. Grund dieser Limitierung sind zeitveränderliche Hintergrundsignale, die dem eigentlichen Messsignal (Absorptionsspektrum) überlagert sind, und deren Ursache in der Interferenz des Laserstrahles mit Streulicht und/oder Rückreflexionen von optischen Bauteilen liegt. Das Interferenzsignal hängt dabei stark vom optischen Aufbau ab und kann sich somit aufgrund z.B. thermischer Ausdehnung einzelner Systemkomponenten ändern. Dieses veränderliche Hintergrundsignal ist den Absorptionsspektren überlagert und führt bei der Auswertung der aufgezeichneten Spektren zu einer Drift in der ermittelten Konzentration.

In einigen Fällen besteht die Möglichkeit das Hintergrundsignal aufzuzeichnen, während man das Messsystem mit Null-Luft (einem Gasgemisch, dass das zu messende Gas nicht enthält) spült. Das Hintergrundsignal kann anschließend vom eigentlichen Messsignal subtrahiert werden. Diese Technik ist jedoch nicht auf alle Gase gleichermaßen anwendbar. Gase wie z.B. Wasserdampf (H_2O) werden stark von den meisten Oberflächen adsorbiert. Dies führt in der Regel zu relativ langen Austauschzeiten, die es nicht erlauben, zwischen Messgas und Null-Luft zu wechseln. Unter solchen Umständen ist das Aufzeichnen von Hintergrundsignalen nicht praktikabel. Das Messinstrument muss daher eine möglichst geringe Nachweisgrenze bei geringen Mittelungszeiten aufweisen, um die geforderte Nachweisgrenze zu erreichen.

Zusätzlich zu einer möglichst niedrigen Nachweisgrenze sind für den Einsatz eines Instruments auf einem Forschungsflugzeug weitere Anforderungen gegeben. Diese beziehen sich auf Größe und Gewicht des Instruments und können aufgrund des begrenzen Platzangebots und der limitierten Payload über den Einsatz eines Instruments auf einem Forschungsflugzeug entscheiden. Das in der vorliegenden Arbeit beschriebene Diodenlaser-Spektrometer zur Bestimmung der isotopischen Zusammensetzung atmosphärischen Wasserdampfs erfüllt

diese strengen Anforderungen. Bei der Entwicklung wurde eine möglichst kompakte und leichte Bauweise gewählt.

Sehr genauer Spurengasnachweis: Die Messung atmosphärischer Spurengase, wie z.B.

Wasser (H_2O) und seine Isotopologe oder Formaldehyd (CH_2O), stellt hohe Anforderungen an die Nachweisgrenze des jeweiligen Messinstruments. Wie oben beschrieben, kann die Nachweisgrenze durch Mittelwertbildung verbessert werden. Die maximale Mittelungszeit ist allerdings in der Regel auf 30 s bis 100 s begrenzt. Um die gewünschte Nachweisgrenze auch innerhalb relativ geringer Mittelungszeiten zu erreichen, ist es daher erforderlich, das Messsystem möglichst rauscharm zu gestalten.

Beim Aufbau des in dieser Arbeit beschriebene Diodenlaser-Spektrometer zur Messung der isotopischen Zusammensetzung von H_2O wurde daher besonderer Wert auf die Auswahl rauscharmer Systemkomponenten gelegt. Möglichst kurze optische Wege und robuster optisch-mechanischer Aufbau minimieren weiterhin vibrationsinduziertes Rauschen und (thermische) Drift. Dadurch konnte für eine Mittelungszeit von 30 s eine Nachweisgrenze (optische Dichte) von $OD = 4.35 \times 10^{-6}$ erzielt werden. Für die Messung der Isotopenverhältnisse $\delta^{17}O$ und $\delta^{18}O$ in Wasserdampf bedeutet dies eine Nachweisgrenze von 2 ‰ und 6.25 ‰ bei einem Mischungsverhältnis von 90 ppmv. Diese Nachweisgrenze zählt zu den besten veröffentlichten Ergebnissen für die Messung der isotopischen Zusammensetzung von H_2O .

Kompaktes Diodenlaserspektrometer: Für den Einsatz auf Forschungsflugzeugen konzipierte Messinstrumente müssen — neben den genannten Anforderungen an die Nachweisgrenze — eine Reihe von Anforderungen bezüglich des Instrumentendesign erfüllen. Dies gilt insbesondere für den Einsatz des hier beschriebenen Spektrometers zur Messung der isotopischen Zusammensetzung atmosphärischen Wasserdampfs im Rahmen des CARIBIC Projekts sowie auf dem neuen Forschungsflugzeug HALO. Das Instrument muss dabei für den Einbau in ein 19-Zoll Rack ausgelegt sein. Aufgrund von Gewichtsbeschränkungen sollte die Masse 40 kg nicht überschreiten. Weiterhin muss das Instrument vollautomatisch betrieben werden, da während des Fluges kein Bedienpersonal vorgesehen ist. Durch Auswahl geeigneter Systemkomponenten sowie durch ein sehr kompaktes optisches System konnten diese Anforderungen erfüllt werden. Das in dieser Arbeit vorgestellte Spektrometer ist $45 \times 56 \times 35 \text{ cm}^3$ groß und hat eine Masse von ca. 35 kg. Es zählt damit zu den kompaktesten Spektrometern für den Flugzeugeinsatz weltweit bei gleichzeitig sehr niedriger Nachweisgrenze.

Kompensation systematischer Drift: Durch eine selektive Modulation des Absorptionskoeffizienten einer Absorptionslinie konnte systematische Drift bei der spektroskopischen Messung von Formaldehyd (CH_2O) vollständig kompensiert werden. Die verwendete Methode basiert auf dem Stark-Effekt, bei dem die Energieniveaus einer Absorptionslinie durch Anwendung eines externen, periodisch modulierten elektrischen Feldes aufgespalten werden. Diese Aufspaltung führt dazu, dass die gesamte Absorptionslinie verformt wird, was einer periodischen Änderung des Absorptionskoeffizienten entspricht. Das entsprechende Absorptionssignal konnte mit Hilfe zweier Verfahren — einer Subtraktionstechnik sowie Detektion mittels Lock-in-Verstärker — detektiert werden. Es ist frei von störenden Hintergrundsignalen.

Für die Durchführung der Messungen wurde eine neuartige Multireflexionszelle verwendet, mit deren Hilfe bis zu 40 m Absorptionsstrecke erreicht werden können. Die Zelle enthält zwei zylindrische Elektroden zum Anlegen eines externen elektrischen Feldes. Durch die selektive Modulation des Absorptionskoeffizienten mittels Stark-Effekt konnten Stabilitätszeiten von über 1 000 s erreicht werden, was einer Verbesserung um mehr als den Faktor zehn gegenüber den meisten publizierten Werten entspricht.

Achievements

The present dissertation deals with the main aspects of airborne in-situ trace-gas detection by means of tunable diode-laser spectroscopy, namely with the requirements for compact and lightweight instrumentation having high sensitivity.

Sensitivity is a term for the limiting uncertainty of a particular measurement. For example, with concentration measurements, the sensitivity of an instrument marks the lowest concentration of a target gas that can be measured. High sensitivity requires a well designed instrument, which requires low-noise components. For a diode-laser spectrometer, the crucial components are the laser source as well as the detector and preamplifier electronics. If the sensitivity needs to be further improved, the recorded data can be averaged. For numerous statistically independent measurements, averaging will improve the sensitivity proportional to the square root of the averaging time.

This averaging time is, however, often limited to between 30 s and 100 s by systematic drift. The reason for this drift are unwanted, time-dependent background structures that are superimposed on the measured absorption spectra. These background structures are caused by interference of back-reflected (from surfaces of optics such as lenses or windows) or scattered light with the main laser beam. The interference signal depends strongly on the optical setup, and it changes, e.g., through thermal expansion of optical components. The drifting background signal in turn induces a drift in the concentration values, that are deduced from the absorption spectra.

For certain applications it is possible to record the unwanted background structures. This can be achieved by flushing the absorption cell of the spectrometer with air scrubbed of the target species (zero air). During this flushing period, a background spectrum can be recorded, which then can be subtracted from the absorption spectra of the target species. Unfortunately, this background-subtraction approach is not applicable to every target species. Molecules such as water (H_2O) are adsorbed to any surface, and flushing the absorption cell with dry air will lead to very long exchange times, which in turn prevents background measurements. As background measurements are impractical for these molecules, the sensitivity of the spectrometer must be high enough in order to reach the desired detection limit within short averaging times of approximately 30 s.

In addition to high sensitivity measurement capabilities, spectrometers deployed aboard research aircrafts are required to be very compact and lightweight. These requirements can only be met by a proper selection of system components and a compact optical design. Based on measurements of water (H_2O) vapor isotopic ratios and formaldehyde (CH_2O), the considerations above have been applied towards an improved sensitivity as well as a compact and lightweight spectrometer design.

High sensitivity measurements: Measurement of many atmospheric constituents, such as formaldehyde (CH_2O) as well as water (H_2O) and its isotopologues discussed in the present dissertation, requires very high sensitivity. While the sensitivity can be improved by averaging of spectral data, the averaging time is generally limited to 30 s to 100 s because of instrument drift. Low-noise spectrometer design is required in this case in order to achieve the required detection limit within a relatively short averaging time.

For the design of the H_2O isotopic ratio spectrometer, particular care was taken in selecting low-noise system components. Furthermore, the optical part of the spectrometer was designed to maintain short optical paths in order to minimize vibration-induced noise and thermal drift. This resulted in an absorbance sensitivity (optical density) of $\text{OD} = 4.35 \times 10^{-6}$ for measurements averaged over 30 s. Applied to measurements of $\delta^{17}\text{O}$ and $\delta^{18}\text{O}$ isotopic ratios, the sensitivity achieved was 2‰ and 6.25‰, respectively, for a H_2O mixing ratio of 90 ppmv. This precision is among the best published for H_2O isotopic ratio measurements.

Highly compact spectrometer design: Scientific instruments aboard airborne research platforms require the instrument to be extremely compact and lightweight. For the envisaged deployment of the water vapor isotopic ratio spectrometer aboard the CARIBIC and HALO research platforms, this instrument must be 19 inch rack compatible at a mass below 40 kg, and must be operated in a fully autonomous mode. Careful selection of system components and a compact optical design allowed meeting these requirements. The final instrument has dimensions of only $45 \times 56 \times 35 \text{ cm}^3$ at a mass of around 35 kg. In addition to its high sensitivity, the spectrometer is among the most compact instruments published so far.

Compensation of systematic drift: A novel approach compensates for systematic drift that is commonly found in laser spectrometers and generally limits the valid averaging time for spectral data to between 30 s and 100 s. This approach — which was applied to measurements of formaldehyde (CH_2O) — is based on a selective sample modulation by means of the Stark effect. A periodic external electric field applied to the CH_2O gas splits the ground state and the excited state of a specific absorption line. This splitting yields a periodic deformation of the absorption line and thus a modulation of the absorption coefficient. The corresponding absorption signal could be measured both by means of a subtraction technique as well as using a lock-in amplifier. Due to the highly selective modulation, the measured signal does contain only this fraction of the CH_2O absorption signal that is affected by the electric field. The background signal is thus completely removed.

For these measurements, a novel multipass absorption cell design has been employed that allows for absorption path lengths of up to 40 m. The cell contains two cylindrical electrodes to apply an external electric field to the target gas. The selective sample modulation by means of the Stark effect yields stability times routinely exceeding 1 000 s. This corresponds to an increase of more than a factor of ten over values published in the literature.

Contents

1	Spectroscopic trace gas detection	1
1.1	Laser spectroscopy for trace gas detection	2
1.1.1	Molecular absorption spectra	2
1.1.2	Linewidth broadening	3
1.1.3	Absorption	6
1.1.4	Advantages of laser spectroscopy	8
1.2	Limitations of laser spectroscopy	10
1.2.1	Low absorption	11
1.2.2	Noise and drift	11
1.3	Sensitivity improvement	15
1.3.1	Multipass absorption cell	15
1.3.2	Laser, detector, and setup	16
1.3.3	Modulation spectroscopy	17
1.4	Important atmospheric trace gases	22
1.4.1	Water vapor isotopic ratios	24
1.4.2	Formaldehyde	28
1.5	Airborne platforms and instrument requirements	29
1.5.1	Long-term passenger-aircraft project CARIBIC	29
1.5.2	New German research aircraft HALO	31
1.5.3	Instrument requirements	32
2	Sensitive H₂O isotopic ratio measurements	35
2.1	Existing techniques for isotopic ratio measurements	36
2.2	Spectrometer design	37
2.2.1	Optics	38
2.2.2	Laser and photodetector	40
2.2.3	Calibration	45
2.2.4	Data acquisition	51
2.2.5	Conclusion	54
2.3	System stability and detection limit	55
2.3.1	Signal-to-noise ratio analysis	55
2.3.2	Detection limit and system stability	63
2.3.3	Measurement accuracy	68
2.3.4	Conclusion	71
2.4	Performance specifications	71
2.5	Future improvements	73

3 A novel approach to CH₂O measurements	75
3.1 Stark effect	77
3.2 Multipass absorption cell for Stark modulation	81
3.2.1 Reentrant condition	81
3.2.2 Misalignment analysis	82
3.2.3 Cell design	86
3.2.4 Conclusion	86
3.3 Drift compensation by Stark modulation	88
3.3.1 Spectrometer setup and data acquisition	88
3.3.2 Electric breakdown	91
3.3.3 Alternate measurements of signal and background	91
3.3.4 Interleaved measurement of signal and background	93
3.3.5 Conclusion	94
3.4 System stability and detection limit	96
3.4.1 Alternate measurement of signal and background	96
3.4.2 Interleaved measurement of signal and background	98
3.4.3 Detection limit	100
3.4.4 Conclusion	102
3.5 Future improvements	103
3.6 Applicability of Stark modulation to other gases	103
4 Summary	105
Appendices	
A Absorption signals at wavelength modulation	109
B Stark coefficients of H ₂ O absorption lines	114
List of Figures	121
List of Tables	123
Bibliography	125
Acknowledgments	137
List of own Publications	139
Curriculum Vitae	141

Chapter 1

Laser-based spectroscopic trace gas detection

The present Chapter first reviews the fundamental aspects of absorption spectroscopy for trace gas detection. The focus thereby lies on laser-based spectroscopy. A description of the origin and properties of molecular absorption spectra is followed by an introduction to lineshape functions and lineshape-broadening mechanisms that play an important role in high-resolution spectroscopy. A discussion of the advantages of laser-based absorption spectroscopy finalizes Section 1.1.

In Section 1.2 the sensitivity limitations of laser-based absorption spectroscopy are described. The sensitivity limitations are generally related to the very low absorption signals of around 5×10^{-6} , which are often encompassed in atmospheric trace gas measurements. In addition, the sensitivity may be limited by noise contributions of various system components, such as the laser source and the detector. Finally, drift phenomena are present in most laser spectrometers. Drift is commonly caused by time-dependent spectral background, which limits the valid averaging time for spectral data and thus the achievable sensitivity.

Means to improve the sensitivity of laser spectrometers are presented in Section 1.3. Sensitivity improvement may be achieved by selection of low-noise laser and detector, as well as by a rugged optical setup. The sensitivity may also be improved by long path lengths, which can be realized by multiple pass absorption cells. Finally the concept of modulation spectroscopy as a means for noise reduction will be discussed.

Section 1.4 will introduce two important atmospheric trace gases, namely water (H_2O) vapor and its stable isotopologues as well as formaldehyde (CH_2O). Water plays an important role in the global energy budget, and its isotopologues can be used as a tracer for transport processes. Formaldehyde is an indicator for air quality and ozone (O_3) production.

Finally, two airborne research platforms are described in Section 1.5 that are available for envisaged in-situ measurements of H_2O isotopic ratios with the laser spectrometer described in Chapter 2 of the present dissertation. The Section ends with a description of the requirements for this instrument. These requirements include size and weight constraints as well as sensitivity constraints, which need to be fulfilled in order to make scientifically meaningful measurements.

1.1 Laser spectroscopy for trace gas detection

In the following Sections, the fundamentals of absorption spectroscopy are reviewed. In Section 1.1.1 the origin of molecular absorption spectra due to excitation of rotational and/or vibrational energetic states is described. This is followed by an introduction to linewidth-broadening mechanisms and the resulting lineshape functions in Section 1.1.2. Linewidth-broadening is crucial for applications where high spectral resolution is required in order to avoid absorption contributions of multiple absorbing species. Finally, Section 1.1.3 briefly reviews Beer-Lambert's law. It relates spectroscopic properties, such as the gas concentration and absorption linewidth, as well as the absorption path length to the transmitted intensity that is passed through an absorbing medium.

1.1.1 Molecular absorption spectra

Laser absorption spectroscopy of molecules is based on the excitation of molecules from a ground state into an excited state, whereby the photon energy is absorbed by the molecule. Depending on the photon energy, the molecule changes its rotational, vibrational, or electronic energy.

In this dissertation we will only consider photon energies with a corresponding wavelength λ in the infrared spectral region, where rotational and vibrational absorption transitions are excited. The photon energy for pure rotational transitions thereby is, expressed in wavenumbers ($\nu = 1/\lambda = f/c$),¹ in the order of tens to a few 100 cm^{-1} ($\lambda = 1\text{ mm}$ to tens of μm). Vibrational and rotational-vibrational states can be excited by photons in the infrared spectral region between 500 cm^{-1} and 10000 cm^{-1} (between $\lambda = 20\text{ }\mu\text{m}$ and $\lambda = 1\text{ }\mu\text{m}$).

Due to the unique properties (i.e., mass distribution and atomic-bond strength) of the different molecules, the absorption spectra in the infrared spectral region have a very distinct shape that is characteristic to the specific molecule. The infrared spectral region is therefore commonly termed the fingerprint spectral region. This distinctness can be used to identify the molecules of an unknown gas or to quantify the concentration of molecules in a gas mixture. A term often used in this regard is the volume mixing ratio (or short mixing ratio), which is commonly given in parts per million by volume (ppmv). It is equivalent to the mole fraction of a certain molecular species in a gas mixture.

The rotational energy of a molecule depends on its mass distribution, i.e., the mass of the atoms and their distance from the center of gravity, which is expressed as the molecule's mass moment of inertia. If the molecule rotates it possesses an angular momentum J . Based on the solution of Schrödinger's equation, J is quantized, i.e., the molecule rotates only at distinct angular frequencies, leading to discrete rotational energy states. These energy states are expressed in terms of J , and the selection rule for vibrational transitions of polyatomic molecules is $\Delta J = 0, \pm 1$ [Graybeal, 1988].

The rotational energy of molecules is generally much smaller than the thermal energy ($E_{\text{thermal}} = k_B T$),² and at room temperature, where $E_{\text{thermal}} = 0.026\text{ eV} \approx 208\text{ cm}^{-1}$, the molecules can always be found in excited rotational states.

¹The speed of light (in vacuum) is $c = 2.997\,925\text{ m/s}$

²The Boltzmann constant is $k_B = 1.380\,650\,4 \times 10^{-23}\text{ J/K}$.

The number of rotational states depends on the complexity of the molecule. The three-atomic water molecule depicted in Fig. 1.1 (b) has three different moments of inertia about three orthogonal axes of rotation. As the molecule can rotate about any of these axes, many rotational states exist. In contrast, a diatomic molecule has only one non-zero moment of inertia and thus less rotational energy states.

In addition to rotation, the molecule may also vibrate. A linear polyatomic molecule with m atoms has $3m - 5$ vibrational degrees of freedom, and a non-linear polyatomic molecule has $3m - 6$ vibrational degrees of freedom [Graybeal, 1988]. When vibrating, the molecule can be described as a harmonic oscillator, where the oscillation frequency depends on the bond energy of the molecule. The vibration frequency is also quantized, and only discrete vibrational states v are allowed. Water for example has three fundamental vibrational states as depicted in Fig. 1.1 (a). As the fundamental vibrations are independent, the total vibrational energy of the molecule can be considered as the sum of the individual components. As a consequence one may not only observe transitions between fundamental vibrational energy states, but also transitions due to a combination of vibrational transitions as well as overtone transitions [Finlayson-Pitts and Pitts, Jr., 2000]. An example for the former case is the transition from a rotational energy level of the v_1 vibrational ground state into a rotational energy level of the v_2 excited vibrational state. Overtone transitions, on the other hand, are transitions where $\Delta v = \pm 2, \pm 3, \dots$

The energy required to excite vibrational transitions is generally much larger than the thermal energy ($k_B T$) at room temperature, and basically all molecules are therefore in their vibrational ground state.

Fig. 1.1 (c) depicts a schematic energy diagram with the ground vibrational state $v_1 = 0$ and the first excited state $v_1 = 1$. Superimposed to these vibrational states are the rotational states described by their rotational quantum number J . For absorption transitions as depicted, the transitions with $\Delta J = +1$ are denoted as *R*-branch, and the transitions with $\Delta J = -1$ are denoted as *P*-branch. The *R*-branch is thus located to the higher energy side of the energy difference between the two vibrational states, and the *P*-branch is located at the lower energy side. Transitions with $\Delta J = 0$ are denoted as *Q*-branch, and are located near the difference of the two vibrational energy levels involved in the transition [Graybeal, 1988].

Since polyatomic molecules may rotate about three mutually perpendicular axes and have at least two vibrational degrees of freedom, their absorption spectra are generally very complex. Fundamental transitions, such as the ones schematically depicted in Fig. 1.1 (c), as well as combination and overtone transitions result in a multitude of absorption lines.

1.1.2 Linewidth broadening

Linewidth broadening mechanisms that are relevant for the measurement of gaseous atmospheric constituents are Doppler broadening and collisional broadening. The former mechanism is induced by the temperature-induced motion of the absorbing molecules, while the latter mechanism originates from collisions of molecules at elevated gas pressure. It is only at very low gas pressure and temperature that the natural linewidth is relevant — it is, however, introduced for the sake of completeness.

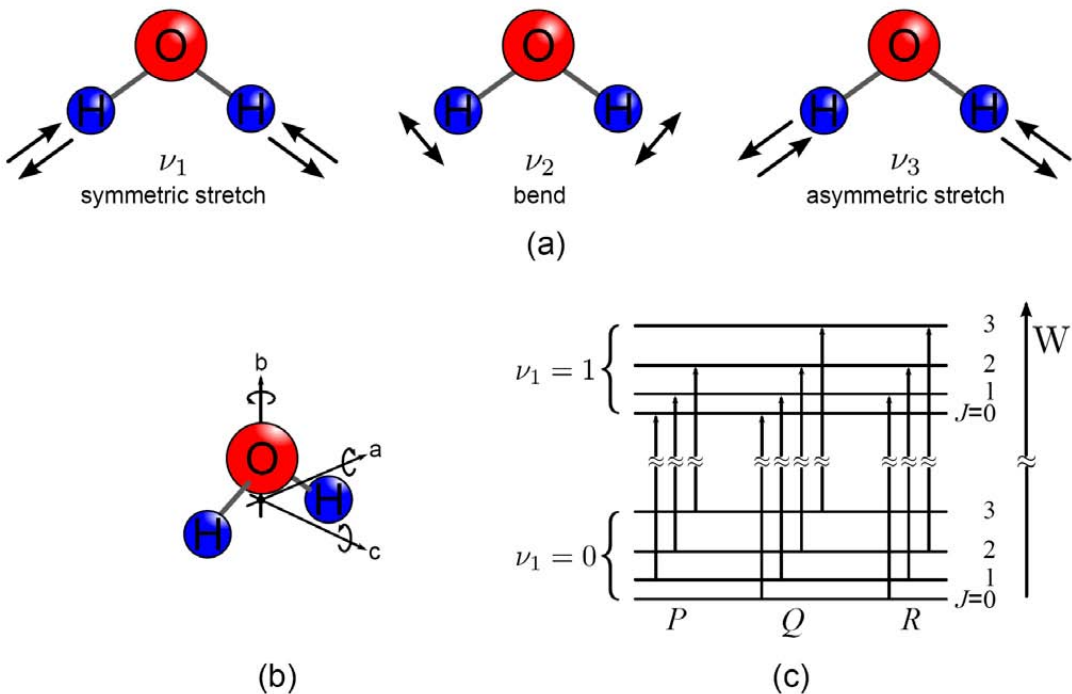


Figure 1.1: (a) Fundamental vibration modes of the water molecule $\nu_1=3\,657\,\text{cm}^{-1}$, $\nu_2=1\,595\,\text{cm}^{-1}$, and $\nu_3=3\,756\,\text{cm}^{-1}$ [Waewsak, 2004]. (b) Rotational degrees of freedom of the water molecule along with the respective rotational axes. (c) Schematic energy diagram with vibrational states $v_1 = 0$ and $v_1 = 1$ and rotational states with quantum numbers $J = 0 \dots 3$. Transitions with $\Delta J = +1$ are denoted as R-branch, transitions with $\Delta J = 0$ are denoted as Q-branch, and transitions with $\Delta J = -1$ are denoted as P-branch [Graybeal, 1988].

Natural linewidth

The discreteness of the energetic states of a molecule is somewhat weakened by Heisenberg's uncertainty principle, which relates the uncertainty of the energetic states (or energy levels) to their lifetime, so that the difference in wavenumbers becomes

$$\gamma_N = \frac{1}{2\pi c} \left(\frac{1}{\tau'} + \frac{1}{\tau''} \right), \quad (1.1)$$

where τ'' and τ' denotes the lifetime of the ground state and excited state, respectively.³ As a consequence the absorption transition is broadened. Its half width at half maximum (HWHM) is γ_N , and the normalized lineshape takes the form of a Lorentzian function (with area 1) [Graybeal, 1988]

$$\Gamma_N(\nu) = \frac{1}{\gamma_N \pi} \frac{\gamma_N^2}{(\nu_0 - \nu)^2 + \gamma_N^2}. \quad (1.2)$$

³Certain absorption transitions have an excited ground state — such as a thermally excited rotational state or an excited vibrational state — and their ground-state lifetime τ'' is finite [Demtröder, 1996].

The quantity v_0 denotes the wavenumber at the center of the absorption transition, i.e., the maximum of the Lorentzian lineshape function.

In addition to the natural line broadening, absorption lines are further widened by Doppler broadening and at higher gas pressure by collisional broadening which is often referred to as pressure broadening.

Doppler broadening

If a molecule has a velocity component along the propagation direction of a beam of light, the frequency at which the molecule absorbs electromagnetic radiation is shifted due to the Doppler effect. The velocity of the molecule depends on the temperature T , and the molecular weight is M . As the velocity terms in the direction of the light, which excites a molecular absorption transition, are random and independent, the normalized lineshape function takes the form of a Gaussian function [Demtröder, 1996; Tittel *et al.*, 2003]

$$\Gamma_D(v) = \frac{1}{\gamma_D} \sqrt{\frac{\ln(2)}{\pi}} \exp \left\{ -\ln(2) \left(\frac{v - v_0}{\gamma_D} \right)^2 \right\} , \text{ where} \quad (1.3)$$

$$\gamma_D = \frac{v_0}{c} \sqrt{\frac{2 \ln(2) k_B T}{M}}$$

is the HWHM of the Gaussian lineshape function.

Collisional broadening

Collisions of two molecules can lead to the reduction of the lifetime of the molecules energetic states, and according to Heisenberg's uncertainty principle (Eq. 1.1) to an increased linewidth. As the likelihood of collisions increases at higher pressure, collisional broadening dominates at elevated pressures (typically at $p \gtrsim 100$ hPa). The normalized lineshape takes the form of a Lorentzian function [Tittel *et al.*, 2003]

$$\Gamma_C(v) = \frac{1}{\gamma_C \pi} \frac{\gamma_C^2}{(v - v_0)^2 + \gamma_C^2} , \text{ with} \quad (1.4)$$

$$\gamma_C = \gamma_C^0 p \sqrt{\frac{T}{T_0}} .$$

where γ_C is the HWHM, γ_C^0 is the coefficient of pressure broadening ($\text{cm}^{-1}/\text{bar}$), p is the gas pressure (bar), and T is the absolute gas temperature (K).

Combined broadening

At the limits of very low and very high pressure the lineshape can be approximated by Gaussian and Lorentzian lineshapes, respectively. In the intermediate case ($\gamma_D \approx \gamma_C$), where neither Doppler nor collisional broadening is the dominating mechanism, the lineshape function takes the form of a Voigt profile, which is the convolution of Gaussian and Lorentzian lineshape

function [Demtröder, 1996]. An expression for the normalized Voigt profile is given by *Huang and Yung* [2004]

$$\Gamma_V(v) = \frac{\gamma_C}{\pi^{\frac{3}{2}} \gamma_D^2} \int_{-\infty}^{+\infty} \frac{e^{-y^2}}{\left(\frac{v-v_0}{\gamma_D} - y\right)^2 + \left(\frac{\gamma_C}{\gamma_D}\right)^2} dy , \quad (1.5)$$

and the HWHM γ_W of the Voigt lineshape is [Olivero and Longbothum, 1977]

$$\gamma_W = 0.5346\gamma_L + \sqrt{0.2166\gamma_L^2 + \gamma_D^2} . \quad (1.6)$$

Humlcek [1982] has developed an approximation to the integral in Eq. 1.5 that allows for accurate and fast calculation of the Voigt profile.

It should be noted here that while broadening of absorption lines is an important aspect of optical spectroscopy, exact knowledge about the lineshape function is only necessary when quantitative information (gas concentration) is deduced employing Beer-Lambert's law (Section 1.1.3). In this case the gas concentration can be determined by fitting the appropriate lineshape function to a measured spectrum. In such measurements, calibration with a known standard is often not performed, and the accuracy of these measurements depends on the knowledge of the absorption line shape, broadening coefficient, and integrated line strength. Concentration retrieval in this dissertation was always done by active calibration employing calibration gas standards, so that a knowledge of the lineshape is not required.

Fig. 1.2 gives an example spectrum of 100 ppmv water at a pressure of 70 hPa (*red* trace) and 1 000 hPa (*black* trace). The spectra were calculated employing the Voigt approximation by *Humlcek* [1982] using a software code kindly provided by Dr. Frank *Hase* [2004] (Institute of Meteorology and Climate Research). Due to the substantial broadening of the absorption lines at ambient pressure (1 000 hPa), high resolution spectroscopy is mostly performed at reduced pressure. For example, the three isotopologic water absorption lines around $v = 3663 \text{ cm}^{-1}$, which are of interest in the present work, are not clearly resolved at ambient pressure, where pressure broadening is dominant.

For selective measurements the absorption lines must be probed with light having a narrow emission spectrum, i.e., narrower than the absorption linewidth. This could be achieved by passing light with a broad emission spectrum through a monochromator. Since the invention of wavelength-tunable lasers however, these new light sources have found increasing interest for probing narrow molecular absorption lines. For example, a distributed feedback diode laser at $\lambda = 2.7 \mu\text{m}$, which has been used to probe absorption lines of water isotopologues, has a linewidth (FWHM) of about 10 MHz, whereas the width of the absorption lines probed is $\text{FWHM} \approx 600 \text{ MHz}$ at a pressure of 70 hPa.

1.1.3 Absorption

Absorption spectroscopy is generally based on Beer-Lambert's law, which describes the exponential decay of electromagnetic intensity I transmitted along a certain path length x through an absorbing medium with the frequency-dependent absorption cross-section $\alpha(v, N)$. The absorption cross-section is determined by the integrated line strength S_{ij} (integrated over v) [in $\text{cm}^2/(\text{cm molecule})$] of a particular absorption transition from energetic ground state i to

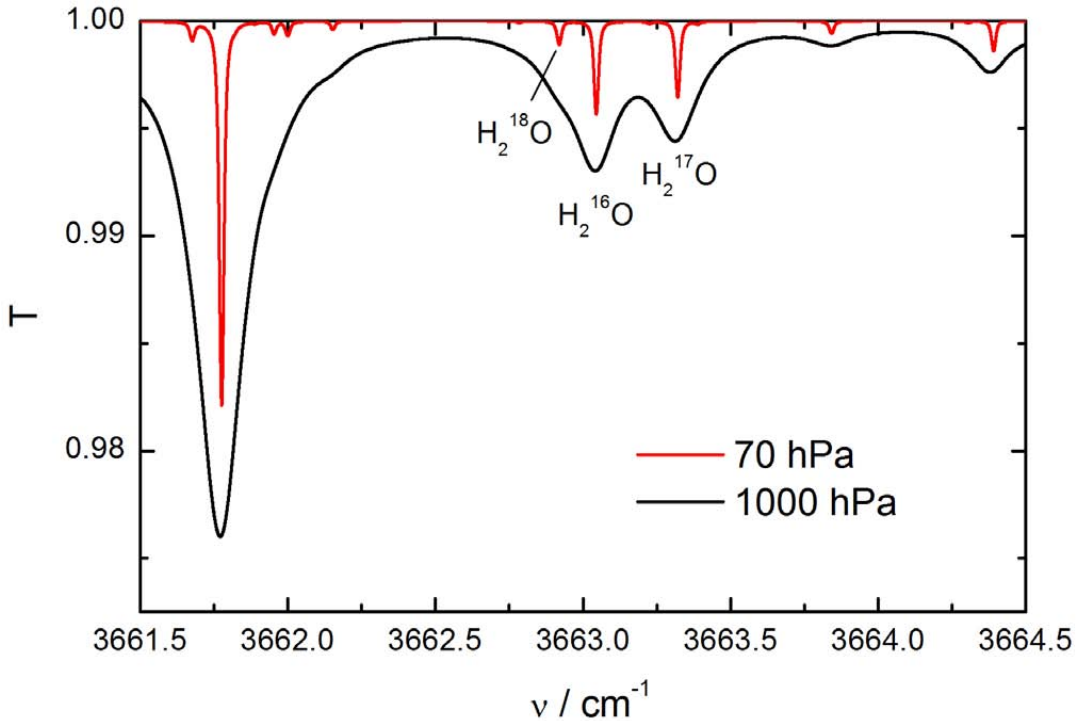


Figure 1.2: Calculated H_2O transmission spectra at 1 000 hPa (black trace) and 70 hPa (red trace). A H_2O mixing ratio of 100 ppmv and an absorption path length of 76 m was assumed for the calculation. Reduced gas pressure is a prerequisite for high selectivity as the absorption lines of interest around 3 663 cm^{-1} are not resolved at ambient pressure.

the excited state j , the appropriate lineshape function $\Gamma(v)$ (in cm), and the concentration of the absorbing molecules N (in molecules/cm³)

$$\alpha(v, N) = S_{ij}\Gamma(v)N. \quad (1.7)$$

Neglecting particle-related scattering the transmission T is expressed by [Tittel *et al.*, 2003]:

$$T(x, v, N) = \frac{I(x, v, N)}{I_0} = \exp \{-\alpha(v, N)x\} = \exp \{-S_{ij}\Gamma(v)Nx\}. \quad (1.8)$$

The integrated line strength depends on the population of the ground-state energy level E'' , which is proportional to $\exp(-E''/k_B T)$ and depends on the gas temperature T as given by the Boltzmann distribution [Hanson, 2002]. The combined quantity $\alpha(v)x$ is referred to as absorbance or optical density (OD)

$$\text{OD} = -\ln \left[\frac{I(x, v, N)}{I_0} \right] \quad (1.9)$$

and is therefore the exponent of Beer-Lambert's law. For low absorbances $\alpha(v)x \ll 1$, Beer-Lambert's law can be approximated by

$$T(x, v, N) \approx [1 - S_{ij}\Gamma(v)Nx], \quad (1.10)$$

where the transmitted intensity is linearly dependent on the molecular concentration N . The error remains within 1 % for $\alpha(v)x \leq 0.1$. For example, consider the H_2^{16}O absorption line at around $3\,663\,\text{cm}^{-1}$ at a pressure of 70 hPa as depicted in Fig. 1.2 (red trace). For an absorption path length of 76 m, and a water mixing ratio of 100 ppmv, this absorption line has an absorbance at the line center of $\text{OD} = 4.35 \times 10^{-3}$. This indicates that the linear approximation of Beer-Lambert's law remains within a 1 % error for a H_2O mixing ratio up to 2 300 ppmv.

Important parameters that define an absorption line, such as the integrated line strength and broadening coefficient, can be found for many molecules in extensive databases such as the HITRAN (high-resolution transmission) molecular absorption database [Rothman *et al.*, 2005]. These parameters along with the appropriate lineshape function can be used to calculate absorption spectra for a single gas species as well as for multi-species gas mixtures. In direct absorption measurements these parameters can be used to obtain quantitative information on the gas species investigated. Measurement accuracy in this case strongly depends on how well the absorption-line parameters and the absorption path length are known.

1.1.4 Advantages of laser spectroscopy

In-situ trace-gas detection for atmospheric research has been performed by several techniques other than laser spectroscopy. These techniques include mass spectrometry, gas chromatography, chemoluminescence detection, and fluorescence spectroscopy as the most commonly used techniques.

Mass spectrometry (MS) makes use of the mass difference of different molecules. The molecules to be measured are first ionized. An electric field can then be applied to the charged molecules in order to affect their path and/or their velocity. Different molecular masses thus lead to different paths and/or velocities, i.e., the molecular species are separated and can be detected sequentially. The detection is mostly performed by electron multipliers, where the ions hit a surface and produce free electrons which are then multiplied by an avalanche effect.

While MS can provide very high sensitivity, selectivity is often limited due to mass overlap of certain molecules. For example, the water isotopologues H_2^{17}O and HDO both have mass $M = 19$. This mass overlap thus requires pre-preparation of the molecular species to be detected. It should be noted, though, that mass spectrometry is advantageous over laser spectroscopy for the detection of large molecules. This is because the absorption spectra of large molecules tend to show very broad absorption features due to the very high number of closely spaced absorption lines. Mass spectrometry can provide the necessary selectivity if no mass overlap exists.

Gas chromatography (GC) is a technique, where the molecular species to be measured is vaporized (if present in solid or liquid phase) and the gas is subsequently flown through a column, which's walls are coated by a liquid or polymeric substance. The interaction of the gaseous molecular species with the walls of the column causes the different species of the

sample gas mixture to leave the column at different times. This effect is due to the different adsorption coefficients of the different molecules. The molecular species can thus be identified qualitatively by the time they require to pass the column. Detection is performed by, e.g., a flame-photometric detector or by a mass spectrometer. These detectors also allow for quantitative measurements.

Due to the principle of GC, only sequential measurements of different species can be performed. In addition, the required time for a measurement can be relatively high. Depending on the length of the column, measurement times may reach several minutes [Wert, 2002]. Particular for in-situ atmospheric measurements aboard aircraft platforms, this measurement times are often too long to detect small-scale atmospheric processes.

Chemoluminescence relies on the chemical reaction of the molecular species of interest with the surface of a polymeric dye. The reaction energy excites the dye molecules, and a fraction of this excitation energy is emitted as photons (luminescence) when the excited molecules return to their energetic ground state. Chemoluminescence has been used for in-situ measurements of ozone (O_3) and nitrogen oxides (NO_y) (among others) [Brenninkmeijer *et al.*, 2007; Güsten *et al.*, 2002].

Chemoluminescence offers the advantage of fast measurements (around 10 Hz) [Brenninkmeijer *et al.*, 2007]. The technique is highly selective, but it has only been developed for the detection of a few atmospheric species. The chemical reactions that take place during the measurement are irreversible, and regular replacement of the dye is required. Chemoluminescence is not an absolute measurement technique, and regular calibration is necessary.

Within fluorescence spectroscopy, the molecules of interest are excited by photon absorption. As the excited molecules return into their energetic ground state, they emit their excess energy in terms of photons, and this fluorescence signal can be detected. Gerbig *et al.* [1999] have performed in-situ measurements of carbon monoxide (CO), where the CO molecules are excited by ultra violet (UV) light from a CO_2 discharge lamp ($\lambda \approx 150\text{ nm}$). The resulting fluorescence is detected using a photomultiplier tube.

Fluorescence spectroscopy is reported to be a highly linear measurement technique with good reproducibility and fast response [Brenninkmeijer *et al.*, 2007]. Additionally, this technique allows for very compact instrumentation comprising an optically and electronically relatively simple and robust setup. On the other hand, the selectivity is somewhat reduced due to the very broad molecular/atomic absorption features in the UV spectral region. Fluorescence spectroscopy is basically feasible in the infrared (IR) spectral region, where the spectral lines are much narrower than in the UV. However, spontaneous emission of IR photons is much weaker than for UV photons due to non-radiative transitions [Hanson, 2002]. Quenching effects, where the excitation energy of the molecule is transferred non-radiatively to, e.g., a collision partner, might further reduce the fluorescence signal. In addition, only a fraction of the fluorescence photons, which are emitted into all directions, can be detected [Demtröder, 1996]. The fluorescence signal can be increased to some extend by collection optics.

In contrast to the measurement techniques introduced above, laser spectroscopy provides several advantages for atmospheric trace gas detection, and the most important advantages are presented below.

High spectral power density: The laser is a monochromatic light source, i.e., the emission spectrum is very narrow, and the full width at half maximum (FWHM) typically ranges

between 1 MHz and a few tens of MHz. In addition, lasers for spectroscopic measurements provide output powers in the milliwatt regime. Both narrow emission spectrum and relatively high power result in a very high spectral power density.

High spectral power density offers some unique advantages [Demtröder, 1996]. The emission spectrum is much narrower than the molecular absorption lines at typical sample pressures of 50 hPa – 1 000 hPa. For example, the linewidth (FWHM) of the H₂O absorption lines around 2.73 μm (see Fig. 1.2 on Page 7) at a pressure of 70 hPa is around 600 MHz. In contrast, the width (FWHM) of the laser used to probe these absorption lines is around 10 MHz.⁴ This means, that the entire laser emission spectrum overlaps with the absorption spectrum of the molecular absorption line, and the laser output power can fully be used to record absorption spectra at a very high signal-to-noise ratio (SNR). High SNR also leads to a relatively fast measurement time of the order of seconds to around one minute.

Good collimation: Laser radiation can be very well collimated (transformed into a nearly parallel beam). This fact allows to realize long absorption paths of up to several tens of meters [Dyroff *et al.*, 2004; Herriott *et al.*, 1964; McManus *et al.*, 1995; Richard *et al.*, 2002; White, 1942] in multipass absorption cells (see Section 1.3.1 on Page 15). The long absorption paths enable both measurements of absorption transitions with a very small line strength, as well as very small concentrations of molecular species.

High selectivity: Absorption spectroscopy with lasers provides a very high potential for molecule-selective measurements without the need of sample preparation. Unlike in mass spectrometry, where several species may occupy the same mass, laser spectroscopy probes isolated absorption lines that can be clearly attributed to a certain molecular species. This technique even allows for simultaneous measurement of multiple species, provided that the respective absorption lines are closely separated [Li *et al.*, 2004; Moreau *et al.*, 2005; Webster *et al.*, 2001].

Compact instrument design: For the use aboard aircraft and balloon platforms, further constraints apply. Since space and payload is generally very limited, the instruments are required to be small and lightweight [Kerstel *et al.*, 2006; Kormann *et al.*, 2005; Viciani *et al.*, 2008; Webster *et al.*, 1994; Weidmann *et al.*, 2005]. Properly engineered, laser spectrometers can meet these requirements, and the water isotopic-ratio laser spectrometer described in the present dissertation is an example of a combination of all the above advantages into a very compact, lightweight, selective, and highly sensitive instrument.

1.2 Limitations of laser spectroscopy

The limitations of laser spectroscopy in atmospheric research originate from the need to detect very low mixing ratios of gases, which are typically in the order of parts per trillion by volume (pptv) to parts per million by volume (ppmv) range. In Section 1.2.1 an example based

⁴In contrast to the FWHM of the laser emission spectrum at 2.73 μm mentioned above, the FWHM of black-body radiation with a peak at the same wavelength ($T = 1\,060\text{ K}$) is approximately $1.33 \times 10^{14}\text{ Hz}$ (3.3 μm).

on water isotopic ratio measurements is given that indicates how large the absorption signals must be in order to conduct meaningful measurements. Such low absorption signals require low noise instrumentation that is in addition immune to systematic drift. Section 1.2.2 introduces to the most important limitations of laser-based trace-gas detection, namely noise and systematic drift. For a given absorption signal, the noise determines the sensitivity of the spectrometer. For statistically independent Gaussian distributed signals, averaging may reduce the noise. However, systematic drift typically limits the averaging time within which the noise can be effectively reduced. This maximum averaging time as well as the detection limit can be determined by means of the Allan variance method.

1.2.1 Low absorption

Most atmospheric gases are present at mixing ratios in the range of parts per trillion by volume (pptv) to parts per million by volume (ppmv). To investigate the processes of interest, the measurement uncertainties have to be a factor of 10 to 100 lower. Even when molecular absorption transitions with a high integrated line strength are probed, it is often the case that absorption path lengths of a few tens of centimeters are too short to achieve the necessary absorption signal.

Considering the water vapor isotopic ratio measurements described in the present work, the detection limit of the major isotopologue H_2^{16}O is required to be of the order of 100 ppbv, where one calculates a line-center absorbance of 5.7×10^{-8} for a gas pressure of $p = 70 \text{ hPa}$ and an absorption path length of 1 m. This means that an extremely small change in the laser power transmitted through the absorbing medium (gas) of the order of 5.7×10^{-8} must be detected, which corresponds to a power attenuation of $2.5 \times 10^{-7} \text{ dB}$. Such a low detection limit is well below of what has been achieved by laser spectroscopy, even for the most sensitive instruments.

Therefore, different techniques have been developed to achieve higher absorption path lengths. The absorption signal and thus the measured signal scales directly with the absorption path length (see Beer-Lambert's law in Eq. 1.8). These techniques range from long free-space optical paths in the atmosphere, folded paths using retro reflectors or multiple-pass cells, to resonant optical cavities. Using these techniques, it is thus possible to increase the absorption path length to a range between several meters and several kilometers.

In the present work, multiple pass absorption cells are used, where the laser beam is reflected between two mirrors. These cells are closed from the environment and can be operated at reduced pressure to reduce absorption line broadening and thus increase selectivity. Furthermore, closed cells allow for an active calibration scheme, which is necessary where high absolute accuracy is required.

1.2.2 Noise and drift

The sensitivity — or detection limit — of a spectrometer is determined by the signal-to-noise ratio (SNR) with which the spectral data are recorded.

The signal is determined by the laser power incident on the detector as well as on the strength of the absorption signal. For tunable diode laser spectrometers, typical laser powers are in the $500 \mu\text{W}$ to 10 mW regime. With the use of multipass absorption cells, the power

incident on the detector is reduced due to the imperfect reflectivity of the cell mirrors. For example, the power transmission through a multipass cell with 238 passes and a mirror reflectivity of 99 % is around 9 %. Dust on the mirror surfaces will further reduce the transmission. Typical absorption signals for trace gas measurements are of the order of $OD = 1 \times 10^{-5}$ to 1×10^{-4} at the center of the absorption line.

The detection system of a laser absorption spectrometer in the simplest case comprises a laser, a detector and a preamplifier. These components may lead to noise that is superimposed on the signal, and which determines the SNR. The SNR is defined as

$$SNR = \frac{\sigma_x}{\bar{x}}, \quad \sigma_x = \sqrt{(x - \bar{x})^2}, \quad (1.11)$$

Here \bar{x} is the mean and σ_x is the standard deviation of the random signal x .

The laser source introduces noise due to the quantized nature of the emitted photons. This noise, which is commonly termed Poisson noise, is unavoidable, and it only depends on the emitted laser power. Noise originating from electronic devices can be caused by the discreteness of the charge carriers that have to pass a potential barrier such as the pn-junction of a photodiode. Like photon noise, this noise is unavoidable. At the detection of light it is not possible to distinguish between noise that is due to photons or due to the detector. The resulting noise is commonly termed shot noise. Shot noise from transistors within the preamplifier, and thermal noise — which is due to random thermal fluctuation of electrons in resistors — also contribute to the total noise of the detection system.

In addition to Poisson noise, the laser may show excess noise, which is due to spontaneously emitted photons or — in case of multiple longitudinal modes — mode-competition noise. This excess noise depends on the device structure. A more detailed description of these noise sources is given in Section 2.3.1 on Page 55.

For many atmospheric trace-gas measurements, absorbance sensitivities in the lower 10^{-5} to the 10^{-6} range are required. Such a low detection limit can only be achieved with low-noise instrumentation that comprises a low-noise laser source as well as a low-noise detector and preamplifier. But even with the best absorbance sensitivity of $\sim 7.5 \times 10^{-6}$ measured in one second [Weibring *et al.*, 2006], the spectral data have to be averaged over one minute or longer.

The individually recorded spectroscopic data can be assumed as statistically independent measurements. It can further be assumed that the process leading to the random fluctuation of the signal is ergodic. This means that the statistical properties (mean value \bar{x} and variance σ_x^2) of a single measurement are representative for an ensemble of measurements of the same kind. In this case, averaging of an ensemble of N measurements will lead to a reduction of the variance by [Profos and Pfeifer, 1997]

$$\sigma_N^2 = \frac{1}{N} \sigma_x^2. \quad (1.12)$$

As the process is assumed to be ergodic, the ensemble average is equivalent to the time average, and consequently the variance is reduced in proportion to the averaging time τ

$$\sigma_\tau^2 = \frac{1}{\tau} \sigma_x^2. \quad (1.13)$$

However, the averaging time is often limited to about 30 s to 60 s due to time-dependent background (etalon) structures superimposed on the spectra. A fraction of the laser radiation might be reflected back from surfaces of optical components (lenses, windows, etc.) and

may interfere with the main laser beam. As the laser wavelength is tuned over a wavelength region of interest, this results in a periodic structure superimposed on the measured spectra. Such structures are known from Fabry-Pérot interferometers. As the frequency and phase of the background structure depends on the optical setup, the structure may change due to, e.g., thermal expansion of optical components. As a consequence, the background structures change over time. Within a laser spectrometer the background structures can have multiple time constants, frequencies, and phases. Their variation with time induces changes in the measured trace-gas concentration. This so-called drift reduces the effectiveness of time averaging [Werle *et al.*, 1993].

It is therefore important to quantify the maximum time in which averaging of spectral data can improve the detection limit. This can be achieved by analyzing time-series data by means of the Allan variance method [Allan, 1966; Werle *et al.*, 2004].

Consider a time series of mixing ratio measurements, such as the simulated one depicted in Fig. 1.3 (a). The data set is recorded within a constant detection bandwidth of 1 Hz, i.e., a measurement every one second ($\Delta t = 1$ s). The random fluctuation of the data is due to the finite signal-to-noise ratio of the detection process, and for this simulation $\sigma^2 = 1$ (ppmv)² was chosen. A drift within the data was simulated by adding a curve with constant slope⁵, as indicated by the dashed line in Fig. 1.3 (a).

The data set thus recorded can be divided into m subgroups of length τ , where each subgroup has $N = \tau/\Delta t$ elements. The mean value of each subgroup is $A_s(\tau)$. The Allan variance σ_{Allan}^2 is then defined as the mean squared deviation of adjacent averages of integration time τ [Werle *et al.*, 2004]

$$\sigma_{\text{Allan}}^2(\tau) = \frac{1}{2m} \sum_{s=1}^m [A_{s+1}(\tau) - A_s(\tau)]^2. \quad (1.14)$$

The Allan variance versus integration time is generally plotted on a log-log-scale. For the simulated time series it is depicted in Fig. 1.3 (b). For short integration times τ , σ_{Allan}^2 decreases proportional to the integration time until a minimum is reached. The integration time at this minimum is denoted as the optimum integration time or the stability time τ_{opt} . In the present example, the stability time is $\tau_{\text{opt}} \approx 20$ s. At integration times longer than τ_{opt} , drift dominates the system, and the variance increases. Analyzing the data set in this manner thus provides a means to predict the detection limit of the detection system for a given averaging time [Werle *et al.*, 2004], where the lowest detection limit (highest sensitivity) is achieved at τ_{opt} . The detection limit in this example is $\sigma \approx 265$ ppbv for averaging over 20 s.

For conducting atmospheric trace-gas detection with laser spectrometers, high stability times are desired in order to achieve high sensitivity by means of data averaging. In case of high stability times, the background structures can be recorded frequently by flushing the absorption cell with zero air, i.e., by a gas mixture without the target species. The background spectra can then be subtracted from the sample spectra to achieve background free spectra of the target gas of interest [Werle *et al.*, 2004].

However, the flushing and the resulting gas exchange times lead to a considerable degradation of the system's duty-cycle. In addition, especially on high-speed airborne platforms, relatively small spatial and short temporal atmospheric inhomogeneities cannot be measured

⁵A constant slope is often a good approximation for drift within observation times of a few minutes.

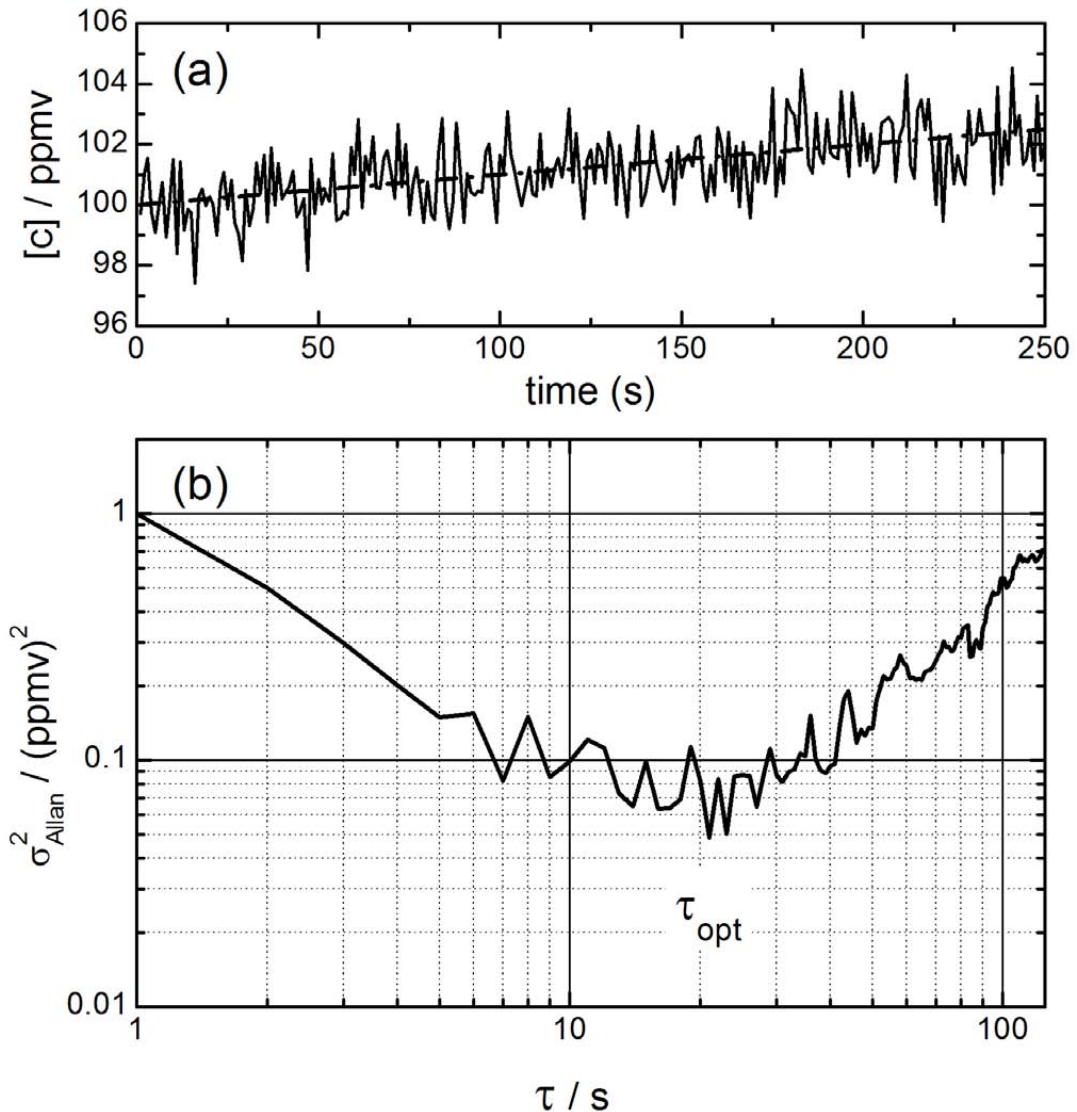


Figure 1.3: (a) Simulated time series of volume mixing-ratio data. A curve with a constant slope (dashed line) has been added to simulate systematic drift. (b) Allan variance of the time-series data in Fig. (a). For short integration times, the Allan variance decreases proportional to the integration time. After an integration time of around 20 s — which is denoted as the stability time τ_{opt} — the variance increases due to systematic drift.

when performing background measurements. Especially for polar molecules, exchange times can be significant due to adsorption and desorption to the absorption cell and tubing walls. For water vapor in particular, which is a target gas of interest within the present work, background measurements are impractical due to the high exchange times. In this case, high sensitivity at short integration times is required in order to reach the necessary detection limit within the stability time of the spectrometer.

1.3 Sensitivity improvement

The sensitivity of a laser spectrometer is proportional to the signal-to-noise ratio (SNR) of the recorded data. The signal is determined by the gas concentration and by the absorption path length. While the gas concentration cannot readily be increased to reach a higher signal level, the absorption path length can be increased using multipass absorption cells as will be explained in Section 1.3.1. In order to reach high sensitivity, the noise of the detection system must be minimized. In Section 1.3.2 suggestions as to the selection of low-noise system components, such as laser, detector and preamplifier as well as the optical setup are given. While proper spectrometer design and low-noise lasers and detectors are a prerequisite for high-sensitivity measurements, often the signal-to-noise ratio must be further improved. This can be achieved by means of modulation-spectroscopy techniques, which are introduced in Section 1.3.3. These techniques realize narrow-band filtering using a lock-in amplifier.

1.3.1 Multipass absorption cell

Multipass absorption cells have been developed as a means for signal enhancement, as the absorption signal is directly proportional to the interaction length of the laser radiation and the trace gas. Different cell designs have been realized. In chronological order, the first long-path cell was proposed by *White* [1942]. This cell comprises three concave spherical mirrors, between which the laser beam is multiply reflected. Using three mirrors makes this approach somewhat bulky and complicated to align.

Herriott et al. [1964] have proposed a design that comprises only two concave spherical mirrors with equal radius of curvature r . The mirrors are separated by a distance d close to the mirror radius of curvature. The front mirror contains a coupling hole through which the laser beam is coupled into the cell, as depicted in Fig. 1.4(a). Note that the spot size is depicted decreasing with increasing number of reflections for a better illustration. If the laser beam is directed onto a circle on the rear mirror, the spots on the mirrors form a circular spot pattern. After a certain number of passes through the cell, the laser beam exits the cell through the same coupling hole but inverted angle. This reentrant condition depends on the mirror radius of curvature and the mirrors' separation. Absorption path lengths of up to ≈ 50 m are feasible for a cell base length of 0.5 m and reasonably sized mirrors ($\varnothing \leq 10$ cm).

In order to better fill the mirror surface and to reach a higher number of passes per unit volume, *McManus et al.* [1995] have proposed a design that contains two astigmatic concave mirrors, i.e., the mirrors have two different radii of curvature in orthogonal directions. In this case, the laser beam is injected into the cell through a coupling hole in the center of the front mirror [Fig. 1.4 (b)]. Due to the slight astigmatism of the mirrors, the spots on the mirrors form a Lissajous pattern and thus more evenly fill the mirror surface. Absorption path lengths of up to 250 m for a cell base length of ≤ 1 m have been realized with this approach [Dyroff, 2003; *McManus et al.*, 1995; *Richard et al.*, 2002]. Fig. 1.4(b) shows such a cell geometry, where the spot pattern corresponds to 238 passes.

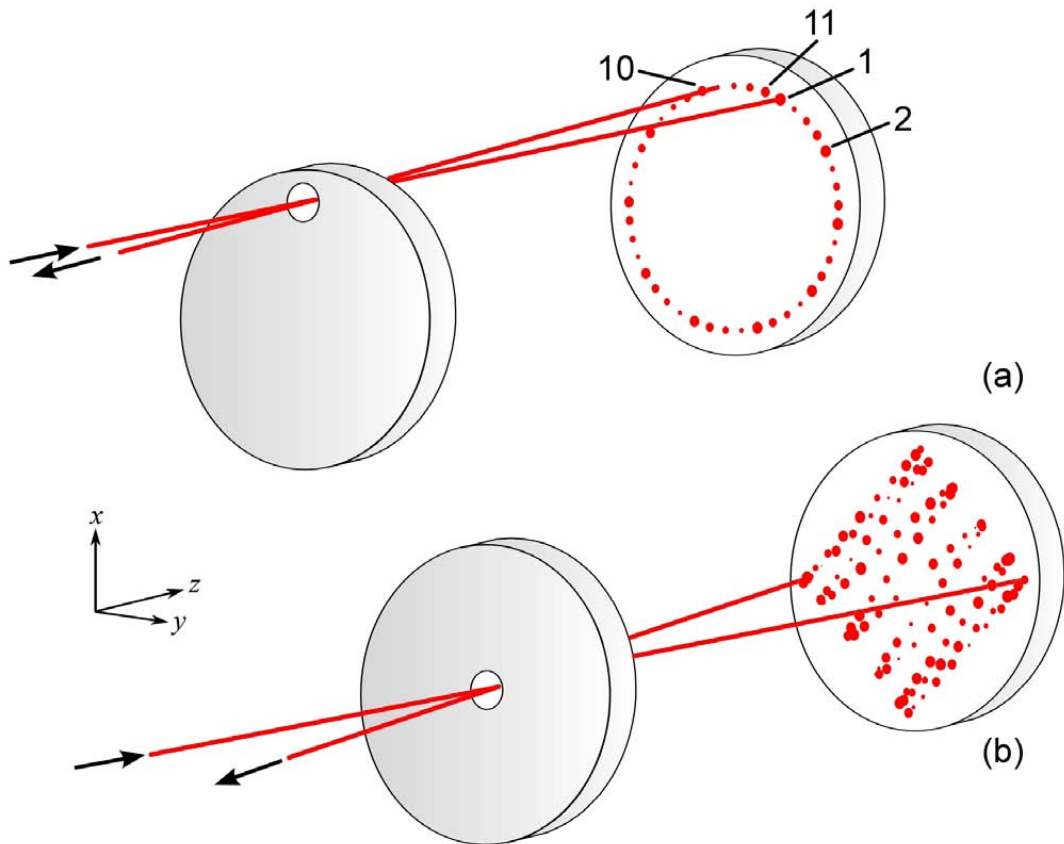


Figure 1.4: Two possibilities to achieve a high absorption path length. In both Figures, the spot size is depicted decreasing with increasing number of reflections for better illustration. **(a)** Multipass cell approach by *Herriott et al.* [1964], where the laser beam is reflected between two spherical mirrors. Depicted is a spot pattern for 82 passes within the cell. For this configuration, the spots form a circle on the mirror surface. The numbers indicate the number of the respective reflection on the rear mirror. **(b)** Multipass cell approach by *McManus et al.* [1995] that comprises two astigmatic mirrors. The spots on the mirrors form a Lissajous pattern, and it is generally possible to reach a higher number of passes per unit volume. In this case, a cell with 238 passes is shown.

1.3.2 Laser, detector, and setup

The prerequisite for high sensitivities with detectable changes of the mixing ratio of around 5×10^{-6} is the use of a low-noise laser and detector. Low-noise lasers emit in a single longitudinal mode. In multimode lasers, however, amplitude modulation of the output power due to random power fluctuations within multiple emission modes is observed. In order to reach optimum performance, a low-noise current source and a high-quality temperature controller are also required. Noise superimposed to the laser injection current transforms into a random amplitude modulation of the laser output as well as a random wavelength modulation, both of which can significantly reduce the performance of a laser spectrometer. Laser temperature fluctuations can lead to a significant modulation of the emission wavelength, which can result in jitter or long-term drift.

As the sensitivity of the detection system is determined by the signal-to-noise ratio, the detector should have both low noise and high responsivity. The detector responsivity depends on the detector material and laser wavelength. In general, the peak responsivity of the detector should closely match the laser operation wavelength in order to achieve the maximum signal. Detector material selection is governed by the laser operation wavelength.

The noise of the detection process is due to the random fluctuations of the detected photons (Poisson noise). Furthermore, it is due to charge carriers, that are randomly passing the pn-junction of the detector because of their thermal energy ($k_B T$). This yields a random noise current in the external circuitry. Cooling of the detector diode can therefore reduce this noise current. Temperatures as low as -80°C can be achieved by thermoelectric coolers. If lower temperatures are required, the detectors are mostly cooled to liquid nitrogen temperatures ($\approx 77\text{ K}$).

Finally, the optical setup must be extremely rugged to avoid amplitude modulation due to vibration of optical components. Therefore, short free-space optical paths should be used. Furthermore, the setup must be insensitive with respect to temperature changes for reducing temperature-induced misalignment of optical components.

1.3.3 Modulation spectroscopy

Modulation techniques have been developed as a means to increase the signal-to-noise ratio of a given measurement by reducing the noise contribution. These techniques generally have a common principle. The signal to be measured is transformed into a periodic signal by modulation of a certain parameter. For spectroscopic measurements, the modulated parameter can for example be the emission wavelength λ (or frequency ν) of a tunable laser source. This technique of wavelength-modulation spectroscopy will be described first. Another technique — which has also been used within the present work — is the modulation of the absorption coefficient of a specific absorption line by means of the Stark effect. This Stark modulation spectroscopy is introduced below. The periodic signal is detected by means of a lock-in amplifier, and the working principle of which will be described at the end of this Section.

Wavelength-modulation spectroscopy

Wavelength-modulation spectroscopy is a well established technique to increase the signal-to-noise ratio [Arndt, 1965; Bomse *et al.*, 1992; Fried *et al.*, 1993; Hager, Jr. and Anderson, 1970; Iguchi, 1986; Olson *et al.*, 1980; Reid and Labrie, 1981; Reid *et al.*, 1980; Uehara, 1998; Wahlquist, 1961; Werle, 1998]. The absorption signal, which is obscured by noise, is transformed into a periodic signal by modulating the emission frequency ν of a tunable laser source at a specific (angular) frequency $\omega_{\text{mod}} = 2\pi f_{\text{mod}}$. An example — which shows a section of an absorption spectrum — is depicted in Fig. 1.6(a) on Page 23. Thereby, the emission frequency ν of the laser source is modulated with a modulation amplitude a around an operating point $\bar{\nu}$ by $\Delta\nu = a \cos(\omega_{\text{mod}} t)$. The sweep rate of the laser emission frequency is assumed to be very small compared to the modulation frequency ($\omega_{\text{scan}} \ll \omega_{\text{mod}}$). The resulting absorption signal $A(\bar{\nu} + \Delta\nu)$ depends on $\bar{\nu}$ and the modulation of ν . It can be expanded into a

Taylor series at \bar{v} [Preston and Dietz, 1991; Werle, 1998]

$$A(\bar{v} + \Delta v) = A(\bar{v}) + \frac{dA(\bar{v})}{dv} \Delta v + \frac{1}{2} \frac{d^2 A(\bar{v})}{dv^2} \Delta v^2 + \dots \quad (1.15)$$

With $\Delta v = a \cos(\omega_{\text{mod}} t)$ and minor rearrangements⁶ the Taylor series becomes

$$A(\bar{v} + \Delta v) = A(\bar{v}) + \frac{dA(\bar{v})}{dv} a \cos(\omega_{\text{mod}} t) + \frac{1}{2} \frac{d^2 A(\bar{v})}{dv^2} \frac{1}{2} a^2 [1 + \cos(2\omega_{\text{mod}} t)] + \dots \quad (1.16)$$

Modulation of v thus produces a signal $A(\bar{v} + \Delta v)$ that has components which are periodic with the modulation frequency ω_{mod} and its higher harmonics ($2\omega_{\text{mod}}, 3\omega_{\text{mod}}, \dots$).

Demodulation of the signal $A(\bar{v} + \Delta v)$ with a lock-in amplifier (see explanation on Page 21) at the modulation frequency ω_{mod} yields a signal proportional to the first derivative of $A(\bar{v})$. Demodulation at twice the modulation frequency ($2\omega_{\text{mod}}$) yields a signal proportional to the second derivative of $A(\bar{v})$. If the operating point is slowly scanned over the absorption line, one obtains a first- or second-derivative spectrum, respectively. For this reason, wavelength-modulation spectroscopy is often referred to as derivative spectroscopy.

While for small modulation amplitudes a the Taylor series expansion is valid, for large a it diverges [Wilson, 1963]. Reid and Labrie [1981] suggest to use a Fourier expansion that is valid for arbitrary a . As the time dependent term of $A(\bar{v} + \Delta v)$ is chosen to be an even function of time, a cosine-Fourier expansion is valid:

$$A(\bar{v} + \Delta v) = \frac{B_0}{2} + \sum_{n=1}^{\infty} B_n(\bar{v}) \cos(n\omega_{\text{mod}} t) , \quad (1.17)$$

where the n^{th} ($n = 0 \dots \infty$) Fourier coefficient is calculated by

$$B_n(\bar{v}) = \frac{1}{\pi} \int_0^{2\pi} A(\bar{v} + \Delta v) \cos(n\omega_{\text{mod}} t) dt . \quad (1.18)$$

The shape of the resulting signal remains similar to the n^{th} derivative as can be seen in Fig. A.1 in Appendix A. However, at very large modulation amplitude ($a \gtrsim 3 \text{ HWHM}$), the second-derivative absorption line becomes significantly broadened, and the line-center signal is reduced. Appendix A shows the resulting second-derivative signals of a Lorentzian and Gaussian lineshape at different modulation amplitudes. The calculation of analytical expressions of the Fourier coefficients of several lineshape functions has been performed by Wahlquist [1961], Arndt [1965], Reid and Labrie [1981], and Iguchi [1986]. It was furthermore determined by Reid and Labrie [1981], that for a sinusoidal modulation of v , the maximum second derivative signal at the line center is achieved by adjusting the modulation amplitude to $a = 2.2\gamma$, where γ is the HWHM of the lineshape function. This is also depicted in Appendix A.

Fig. 1.5 shows the basic principle of wavelength modulation spectroscopy. The top trace depicts a Lorentzian lineshape (black trace). The laser emission frequency is modulated about a mean frequency \bar{v} , which is considered as operating point (gray circle), by a sinusoidal

⁶using the relations $\cos(2\alpha) = \cos^2(\alpha) - \sin^2(\alpha)$ and $1 = \cos^2(\alpha) + \sin^2(\alpha)$

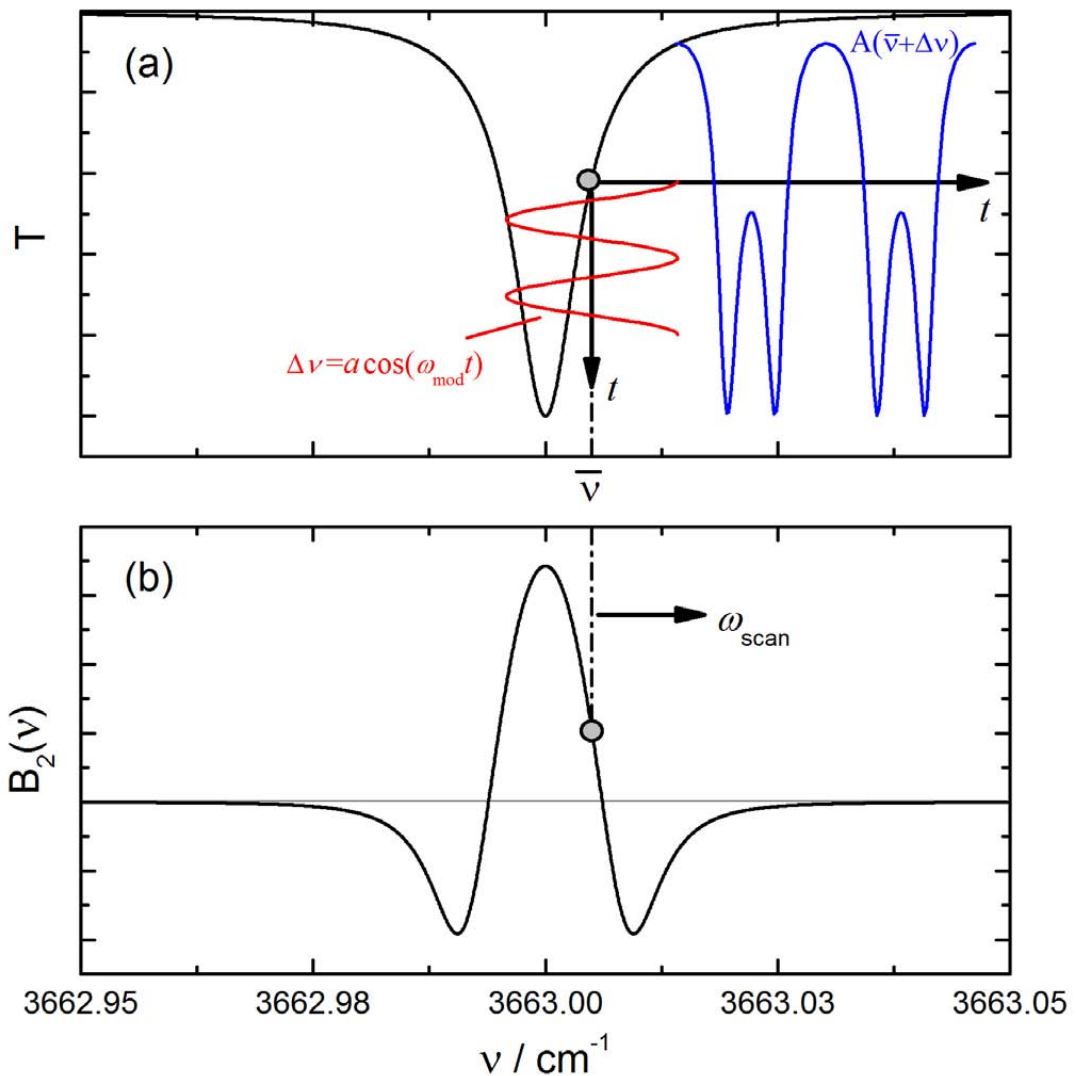


Figure 1.5: (a) Arbitrary calculated direct transmission spectrum (*black* trace) based on a Lorentzian lineshape function. For any wavelength within the spectrum, the laser wavelength is modulated by a sinusoidal waveform with a modulation amplitude corresponding to approximately 2.2 times the HWHM of the absorption line (*red* trace). This wavelength modulation transforms into an amplitude modulation, and the resulting signal (*blue* trace) contains contributions of the modulation frequency (ω_{mod}) and its higher harmonics ($2\omega_{\text{mod}}$, $3\omega_{\text{mod}}$, etc.). (b) Absorption signal containing only the contribution of the second harmonic of the modulation frequency ($2\omega_{\text{mod}}$). The resulting line shape is similar to the second-derivative of the direct transmission spectrum.

function $\Delta\nu = \bar{\nu} + a \cos(\omega_{\text{mod}} t)$ (*red* trace). Thereby the absorption signal is also modulated, and the signal $A(\bar{\nu} + \Delta\nu)$ at the detector has the time-dependent form as shown by the *blue* trace. Demodulation of $A(\bar{\nu} + \Delta\nu)$ with a lock-in amplifier at twice the modulation frequency ($2\omega_{\text{mod}}$) results in the second-derivative spectrum depicted in Fig. 1.5 (b).

Wavelength modulation spectroscopy, and second harmonic detection in particular offers advantages over direct absorption measurements. The most important advantage is related

to the fact that with second harmonic detection a signal in proportion to the curvature of the absorption profile is detected. The target gas is confined in an absorption cell, and the absorption experiments are generally performed at reduced pressure to enhance selectivity. The absorption lines from gases inside the cell are narrow, and their curvature is high compared to the curvature of the absorption line of the target gas outside the absorption cell, which is generally at ambient pressure (compare with Fig. 1.2 on Page 7). The second-derivative signal contribution of the “broad” absorption at ambient pressure is therefore minimized although the absolute absorption signals might be similar [Demtröder, 1992].⁷

Wavelength-modulation spectroscopy thus can reduce uncertainties due to concentration changes within the free-space optical path of the spectrometer. Furthermore, the signal of broad and unresolved absorption features of large organic molecules is also separated from the signal of the narrow absorption lines of the target gas of interest [Tittel *et al.*, 2003].

Furthermore, as discussed by Iguchi [1986], unwanted etalon fringes can be reduced by proper choice of the modulation amplitude a . The etalon fringes are caused by interference between partially reflected beams of the laser radiation at transmissive optics within the laser beam path, or within the multipass absorption cell. By avoiding transmissive optics, or at least by using antireflective coatings, etalon fringes can be minimized to some extend. However, fringes originating from inside the absorption cell cannot completely be avoided, even by the most careful alignment. In a typical spectrometer setup employing multipass absorption cells, the free spectral range (FSR) of the etalon fringes is often similar to the width of the absorption lines at reduced pressure (50–100 hPa), i.e., a few 100 MHz. Iguchi [1986] has shown that such fringes can effectively be eliminated by only slight adjustments to the modulation amplitude (See Appendix A for a description of etalon signals at different modulation amplitudes). This effect was also used in the present water isotopic ratio spectrometer (Chapter 2). It must be pointed out, though, that this technique does only reduce the magnitude of one fringe structure, thereby mitigating the associated errors.

Wavelength-modulation spectroscopy has been widely used in atmospheric-chemistry studies. For a detection bandwidth of 1 s, absorbance sensitivities in the order of $OD = 10^{-5}$ to the lower 10^{-6} have been achieved [Bomse *et al.*, 1992; Carlisle and Cooper, 1990; Durry *et al.*, 2002; Dyroff, 2003; Goldstein *et al.*, 1992; Kerstel *et al.*, 2002; Kormann *et al.*, 2005; Lübben *et al.*, 1999; Webster *et al.*, 1994; Weibring *et al.*, 2006; Wert *et al.*, 2003a; Wienhold *et al.*, 1998].

Stark modulation spectroscopy

Another promising modulation technique, which has been studied in the present work, and which is described in Chapter 3, employs the selective modulation of the absorption coefficient of an absorption line. With formaldehyde (CH_2O) as the target gas, the Stark effect was used to modulate the absorption coefficient of a rotational-vibrational absorption line by applying a modulated external electric field to the gas. The electric field causes a splitting of the

⁷ Assume a measurement probing the H_2^{16}O absorption line at $3\,663\,\text{cm}^{-1}$ (Fig. 1.2 on Page 7), where inside the absorption cell $p = 70\,\text{hPa}$, $l = 76\,\text{m}$, and $[\text{c}] = 100\,\text{ppmv}$. A H_2O mixing ratio of around $6\,000\,\text{ppmv}$ yields a residual absorption signal equivalent to that inside the cell at a free-space optical path of 1 m. However, second-harmonic detection eliminates most of this residual signal.

ground state and the excited state of the absorption transition. As a result, the lineshape of the absorption transition becomes deformed. This deformation results in an amplitude modulation for any given point of the absorption line. The amplitude-modulated absorption signal can be detected by means of a lock-in amplifier (see description below), which is referenced to the Stark modulation frequency.

Stark modulation is highly selective. First, the absorbing gas must possess a reasonable permanent dipole moment. Furthermore, the ground state and the excited state must have closely separated neighboring energy states with which they can interact (see Section 3.1 for a more detailed description). Even for a very well suited absorbing molecule, such as CH₂O, the majority of the absorption lines does not show a large Stark effect. Stark modulation spectroscopy is thus highly selective and can not only be used to reduce noise, but also to suppress time-dependent spectral background structures. These structures commonly degrade the spectrometer performance by introducing drift, which in turn limits the maximum averaging time of independent spectral data, and thus reduces the detection limit. Stark modulation spectroscopy is furthermore useful as it reduces influences of other molecular absorbers that do not show a Stark effect.

It must be noted, though, that the Stark modulation technique can only be applied to absorption lines of molecules that show a relatively large Stark effect. A more detailed discussion on the applicability to other molecules than formaldehyde is given in Section 3.6.

Lock-in amplifier

The lock-in amplifier (LIA) can be used to detect signals, which are modulated at a specific reference frequency. Lock-in measurements therefore require a reference signal, and in all experiments within the present dissertation, this reference signal was provided by the excitation source (homodyne detection), i.e., a function generator. The LIA is basically a multiplier with a low-pass filter at its output, as depicted in Fig. 1.6 (b). The detector signal V_{sig} is multiplied by the reference signal V_{ref} , and the resulting signal is low-pass filtered.

In the present work, wavelength-modulation spectroscopy with second-harmonic detection has been carried out, and the working principle of the lock-in amplifier will be described based on the demodulation of the detector signal at twice the modulation frequency ($2\omega_{\text{mod}} = 4\pi f_{\text{mod}}$).

Consider the detector-signal component to be measured to be of the form $V_{\text{sig}} \sin(2\omega_{\text{mod}}t + \phi_{\text{sig}})$, i.e., a signal amplitude V_{sig} at a certain angular frequency $2\omega_{\text{mod}}$ and phase ϕ_{sig} . The reference signal can be expressed similarly by $V_{\text{ref}} \sin(2\omega_{\text{mod}}t + \phi_{\text{ref}})$. The detector signal and the reference signal are multiplied and low-pass filtered, and the resulting signal V_{LIA} becomes [Vogelsang, 2004]

$$\begin{aligned}
 V_{\text{LIA}} = & \frac{1}{\tau} \int_0^\tau V_{\text{sig}} V_{\text{ref}} \sin(2\omega_{\text{mod}}t + \phi_{\text{sig}}) \sin(2\omega_{\text{mod}}t + \phi_{\text{ref}}) dt \\
 V_{\text{LIA}} = & \frac{1}{\tau} \int_0^\tau \frac{1}{2} V_{\text{sig}} V_{\text{ref}} \cos[\underbrace{(2\omega_{\text{mod}} - 2\omega_{\text{mod}})}_0 t + \phi_{\text{sig}} - \phi_{\text{ref}}] dt - \\
 & \frac{1}{\tau} \int_0^\tau \frac{1}{2} V_{\text{sig}} V_{\text{ref}} \cos[\underbrace{(2\omega_{\text{mod}} + 2\omega_{\text{mod}})}_{4\omega_{\text{mod}}} t + \phi_{\text{sig}} + \phi_{\text{ref}}] dt .
 \end{aligned} \tag{1.19}$$

V_{LIA} thus contains two signal components, a DC signal at the difference frequency (0) and an AC signal at the sum frequency ($4\omega_{\text{mod}}$). The signal V_{LIA} is low-pass filtered with a bandwidth $\Delta f = 1/\tau \ll f_{\text{mod}}$. Consequently, only the DC signal component is passed through the filter (the integral in line 3 of Eq. 1.19 becomes 0) and V_{LIA} becomes

$$V_{\text{LIA}} = \frac{1}{2} V_{\text{sig}} V_{\text{ref}} \cos(\Delta\phi) , \text{ with} \tag{1.20}$$

$$\Delta\phi = \phi_{\text{sig}} - \phi_{\text{ref}}.$$

Furthermore, due to the $\cos(\Delta\phi)$ dependence of V_{LIA} on the phase difference $\Delta\phi$, only signal components at $\Delta\phi = 0$ are passed. This phase difference $\Delta\phi$ — which can be adjusted at the lock-in amplifier — can be due to different cable lengths of detector signal and reference signal, as well as due to the optical path length within the setup. The lock-in amplifier therefore represents a bandpass filter, which is centered at the modulation frequency ω_{mod} , or in case of second-harmonic detection, at $2\omega_{\text{mod}}$ [Meade, 1983]. The modulation frequency can be chosen such that it is within a low-noise region of the noise spectrum of the detection system, as depicted in Fig. 1.6(c) [Demtröder, 1996].

It is worth to note that the second-harmonic signal could also be isolated using a passive bandpass filter. However, passive filters can drift whereas the lock-in amplifier is — for homodyne detection — always locked to the excitation frequency.

Modulation spectroscopy with second-harmonic detection offers some unique possibilities for noise reduction. Any noise that is present at frequencies which do not lie within the narrow filter bandwidth Δf around the modulation frequency is filtered out by the low-pass filter. The low-pass filter bandwidth can basically be reduced to $\Delta f \ll 1 \text{ Hz}$. For spectroscopic measurements, where spectra are recorded at a certain scan frequency ω_{scan} (typically 10–50 Hz), this scan frequency must lie within the bandwidth of the low-pass filter [Fig. 1.6(d)].

1.4 Important atmospheric trace gases

While basically all atmospheric constituents play a role in chemical and physical processes within the atmosphere, the present dissertation deals with only two of them. Water vapor is

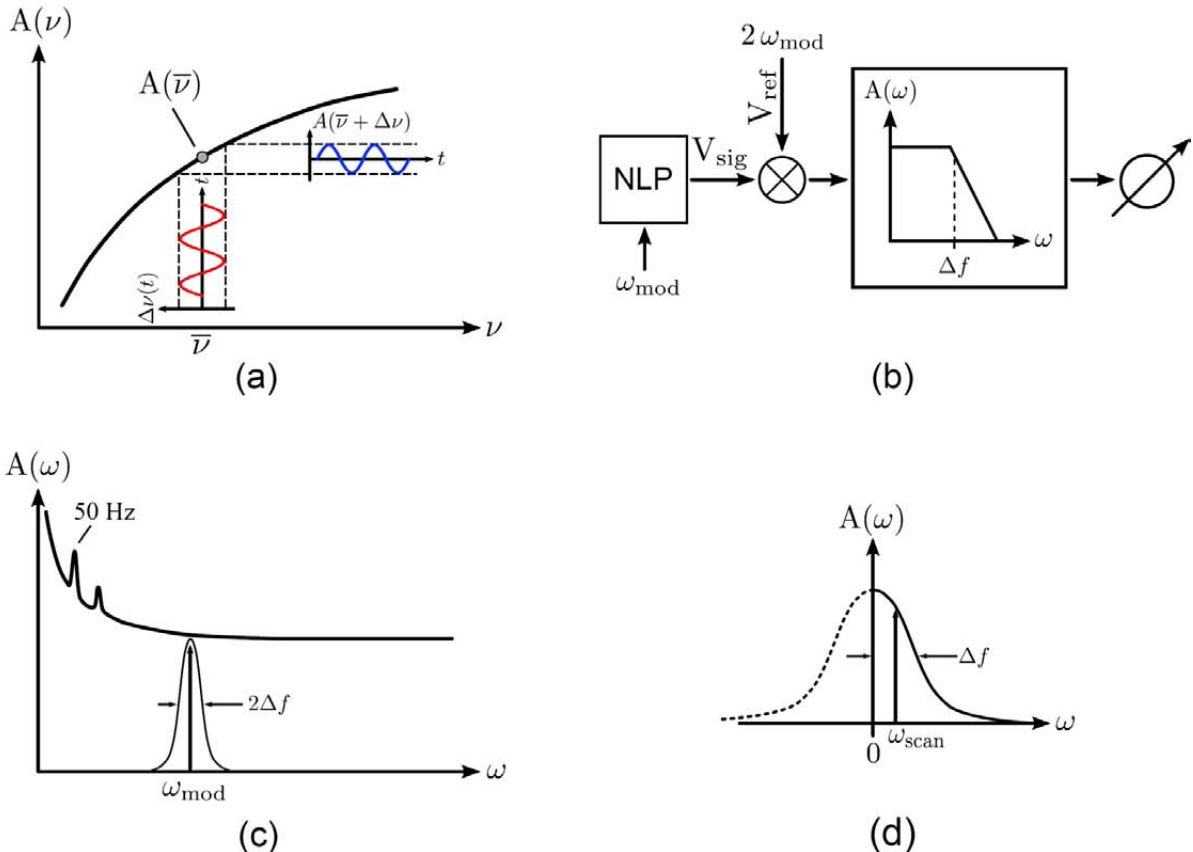


Figure 1.6: (a) Arbitrary signal $A(\nu)$ (black trace). ν is modulated about $\bar{\nu}$ with a modulation amplitude a at a modulation frequency ω_{mod} by $\Delta\nu(t) = a \cos(\omega_{\text{mod}} t)$, red trace). Due to the non-linear curve $A(\nu)$, the resulting signal $A(\bar{\nu} + \Delta\nu)$ (blue trace) has signal components at ω_{mod} and its harmonics ($2\omega_{\text{mod}}$, $3\omega_{\text{mod}}$, ...).

(b) The lock-in amplifier is a multiplier followed by a low-pass filter. A signal is modulated at ω_{mod} . Due to a non-linear process (NLP) such as in Fig. (a), the resulting signal also has a component at twice the modulation frequency ($2\omega_{\text{mod}}$). The lock-in amplifier is referenced to $2\omega_{\text{mod}}$ to detect this signal component. (c) The modulation frequency ω_{mod} is chosen in a low-noise region of the noise spectrum $A(\omega)$ of the photocurrent. (d) The modulation frequency is converted into a DC signal and the low-pass filter with the bandwidth Δf is used to eliminate higher frequency noise. The frequency to record absorption spectra ω_{scan} must be located within the pass-band of the filter.

an effective greenhouse gas and a partner of many important atmospheric chemical reactions. Section 1.4.1 reviews the importance of water and introduces to isotopic ratios⁸ and their usefulness as a tracer for atmospheric transport processes. Formaldehyde is an important gas in atmospheric chemistry, and its importance is described in Section 1.4.2. Both gases have in common that their measurement is challenging due to the high sensitivity requirements.

1.4.1 Water vapor isotopic ratios

Without an atmosphere, the temperature on Earth would be around -18°C , due entirely to absorption of solar radiation by the Earth's surface. The existence of Earth's present atmosphere raises the temperature to an average of around $+15^{\circ}\text{C}$ due to the natural greenhouse effect. Atmospheric water vapor (H_2O) plays an important role in the global radiation budget [Marsden and Valero, 2004], and it provides the largest contribution ($\approx 70\%$) to the natural greenhouse effect. This corresponds to a temperature increase of $\approx 20^{\circ}\text{C}$. Without this contribution life on Earth as found to date would not be possible. Other important gases involved in the natural greenhouse effect are carbon dioxide (CO_2 , 26 % contribution), ozone (O_3 , < 8 % contribution), nitrous oxide (N_2O , 4 % contribution), and methane (CH_4 , 2 % contribution) [Houghton *et al.*, 2001].

Besides being a greenhouse gas, water vapor transports huge amounts of latent heat [Roedel, 1992], and is thus a key player in the energetic budget of the atmosphere. Water is particularly prominent in driving convection and thunderstorms.

H_2O is also involved in many important chemical reactions in the atmosphere. It is the major source of OH-radicals, which is by far the most important oxidant for virtually all organic and inorganic pollutants and compounds.

At very low temperatures near the poles, water, along with nitric and sulfuric acids, forms particles of polar stratospheric clouds (PSCs) [Gao *et al.*, 2004]. Due to chemical reactions at the surface of the PSC-particles, inactive chlorine compounds are transformed into active ones, which in turn can decompose stratospheric O_3 . This is believed to lead to the well known ozone hole over the poles in polar spring.

In contrast to the relevance of H_2O in Earth's atmosphere, its transport processes and paths are still not sufficiently understood, in particular since water is present in gaseous, liquid, and solid phase [Zahn *et al.*, 2006]. This is even more important as the atmospheric water is estimated to be completely exchanged about every nine to ten days [Häckel, 2005], and the highly dynamic H_2O transport is linked to that of other atmospheric constituents as well.

One important scientific question related to the contribution of water to both the global radiation budget and to H_2O -related chemistry is the water transport from the Earth's surface through the troposphere into the stratosphere. It has been recognized that there exists a trend

⁸The International Union of Pure and Applied Chemistry (IUPAC) defines *isotopes* as atoms with the same number of protons but a different number of neutrons, whereas *isotopologues* are molecules which differ only by their isotopic composition [Brenninkmeijer *et al.*, 2003]. The term *isotopomer* (short for isotopic-isomer) is sometimes used, but it is incorrect in this case since it should be used to refer to a molecule with the same isotopic atoms as another molecule, but in a different arrangement. Water does not have any isotopomers, whereas ozone (O_3), for example, has multiple isotopomers including $^{16}\text{O}^{18}\text{O}^{16}\text{O}$ and $^{18}\text{O}^{16}\text{O}^{16}\text{O}$, which are also minor isotopologues.

of increasing stratospheric water concentration by as much as 50 % during the last half century that has not been understood yet [Oltmans *et al.*, 2000; Rosenlof, 2003; Rosenlof *et al.*, 2001]. The important question is: how does water enter the stratosphere? Since different transport processes leave different isotopic signatures of the water vapor (as will be discussed below), the measurement of the isotopic composition of water in an air-mass can significantly improve our understanding of both the origin and the type of transport of this air-mass.

Isotope fractionation effects

The isotopic ratio R of a certain compound is generally expressed as the ratio of the less abundant isotopologue to the most abundant isotopologue. Because the natural variation is generally small, these ratios are expressed in per mille (‰) relative deviation to the respective reference (standard) material [Brenninkmeijer *et al.*, 2003]. Using the oxygen isotopologue H_2^{18}O as an example, this deviation is expressed by

$$\delta^{18}\text{O} = \frac{R_{\text{sample}}}{R_{\text{reference}}} - 1 \quad , \quad (1.21)$$

where $R = \text{H}_2^{18}\text{O}/\text{H}_2^{16}\text{O}$ denotes the ratio of the mixing ratios of H_2^{18}O and H_2^{16}O . Negative δ -values therefore denote a sample that is depleted in less abundant isotopologues (in this case H_2^{18}O) relative to the reference material.

As for water, the reference standard is the **Vienna Standard Mean Ocean Water** (VSMOW)⁹, as defined by the International Atomic Energy Agency (IAEA) [Gonfiantini, 1978; Wise and Watters Jr., 2005]. Further standards (depleted in heavy, less abundant isotopologues), that have been defined by the IAEA are the Greenland Ice Sheet Precipitation (GISP), and the Standard Light Antarctic Precipitation (SLAP) standards. These standards are referenced to VSMOW, and their δ -values are listed in Tab. 1.1 [Barkan and Luz, 2005; Wise and Watters Jr., 2005].

Isotopic ratios of atmospheric water vapor should always be given relative to VSMOW, even though the use of working standards with different isotopic composition is possible (and more convenient). These working standards, however, need to be measured accurately and precisely with respect to VSMOW, e.g., by mass spectrometry. In the present dissertation, two working standards have been used; (a) melt water from an antarctic ice-core (AIC-48), and (b) local ground-water (GW-9). Both standards have been measured in terms of their isotopic composition by mass spectrometry [Wagenbach, 2008], and their isotopic composition is also listed in Tab. 1.1.

The amount of water in the troposphere almost entirely depends on the amount evaporated. Since evaporation depends on temperature, most H_2O is evaporated from the oceans in the tropics and subtropics, where both air and water are warm. The process of evaporation leads to the first fractionation. This isotopic fractionation is a change in the isotopic composition of a compound due to slight differences in vapor pressure (equilibrium fractionation). The vapor pressure of the heavier isotopologues H_2^{18}O , H_2^{17}O , and HDO is slightly lower compared

⁹The relative abundances of the stable isotopologues H_2^{16}O , H_2^{18}O , H_2^{17}O , and HDO in VSMOW are 0.997 317, $1.999\,83 \times 10^{-3}$, $3.718\,84 \times 10^{-4}$, and $3.106\,93 \times 10^{-4}$, respectively.

Table 1.1: Internationally accepted isotopic reference materials (VSMOW, GISP, and SLAP) and working standards (GW-9, AIC-48) of the present study and their isotopic composition with respect to VSMOW. Due to the definition of the δ -scale, the δ -values of VSMOW equal zero.

	$\delta^{17}\text{O} / \text{\textperthousand}$	$\delta^{18}\text{O} / \text{\textperthousand}$	$\delta\text{D} / \text{\textperthousand}$
VSMOW	0	0	0
GISP	-13.12	-24.78	-189.5
SLAP	-29.48	-55.5	-428.0
GW-9	-4.5	-9	-70
AIC-48	-23.8	-47.6	-366

to that of the lightest (and most abundant) isotopologue H_2^{16}O . For example, at 20°C , the H_2O vapor just above the ocean is depleted in heavier isotopologues by $\delta^{18}\text{O} = -12.1\text{\textperthousand}$, $\delta^{17}\text{O} = -6.4\text{\textperthousand}$, and $\delta\text{D} = -80\text{\textperthousand}$ (Fig. 1.7).

The second fractionation — which is denoted as kinetic fractionation — occurs during the transport through the laminar-viscous boundary layer just above the water surface (thickness only a few millimeters). The diffusion is quantified by the diffusion constant of the individual isotopologue. It determines for example the so-called deuterium excess, i.e., the $10\text{\textperthousand}$ offset in Eq. 1.25. During evaporation the kinetic fractionation enhances the equilibrium fractionation, leading to a higher depletion in heavier isotopologues in the vapor phase. During condensation, it reduces the fractionation, leading to slightly less depleted vapor phase.

Upon evaporation, the moist and warm air is lifted to higher altitudes, where it cools and subsequently condenses. The process of condensation is more complex than that of evaporation. Two extremes may be considered: (i) the precipitate remains in the cloud, where precipitate and vapor are in equilibrium, and (ii) the precipitate is removed from the cloud immediately (Rayleigh distillation). For the former case, *Roedel* [1992] shows that the remaining vapor is nearly linearly depleted in heavier isotopologues with increasing condensation. In the case of Rayleigh distillation, precipitate and vapor are no longer in equilibrium, as the precipitate is removed from the cloud. In this case the remaining vapor is depleted exponentially with the amount of water left in the cloud.

In the event of convection, mostly ice particles are formed. This leads to the preservation of the isotopic ratio of the frozen water. These ice particles may be lifted even across the tropopause into the lowermost stratosphere, which leads to the stratospheric water locally being much less depleted in heavier isotopologues. This effect is called ice lofting, and was confirmed by in-situ isotopic-ratio measurements by *Webster and Heymsfield* [2003].

Fig. 1.7 depicts — in a simplified manner — the transport of water, from the source (ocean) to the sink (precipitation over ocean and land). Depending on the temperature, the isotopic fractionation ranges typically from $\delta^{18}\text{O} \approx -12\text{\textperthousand}$ and $\delta\text{D} \approx -80\text{\textperthousand}$ above the ocean to values substantially more depleted in the lower stratosphere ($\delta^{18}\text{O} \approx -160\text{\textperthousand}$ to $-100\text{\textperthousand}$ and $\delta\text{D} \approx -800\text{\textperthousand}$ to $-600\text{\textperthousand}$). In mid-latitudes, such as continental Europe, the depletion of heavy isotopologues in precipitation with respect to VSMOW is around $\delta^{18}\text{O} \approx -10\text{\textperthousand}$ to $-6\text{\textperthousand}$ and $\delta\text{D} \approx -70\text{\textperthousand}$ to $-40\text{\textperthousand}$, with higher depletion towards the east due to the generally westerly wind conditions [Roedel, 1992].

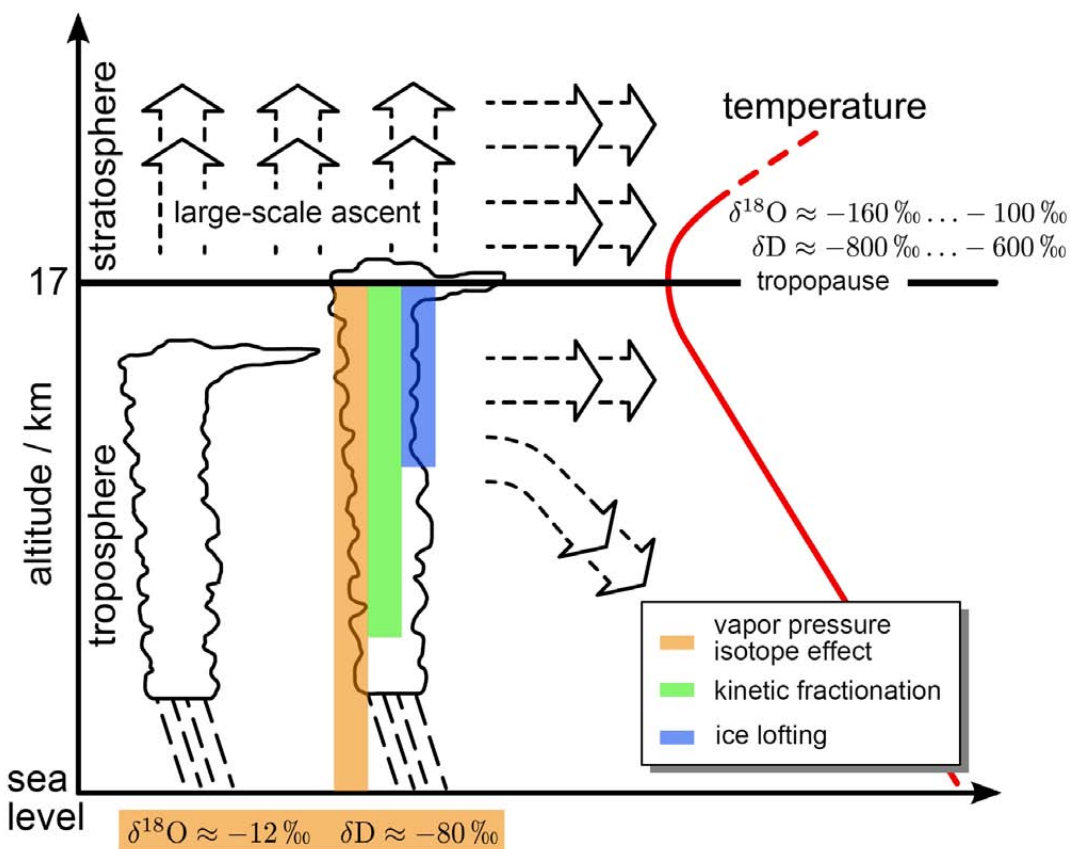


Figure 1.7: Fundamentals of atmospheric transport in the atmosphere. Water is mostly evaporated in the tropics and subtropics. The moist air ascends, and in strong convective systems may penetrate into the lowermost stratosphere. In addition to vertical transport, horizontal transport occurs. The isotopic ratios are fractionated due to vapor-pressure isotope effects (equilibrium fractionation), i.e., during evaporation and condensation, and different masses of the isotopologues (kinetic fractionation) during diffusion processes. In the case where water droplets freeze and ascent into the upper troposphere and lower stratosphere (ice lofting), the isotopic ratio during freezing is preserved, leading to less depletion in heavier isotopologues in the UT/LS.

In the consideration of isotope fractionation effects, two important relations have been found in the past. First, the fractionation of the oxygen isotopologues H_2^{17}O and H_2^{18}O is correlated due to the mass dependence of the fractionation, and *Meijer and Li* [1998] have determined empirically the relation

$$\ln(1 + \delta^{17}\text{O}) = 0.528 \ln(1 + \delta^{18}\text{O}) . \quad (1.22)$$

If the fractionation is determined only by the mass of the isotopologues, we can write

$$\ln(1 + \delta^{17}\text{O}) - 0.528 \ln(1 + \delta^{18}\text{O}) \equiv 0 . \quad (1.23)$$

The deviation from this relation is termed the $\Delta^{17}\text{O}$ anomaly

$$\Delta^{17}\text{O} = \ln(1 + \delta^{17}\text{O}) - 0.528 \ln(1 + \delta^{18}\text{O}) . \quad (1.24)$$

The deviation is caused by mass-independent fractionation. *Franz and Röckmann* [2005] have recently confirmed by analysis of lower stratospheric H₂O samples collected in the southern hemisphere, that the deviations due to mass-independent fractionation are very small (< 2‰) around the tropopause.

Second, *Craig* [1961] has determined a linear dependence of δD and $\delta^{18}\text{O}$ values, which is due to the linear dependence of the isotopic ratios to the equilibrium fractionation. This dependence is commonly referred to as the meteoric water line and was experimentally found to be

$$\delta D = 8 \delta^{18}\text{O} + 10\text{‰} . \quad (1.25)$$

The 10‰ offset is denoted as the deuterium excess and is due to kinetic fractionation. A deviation from the meteoric water line is generally only induced by kinetic fractionation during evaporation.

The measurement of water vapor isotopic ratios therefore provides a means to link a certain condensation history to an airmass. If measurements reveal that water in an airmass is isotopically substantially heavier than one would expect following condensation and Rayleigh distillation, then one can expect this airmass to have experienced a condensation history such as ice lofting, where the isotopic composition was fixed at an early stage, followed by transport. On the other hand, if the isotopic composition can be explained by Rayleigh distillation, one can link a source to the airmass under investigation via the (generally) well known temperature of the ocean as well as the airmass. Deviation from the meteoric water line can in turn be linked to substantial kinetic fractionation effects [Zahn, 2001].

1.4.2 Formaldehyde

Formaldehyde (CH₂O) is one of the most abundant gas phase carbonyl compounds (i.e., molecules containing a O-H double bond) found in the atmosphere. It originates directly or indirectly from many anthropogenic and biogenic processes, such as incomplete fossil fuel combustion, industrial emissions from e.g. power plants or petrochemical industry, biomass burning or vegetative emission. The indirect formation involves the oxidation of terminal alkenes, mostly ethene (C₂H₄) and propene (C₃H₆), and to a lesser extend methane (CH₄).

The measurement of the precursors to CH₂O is typically done by means of gas chromatography. This technique can be applied in the laboratory to gas samples that have been collected, or can be performed in situ. However, the number of measurements is limited by the number of sample containers available, and in-situ measurements mostly take around 15 min [Wert, 2002].

Formaldehyde measurements can be used in this respect as indirect quantity to its precursors (CH₄, C₂H₄, C₃H₆). In addition, CH₂O production also leads to the production of ozone (O₃), which is an important gas for urban and regional air quality assessment. CH₂O measurements are thus useful to determine the sources of photochemical O₃ production, and laser spectroscopy provides a means for fast measurements on the order of 1 s to 60 s.

Formaldehyde has been measured by several techniques in the past [*Hak et al.*, 2005, and references therein], including high pressure liquid chromatography (HPLC), long path length differential optical absorption spectroscopy (DOAS), and tunable diode laser absorption spectroscopy (TDLAS). CH₂O mixing ratios found in the atmosphere range between around 50 pptv in the clean troposphere to around 30 ppbv in polluted areas [Wert, 2002]. While the

above techniques may be capable of detecting these small mixing ratios, only TDLAS is capable to provide high sensitivity measurements at a fast response time.

The small CH_2O mixing ratios, particularly in the clean troposphere, require extremely sensitive instrumentation [Kormann *et al.*, 2003; Roller *et al.*, 2006; Weibring *et al.*, 2007; Wert *et al.*, 2003a], with detection limits of around $\text{OD} = 1 \times 10^{-6}$ (absorbance) at a typical absorption path length of 100 m and a pressure of 70 hPa. As discussed in Section 1.2, high precision measurements require — where applicable — the recording and subtraction of background spectra, which significantly reduces the duty cycle of the measurement. This in turn limits the maximum averaging time to improve the sensitivity, as well as the spatial resolution of airborne measurements. In areas with localized CH_2O production this may prevent the study of these sources. The sample modulation technique based on the Stark effect, as described in Chapter 3, can provide a means to overcome this limitation.

1.5 Airborne research platforms and instrument requirements

While airborne measurements of formaldehyde are basically feasible, and have been successfully performed aboard different airborne platforms in the past [Fried *et al.*, 1999; Weibring *et al.*, 2007; Wert *et al.*, 2003a,b], they are not subject of the present dissertation.

For future airborne deployment of the water isotopic ratio spectrometer described in Chapter 2, there are two potential aircraft platforms available, namely the passenger-aircraft based platform CARIBIC (Section 1.5.1), and the new German high altitude research aircraft HALO (Section 1.5.2) as described below. Employment of measurement instrumentation aboard these platforms places various constraints to the instrument, such as high sensitivity and a compact and lightweight instrument design. The requirements are described in Section 1.5.3.

1.5.1 Long-term passenger-aircraft project CARIBIC

The first platform for potential employment is the measurement container within the **CARIBIC**¹⁰ (Civil Aircraft for the Regular Investigation of the atmosphere Based on an Instrument Container) project [Brenninkmeijer *et al.*, 2007]. Within CARIBIC, an air-freight container is equipped with currently 15 instruments (1.5 tons) that probe different atmospheric molecular compounds as well as aerosol particles of the atmosphere. The container is regularly (about four flights per month) employed on intercontinental flights aboard a Lufthansa Airbus A 340-600 (Leverkusen). This aircraft is equipped with a special inlet system located at the lower side of the aircraft fuselage as depicted in Fig. 1.8. The inlet hosts both forward and sideways facing tubing to sample total (cloud) water and vapor phase water, respectively, a forward facing tube for collection of trace gases, telescopes for differential optical absorption spectroscopy (DOAS) measurements, as well as a forward facing camera. Upon sampling, the air is distributed to the various instruments through heated tubes for either in-situ analysis or collection, where the collected air samples are later analyzed in the laboratory.

¹⁰www.caribc-atmospheric.com



Figure 1.8: Lufthansa Airbus A340-600 “Leverkusen” (Photograph © Florian Kondziela, www.airliners.net). The aircraft is equipped with an inlet system located at the lower side of the fuselage in front of the wing section. The inlet system provides ports to sample trace gases (b), aerosols (c), as well as both total and gas-phase water (d). A forward facing camera system (a) is used to record videos of the flights for better linkage of weather conditions and measurement data. The inlet system is heated to maximize time response and to evaporate cloud droplets or ice particles. The CARIBIC container with the various instruments is located in the cargo bay of the aircraft above the inlet system.

This passenger aircraft is operated at cruising altitudes between 10 km and 12 km, and consequently mostly air of the transition layer between troposphere and stratosphere (tropopause) is sampled. At higher latitudes, however, the aircraft commonly reaches stratospheric air. The measurement container has been employed en route south America, China, and recently India. The routes are thereby subject to the airline-internal employment of this particular aircraft and can not be freely chosen.

1.5.2 New German research aircraft HALO

The second potential platform is the new German high altitude research aircraft **HALO**¹¹ (**H**igh **A**ltitude and **L**ong **R**ange Research Aircraft). The HALO-aircraft is based on a G550 business jet from Gulfstream Aerospace Cooperation (Fig. 1.9). Modifications to transform the regular business jet into a research aircraft are currently being made by Gulfstream and the RUAG company in Oberpfaffenhofen, where the aircraft will be stationed. This aircraft provides very long range capabilities (≈ 10000 km) along with a relatively high maximum altitude (> 15 km). The maximum payload of around three tons enables employment of a number of instruments simultaneously. The aircraft will be operated by the Flight-Department of the DLR¹² in Oberpfaffenhofen, Germany. Scientific operation with HALO will presumably start in July 2009 with a number of demonstration missions. The missions intended for employment of the present water isotopic ratio spectrometer are:

TACTS This mission is scheduled for Sep.–Oct. 2009 and the scientific objective is to study transport within and composition of the upper troposphere and lowermost stratosphere, which plays an important role for the atmospheric chemical and radiative budgets.

ML-CIRRUS is proposed to further improve our understanding of the formation, lifetime, properties, and radiative impact of mid-latitude cirrus clouds. These clouds play an important role for climate and air chemistry. Furthermore, this mission provides the possibility for validation of satellite measurements. ML-CIRRUS is scheduled for Nov.–Dec. 2009.

POLSTRACC This measurement campaign is envisaged to provide new scientific knowledge on the evolution of ozone, cirrus clouds, denitrification and stratosphere-troposphere exchange in the Arctic in times of a changing climate. The mission is scheduled for Feb.–Mar. 2010.

Employment of the present water isotopic ratio spectrometer is subject to constraints related to space and weight as well as measurement performance in terms of sensitivity. These constraints are described in more detail below.

¹¹www.halo.dlr.de

¹²Deutsches Zentrum für Luft- und Raumfahrt

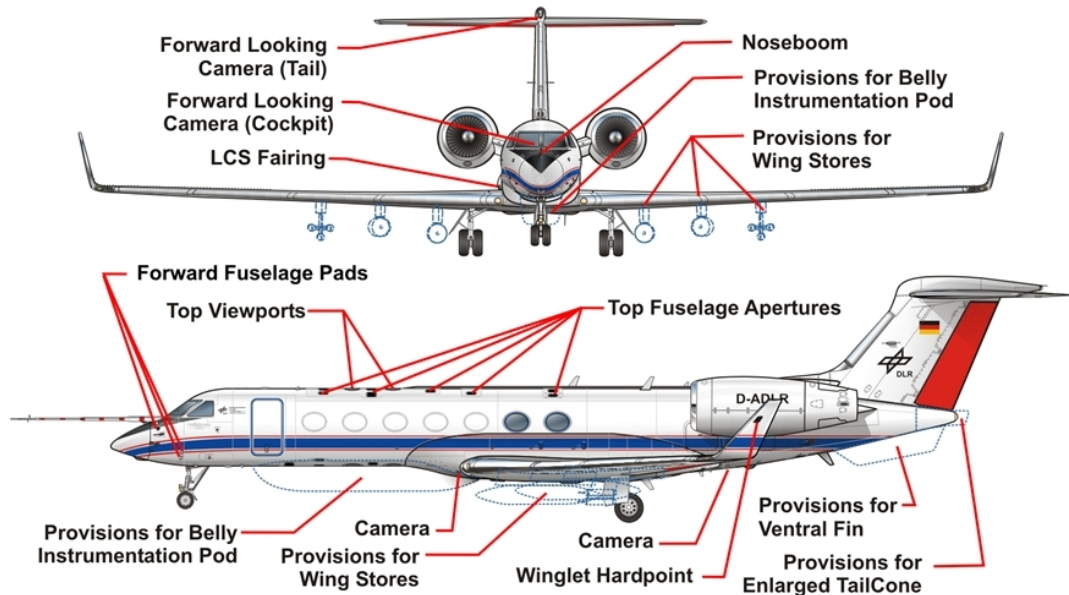


Figure 1.9: The new German High Altitude and Long Range Research Aircraft (HALO). This platform is based on a Gulfstream business jet and is currently modified into a research platform by Gulfstream and the RUAG company in Oberpfaffenhofen. Research instrumentation will be located in the cabin as well as in various wing pods as well as a belly pod. Outside air can be sampled through various fuselage apertures. Since 2004, a similar aircraft (HIAPER) is successfully operated by the United States National Science Foundation and the National Center for Atmospheric Research.

1.5.3 Instrument requirements

Due to the relatively low cruising altitude of around 10...12 km of commercial airliners, the air sampled during CARIBIC flights is mostly of tropospheric origin, with occasional stratospheric intrusions [Zahn, 2008]. In the troposphere, the water vapor mixing ratio ranges between > 5000 ppmv near the ground to approximately 10 ppmv in the upper troposphere. In the stratosphere in contrast, the water mixing ratio is generally much lower ($\approx 3 \dots 5$ ppmv). On the other hand, the HALO research aircraft, having a certified cruising altitude of 15 km, provides the capability of extensive flights into the dry stratosphere. This means that the spectrometer must be capable to measure isotopic ratios within a large range of water mixing ratios, and must provide the necessary sensitivity (precision).

The expected changes in isotopic ratio (deviation from ocean water) are thereby around $\delta^{18}\text{O} = -160$ to $-100\text{\textperthousand}$ for H_2^{18}O and approximately half of that for H_2^{17}O . The envisioned measurement precision for $\delta^{17}\text{O}$ and $\delta^{18}\text{O}$ is about $20\text{\textperthousand}$ for water mixing ratios between 25 ppmv and 100 ppmv. Changes in HDO, which is not further discussed in the present work, are much larger ($\delta\text{D} = -800$ to $-600\text{\textperthousand}$), and therefore the required measurement precision is about $50\text{\textperthousand}$. Measurements of HDO and consequently δD will be possible with an upcoming version of this instrument, as discussed in Chapter 2.5.

In addition to the high sensitivity requirements, measurement accuracy is crucial. The envisioned strategy to achieve high accuracy is to perform in-flight calibration of the instrument by providing a well characterized measurement standard. To this end, a strong effort

led to the development of a suitable calibration gas generator, which is described in detail in Section 2.2.3.

Regardless of the aircraft used, these platforms add mechanical requirements to the measurement instrument that very much differ from laboratory or ground-based applications. On airborne platforms one generally has to deal with mechanical vibration and shock, that may induce alignment changes in optical equipment, and thus may potentially lead to a degradation in instrument performance. In addition, aircraft cabin temperature and pressure changes by as much as 30 °C and 200 hPa, respectively, thus inducing mechanical deformation of components of the instrument [Dyroff, 2003; Dyroff *et al.*, 2004]. Therefore the instrument must provide temperature stabilization and a rugged design in order to minimize performance degradation.

On the other hand, and in particular for the CARIBIC and HALO platforms, instrument space and weight are extremely limited. Any of the instruments employed on these platforms need to fit in 19-inch racks, where the height of the present instrument is limited to < 40 cm. The instrument weight is limited to about 40 kg. In contrast to other high-sensitivity laser spectrometers employed on different airborne platforms [Hanisco *et al.*, 2007; Kormann *et al.*, 2005; Webster *et al.*, 1994; Wert *et al.*, 2003a], these constraints are rather tight, especially because the instrument performance needs to be comparably good, or perhaps better, than standard equipment.

Furthermore, the present instrument is required to operate in a fully autonomous mode, including warmup phase, frequent calibration, and must be able to deal with changing environmental conditions such as cabin temperature and sample gas pressure. This is in contrast to other, larger airborne platforms, such as the National Center for Atmospheric Research (NCAR) C-130. On these platforms, a human operator attends the flights, handles the instrument and can react to perturbations of the measurement conditions.

Chapter 2

Highly sensitive measurements of water vapor isotopic ratios

In the present Chapter, the design and performance analysis of a highly sensitive laser spectrometer for water vapor isotopic ratio measurements is presented. Measurements of the isotopic ratio of water are a valuable tool to study atmospheric transport processes. Despite its usefulness, such measurements have only been performed by a few research groups, and Section 2.1 reviews the techniques applied and the results that have been achieved.

Section 2.2 then describes the design of the laser spectrometer. This includes the description of the optical part of the spectrometer in Section 2.2.1. Section 2.2.2 then discusses the selection of suitable absorption lines, which goes hand in hand with the selection of the laser source and the photodetector. A suitable set of strong absorption lines as well as low-noise laser and detector is a prerequisite for high-sensitivity isotopic-ratio measurements. In addition to a high sensitivity, regular calibration is important in order to achieve high accuracy. To this end, a calibration-gas source has been built, and its design is described in Section 2.2.3. Finally, Section 2.2.4 describes the data acquisition and post-processing procedure, which is used to determine the isotopic ratio of water vapor within a (generally) unknown gas mixture.

The present spectrometer has been extensively tested in order to determine the system stability time and the detection limit for isotopic ratio measurements (Section 2.3). As a first step, the signal-to-noise ratio of the detection system, comprising the laser diode and the detector/preamplifier, has been studied. The analysis is described in Section 2.3.1. This is followed by a description of isotopic-ratio measurements in Section 2.3.2. These measurements have been performed in order to determine the detection limit as well as the stability time of the spectrometer. Several aspects are discussed that may determine the stability time. Finally, the spectrometer response to different isotopic water standards has been tested. The results, which are discussed in Section 2.3.3, are used to determine the accuracy of the spectrometer. A conclusion (Section 2.3.4) finalizes the this Section.

The performance specifications of the final instrument are summarized in Section 2.4. This Section presents in a compact form the physical properties of the present spectrometer as well as its detection limit and accuracy.

A discussion of techniques that may potentially lead to an even more improved sensitivity is given in Section 2.5.

2.1 Existing techniques for airborne isotopic ratio measurements

Water isotopologues have found increasing interest during the last decade as a means to better understand the transport processes of water in the atmosphere. The first measurements have been made by remote sensing from balloon or spaceborne platforms [Dinelli *et al.*, 1991; Moyer *et al.*, 1996; Rinsland *et al.*, 1984, 1991], and a number of further remote measurements with different instruments have followed [Herbin *et al.*, 2007; Johnson *et al.*, 2001; Nassar *et al.*, 2007; Payne *et al.*, 2007; Steinwagner *et al.*, 2007; Urban *et al.*, 2007; Worden *et al.*, 2006]. While these measurements can improve our understanding of large-scale processes, in-situ measurements are necessary to provide inside into small scale processes, such as isolated convective cells in tropical latitudes. However, the number of in-situ instruments and measurements is still very limited until to date.

Zahn [2001] and Franz and Röckmann [2005] have measured water isotopic ratios by collecting water samples in situ using a cold trap, with subsequent laboratory-based analysis by mass spectrometry. While mass spectrometry is capable to deliver high precision measurements (about 0.2 ‰), a relatively large water sample is required. This in turn requires long sampling times (about 20 min) during the flight, especially at low water concentrations, which limits the spatial resolution of the measurement. In addition, the technique requires substantial sample preparation due to mass-overlap of the H₂¹⁷O and HDO water isotopologues (both M=19).

Webster and Heymsfield [2003] have measured H₂O isotopic ratios in the 1 484 cm⁻¹ (6.74 μm) spectral region employing the ALIAS tunable diode laser spectrometer [Webster *et al.*, 1994], which is based on wavelength-modulation spectroscopy using a 80 m multipass absorption cell. This instrument was employed for a total of eleven flights aboard the NASA WB-57 aircraft during the CRYSTAL-FACE¹ campaign in 2003 [Jensen *et al.*, 2004; Webster and Heymsfield, 2003, see also supplemental online material]. The instrument calibration is performed pre-flight using certified water samples, and the reported uncertainty is 50‰ for water vapor mixing ratios ≥ 10 ppmv, and larger for water vapor mixing ratios < 10 ppmv.

Kerstel *et al.* [2006] measured H₂O isotopic ratios in the 7 183 cm⁻¹ (1.39 μm) spectral region using their IRIS instrument. The instrument is based on optical feedback cavity-enhanced absorption spectroscopy (OF-CEAS) [Morville *et al.*, 2005], where a laser beam is coupled into the fundamental mode of a high finesse optical cavity. A detector behind the cavity measures the transmission spectrum of the cavity. Due to the high reflectivity of the cavity mirrors, an effective optical path length of > 4 km ($\sim 20\mu\text{s}$ residence time) has been reached. The instrument calibration is performed in the laboratory using two different isotopic standards.

The instrument was flown on a few engineering flights aboard the NASA WB-57 aircraft in 2006. At very stable conditions, the uncertainties in isotopic ratios are reported to be 1 ‰, 3 ‰, and 9 ‰ for $\delta^{18}\text{O}$, $\delta^{17}\text{O}$, and δD , respectively, for data averaged over 30 s and at a total water mixing ratio of about 200 ppm. However, the precision achieved is generally worse because the averaging time is limited by systematic drift [Kerstel *et al.*, 2006; Kerstel, 2007].

Hanisco *et al.* [2007] report on the application of two instruments developed simultaneously, the integrated cavity output spectrometer (ICOS) [Sayres, 2006] to measure $\delta^{18}\text{O}$, $\delta^{17}\text{O}$,

¹Cirrus Regional Study of Tropical Anvils and Cirrus Layers Florida Area Cirrus Experiment

and δD , and the laser induced fluorescence spectrometer (HOxotope) to measure δD [*St.Clair et al.*, 2006]. Both instruments flew on the NASA WB-57 aircraft as part of the AVE-WIIF² campaign during June and July 2005.

The ICOS device measures in the 1484 cm^{-1} ($6.74\text{ }\mu\text{m}$) spectral region, where the laser beam is injected into a high finesse cavity at an off-axis direction. The laser beam therefore produces a spot pattern much like in a Herriott cell, however providing a much greater effective optical path length of up to 4.2 km [Sayres, 2006] as the laser beam does not fully exit the cavity after fulfilling the reentrant condition (compare with Eq. 3.6). The system is calibrated in-flight using a 20 ppmv standard from a gas cylinder [Sayres, 2006]. This gives rise to potential fractionation effects as water sticks to the cylinder walls, thus leading to a slightly different isotopic ratio (remaining water in the cylinder is expected to be heavier than outgoing water). The calibration uncertainty of this instrument is reported to be 50‰ [Hanisco *et al.*, 2007]. The instrument weights about 250 kg , and requires about 1.5 kW of power [Moyer *et al.*, 2007].

Within the HOxotope instrument, water is first photolyzed with an excimer lamp at 172 nm , producing ground state OH and OD radicals. The radicals are excited with laser radiation at 287 nm from a frequency-doubled dye laser. Fluorescence of neighboring OH and OD emission lines is detected at 309 nm [*St.Clair et al.*, 2006]. The calibration with water standards is performed in the laboratory, and the calibration uncertainty of this instrument is reported to be 50‰ [Hanisco *et al.*, 2007; *St.Clair et al.*, 2006].

The three groups mentioned above are — to the best of my knowledge — at present the only groups worldwide that work (or have worked) on in-situ measurement of water isotopic ratios. Their instruments have been successfully employed during relatively short measurement campaigns to study rather isolated atmospheric phenomena. However, due to the scarcity of the conducted measurements, the transport of water in the upper troposphere and lower stratosphere (UT/LS) is presently still relatively poorly quantified. In this context I believe that the unique possibilities for long-term employment of the present isotopic ratio spectrometer aboard the CARIBIC as well as HALO aircraft (see Section 1.5) will ultimately lead to a better understanding of transport processes in Earth’s atmosphere.

2.2 Spectrometer design

In the following Sections the various aspects of the design of the present water isotopic ratio spectrometer are described. First, the design of the optical layout of the spectrometer is described in Section 2.2.1. This layout, which includes an astigmatic multipass absorption cell, is highly compact in order to meet the size requirements aboard research aircraft. The Section continues with a discussion on the selection of suitable absorption lines, which is closely related to the selection of a laser source and detector (Section 2.2.2). This is followed by the description of the sampling system and the calibration gas source in Section 2.2.3. The calibration gas source has been developed to achieve a high measurement accuracy by regular calibration of the spectrometer with known isotopic water standards. The data acquisition and the

²Aura Validation Experiment Water Isotope Intercomparison Flight

procedure to determine the isotopic ratios from raw H₂O spectra is described in Section 2.2.4. Finally, a conclusion of the spectrometer design is made in Section 2.2.5.

2.2.1 Optics

The optical part of the isotopic ratio spectrometer is depicted schematically in Fig. 2.1. It comprises a distributed feed-back (DFB) diode laser³ emitting in a single longitudinal mode around 3 663 cm⁻¹ (2.73 μm) as described in Section 2.2.2. The laser chip is mounted inside a TO-8 package which also contains a Peltier element and a thermistor to maintain a certain laser temperature (here of 35 °C).

The converging laser beam is first collected by an $f = 25$ mm focal length (NA = 0.45) plano-convex CaF₂ lens. It is then focused into a multipass absorption cell by means of a Galileo-type telescope. The telescope consists of an $f = 300$ mm concave mirror, followed by an $f = -120$ mm convex mirror. A flat mirror in front of the multipass cell is used to align the laser beam into the cell, and to align the output beam via an $f = 100$ mm convex focusing mirror onto the sample detector⁴ (SD). The collimation lens, the MPC- and reference-cell windows, as well as both detectors are slightly tilted with respect to the optical axis to minimize back-reflection along the optical axis.

The multipass absorption cell⁵ (MPC) is an astigmatic Herriott-type cell as proposed by *McManus et al.* [1995]. It contains two $\phi = 3.8$ cm astigmatic concave mirrors in a near-confocal arrangement. The base length of the cell is 320 mm, and the cell volume is 0.5 l. The laser beam is coupled into the MPC at an angle of 3.2° within the horizontal plane through a 4 mm diameter coupling hole located in the center of the front mirror. The beam is then reflected 238 times within the cell, thereby accumulating 76 m of absorption path. Due to the astigmatism of the mirrors, the spots on the mirror surfaces form a Lissajous pattern as depicted in Fig. 2.1 (b). Note, that for a better illustration, the spots are depicted with decreasing spot size for increasing number of reflection. The laser beam exits the MPC through the same coupling hole, but at inverted angle, and is then focused onto the sample detector using a $f = 100$ mm concave mirror.

A fraction (8 %) of the laser power is picked-off by a pellicle beam-splitter and aligned through a reference cell containing pure H₂O at a pressure of 25 hPa. The reference beam is then focused onto the reference detector⁶ (RD) by means of a $f = 100$ mm concave mirror. The reference signal is used for active stabilization of the laser wavelength.

The beam of a visible diode-laser (not shown in Fig. 2.1 (a) for simplicity) is co-aligned to the infrared laser beam using a second (removable) pellicle beam splitter located in the collimated path of the infrared laser beam. This visible beam is used to assist the alignment procedure of the infrared laser through the multipass absorption cell.

All optical components are mounted on a 520x400 mm² custom-made aluminum optical breadboard⁷. The breadboard is designed of an aluminum sandwich structure, where the top-

³NanoPlus GmbH, Gerbrunn, Germany

⁴Model J19-TE4, LaserComponents GmbH, Garching, Germany

⁵Model AMAC-76, Aerodyne Research Inc., Billerica, MA, USA

⁶Model J12-TE2, LaserComponents GmbH, Garching, Germany

⁷Thorlabs GmbH, Dachau, Germany

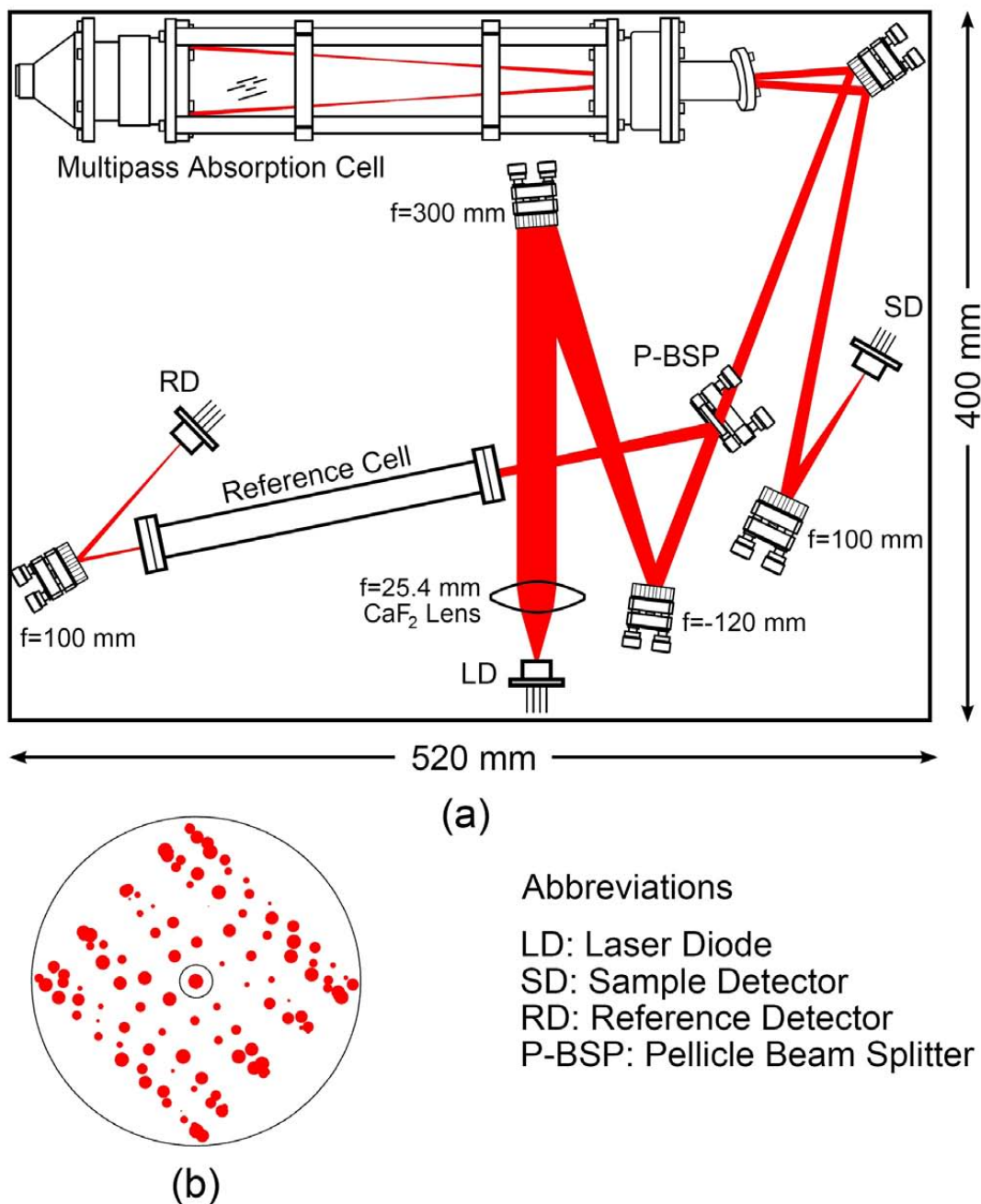


Figure 2.1: (a) Schematic of the optical design of the spectrometer. The laser beam is collected by a $f = 25 \text{ mm}$ plano-convex CaF_2 lens, and then imaged into the center of a multipass absorption cell by means of a telescope consisting of a $f = 300 \text{ mm}$ concave spherical mirror, followed by a $f = -120 \text{ mm}$ convex spherical mirror. After 238 passes through the absorption cell the laser beam is focused on the sample detector (SD) using a $f = 100 \text{ mm}$ spherical mirror. A fraction of the laser power (8 %) is picked-off by a pellicle beam-splitter and directed through a reference cell containing pure water at 25 hPa. The reference beam is then focused onto the reference detector (RD) by a $f = 100 \text{ mm}$ spherical mirror. (b) Calculated spot pattern on the front mirror of the multipass cell. For better illustration, the spot size is depicted decreasing with increasing number of reflections. Due to the astigmatism of the mirrors, the spots on the mirror surfaces form a Lissajous pattern.

Abbreviations

- LD: Laser Diode
- SD: Sample Detector
- RD: Reference Detector
- P-BSP: Pellicle Beam Splitter

and bottom plates are solid, and the core is made of a thin honeycomb structure. This design allows for high stability at a relatively light weight. The breadboard is mounted on vibrational-damping elements⁸ to reduce misalignment effects due to instrument vibration during airborne operation.

2.2.2 Laser and photodetector

The selection of suitable absorption lines for isotopic ratio measurements is one of the most important aspects in the design of an absorption spectrometer. The absorption lines can have a direct impact on the performance of any spectrometer, including sensitivity or measurement precision as well as selectivity.

However, the selection of an appropriate laser source as well as detector goes hand-in-hand with the selection of absorption lines. Availability of laser emission wavelengths, compactness of the laser source, and the complexity of operation does add additional constraints.

Constraints on absorption line selection

The measurement of isotopic ratios — or any molecule in general — requires probing of isolated absorption lines. Therefore such measurements are usually performed in the near infrared (N-IR) to mid-infrared (mid-IR) spectral region, where most smaller molecules exhibit a unique spectrum of rotational-vibrational absorption lines (see Section 1.1).

Even though high selectivity of absorption lines for single molecular species can be achieved by reducing the gas pressure, cross-interference with other molecular species is most often present in a gas mixture such as Earths atmosphere. Finding of suitable absorption lines thus requires knowledge about as many absorption lines as possible of all molecular species present in the gas mixture to be analyzed. The required data, i.e., line-center frequency v_0 , integrated line strength S_{ij} , and pressure broadening coefficient γ_C^0 can be found in extensive databases such as the HITRAN database [Rothman *et al.*, 2005]. Fig. 2.2(a) depicts the integrated line strengths of water (red) along with other potentially interfering molecular species in the spectral region of 1 000–10 000 cm⁻¹ (10–1 μ m) as listed in the HITRAN database.

The measurement of isotopic ratios places certain constraints on the selection of absorption lines because in this case multiple absorption lines (one pair per isotopic ratio) need to be probed simultaneously. These constraints are

Similar absorption cross-section at abundance levels of interest to avoid, e.g., saturation of one absorption line at a common absorption path length. Even though this constraint can be overcome by using different absorption path lengths for the different absorption lines [see McManus *et al.*, 2002; Waechter and Sigrist, 2007, for measurements of CO₂, CH₄, and N₂O isotopologues], it adds complexity and increases the size of the spectrometer.

One laser should access the absorption lines within a single scan, which requires the absorption lines to be located in a relatively narrow spectral window. The use of multiple lasers would add a great amount of complexity to the spectrometer, both in terms of the optical

⁸Enidine, Weil am Rhein, Germany

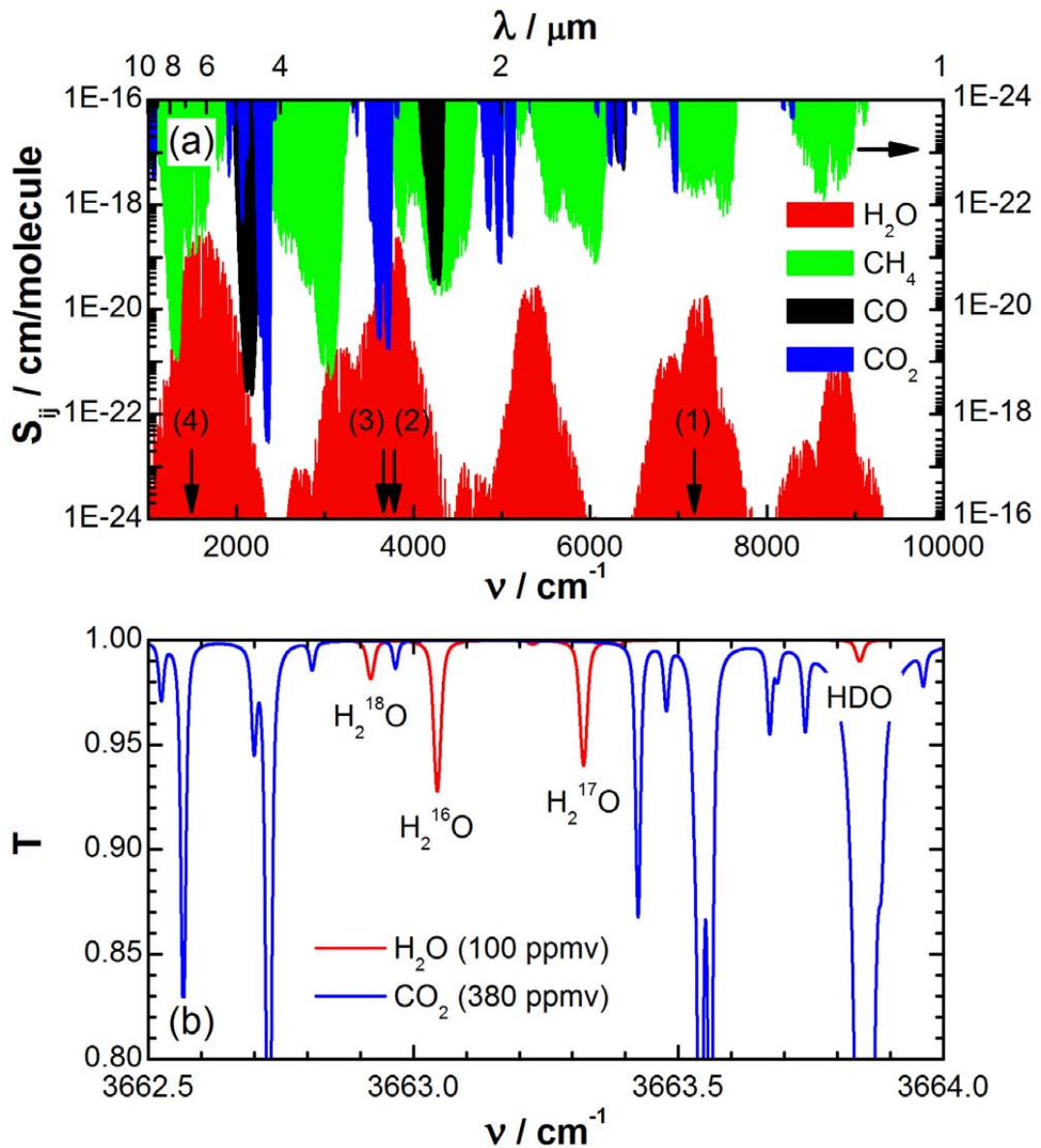


Figure 2.2: (a) Plot of the integrated line-strength versus wavenumber of H_2O along with other important and potentially interfering molecular species. Only those lines are shown that exhibit a line-strength of $\geq 1 \times 10^{-24} \text{ cm}^2/\text{cm}\cdot\text{molecule}$. Weaker lines are generally not suitable to detect low concentration levels of these molecules. The wavenumber range of 1000 cm^{-1} – 10000 cm^{-1} corresponds to a wavelength range of $10 \mu\text{m}$ to $1 \mu\text{m}$. The labels (1), (2), (3), and (4) mark the four most suitable spectral windows for water vapor isotopic ratio measurements. (b) Calculated transmission spectrum of 100 ppmv H_2O and 380 ppmv CO_2 at a gas pressure of 50 hPa, and an absorption path length of 76 m. The window region corresponds to label (3) in (a). Labeled are the absorption lines of the four stable isotopologues of H_2O .

layout as well as the data acquisition. *Wienhold et al.* [1998] have successfully realized such an instrument employing three lasers, however at the cost of a reduced duty cycle due to the time-multiplexed operation of the three lasers.

Similar ground-state energy E'' because the integrated line strength S_{ij} depends on the population of ground-state level and this population in turn depends on temperature. *Gianfrani et al.* [2003] give an approximation of the temperature dependent integrated line strength as

$$S_{ij}(T) = S_{ij}(T_0) \left(\frac{T_0}{T} \right)^{3/2} \exp \left[-hc \frac{E''}{k_B} \left(\frac{1}{T} - \frac{1}{T_0} \right) \right]. \quad (2.1)$$

This can — at largely different E'' — lead to large temperature-dependent uncertainties in isotopic ratio, when the temperature drifts between the recording of the calibration spectrum and the actual ambient spectrum.

The measurement of the isotopic ratios $\delta^{17}\text{O}$, $\delta^{18}\text{O}$, and δD of all stable isotopologues of water requires probing of absorption lines of the four isotopologues H₂¹⁶O, H₂¹⁷O, H₂¹⁸O, and HDO. Localization of suitable spectral windows has been done reviewing the literature as well as by screening of the HITRAN database [*Rothman et al.*, 2005]. The results of this screening indicate that there exist only two spectral windows in the N-IR to mid-IR spectral region where all four absorption lines can be probed that fulfill all the constraints mentioned above. These windows are found

- in the N-IR at 7 183 cm⁻¹ (1.39 μm), previously been investigated by *Kerstel* [2007] and *Gianfrani et al.* [2003] and marked as (1) in Fig. 2.2 (a).
- in the mid-IR at 1 484 cm⁻¹ (6.74 μm), where isotopic ratios have been measured by *Webster and Heymsfield* [2003] and *Hanisco et al.* [2007]. This window is marked as (4) in Fig. 2.2 (a).

The absorption lines in the N-IR [position (1) in Fig. 2.2 (a)] can be probed with radiation of diode-lasers from the telecom market. These lasers are relatively low-cost and can be operated at room-temperature. However, the integrated line strength of the H₂O absorption lines is around one order of magnitude weaker than for the lines in the mid-IR located in a fundamental rotation-vibration band of water.

The mid-IR spectral window at 1 484 cm⁻¹ (6.74 μm) [position (4) in Fig. 2.2 (a)] is well suited in terms of the spectroscopic constraints discussed above. On the other hand, available laser sources — such as lead-salt tunable diode-lasers or quantum-cascade lasers — as well as detectors in this spectral region require cryogenic operation at liquid nitrogen temperatures. Unfortunately, on both the CARIBIC and the HALO airborne platforms, such lasers/detectors are impossible to use due to the physical size of the dewars required to house the laser and detectors. On the CARIBIC passenger aircraft liquid nitrogen is prohibited due to safety concerns.

It was therefore decided to include spectral windows that would allow to probe three of the four absorption lines, and in the N-IR spectral region around $2.7\text{ }\mu\text{m}$ two spectral windows can be found, namely

- in the N-IR at 3765 cm^{-1} ($2.66\text{ }\mu\text{m}$), not previously been investigated but very recently confirmed to be suitable by studying ATMOS spectra kindly provided by Dr. Goefrey Toon, NASA Jet Propulsion Laboratory. This spectral window is marked as (3) in Fig. 2.2 (a) and allows to probe H_2^{16}O , H_2^{18}O , and HDO.
- in the N-IR at 3663 cm^{-1} ($2.73\text{ }\mu\text{m}$), previously investigated by *Kerstel et al.* [1999]. While in this spectral window [(2) in Fig. 2.2 (a)] all four absorption lines are found at relatively high integrated line strength, unfortunately the HDO absorption line is completely obscured by a strong CO_2 absorption line.

For the present spectrometer the spectral window at 3663 cm^{-1} ($2.73\text{ }\mu\text{m}$) was chosen even though the HDO absorption line is obscured by CO_2 absorption [Fig. 2.2 (b)]. While the HDO absorption line could be probed when working with pure water samples, as has been done by *Kerstel et al.* [1999], HDO measurements are not possible for a gas mixture of atmospheric composition. Therefore, HDO measurements have not been conducted within the present work.

It was initially planned to realize a multi-laser approach similar to the one by *Wienhold et al.* [1998], where absorption lines of H_2^{16}O , H_2^{17}O , and H_2^{18}O could be probed at 3663 cm^{-1} and HDO could be probed at a different wavelength, e.g., at 3765 cm^{-1} ($2.66\text{ }\mu\text{m}$). However, during the course of instrument development this strategy has proven to be incompatible with the size constraints on our instrument.

In the future it is planned to operate the instrument using a laser emitting at 3765 cm^{-1} ($2.66\text{ }\mu\text{m}$), where the isotopic ratios $\delta^{18}\text{O}$ and δD can be measured. This spectral window has previously not been used but the screening of the HITRAN database as well as inspection of atmospheric absorption spectra from remote sensing measurements have shown its good potential. A more detailed discussion is found in Section 2.5.

At wavelengths around $2.7\text{ }\mu\text{m}$, extremely compact DFB tunable diode-lasers based on GaInAsSb/AlGaAsSb semiconductor materials [*Rößner et al.*, 2005] have emerged in recent years, and their emission wavelength can very well be matched to the wavelength region of interest. These lasers can be operated at room-temperature and are mounted in a standard TO8 package, including peltier element and thermistor for thermoelectric temperature controlling. For the present work, one such laser from NanoPlus was selected, and its characteristics are described below.

Absorption line parameters of the lines found in the 3663 cm^{-1} ($2.73\text{ }\mu\text{m}$) spectral window are given in Tab. 2.1. The relative change of the integrated line strength [$S_{ij}(T)/S_{ij}(T_0)$, see Eq. 2.1 on Page 42] is calculated based on a 1 K temperature change around a base temperature of $T_0 = 40^\circ\text{C}$ and is given in per mille. The temperature dependence of the single absorption lines can lead to an uncertainty $\varepsilon^{18}\text{O}$ in the determination of the isotopic ratio (here $\delta^{18}\text{O}$ as example), when the temperature changes after the spectrometer has been calibrated.

Based on the definition of the isotopic ratio (δ -notation, Eq. 1.21 on Page 25) the temperature-dependent uncertainties have been calculated using

$$\varepsilon^{18}\text{O} = \left[\frac{S^{18}\text{O}(T)/S^{16}\text{O}(T)}{S^{18}\text{O}(T_0)/S^{16}\text{O}(T_0)} - 1 \right]. \quad (2.2)$$

For $T_0 = 40^\circ\text{C}$ and $T = 41^\circ\text{C}$ they were found to be $\varepsilon^{17}\text{O} = -2.7\text{\textperthousand}$, $\varepsilon^{18}\text{O} = -1.4\text{\textperthousand}$, and $\varepsilon\text{D} = -3.6\text{\textperthousand}$. This means that the isotopic ratios would be underestimated at increasing temperature. The calculated uncertainties for a 1 K temperature change are relatively small compared to the expected overall uncertainties of around 20% at low H₂O concentrations. Temperature controlling of the spectrometer to $T = 40 \pm 0.2$ K is therefore sufficient.

Table 2.1: Absorption line parameters of the stable isotopologues of water near 3 663 cm⁻¹ as found in the 2004 edition of the HITRAN database. The relative change of the integrated line strength $S_{ij}(T)/S_{ij}(T_0)$ has been calculated for a gas temperature of $T_0 = 40^\circ\text{C}$ and a temperature change of 1 K using Eq. 2.1 on Page 42. The HDO absorption line is obscured by a strong CO₂ absorption line under atmospheric conditions and is therefore not been investigated in the present work.

	v_0 (cm ⁻¹)	$S_{ij} \times 10^{-23}$ (cm ² /cm molec.)	E'' (cm ⁻¹)	γ (cm ⁻¹ /bar)	$S_{ij}(T)/S_{ij}(T_0)$ (%)
H ₂ ¹⁸ O	3 662.919 60	2.110	398.360 5	0.089 6	1.1
H ₂ ¹⁶ O	3 663.045 22	8.512	586.479 2	0.088 4	3.8
H ₂ ¹⁷ O	3 663.321 31	7.221	224.304 2	0.092 0	-1.5
HDO	3 663.841 91	1.222	100.390 9	0.095 9	-3.3

Laser selection and characteristics

The laser used in the present work is based on GaInAsSb/AlGaAsSb semiconductor technology⁹ [Rößner *et al.*, 2005]. The laser is grown by molecular beam epitaxy (MBE), and the active laser region is formed as a ridge waveguide around $6\text{ }\mu\text{m} \times 1.5\text{ }\mu\text{m}$ wide. The waveguide core is manufactured of GaInAsSb, whereas the cladding consists of AlGaAsSb, which has a lower refractive index, thus enabling waveguiding in the active region. Bragg gratings fabricated of chromium (Cr) provide a wavelength-selective distributed feedback within the laser active region. These gratings are located laterally on both sides of the ridge waveguide.

The characteristics of the laser (# 157/3-7) used in the present study are presented in Fig. 2.3. The laser threshold current is around 29 mA, and the slope efficiency is 0.045 W/A. While the laser is operated at a constant temperature of 35°C, the temperature tunability is around 0.21 nm/K. This tunability is used to coarsely match the emission wavelength to the absorption region of interest. Fine tuning of the laser wavelength is achieved by sweeping of the laser injection current, where the laser wavelength can be tuned by 0.039 4 nm/mA.

⁹The exact material composition is not provided by NanoPlus Lasers GmbH [Werner, 2008]

The absorption lines of interest [yellow-shaded region in Fig. 2.3 (a)] are reached at a laser temperature of 35 °C and an average laser injection current of approximately 90 mA.

The laser emits in a longitudinal single mode [Fig. 2.3 (b)]. The side-mode suppression ratio is > 30 dB, and the emission line width is approximately 10 MHz. Due to the rectangular cross section of the laser active region, the laser beam has an elliptical intensity distribution. The full beam divergence of this type of laser is typically 50 deg and 30 deg for the fast and the slow axis, respectively [nanoplus GmbH, 2008].

Detector selection

The selection of a suitable detector is among the most important aspects of any laser spectrometer design, as the detector can often be considered as the limiting element in the detection chain. In addition to its noise performance, the same constraints in terms of size/weight and cryogenic cooling apply as do for the laser.

For the wavelength region around 2.7 μm detectors based on Indium Arsenid (InAs) or Mercury Cadmium Telluride (HgCdTe) are most suitable. In the present work a InAs detector¹⁰ with a two-stage Peltier cooler was selected as the reference detector, where ultimate performance is not required. This detector is operated at -40°C , and its responsivity is $S = 1.25 \text{ A/W}$. The detector photocurrent is amplified by a transimpedance amplifier with a feedback resistance of $R_F = 2.5 \times 10^4 \Omega$ and a low-pass bandwidth of $\Delta f = 188 \text{ kHz}$.

A HgCdTe detector¹¹ with a four-stage Peltier cooler was selected as the sample detector. This detector is operated at -70°C and has a specified responsivity of $S = 1.78 \text{ A/W}$. The detector photocurrent is amplified by a transimpedance amplifier with a feedback resistance of $R_F = 1 \times 10^5 \Omega$ and a low-pass bandwidth of $\Delta f = 315 \text{ kHz}$. The wavelength-dependent responsivity of the detectors is depicted in Fig. 2.4. Also shown is the theoretical responsivity based on an assumed external quantum efficiency¹² of $\eta = 1$.

2.2.3 Calibration

Calibration is one of the most important aspects of spectroscopic measurements, not only for measurements of absolute concentrations of trace gases, but also, and particularly, for isotopic ratio measurements. Even though other research groups try to avoid active calibration by careful measurement of absorption line parameters, we believe that there are several advantages to it. First, exact knowledge about the absorption line parameters, such as the integrated line strength and pressure broadening coefficient is not necessary. Second, active calibration readily includes laser characteristics, such as the laser emission linewidth or a potential non-

¹⁰Model J12-TE2, LaserComponents GmbH, Garching, Germany

¹¹Model J19-TE4, LaserComponents GmbH, Garching, Germany

¹²The responsivity of a detector is defined as the effectiveness of conversion of photons into electrons, i.e., the number of electrons produced by a certain number of photons. It can be expressed as

$$S = \eta \frac{e\lambda}{hc} .$$

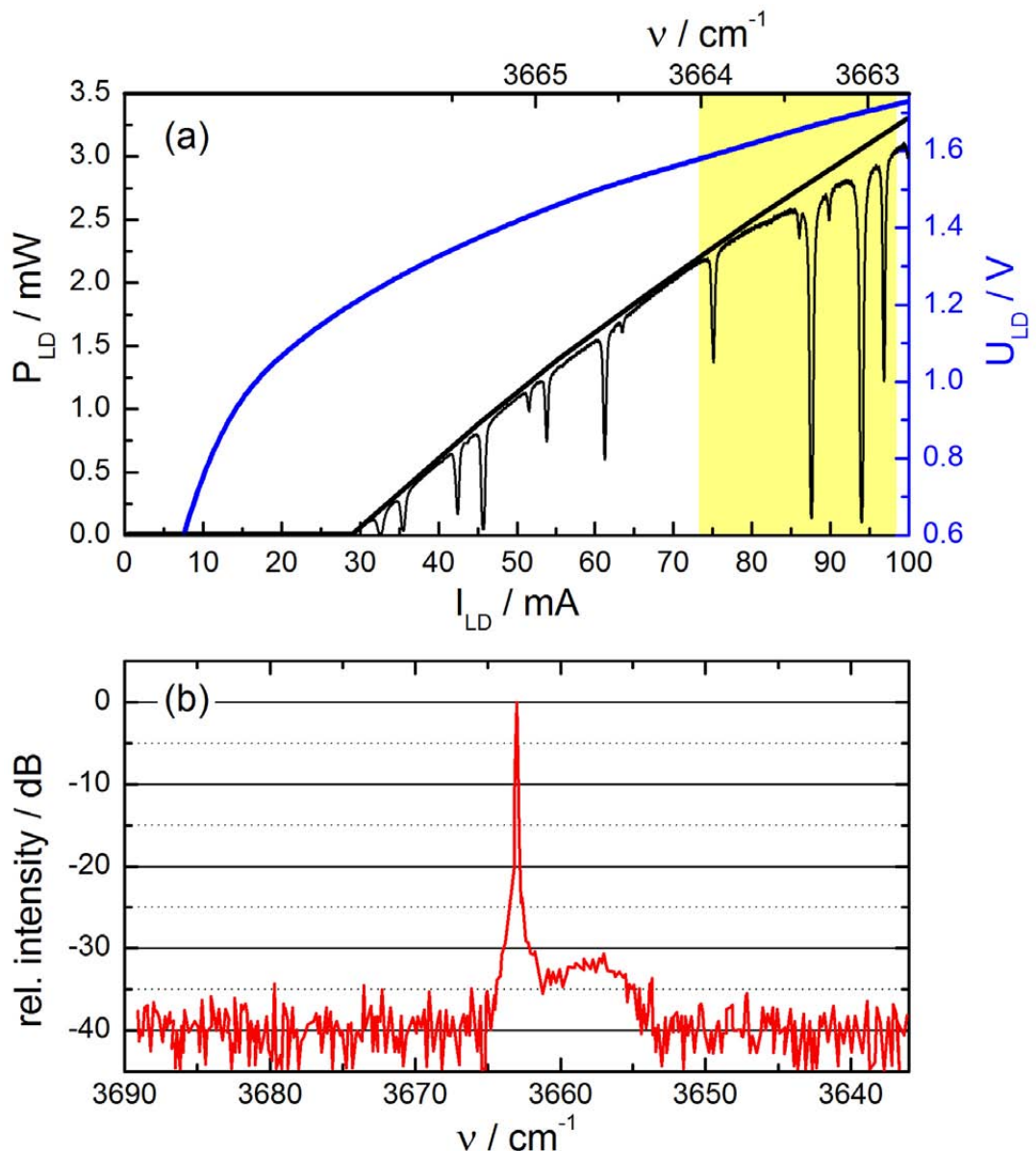


Figure 2.3: (a) Characteristics of the NanoPlus diode laser # 157/3-7 with laser power (thick *black* trace) and laser voltage (*blue* trace) versus laser injection current at a laser temperature of 35 °C. Also shown is a high-concentration H₂O absorption spectrum (thin *black* trace) with the spectral region of interest highlighted by the *yellow*-shaded area. (b) Emission spectrum of the diode laser (reproduced from specification sheet) showing laser emission in a single longitudinal mode with a side-mode suppression ratio of >30 dB.

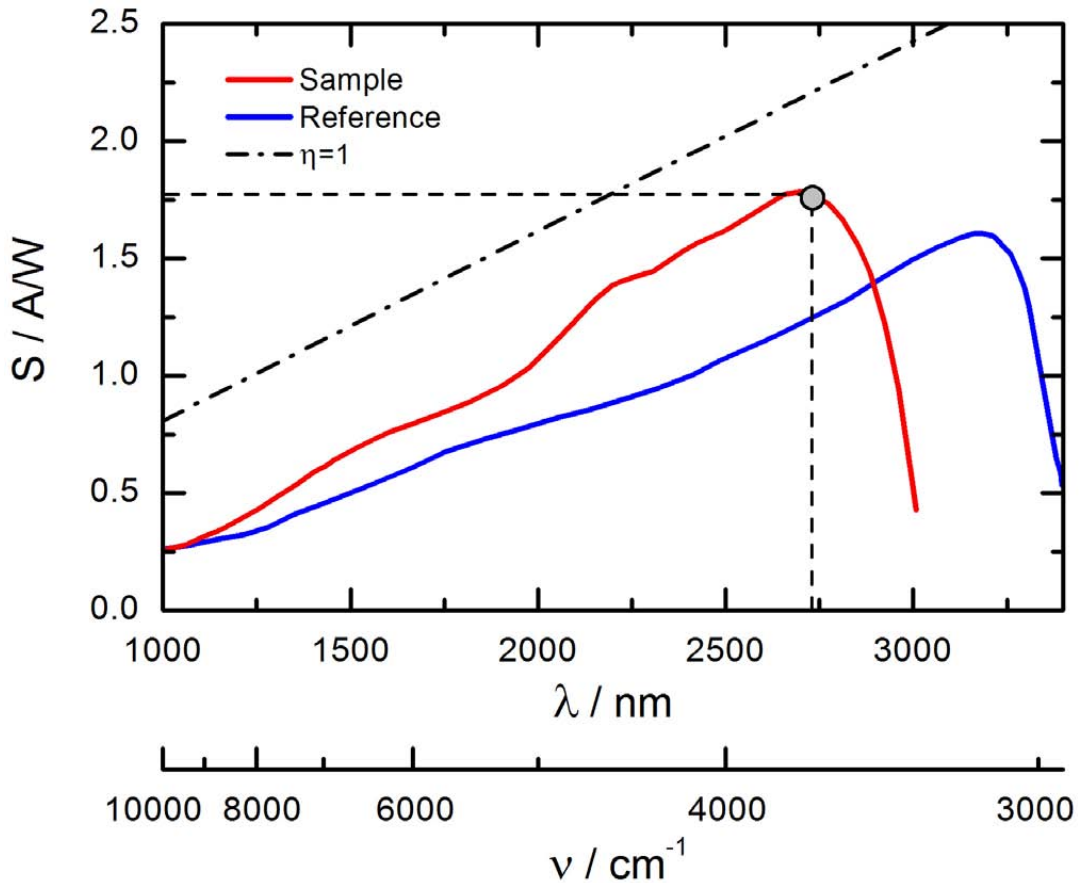


Figure 2.4: Responsivity of the four-stage Peltier-cooled photovoltaic HgCdTe detector (red trace, reproduced from data sheet) used as sample detector at -70°C . The laser wavelength of $2.73\ \mu\text{m}$ (indicated by the dashed line) closely matches the peak responsivity of the sample detector of $S = 1.78\ \text{A/W}$. The blue trace depicts the responsivity of the InAs detector used as reference detector. At $2.73\ \mu\text{m}$ the responsivity is $S = 1.25\ \text{A/W}$.

linearity of the wavelength scan. This is particularly important during field measurements, where exchanging of a laser due to failure must be possible in relatively short time.

However, provision of a stable water calibration standard is particularly demanding. Water is a polar molecule, i.e., it sticks to any surface. This implies that humid air can not be stored in a high-pressure gas cylinder without the presence of adsorption and condensation effects to the cylinder walls. Not only would the humidity, i.e. the water vapor concentration, of air taken from a high-pressure gas cylinder change with the amount of air left. In addition, isotopic fractionation effects would occur, which would require a permanent cross-calibration of the calibration standard itself.

Calibration sources for water vapor instrumentation have been designed based on a number of approaches, such as bubblers, permeation tubes, flow-controllers, or capillary-based designs. While these approaches may be well suited for absolute concentration measurements, isotopic ratio measurements place additional constraints. The calibration approaches above rely on the evaporation of water into a flow of dry air. As discussed in Section 1.4.1, evaporation of water causes fractionation due to the slightly different vapor-pressure of the dif-

ferent isotopologues (equilibrium fractionation). It is therefore advantageous to humidify dry air by injecting liquid water. Complete evaporation of the water thus avoids fractionation of isotopologues, and the water vapor of the calibration gas mixture contains the same isotopic composition as the liquid reference water.

Calibration source

In the present work a calibration source based on the injection of small droplets of liquid water into a controlled flow of dry air has been designed (Fig. 2.5). The injection is based on the principle of ink jet printing technology. In the present system, small droplets of water are produced by piezo-driven injection nozzles¹³ that host a glass capillary. At one end of the capillary a nozzle with a $\phi = 30 \mu\text{m}$ is formed. The capillary is surrounded by a tubular piezo actuator that — upon application of a voltage pulse (86 V, 36 μs) — contracts and creates a pressure wave propagating through the glass and into the water. Near the nozzle, the pressure wave accelerates the water within the capillary, and a small liquid water column leaves the nozzle. The column subsequently breaks off, forming a droplet that flies freely through the dry air, where it evaporates entirely. The diameter of each of the droplets is around 40 μm , thus containing $\approx 34 \times 10^{-12} \text{ l}$ of water. The injection frequency of the droplets is continuously tunable between 100 Hz and 1 000 Hz. Since the droplet size depends upon the viscosity of the water, which in turn depends on temperature, the temperature of the injection nozzle is controlled to $40^\circ\text{C} \pm 0.03^\circ\text{C}$ in order to avoid drift in total water concentration.

The flow rate of the dry air is controlled by a mass flow controller¹⁴ with a range of 0.2...5 l(std)/min. At a dry air flow rate of 2 l(std)/min the total water mixing ratio may be varied in a range of 150...1 500 ppmv by variation of the droplet injection frequency. Employing two separate injection nozzles allows to switch between two water standards (see Tab. 1.1) of different isotopic composition to investigate instrument response and exchange times as well as measurement accuracy. The calibration standard is produced in excess of the spectrometer flow rate, and the resulting overflow is dumped into a waist line.

In the laboratory, dry nitrogen (N2 6.0, 99.999 9%) from a 50 l gas cylinder with a residual water mixing ratio of < 0.5 ppmv is used. Due to space and weight constraints on the airborne platforms available, no gas cylinder with dry air can be used while measuring airborne. Therefore, the proposed strategy is the use of a scrubber device, that could be built both small and lightweight. Such a device would host a cartridge containing a certain amount of molecular sieve (around 100 g with a pore width of 0.3 nm), through which the already relatively dry atmospheric air would be guided and thus dried. Preliminary tests (not discussed in detail in the present work) with molecular sieve have demonstrated the potential of this approach. Thereby, a flow of 1 l(std)/min of very humid laboratory air at atmospheric pressure, containing $\gg 10000$ ppmv of water, was dried to about 1 ppmv. For an airborne device it is proposed to operate the scrubber at an elevated pressure of about 2 000 hPa to further reduce re-evaporation of water off the molecular sieve, thus reducing the humidity of the dry air to less than 1 ppmv. The maximum potential error in isotopic ratio induced by 1 ppmv residual water at a calibration mixing ratio of 500 ppmv is thus $1/500 = 2\%$.

¹³Model MD-K-130-010, microdrop Technologies GmbH, Norderstedt, Germany

¹⁴Bronkhorst High-Tech B.V., Ruurlo, Netherlands

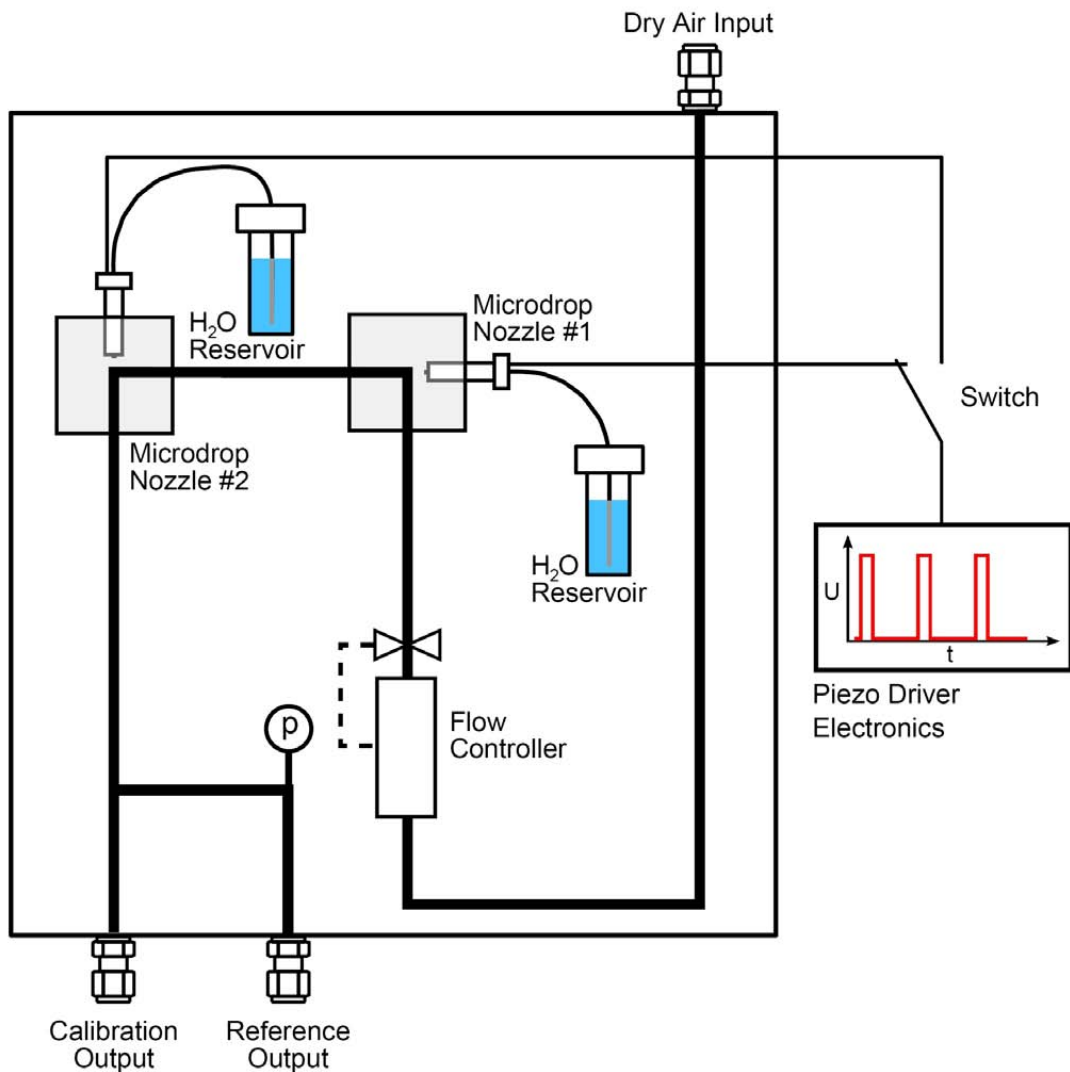


Figure 2.5: Schematic of the calibration source. Dry air at ambient pressure is flown through the system at a flow rate controlled by a flow controller (0...5 l(std)/min). Liquid water is injected as small droplets into the flow of dry nitrogen employing two Piezo-driven injection nozzles. The droplet injection frequency can be adjusted from 100 Hz to 1 kHz. A switch allows to rapidly switch between two water standards of different isotopic composition. The reference output is used to connect a dew-point hygrometer for absolute water concentration measurements.

Tube system

The spectrometer tube system is depicted in Fig. 2.6. It is designed of electropolished stainless steel tubing¹⁵ upstream of the multipass absorption cell, and teflon (PTFE) tubing downstream of the cell. The upstream tubing is heated to 40°C to minimize water adsorption to the tubing walls, thus reducing the gas exchange time of the spectrometer. Solenoid valves are used to

¹⁵ULTRON, Dockweiler AG, Neustadt-Glewe, Germany

switch between calibration, ambient and zero air (dry air) gas flows. A proportional valve¹⁶ upstream of the absorption cell is used to control the pressure in the absorption cell to $p_{MPC} = 70 \pm 0.1$ hPa. The pressure is measured using an absolute pressure gauge¹⁷ connected to the downstream port of the multipass cell.

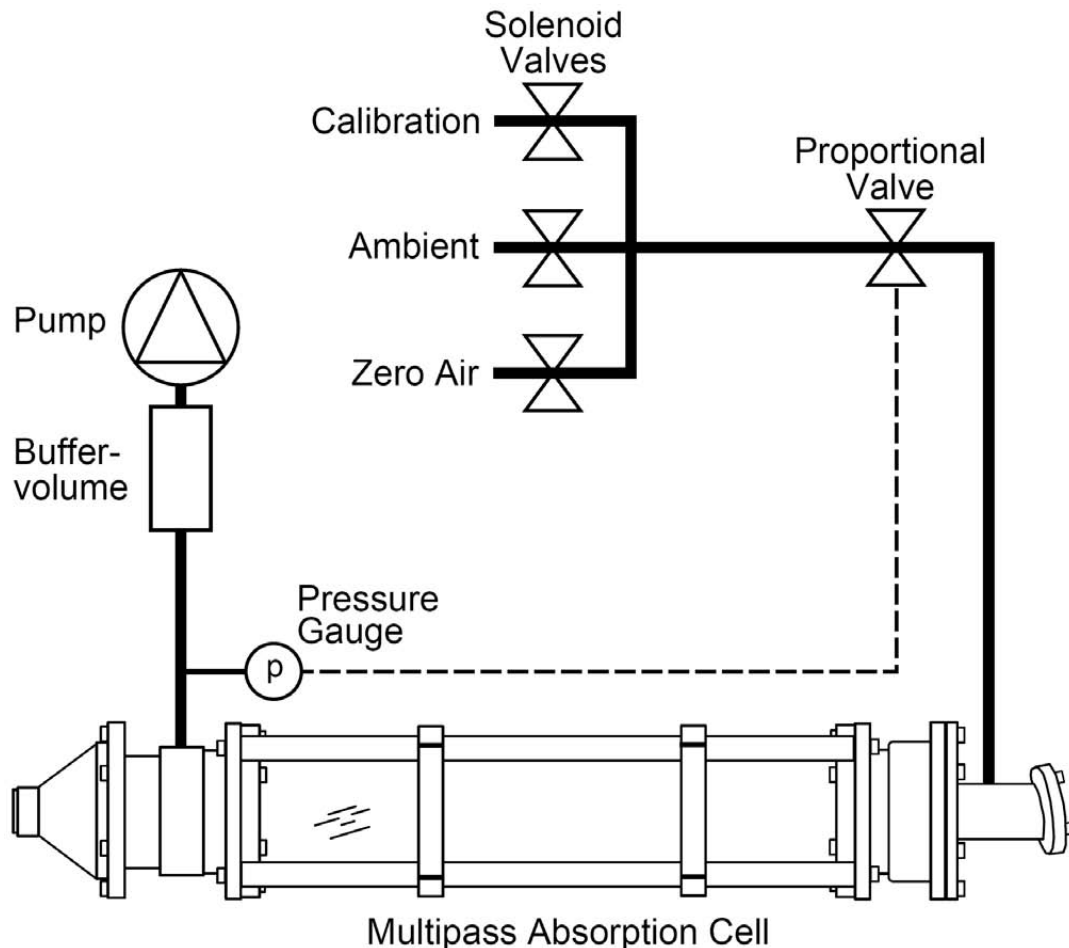


Figure 2.6: Schematic of the gas flow system of the spectrometer. Solenoid valves are used to switch between calibration, ambient and dry air gas flows. A proportional valve upstream of the absorption cell is used to control the pressure in the absorption cell, which is measured using an absolute pressure gauge. Tubing upstream of the absorption cell is made of electropolished stainless steel to minimize water adsorption to the tubing wall, while downstream tubing is made of Teflon (PTFE) to reduce instrument weight.

A membrane pump¹⁸ is used to establish a flow rate of about 1.5 l(std)/min through the absorption cell. The sample residence time in the MPC at 70 hPa is thus 1.5 s. A 2 l buffer volume upstream of the pump reduces pressure fluctuations by the pump's membranes. Depending on the final space and weight restrictions on the particular aircraft, a bigger pump

¹⁶C. Bürkert GmbH und Co. KG, Ingelfingen, Germany

¹⁷PMP-4000, GE Sensing, Bad Nauheim, Germany

¹⁸Model MD1 Vario-SP, Vacuubrand, Wertheim, Germany

may be used to reduce exchange times. When employed on the airplane, the instrument will be connected to the respective inlet by heated stainless steel tubing.

2.2.4 Data acquisition

The present spectrometer is based on wavelength modulation spectroscopy in combination with second harmonic detection, as has been described in Section 1.3.3. Thereby, the laser emission wavelength is scanned over the absorption region of interest at a frequency of $f_{\text{scan}} = 10 \text{ Hz}$ employing a sawtooth ramp to the laser injection current. At the same time the injection current is modulated with a sinusoidal modulation at $f_{\text{mod}} = 57 \text{ kHz}$. The amplitude of the wavelength modulation is about 600 MHz (0.02 cm^{-1}) and corresponds to 2.2 times the half width at half maximum (HWHM) of the absorption lines probed. At this modulation amplitude the maximum second-derivative signal is achieved [Iguchi, 1986].

The detector signals of both the sample and the reference detector are first preamplified by transimpedance amplifiers and then demodulated by two lock-in amplifiers referenced to twice the modulation frequency to achieve second-derivative spectra (Fig. 2.7). The output of both lock-in amplifiers is recorded by a digital signal processing (DSP) computer and the corresponding spectra are stored on a compact flash card.

The second-derivative reference spectra are used for active wavelength stabilization on a scan-by-scan rate, where a DC offset is applied to the laser injection current if the laser wavelength drifts due to slight changes in laser temperature. The sample spectra are used to determine the absolute H_2O mixing ratio in real time based on the H_2^{16}O absorption line. The isotopic ratios $\delta^{17}\text{O}$ and $\delta^{18}\text{O}$ are determined in post processing.

A typical measurement cycle consists of two phases. Each cycle starts with a calibration phase, in which a high signal-to-noise ratio calibration spectrum (30 s AVG) is recorded. Thereby, the multipass absorption cell is flushed with a calibration gas standard of known isotopic composition. This standard is provided by the calibration source described in Section 2.2.3. The absolute water mixing ratio during calibration is typically around 200–500 ppmv. This is followed by the ambient phase, where the absorption cell is flushed with ambient air that contains water vapor at (generally) unknown mixing ratio and isotopic composition. Each phase is followed by a flushing period of 15 s to allow for proper gas exchange in order to minimize systematic error induced by wall effects due to water adsorption to the absorption cell and upstream tubing walls. The two phases are repeated every ten minutes, starting with the recording of a new calibration spectrum.

Calibration spectra are combined to 30 s average spectra, containing 300 single spectra recorded at 10 Hz, to achieve a high signal-to-noise ratio. Ambient spectra are combined to one second averages. Both calibration and ambient spectra are stored on a compact-flash memory card for post processing.

Post processing of the recorded spectra is performed employing a LabView program. Thereby the 30 s calibration spectra as well as the corresponding one-second average ambient spectra are first divided into three appropriately selected windows that contain the isolated absorption lines of the three isotopologues (H_2^{16}O , H_2^{17}O , and H_2^{18}O) being investigated in the present study. Each spectral window contains a certain number of discrete data points n along the (horizontal) wavelength axis as depicted in Fig. 2.8. The entire scan contains $n = 256$ data points.

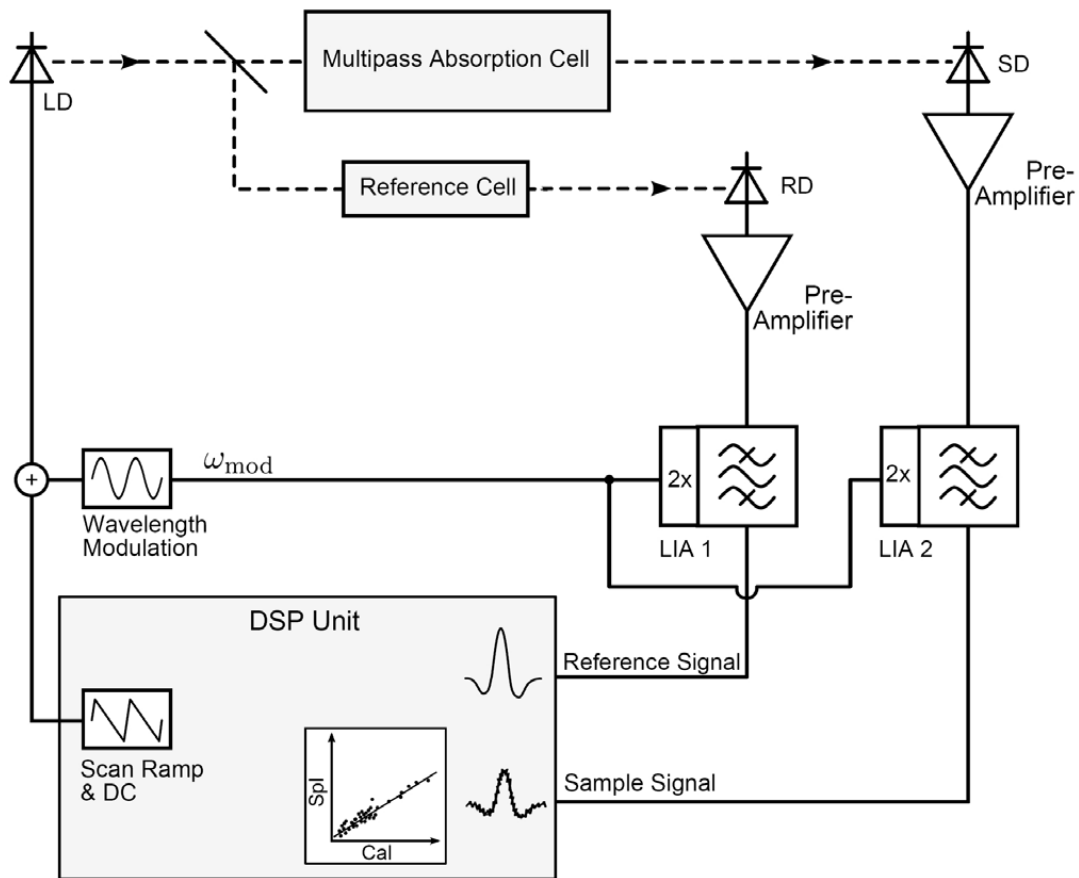


Figure 2.7: Data acquisition scheme of the isotopic-ratio spectrometer. The Laser diode (LD) is provided with a scan ramp (10 Hz sawtooth) and a DC offset to scan over the absorption lines of interest. Additionally a 57 kHz sinusoidal modulation is employed to modulate the wavelength of the laser. The signals of both the sample (SD) and reference detector (RD) are — after being pre-amplified — demodulated by two respective lock-in amplifiers at twice the modulation frequency to record second-derivative spectra. The reference spectra are used for line-locking purposes, and a DC offset is fed back to the laser current to compensate for wavelength drift.

The isotopic ratios are determined employing a multiple linear regression scheme based on singular value decomposition (SVD) [Bomse and Kane, 2006; Werle *et al.*, 2004]. Thereby the ambient spectra are expressed as column vector $\overrightarrow{\text{Amb}}$, where the elements $\text{Amb}_1 \dots \text{Amb}_n$ represent the n data points within the respective absorption line. Matrix ϕ contains four columns that are filled with the previously recorded calibration spectrum ($\text{Cal}_1 \dots \text{Cal}_n$) as well as a pre-defined DC baseline offset ($\text{DC}_1 \dots \text{DC}_n$), linear baseline slope ($\text{Lin}_1 \dots \text{Lin}_n$), and quadratic baseline bend ($\text{Quad}_1 \dots \text{Quad}_n$). The vector \overrightarrow{W} contains the four respective scaling factors for the terms defined in the matrix ϕ .

$$\overrightarrow{\text{Amb}} = \begin{pmatrix} \text{Amb}_1 \\ \text{Amb}_2 \\ \vdots \\ \text{Amb}_n \end{pmatrix} \quad \overrightarrow{\mathbf{W}} = \begin{pmatrix} \mathbf{W}_{\text{Cal}} \\ \mathbf{W}_{\text{DC}} \\ \mathbf{W}_{\text{Lin}} \\ \mathbf{W}_{\text{Quad}} \end{pmatrix}$$

$$\phi = \begin{pmatrix} \text{Cal}_1 & \text{DC} & \text{Lin}_1 & \text{Quad}_1 \\ \text{Cal}_2 & \text{DC} & \text{Lin}_2 & \text{Quad}_2 \\ \vdots & \vdots & \vdots & \vdots \\ \text{Cal}_n & \text{DC} & \text{Lin}_n & \text{Quad}_n \end{pmatrix} \quad (2.3)$$

Vectors $\overrightarrow{\text{Amb}}$ and $\overrightarrow{\mathbf{W}}$ as well as Matrix ϕ form a linear system of equations

$$\overrightarrow{\text{Amb}} = \phi \cdot \overrightarrow{\mathbf{W}}. \quad (2.4)$$

In order to determine the isotopic ratio, the scaling factor of the calibration spectrum to the ambient spectrum (\mathbf{W}_{Cal}) must be found by solving the system of equations:

$$\overrightarrow{\mathbf{W}} = (\phi^T \cdot \phi)^{-1} \cdot \phi^T \cdot \overrightarrow{\text{Amb}}. \quad (2.5)$$

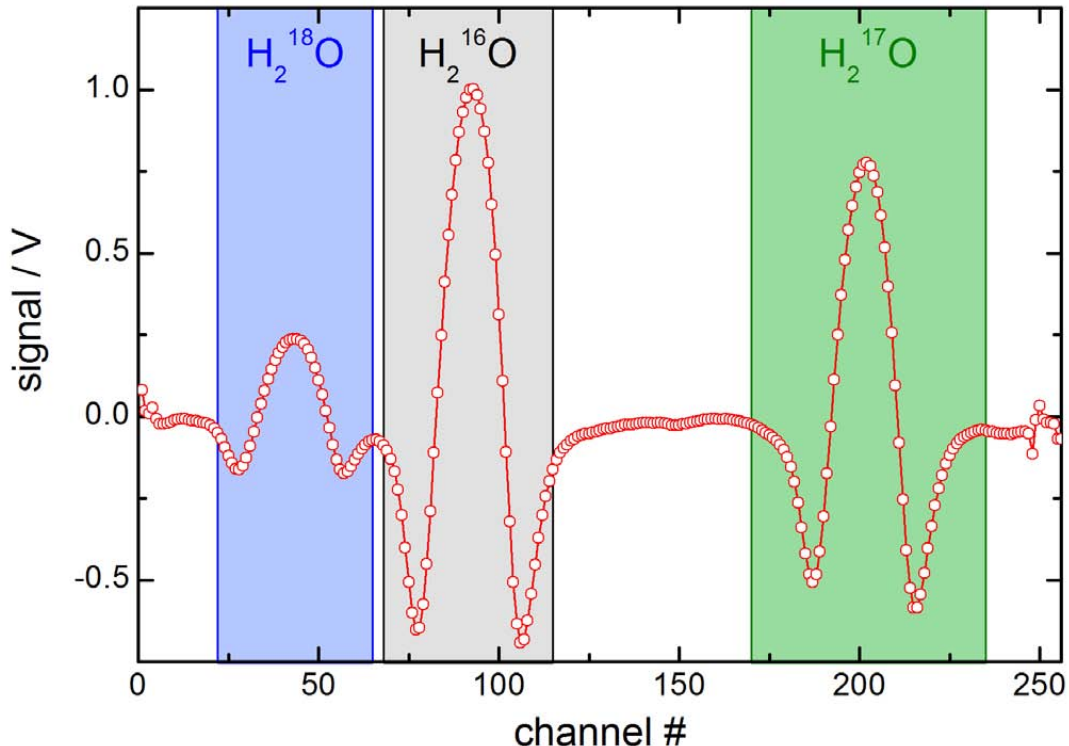


Figure 2.8: Second-derivative spectrum of water isotopologues at $p = 70\text{hPa}$ (700 ppmv, GW-9 standard material, see Tab. 1.1 on Page 26). The entire spectral window contains 256 discrete data points. The parts of the spectral window used for the fit are indicated by the shaded areas for the respective absorption lines.

The expression $(\phi^T \cdot \phi)^{-1} \cdot \phi^T$ is termed pseudo inverse and is used to calculate the inverse of a non-square matrix [Golub and Van Loan, 1996]. Proceeding in this manner results in a direct result for the components of \vec{W} even though the system of equations is overdetermined. It is, however, a prerequisite that $\phi^T \cdot \phi$ can be inverted. The scaling factor W_{Cal} can be expressed as mixing ratio of the ambient spectrum relative to the calibration spectrum, i.e., the fraction of the calibration signal that fits best the actual sample spectrum. The calculation of this relative mixing ratio is performed for all three isotopologues.

Recalling the definition of the isotopic ratio (δ -notation) introduced in Eq. 1.21 on Page 25, and performing minor rearrangements we can write for $\delta^{18}\text{O}$

$$\begin{aligned}\delta^{18}\text{O} &= \frac{([c]^{18}\text{O}/[c]^{16}\text{O})_{\text{Amb}}}{([c]^{18}\text{O}/[c]^{16}\text{O})_{\text{Cal}}} - 1 \\ &= \frac{[c]_{\text{Amb}}^{18}\text{O}/[c]_{\text{Cal}}^{18}\text{O}}{[c]_{\text{Amb}}^{16}\text{O}/[c]_{\text{Cal}}^{16}\text{O}} - 1 \\ &= \frac{W_{\text{Cal}}(\text{H}_2^{18}\text{O})}{W_{\text{Cal}}(\text{H}_2^{16}\text{O})} - 1\end{aligned}\quad (2.6)$$

where the ratios $W_{\text{Cal}}(\text{H}_2^{16}\text{O})$ and $W_{\text{Cal}}(\text{H}_2^{18}\text{O})$ denote the relative mixing ratios for H_2^{16}O and H_2^{18}O , respectively. The isotopic ratio of an unknown sample with respect to a reference standard is thus determined by dividing the relative mixing ratio of the minor isotopologue by that of the main isotopologue.

2.2.5 Conclusion

A laser spectrometer for measurements of water (H₂O) vapor isotopic ratios has been developed. A compact optical setup ($52 \times 40 \text{ cm}^2$) has been realized. This setup contains a lightweight multipass absorption cell to achieve 76 m absorption path length within a 0.51 volume. Thermoelectrically cooled laser and detectors enable cryogenics-free operation. The final spectrometer is highly compact ($57 \times 45 \times 35 \text{ cm}^3$) and lightweight ($< 35 \text{ kg}$), which was an important constraint for future employment of the present spectrometer aboard research aircraft.

A calibration-gas source has been developed, which is based on the injection of small droplets of (liquid) water in dry air. This approach effectively eliminates isotopic fractionation, that would be caused in calibration sources based on evaporation of water.

The spectrometer is based on wavelength-modulation spectroscopy with second-harmonic detection. High accuracy is achieved by regular calibration. A fit algorithm is used, which takes baseline slopes and bends into account and thus achieves improved results over a simple linear regression approach.

2.3 System stability and detection limit

The system stability time is an important measure for a laser spectrometer, as it reflects the maximum allowable time to average statistically independent data. Since averaging of spectral data within the stability time reduces noise, a longer stability time in turn leads to an improved detection limit. Averaging longer than the stability time will no longer improve the detection limit. The stability time is generally limited by time-dependent background signals superimposed on the spectra. As these structures move through the spectrum, they induce slight changes in the retrieved mixing ratio. These changes are denoted as drift. As this drift is often unavoidable, the detection system must be low noise in order to reach the desired detection limit within the stability time of the spectrometer.

Measurements to identify and quantify the noise sources and their contributions to the detection system have been performed, and they are discussed in Section 2.3.1. The various noise sources, that may be present in the detection system, are first introduced. This is followed by a discussion of noise measurements that have been carried out to quantify the noise contributions of the laser and detector/preamplifier. Spectroscopic measurements have been performed to determine the detection limit as well as stability time for $\delta^{17}\text{O}$ and $\delta^{18}\text{O}$ isotopic ratios. These measurements are described in Section 2.3.2. In Addition to the detection limit, the measurement accuracy is the second important measure for an isotopic ratio spectrometer. The accuracy has been determined by analyzing the spectrometer's response to different known isotopic water standards, and the results are given in Section 2.3.3. A conclusion follows in Section 2.3.4.

2.3.1 Signal-to-noise ratio analysis

This Section contains a description of various noise sources that may be present in optical detection systems. These noise sources have been quantified by different measurements and the results allow to derive a formalism for the signal-to-noise ratio of the present spectrometer.

Noise sources

Noise in the detection of light plays an important role as it affects the minimum optical signal that can be measured by a given detection system. Using photodetectors, where photons are converted into electrons, the second central moment of the random noise current can be measured as root-mean-square (rms) deviation (i_{rms}). In the following discussion we are only interested in the fluctuation of a measured signal. This fluctuation is expressed as the average of the squared modulus of a complex rms phasor $\overline{|I|^2}$. If a current-to-voltage converter (transimpedance amplifier) is used, the noise current is transformed into a rms voltage (u_{rms}) at the output of the amplifier. In this case the voltage fluctuation is expressed as $\overline{|U|^2}$. The rms values are considered as a sine wave that can provide the same power as the noise signal. Since the mean value of a sine wave is zero, $\overline{|I|^2}$ and $\overline{|U|^2}$ can also be considered as variance.

The various noise sources that may be present in a laser spectrometer are described below.

(a) Thermal Noise: Thermal noise (or Johnson noise) is due to the thermally excited vibration of discrete charge carriers such as electrons in resistors. For a resistance R at temperature

T , the fluctuation of the voltage measured within a detection bandwidth Δf is [Budde, 1983]

$$\overline{|U_{\text{thermal}}|^2} = 4k_B T R \Delta f , \quad (2.7)$$

where $k_B = 1.38 \times 10^{-23}$ J/K denotes the Boltzmann constant and T is given as absolute temperature in K.

(b) Shot Noise: Shot noise is associated with an electric current flowing across a potential barrier, such as the pn-junction of a photodiode. The electrons pass the potential barrier at random times. Thereby, they follow a Poisson distribution, where the variance of the number of electrons is proportional to the mean number of electrons. The shot noise (variance) of a photocurrent i measured within a detection bandwidth Δf is given by [Budde, 1983]

$$\overline{|I_{\text{shot}}|^2} = 2e\bar{i}\Delta f , \quad (2.8)$$

where $e = 1.602 \times 10^{-19}$ C denotes the electric charge of an electron and \bar{i} is the mean value of the photocurrent. The shot noise current is related to the preamplifier output noise voltage by the feedback resistance (R_F)

$$\overline{|U_{\text{shot}}|^2} = R_F^2 \overline{|I_{\text{shot}}|^2} . \quad (2.9)$$

Introducing the responsivity of the detector S (in A/W) and neglecting thermal noise of R_F , the shot noise voltage can be linked to the mean optical power $\overline{P_{\text{opt}}}$ incident on the detector

$$\begin{aligned} \overline{|U_{\text{shot}}|^2} &= R_F^2 2e\bar{i}\Delta f \\ &= R_F^2 2e\overline{P_{\text{opt}}} S \Delta f . \end{aligned} \quad (2.10)$$

The noise variance ($\overline{|U_{\text{shot}}|^2}$) is thus proportional to the mean optical power, or the relative signal noise decreases with the square root of the optical power incident on the detector.

For both thermal noise and shot noise, reducing the measurement bandwidth Δf by averaging reduces the noise variance proportional to the reduction of bandwidth ($\overline{|U_{\text{noise}}|^2} \propto \Delta f$).

(c) Photon noise: Light can be described as a flux of photons. Each photon has the energy $E = hf = h/c\lambda$, where f is the frequency and λ is the wavelength of the corresponding electromagnetic wave. Even if classical light is both stable in amplitude and phase, the detection will show noise because the number of photons per unit time fluctuates about a mean value \bar{n} .

The photons are generally Bose-Einstein distributed. For natural (thermal) light at typical power levels, however, the mean number of photons \bar{n} is much smaller than the number of modes of the electromagnetic field z ($\bar{n} \ll z$, $n \ll z$), because the photon energy is high. In this case, the Bose-Einstein distribution can be approximated by the Poisson distribution [Dereniak and Boreman, 1996]

$$P(n) = \frac{\bar{n}^n}{n!} e^{-\bar{n}} . \quad (2.11)$$

$P(n)$ denotes the probability to detect n photons when the mean number of photons is \bar{n} . The fluctuation is quantified by its variance, and for a Poisson distribution, this variance equals the mean

$$\sigma^2 = \bar{n} . \quad (2.12)$$

The Poisson distribution is also valid for ideal laser light [Grau, 1969], where, in contrast to natural light, $\bar{n} \gg z$. Eq. 2.12 is of fundamental importance to the detection of light. It indicates, that the standard deviation σ , and thus the signal-to-noise ratio (SNR) will increase with the square root of the number of photons ($\sigma = \sqrt{\bar{n}}$). This is identical to the case of shot noise (Eq. 2.8), where the rms-noise current ($|I_{\text{shot}}|^2$) $^{1/2}$ is proportional to the square root of the mean photocurrent \bar{i} .

If the light is detected, it generates a photocurrent proportional to the mean optical power \bar{P}_{opt} . This photocurrent shows shot noise. In addition, the number of arriving photons is Poisson distributed, and this fluctuation will add to the noise current. As this noise current follows the same expression as the shot noise introduced above, shot noise due to the photocurrent and photon noise are indistinguishable at the detection of light. When thermal noise can be neglected, the shot noise marks the lowest noise level to be reached.

(c) Laser Excess Noise Lasers are not ideal devices, and in addition to the stimulated emission there will always be a fraction of spontaneous emission. Each spontaneously emitted photon adds a small component to the coherent field of the stimulated emission, and this effect may be amplified within the laser resonator. Since the phase of the spontaneous emission is random, this causes small fluctuations in both amplitude and phase of the stimulated emission. The noise contribution of spontaneous emission adds to this noise and is termed excess noise.

Lasers with multiple longitudinal emission modes also show excess noise due to mode competition, because the laser emission wavelength changes randomly between these modes. This process leads to additional amplitude modulation of the laser output power, which may reduce the detection limit of a given detection system. It is noted here, that the diode laser used in the present study emits in a single longitudinal mode.

Noise measurements

To quantify the magnitude of the laser excess noise as well as the signal-to-noise ratio of the present detection system, the laser as well as the sample detector and its preamplifier were analyzed in terms of its

- (1) *Detector/preamplifier dark noise.* This noise is the sum of shot noise due to the detector dark current, thermal noise of resistors, as well as noise that may originate from the preamplifier power supply.
- (2) *Shot noise level*, which marks the lowest noise to be achieved, and is unavoidable for any detection of light.
- (3) *Laser excess noise.* Lasers show additional noise due to spontaneous emission as well as laser mode competition. This additional noise is commonly termed excess noise because it adds to the unavoidable shot noise.

The noise measurements were carried out by measuring the rms noise voltage ($u_{\text{rms}} = [(u - \bar{u})^2]^{1/2}$) at the output of the transimpedance preamplifier of the sample detector using a

digital oscilloscope¹⁹. The oscilloscope was AC-coupled ($\bar{u} = 0$). While the oscilloscope had a detection bandwidth of $\Delta f = 100\text{ MHz}$, the detection bandwidth of the transimpedance preamplifier was $\Delta f_{\text{TIA}} = 315\text{ kHz}$. For the present noise measurements, Δf_{TIA} therefore determined the effective measurement bandwidth.

The detector and preamplifier dark noise was measured by blocking the detector to avoid ambient light on the detector active area. The rms dark noise voltage was measured to be $(|U_{\text{dark}}|^2)^{1/2} = 180.8\text{ }\mu\text{V}$ [$(|I_{\text{dark}}|^2)^{1/2} = 1.808\text{ nA}$] at the given bandwidth of 315 kHz. The dark noise level is indicated by the *blue* horizontal dash-dotted line in Fig. 2.9 (a). Note that the noise variance $|U_{\text{dark}}|^2$ is plotted.

To measure the shot noise limit of the present detection system, the detector was illuminated with light from a halogen lamp at various optical power levels. The halogen lamp is a natural light source and the emitted photons follow approximately a Poisson distribution, i.e., the photons generate shot noise. The measured noise variance ($|U_{\text{shot}}|^2$) of the preamplifier output should therefore be proportional to the optical power \bar{P}_{opt} , as defined in Eq. 2.10. The optical power was adjusted by placing various combinations of Germanium (Ge) neutral density filters inside the light path to attenuate the light emitted from the halogen lamp. The DC output voltage \bar{u} at the preamplifier was converted to optical power using the preamplifier feedback resistance R_F and the detector responsivity S , where $\bar{P}_{\text{opt}} = \bar{u}/(R_F S)$. The results of these measurements are shown by the *red* squares in Fig. 2.9 (a). Also shown is a linear fit to the measured data.

The *blue* dotted trace represents the calculated shot noise (Eq. 2.10) based on the measured \bar{u} and detection bandwidth ($\Delta f = 315\text{ kHz}$). Combining the measured detector/preamplifier dark noise and the calculated shot noise by adding their noise variances leads to the theoretical shot noise level of the detection system, represented as solid *blue* trace in Fig. 2.9 (a). The measured data very well match the theoretical shot noise level, indicating that shot noise is the predominant noise source of this particular detector/preamplifier combination. This level also defines the lowest noise level for the given detection system.

In order to determine the laser excess noise, the laser beam was collimated by a $f = 40\text{ mm}$ CaF₂ lens and the collimated beam was then focused onto the detector using a second $f = 40\text{ mm}$ CaF₂ lens. The optical power incident on the detector was varied from zero, where the laser was turned off, to values close to the saturation of the preamplifier (around $60\text{ }\mu\text{W}$) by placing various combinations of Ge neutral density filters into the collimated beam path.

For the noise measurements the laser was operated DC at an injection current of $I_{\text{LD}} = 90\text{ mA}$, which corresponds to its usual operating point during spectroscopic measurements. As before, the rms-noise voltage was measured at the output of the preamplifier and the variance is displayed as *black* squares in Fig. 2.9 (a). The solid *black* trace shows a parabolic fit to the measured data.

During spectroscopic measurements, where the laser beam is aligned through the multipass absorption cell, the power level incident on the detector is usually around $6\text{ }\mu\text{W}$. This power level is somewhat dependent on alignment, and the typical power level is given as a range between $4\text{ }\mu\text{W}$ and $8\text{ }\mu\text{W}$ as indicated by the hashed area in Fig. 2.9 (a). Within this power range the noise variance ($|U_{\text{laser}}|^2$) is only between 3 % and 8 % above the shot noise level, and

¹⁹Model TDS3014B, Tektronix, Köln, Germany

this fraction increases to approximately 110 % at a power of $60 \mu\text{W}$. This indicates the high capability of the present detection system, where the measured noise level is very close to the fundamental shot noise limit.

To quantify the noise contribution of the laser in the measured data, one can define a relative intensity noise (RIN). It relates the variance of the power fluctuations of the laser ($\overline{\delta P_{\text{opt}}^2}$) measured within a detection bandwidth Δf to the mean laser power $\overline{P_{\text{opt}}}$ [Grau and Freude, 1991]. Since the detector dark noise would lead to an overestimation of the RIN, the equivalent optical noise power $\overline{\delta P_{\text{dark}}^2}$ is subtracted from $\overline{\delta P_{\text{opt}}^2}$, and the RIN is defined here (including shot noise but excluding dark current noise) as:

$$\text{RIN} = \frac{\overline{\delta P_{\text{opt}}^2} - \overline{\delta P_{\text{dark}}^2}}{\overline{P_{\text{opt}}}^2 \Delta f}, \text{ with}$$

$$\overline{\delta P_{\text{opt}}^2} = \overline{|U_{\text{laser}}|^2} / (RFS)^2$$

$$\overline{\delta P_{\text{dark}}^2} = \overline{|U_{\text{dark}}|^2} / (RFS)^2. \quad (2.13)$$

The relative intensity noise was calculated from the measured data and from the fit results and is depicted in Fig. 2.9 (b) as *black* squares and as solid *black* trace, respectively. The relative intensity noise of laser #157/3-7 is $\text{RIN} = 3.7 \times 10^{-15} \text{ Hz}^{-1}$ ($-144.3 \text{ dB Hz}^{-1}$) and it does not depend on the optical power.

The noise measurements described above have also been performed with the laser beam aligned through the multipass absorption cell, i.e., the setup for spectroscopic measurements. Thereby the power level on the sample detector was $\overline{P_{\text{opt}}} \sim 6 \mu\text{W}$, and the measured noise was in very good agreement with the results obtained with the simpler setup described above.

Signal-to-noise ratio

From the noise measurements above one can estimate the optical signal-to-noise ratio (SNR) of the present detection system, which is defined as

$$\text{SNR} = \frac{\overline{P_{\text{opt}}}}{\sqrt{\overline{\delta P_{\text{opt}}^2}}}, \quad (2.14)$$

where $(\overline{\delta P_{\text{opt}}^2})^{1/2}$ denotes the optical noise power as introduced in Eq. 2.13. The optical noise power (*black* trace) and the corresponding SNR (*blue* trace) are depicted in Fig. 2.10 (a). For spectroscopic measurements, the absorption signal is a fraction ΔP of the optical power $\overline{P_{\text{opt}}}$ incident on the detector. For small absorption signals the noise remains practically constant

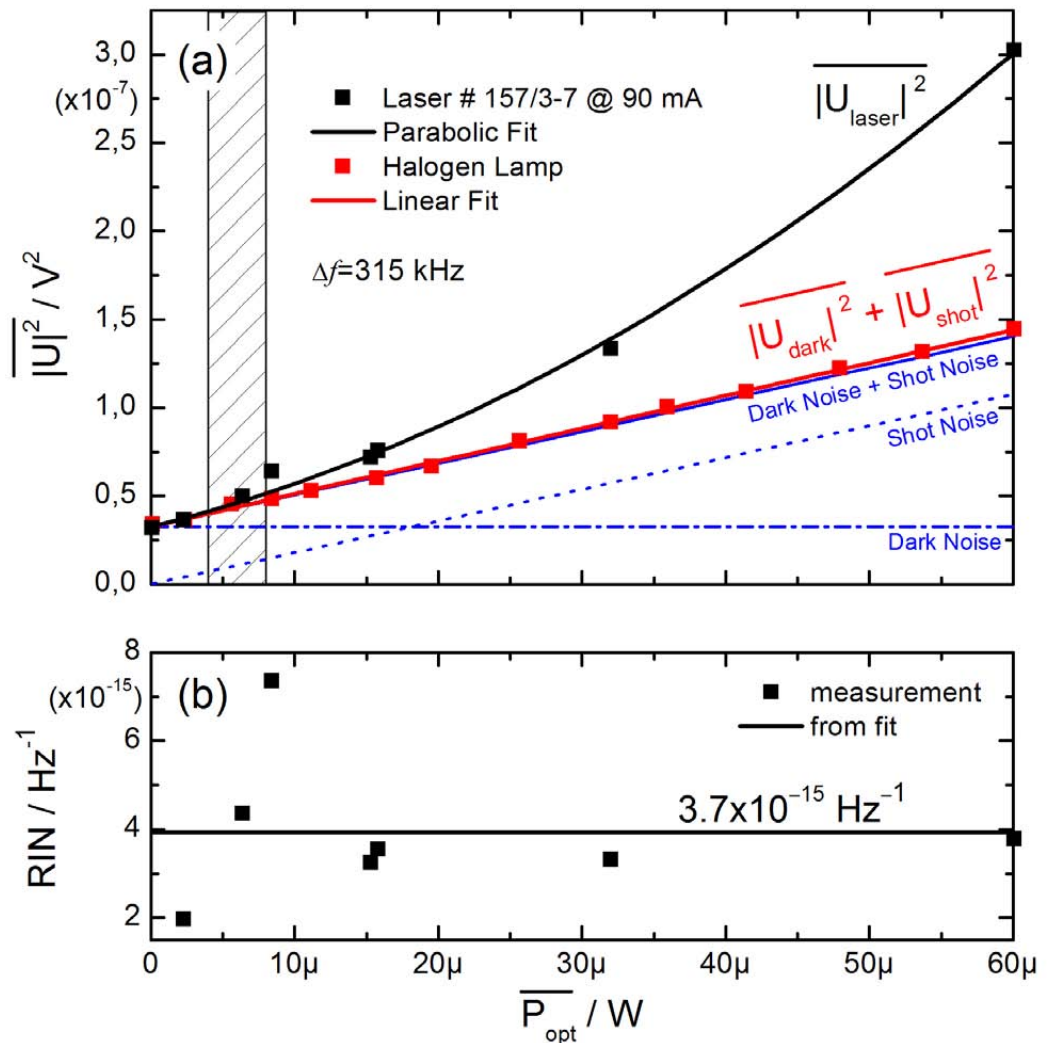


Figure 2.9: (a) Results of different noise ($\overline{|U|^2}$) measurements as a function of optical power $\overline{P}_{\text{opt}}$ taken with a detection bandwidth of 315 kHz. The red squares represent measurements of noise when the detector was illuminated with light of a halogen lamp. The red trace is a linear fit of these measurements. These measurements show very good agreement with the sum (solid blue line) of the theoretical shot noise level (dotted blue line) and the measured dark noise level (horizontal blue line). The black squares represent noise measurements using laser # 157/3-7. These measurements indicate a noise contribution in excess of the shot noise introduced by the laser. The solid black trace represents a quadratic fit to the measurements. (b) Relative intensity noise (RIN) of laser # 157/3-7 (including shot noise but excluding dark current noise) as a function of optical power incident on the detector. The squares and solid line represent the RIN as deduced from measurement and from the fit shown in (a), respectively. The relative intensity noise was determined to be $3.7 \times 10^{-15} \text{ Hz}^{-1}$ ($-144.3 \text{ dB Hz}^{-1}$).

when the laser wavelength is tuned over the absorption line. In this case the SNR becomes

$$\text{SNR}_{\text{spec}} = \frac{\Delta P}{\sqrt{\delta P_{\text{opt}}^2}} = \frac{\overline{P_{\text{opt}}}(1 - T)}{\sqrt{\delta P_{\text{opt}}^2}},$$

and with the transmission

$$\begin{aligned} T &= e^{-\text{OD}} \\ \text{SNR}_{\text{spec}} &= \frac{\overline{P_{\text{opt}}}}{\sqrt{\delta P_{\text{opt}}^2}} (1 - e^{-\text{OD}}). \end{aligned} \quad (2.15)$$

Defining $\text{SNR}_{\text{spec}} = 1$ as the detection limit one calculates the (theoretical) minimum optical density (detection limit) for the given power $\overline{P_{\text{opt}}}$

$$\begin{aligned} \text{OD}_{\text{min}} &= -\ln \left(1 - \frac{\sqrt{\delta P_{\text{opt}}^2}}{\overline{P_{\text{opt}}}} \right) \\ &= -\ln \left(1 - \frac{1}{\text{SNR}} \right). \end{aligned} \quad (2.16)$$

This dependence is depicted in Fig. 2.10 (b) for the measured data of laser #157/3-7 (*black squares*) and for the fit (solid *black* trace), where the bandwidth was reduced to $\Delta f = 1 \text{ Hz}$. Also shown is the OD_{min} for the measured shot-noise level (*red* trace). It can be seen that an increase in signal by increasing $\overline{P_{\text{opt}}}$, e.g., by using higher reflectivity mirrors within the multipass cell, can lead to an increase in SNR by about 5 times.

The *red* circle in Fig. 2.10 (b) depicts the detection limit regularly achieved for spectroscopic measurements. This detection limit is also normalized to a bandwidth of $\Delta f = 1 \text{ Hz}$. It can be seen that the detection limit of spectroscopic measurements agrees very well with the theoretical detection limit (*black* trace).

It must be noted though, that for spectroscopic measurements a bandwidth reduction to 1 Hz could only be achieved when the laser wavelength would not be scanned over the absorption line but rather remained at the absorption line center. This would, however, be at the cost of the spectral lineshape information. This information is used in the actual spectroscopic measurements to correct for wavelength drift and jitter. Jitter is corrected for by shifting the absorption spectra in memory on a scan-by-scan basis in order for them to overlap. Drift, which can be caused by slight changes of the laser temperature, is compensated for by a feedback to the laser injection current.

The actual bandwidth is therefore determined by the required detection limit as well as the need to compensate for drift effects. For the present spectroscopic measurements, an effective detection bandwidth of $\Delta f = 105 \text{ Hz}$ has led to the best results. In this case the spectra are recorded at a scan frequency of 10 Hz. Every data point within the spectral scan is recorded at a bandwidth of $\Delta f_{\text{LIA}} = 333 \text{ Hz}$, which is determined by the low-pass filter of the lock-in amplifier. Averaging the 10 Hz spectra over one second reduces the effective bandwidth by $\sqrt{10}$ to $\Delta f \approx 105 \text{ Hz}$.

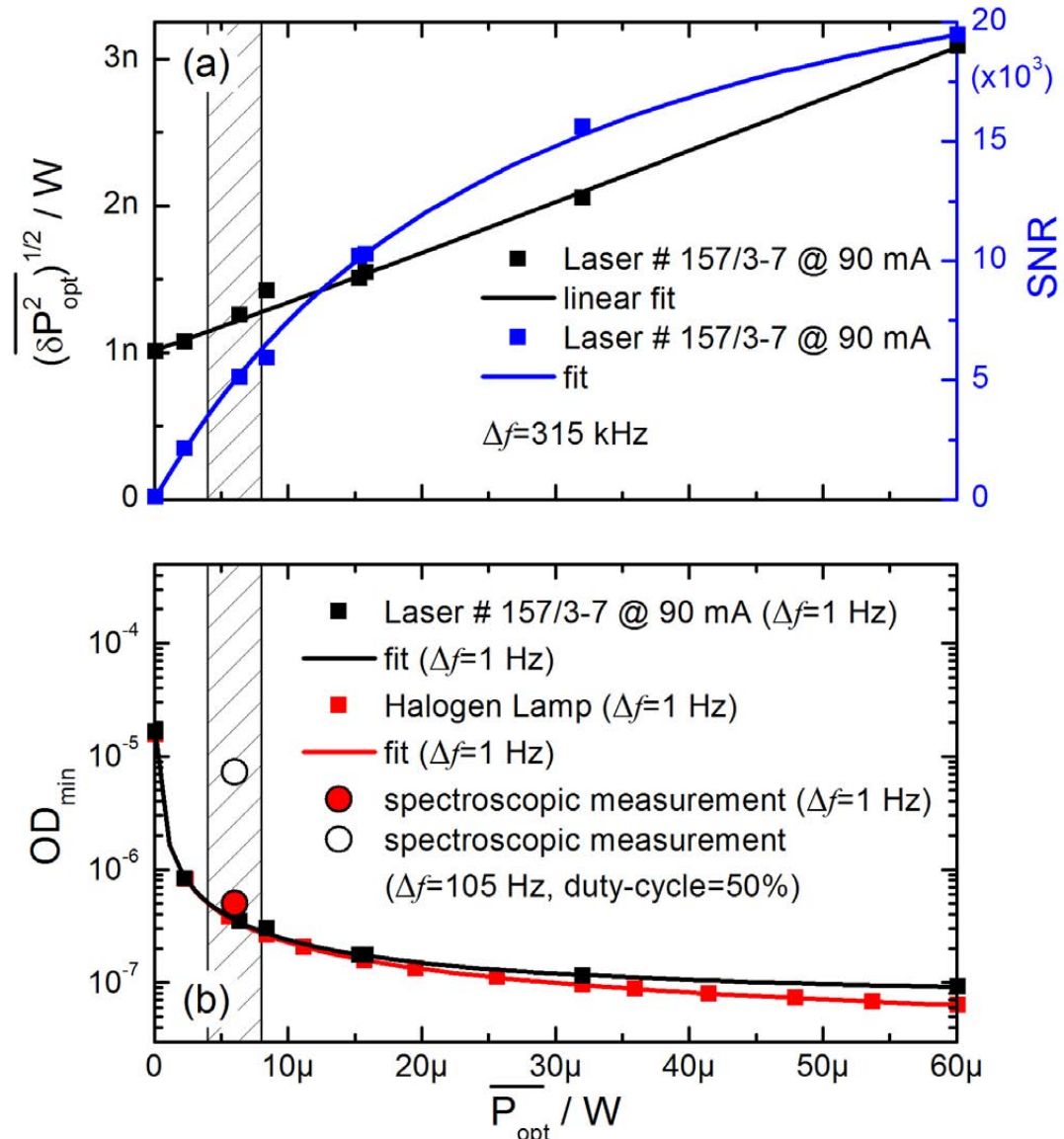


Figure 2.10: (a) The *black* squares represent the optical noise power $(\overline{\delta P_{\text{opt}}^2})^{1/2}$ versus optical power $\overline{P_{\text{opt}}}$ incident on the detector, and the solid *black* trace is the linear fit to these measurements. The detection bandwidth for these measurements is $\Delta f = 315 \text{ kHz}$. The *blue* squares and solid trace depict the signal-to-noise ratio (SNR) as deduced from measurement and fit, respectively. The spectrometer is operated in the $\overline{P_{\text{opt}}} = 4 \dots 8 \mu\text{W}$ regime (depending on alignment) as indicated by the hashed area. (b) Minimum detectable optical density (OD_{min} as defined in Eq. 2.16) normalized to a 1 Hz detection bandwidth as calculated from the measured SNR (*black* trace). Also shown is the OD_{min} for the measured shot-noise level (*red* trace). The results achieved for spectroscopic measurements normalized to $\Delta f = 1 \text{ Hz}$ are indicated by the *red* circle. The actual spectroscopic measurements are performed at an increased bandwidth ($\Delta f \approx 105 \text{ Hz}$) and reduced duty cycle ($\approx 50 \%$) as explained in the text. In this case the minimum optical density is around $\text{OD} = 7.3 \times 10^{-6}$ for a 1 s measurement time as indicated by the *white* circle.

Furthermore, the duty-cycle of the measurement is reduced to $\approx 50\%$ during spectroscopic measurements because a fraction of the scan is not used for concentration or isotopic ratio measurements. This fraction includes the spectral gap between the absorption lines as well as a certain fraction at the beginning of the scan ramp, where the signal is distorted due the rapid change of the sawtooth waveform applied to scan the laser injection current.

Taking the effective bandwidth of $\Delta f = 105\text{ Hz}$ as well as the duty cycle of 50% into account leads to $\text{OD}_{\min} = 7.3 \times 10^{-6}$ achieved for spectroscopic measurements within a measurement time of 1 s [white circle in Fig. 2.10(b)].

2.3.2 Detection limit and system stability

In order to test the sensitivity and maximum allowable averaging time of the spectrometer, the concept of the Allan variance, which was introduced in Section 1.2.2 (Page 13), was applied to spectroscopic measurements of $\delta^{17}\text{O}$ and $\delta^{18}\text{O}$ isotopic ratios. This technique requires the recording of time series data with a data set length much longer than the expected maximum stability time, which is typically around 60 seconds. Therefore, the spectrometer was calibrated with a calibration gas mixture of known absolute H_2O mixing ratio (90 ppmv) and isotopic composition (GW-9 water standard, see Tab. 1.1 on Page 26). Following the calibration, the spectrometer measured the same calibration gas mixture for 500 seconds at a 1 Hz detection bandwidth. In total, $N=17$ such measurements were carried out during three consecutive days. The measured isotopic ratios $\delta^{18}\text{O}$ and $\delta^{17}\text{O}$ of the 17 measurement sequences were then analyzed in terms of the Allan variance.

Fig. 2.11 shows the corresponding Allan plots for $\delta^{18}\text{O}$ [blue, graph (a)] and $\delta^{17}\text{O}$ [green, graph (b)], respectively. For both graphs, the thick solid trace marks the average Allan variance of the $N=17$ measurement sequences, whereas the shaded areas show the range covered by them.

Also shown are the published results of the other relevant groups that conduct in-situ isotopic-ratio measurements; 1: *Webster and Heymsfield* [2003], 2: *Hanisco et al.* [2007], and 3: *Kerstel et al.* [2006]. *Kerstel et al.* [2006] give a measurement uncertainty of $\delta^{18}\text{O} = 1\text{\%}$ and $\delta^{17}\text{O} = 3\text{\%}$ for a water mixing ratio of 200 ppmv at an averaging time of 30 seconds. Both *Hanisco et al.* [2007] and *Webster and Heymsfield* [2003] give a measurement uncertainty of 50% for both isotopic ratios at a water mixing ratio of 10 ppmv at an averaging time of 30 s and 20 s, respectively. These results have been linearly scaled to the water mixing ratio of 90 ppmv used in the present study, as the uncertainty of the isotopic ratio measurement scales with the H_2O mixing ratio.

The Allan plots in Fig. 2.11 provide information on the spectrometer detection limit for a given integration time. For the highest acquisition rate (1 Hz) of the present spectrometer, the average detection limit was determined to be $\delta^{18}\text{O} = 17\text{\%}$ and $\delta^{17}\text{O} = 5.3\text{\%}$. This corresponds to an absorbance sensitivity of $\sim 7.3 \times 10^{-6}$. Averaging over 30 s leads to an improved detection limit of $\delta^{18}\text{O} = 6.25\text{\%}$ and $\delta^{17}\text{O} = 2.07\text{\%}$, corresponding to an absorbance sensitivity of $\text{OD} = 4.35 \times 10^{-6}$. The results are compared in Tab. 2.2 with the results achieved by the other groups mentioned. All results are normalized to a mixing ratio of 90 ppmv and an averaging time of 30 s.

It must be pointed out that the other groups work in different wavelength regions. *Kerstel et al.* [2006] work in the near infrared spectral region (1.39 μm) whereas both *Hanisco et al.*

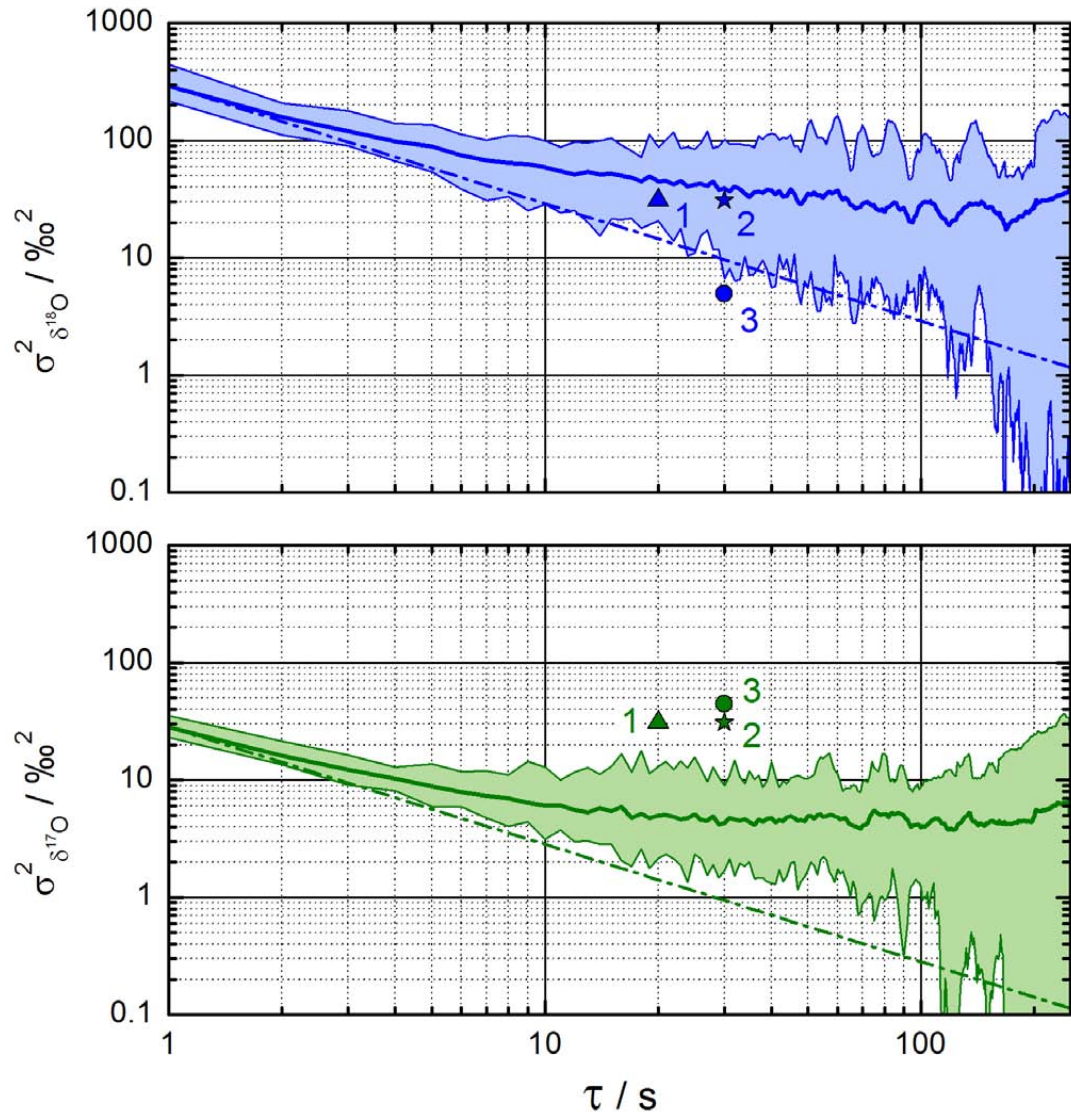


Figure 2.11: Allan variance as function of integration time for $\delta^{18}\text{O}$ (top plot) and $\delta^{17}\text{O}$ (lower plot). The thick solid lines indicate the average result of 17 consecutive measurements where the multipass cell was flushed with a gas mixture containing 90 ppmv H₂O of constant isotopic ratio. The shaded areas indicate the minimum and maximum boundaries. The dash-dotted lines indicate the theoretical white noise behavior, where the variance is reduced proportional to the integration time. The deviation of the measured values from the white noise line is associated to drift and low frequency noise. Also shown are published results from other relevant groups (1: *Webster and Heymsfield [2003]*, 2: *Hanisco et al. [2007]*, 3: *Kerstel et al. [2006]*). These results have been scaled to a water mixing ratio of 90 ppmv.

[2007] and *Webster and Heymsfield* [2003] work around $6.7\text{ }\mu\text{m}$. In the near-IR, the integrated line strength of H_2^{18}O is around 5.3 times larger than that of H_2^{17}O . This may explain the better detection limit in $\delta^{18}\text{O}$ measurements relative to the $\delta^{17}\text{O}$ measurements of *Kerstel et al.* [2006]. The average integrated line strength is ≈ 16 times weaker compared to the absorption lines probed in the present work. At $6.7\text{ }\mu\text{m}$ the H_2^{17}O absorption line is around 5 times weaker than the H_2^{18}O line. Both *Hanisco et al.* [2007] and *Webster and Heymsfield* [2003] give the same detection limit for their $\delta^{18}\text{O}$ and $\delta^{17}\text{O}$ measurements even though the H_2^{18}O absorption line is ≈ 5 times stronger than the H_2^{17}O . An explanation for this is not found in the respective publications. The average integrated line strength is roughly equivalent (78 %) to that found in the present work.

It is also worth to note that both *Kerstel et al.* [2006] and *Hanisco et al.* [2007] employ a much longer absorption path length of $\approx 4\text{ km}$. This is achieved by using resonant optical cavities instead of non-resonant multipass absorption cells. However, their results do not readily reflect this enhanced path length (factor 50 over the present system), which is probably due to increased noise related to the coupling of the laser radiation into the very narrow and discrete cavity modes. Such a setup is extremely susceptible to subtle changes in alignment, which may lead to an amplitude modulation of the radiation transmitted through the cavity. In their case, most of the signal enhancement is apparently compensated for by this additional noise.

For integration times longer than approximately five seconds the average Allan variance (thick traces in Fig. 2.11) of both isotopic ratios deviates from the theoretical white noise behavior, which is indicated by the dashed lines. This can be explained by an additional low-frequency noise contribution (see discussion below). Sometimes this additional noise contribution did not occur, i.e., where the Allan variance nearly matches the white noise line. While the detection limit in the $\delta^{18}\text{O}$ measurements may be improved by averaging over 60 s and longer, the Allan variance of the $\delta^{17}\text{O}$ measurements tends towards a horizontal level after $\approx 30\text{ s}$ averaging before starting to increase at $\approx 100\text{ s}$.

Table 2.2: Comparison of precisions achieved in $\delta^{18}\text{O}$ and $\delta^{17}\text{O}$ measurements in the present work with that of other relevant works. Results of this work have been determined at a water mixing ratio of 90 ppmv and are given for an integration time of 30 s. The results of the other works have been published for or normalized to 30 s integration time and a water mixing ratio of 90 ppmv. Also given are scaling factors for absorption path length and average integrated line strength of the absorption lines probed. These factors are provided to better illustrate the differences of the instruments. ¹*Webster and Heymsfield* [2003], ²*Hanisco et al.* [2007], ³*Kerstel et al.* [2006], ⁴*Moyer et al.* [2007], ⁵estimated from photographs.

	this work	Webster ¹	Hanisco ²	Kerstel ³
$\delta^{18}\text{O}$	6.25 %	4.6 %	5.6 %	2.2 %
$\delta^{17}\text{O}$	2.07 %	4.6 %	5.6 %	6.7 %
path-length factor	1	1.05	≈ 52	≈ 52
line-strength factor	1	0.78	0.78	0.063
instrument mass	35 kg	72 kg	$\approx 250\text{ kg}$ ⁴	45 kg
instrument dimensions	85 l	$\approx 200\text{ l}$	$\approx 500\text{ l}$ ⁵	$\approx 50\text{ l}$

To further investigate the origin of the low-frequency noise, several potentially limiting contributions have been investigated.

(a) Temperature and pressure

The performance fluctuations of the spectrometer described by the shaded areas in Fig. 2.11 could not be linked to environmental parameters such as any of the recorded temperatures (optical breadboard, multipass cell, gas temperature) or gas pressure during the measurements. Furthermore, a near-white noise behavior, e.g., in $\delta^{18}\text{O}$ measurements does not necessarily lead to an equally good performance in $\delta^{17}\text{O}$ measurements, even though both isotopic ratios were measured simultaneously.

(b) Gas flow

Werle and Jäcker [1996] have shown that pressure fluctuations in multiple pass absorption cells, which are related to turbulences in the sample gas flow through the cell, may potentially reduce the effectiveness of averaging. In order to analyze this potential noise contribution, the multipass cell was filled with a gas mixture containing ≈ 90 ppmv at a pressure of 70 hPa. The cell was then closed by valves to establish steady conditions within the cell. In the same manner as described above, 14 measurement sequences of $\delta^{17}\text{O}$ and $\delta^{18}\text{O}$ isotopic ratios were recorded and evaluated in terms of the Allan variance. The corresponding Allan plots for static conditions revealed very similar results to those obtained with a gas flow through the absorption cell. Consequently, pressure fluctuations are not present at a magnitude high enough to explain the additional noise contributions.

(c) Optical feedback

Reflections from optical surfaces, such as mirrors, windows and lenses, may induce feedback of laser radiation into the laser resonator. In the present spectrometer all transmissive optics have therefore been tilted slightly with respect to the optical axis. The only component where tilting is impractical is the multipass absorption cell. Dust on the mirror surfaces, which is unavoidable during operation, may lead to scattering of a fraction of the laser light, and this scattered light may potentially find its way back to the laser source. *Fukuda et al.* [2008] and *Kurosaki et al.* [1994] (among others) have measured an increase of ~ 20 bB of the relative intensity noise (RIN) of different distributed feedback lasers due to optical feedback.

In order to study whether such feed back of laser radiation from the multipass absorption cell (MPC) is responsible for the sometimes degraded performance, experiments were carried out where the MPC was repeatedly blocked and the spectra from the reference arm of the spectrometer were analyzed in terms of the Allan variance as described above. If feedback from the MPC was increasing RIN, one would expect a better performance when the MPC was blocked. However, for a total of 12 measurement sequences, where the MPC was alternately blocked, no significant difference in system performance could be determined.

(d) Jitter and wavelength drift

Low-frequency wavelength drift and jitter on the spectra may also limit the performance of the spectrometer. Wavelength drift can be caused by small changes in the laser temperature. The origin of jitter may be noise on the DC component of the sawtooth scan waveform. Both effects are compensated for by evaluating the 10 Hz reference spectra. In the former case, a DC offset is applied to the sawtooth scan waveform to adjust the laser emission wavelength. Jitter is compensated by shifting of the sample spectra in memory. However, the resolution of the spectra is limited by the number of discrete data points within the scan waveform, i.e. 256 points per full spectrum. Every single absorption line thereby contains about 40 points only. Simulations of second derivative spectra with equivalent resolution revealed that a shift of a sample spectrum relative to the calibration spectrum by one point along the wavelength axis may lead to a relative error of the mixing ratio of about 20 %. Therefore, a linear interpolation routine was implemented into the post-processing software to investigate potential performance degradation due to jitter. The number of points per scan thereby was increased to up to 1 024, i.e., a 4 times improvement. While this interpolation lead to an improved correction of jitter, the correction was only necessary occasionally. During most of the measurements very little correction was applied and thus no significant overall improvement could be observed.

(e) Etalon structures

The averaging is to a considerable extent limited by time-dependent structures (etalon fringes²⁰). Consider a fringe structure as a wavelength-dependent periodic signal that is superimposed on the recorded spectra. Such structures are formed by interference of laser radiation within optical cavities. In a spectrometer such as the present one, such cavities may be formed by two transmissive optical elements along the beam path, where a fraction of the laser radiation is reflected back due to Fresnel reflection²¹. Furthermore, dust on the multipass cell mirrors may lead to scattered light within the cell that may form interference fringes. The free spectral range (FSR) of the fringe, i.e. the spectral period, thereby depends on the effective optical length nl of the cavity. Thereby, n denotes the refractive index of the transmitted medium, and l is the physical length. In laser spectrometers the fringe FSR is often close to the absorption linewidth (300...600 MHz) due to the commonly found length of the free-space optical paths of 0.5 m to 1 m. It is therefore difficult, often impossible to filter such structures out. If l changes, e.g. by a slight temperature drift, the fringe moves through the spectrum, i.e., it changes its phase. Depending on the amplitude, the fringe has a certain contribution to the absorption signal, which is in turn also time-dependent. Assuming, as a first approximation, that the fringe changes its phase steadily, this results in a periodic signal superimposed to the concentration time series.

This periodicity is also found in the Allan plots depicted in Fig. 2.11. Consider the minimum boundary of the $\delta^{17}\text{O}$ Allan plot (lower green trace). This trace departs from the the-

²⁰The term fringe is commonly used in publications and is adapted here for the sake of simplicity.

²¹For example, at the uncoated entrance facet of a glass window or lens, approximately 4 % of the laser radiation is reflected back due to Fresnel reflection.

oretical white noise line at approximately five seconds integration time, but reaches this line again at an integration time of ≈ 100 s. Between 5 s and 100 s integration time, the system was dominated by drift, i.e., the deduced isotopic ratio $\delta^{17}\text{O}$ slowly drifted periodically. At an integration time of ≈ 100 s, one full period of this drift is present within the integration interval and consequently averages to (nearly) zero. However, generally there will not only exist one fringe but rather a superposition of multiple fringes at multiple frequencies, phases, and amplitudes. For the present spectrometer, the average Allan variance, as depicted by the thick traces is Fig. 2.11, therefore lies somewhat above the theoretical white noise line.

It must be stressed out, that even though low-frequency drift limits the improvement of the detection limit by averaging to some extent, the average performance of the present spectrometer is quite remarkable. In fact, the one-second absorbance sensitivity of $\text{OD} = 7.3 \times 10^{-6}$ is — to the best of my knowledge — among the best found within the literature. The sensitivity of isotopic ratio measurements, which is prerequisite for scientific operation of this instrument aboard airborne research platforms, is also highly competitive (compare with the results achieved by the other relevant groups and given in Fig. 2.11 on Page 64 and Tab. 2.2 on Page 65).

2.3.3 Measurement accuracy

In addition to the extensive tests regarding the spectrometer detection limit, the instrument was further tested with respect to its response to water standards of different isotopic composition as a measure of accuracy. Therefore the two working standards GW-9 and AIC-48 (see Tab. 1.1 on Page 26) were used. The spectrometer was calibrated every 10 minutes (600 s) with GW-9 by recording a 30 s calibration spectrum. This was followed by recording sample spectra every second for the following 570 s, i.e., a ten minutes measurement cycle. The standards were switched every 300 s using solenoid valves, thus measurements of both standards were performed during every calibration cycle.

Due to a temporary failure of the calibration unit described in Section 2.2.3, the two standards were provided by a bubbler unit. Thereby, the two gas standards were produced by humidifying a small flow of dry air (N₂ 6.0) in two separate glass bubblers. Each bubbler was filled with one of the liquid water working standards. The small flow of humidified air was subsequently diluted with a larger flow of 2 l(std)/min of dry nitrogen. Either of the water standards was used for this purpose, whereas the other one was dumped. The gas flows were adjusted to achieve a water mixing ratio of around 700 ppmv for both gas standards, which was monitored by a dew-point hygrometer²².

As discussed in Section 1.4.1, evaporation of water, as occurring in the bubbler unit, leads to isotopic fractionation due to the slightly different vapor pressures of the different isotopologues. Thereby the heavier isotopologues are depleted in the gas phase. This fractionation is dependent on temperature, which was therefore controlled to 24 °C. The isotopic fractionation at this temperature is $\delta^{18}\text{O} = -13.5\text{ ‰}$ and $\delta^{17}\text{O} = -7.15\text{ ‰}$. This leads to an isotopic ratio of the two gas standards of around $\delta^{18}\text{O}_{(\text{GW-9})} = -22.35\text{ ‰}$, $\delta^{17}\text{O}_{(\text{GW-9})} = -11.88\text{ ‰}$, $\delta^{18}\text{O}_{(\text{AIC-48})} = -60.43\text{ ‰}$, and $\delta^{17}\text{O}_{(\text{AIC-48})} = -32.4\text{ ‰}$ with respect to VSMOW.

²²Model DewMaster, EdgeTech, Marlborough, MA, USA

Fig. 2.12 (a) shows the results of these measurements. The isotopic ratios $\delta^{17}\text{O}$ and $\delta^{18}\text{O}$ are depicted by the *green* and *blue* points, respectively. The solid horizontal lines indicate the expected δ -values based on equilibrium isotopic fractionation within the bubblers. These values are labeled with their respective water standards.

The isotopic fractionation of the oxygen isotopologues H_2^{17}O and H_2^{18}O in natural water reservoirs is correlated due to the mass dependence of the fractionation (Eq. 1.22 on Page 27), where $\delta^{18}\text{O} \approx 2 \times \delta^{17}\text{O}$. The deviation from this correlation is termed the $\Delta^{17}\text{O}$ -anomaly, and is defined as

$$\Delta^{17}\text{O} = \ln(1 + \delta^{17}\text{O}) - 0.528 \cdot \ln(1 + \delta^{18}\text{O}) . \quad (2.17)$$

For natural liquid water reservoirs $\Delta^{17}\text{O} = 0\text{\textperthousand}$. It could be shown by *Franz and Röckmann* [2005] that this correlation is valid to a very high degree ($\Delta^{17}\text{O} < 2\text{\textperthousand}$) for both tropospheric as well as lower stratospheric water vapor isotopic ratios.

This correlation was used in the present experiment as an additional tool to study the quality of the measured data. Assuming accurate measurements of $\delta^{18}\text{O}$ and $\delta^{17}\text{O}$ one should calculate $\Delta^{17}\text{O} = 0\text{\textperthousand}$. The lower plot in Fig. 2.12 displays the $\Delta^{17}\text{O}$ values calculated from the measured isotopic ratios employing Eq. 2.17. For the entire data set of around 1.75 hours length the mean deviation was calculated to be $\Delta^{17}\text{O} = -0.96\text{\textperthousand}$ at an uncertainty of the one-second measurements of $\sigma = 3.48\text{\textperthousand}$.

However, the measured isotopic ratios $\delta^{18}\text{O}$ and $\delta^{17}\text{O}$ of the more depleted water standard (AIC-48) displayed in Fig. 2.12 (a) tend to be slightly overestimated compared to the expected values. Several reasons can account for this effect.

First, the antarctic water standard had to be purified due to a contamination after its isotopic composition was measured by mass spectrometry. The purification was achieved by distillation at boiling temperatures (100°C). Even though isotope fractionation at high temperatures is rather small compared to room temperature, a small lightening of the distillate may be present.

Second, and believed to be the main cause, is the contribution of residual water absorption at atmospheric pressure within the free-space optical path of the spectrometer (97.5 cm). Though the absorption lines at atmospheric pressure are substantially broader than at the reduced pressure within the multipass absorption cell, a small absorption signal from the $\geq 10000\text{ ppmv}$ H_2O remains even at second-harmonic detection. As a consequence, mixing ratios above the calibration mixing ratio are underestimated, whereas mixing ratios below calibration mixing ratio are overestimated. Assuming a constant absolute H_2O mixing ratio but changing isotopic composition, negative δ -values with respect to the calibration standard will therefore be overestimated, whereas positive δ -values will be underestimated.

The inaccuracy for this particular measurement was around $5 \dots 10\text{\textperthousand}$ for $\delta^{18}\text{O}$ and around $2.5 \dots 5\text{\textperthousand}$ for $\delta^{17}\text{O}$. It must be noted though, that the magnitude depends on the residual H_2O mixing ratio. In order to compensate for this inaccuracy, it is planned to implement a third detector into the spectrometer, which is devoted to detect second-derivative spectra of the residual water. Thereby, the free-space beam path will be matched to the path of the beam within the present sample arm of the spectrometer, i.e. 97.5 cm. Using equal preamplifier gain and accounting for potential differences in detector responsivity will allow subtraction of the residual absorption signal from the sample signal. This will in turn maximize the accuracy of the isotopic ratio measurements.

Short term fluctuations on a time scale of around 100 s may also be noted in the isotopic ratios in Fig. 2.12 (a) as well as the $\Delta^{17}\text{O}$ -values. These fluctuations are attributed to etalon

fringes discussed above. For the present measurements, the uncertainty due to these fringes is approximately 2.5 ‰ and 5 ‰ for $\delta^{17}\text{O}$ and $\delta^{18}\text{O}$, respectively.

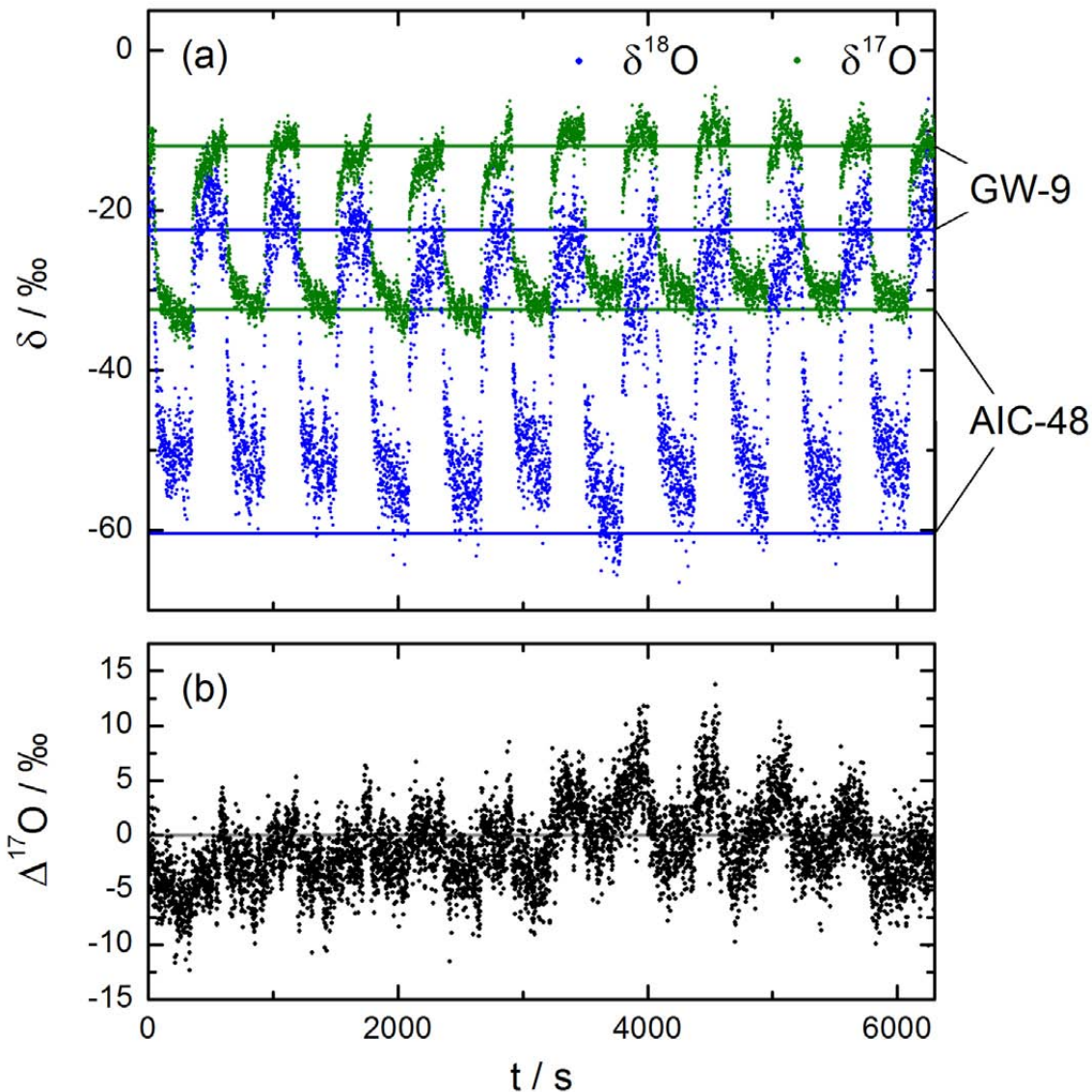


Figure 2.12: The top plot shows results of repeatedly switching between two standards of different isotopic composition every 300 s. The spectrometer was calibrated using the GW-9 standard every 600 s (10 min) as indicated by the light circles. The *green* trace shows the measured $\delta^{17}\text{O}$, and the *blue* trace shows the $\delta^{18}\text{O}$ values at a 1 Hz acquisition frequency. The solid horizontal lines indicate the expected values (assuming true equilibrium condition in bubbler stage). The lower plot gives the $\Delta^{17}\text{O}$ values calculated from the measured data. Due to the strong correlation between $\delta^{17}\text{O}$ and $\delta^{18}\text{O}$ this value should be $\Delta^{17}\text{O} = 0\text{ ‰}$. The results indicate $\Delta^{17}\text{O} = -0.96 \pm 3.48\text{ ‰}$.

2.3.4 Conclusion

The present spectrometer has been analyzed in terms of its potentials and limits towards water (H_2O) vapor isotopic ratio measurements. First, the noise sources within the detection system have been identified and quantified. It could be shown, that the spectrometer is operated only 3 %...8 % above the shot-noise limit. It was determined that laser excess noise is the dominant noise contribution.

Second, spectroscopic measurements of H_2O isotopic ratios ($\delta^{17}\text{O}$ and $\delta^{18}\text{O}$) have been performed in order to determine the spectrometer's stability time and detection limit. Therefore, time-series data of $\delta^{17}\text{O}$ and $\delta^{18}\text{O}$ isotopic ratios have been recorded and have been analyzed by means of the Allan variance method. Stability times of around 30...60 s could be achieved. The corresponding detection limit for isotopic ratio measurements were $\delta^{17}\text{O} = 2.07\text{‰}$ and $\delta^{18}\text{O} = 6.25\text{‰}$ for an averaging time of 30 s and a water mixing ratio of 90 ppmv. These detection limits results are among the best results published for H_2O isotopic ratio measurements by means of diode-laser spectroscopy.

The measurement accuracy of the present spectrometer has been determined by analyzing the response of the spectrometer to H_2O standards of different isotopic ratio. The measurements revealed an accuracy of 2.5...5‰ for $\delta^{17}\text{O}$ and 5...10‰ for $\delta^{18}\text{O}$, respectively.

2.4 Performance specifications

In this Section the performance specifications of the compact water vapor isotopic ratio spectrometer are summarized. Fig. 2.13 shows a photograph of the spectrometer with the enclosure of the optical part removed. The lower (closed) part of the instrument contains the electronics for housekeeping and data acquisition. The optics are mounted on a custom aluminum breadboard of $52 \times 40\text{ cm}^2$ mounted on shock mounts.

The computer display is used in the laboratory for raw-data display. All data are stored on a compact-flash card for further analysis during post-processing.

The instrument physical properties and measurement specifications are summarized in Tab. 2.3.

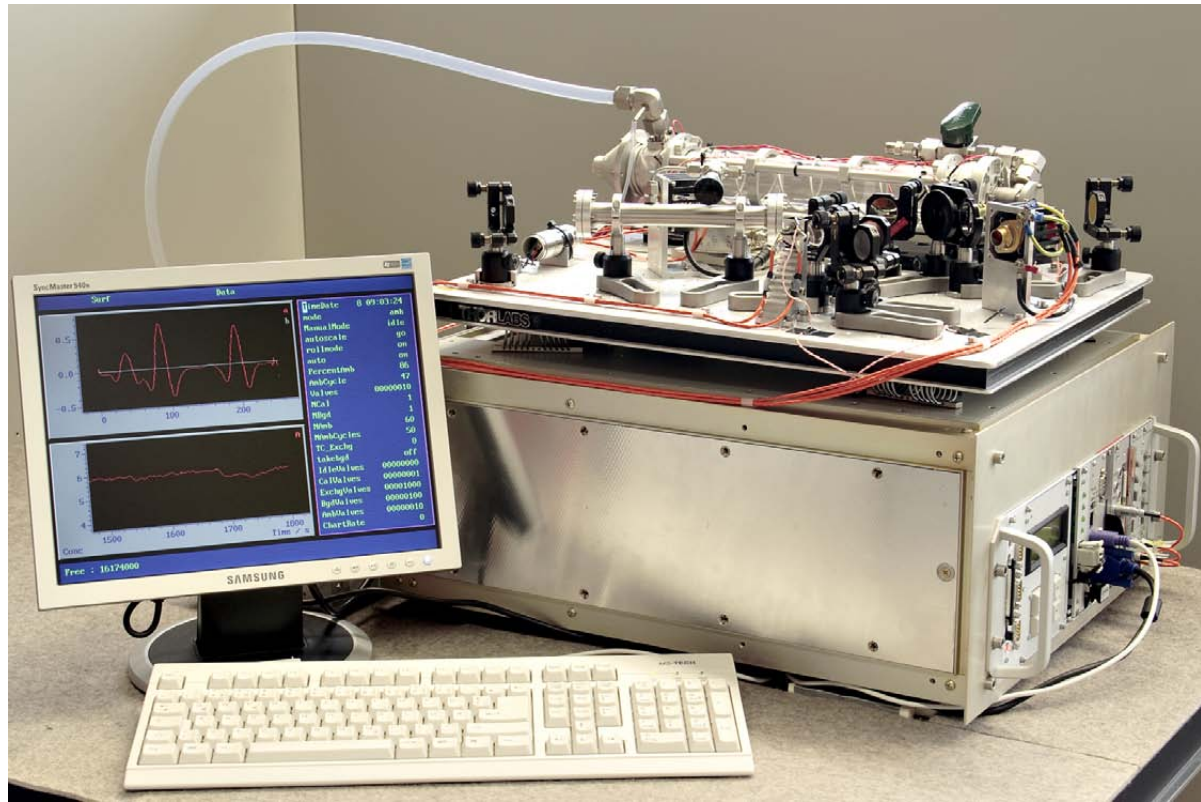


Figure 2.13: Photograph of the water vapor isotopic ratio spectrometer. The cover was removed for better illustration. The lower compartment contains all electronics. Mounted on vibration isolating elements above is the breadboard with the optical setup. Display and keyboard are for laboratory use only.

Table 2.3: Instrument specifications of the water vapor isotopic ratio spectrometer. The physical properties are given excluding the pump, which is subject of available space and weight for the specific airborne platform.

Physical properties		
Dimensions (L × W × H)	$56 \times 45 \times 35 \text{ cm}^3$	
Instrument mass	35 kg (excl. pump)	
Power consumption	max. 200 W (excl. pump)	
Operation mode	autonomous	
Measurement specifications		
Mixing ratio range	5...10 000 ppmv	
	$\delta^{17}\text{O}$	$\delta^{18}\text{O}$
Precision (30 s averaging, 90 ppmv)	2 %	6.25 %
Measurement accuracy	2.5...5 %	5...10 %

2.5 Future improvements

The present version of this instrument already includes various improvements over an earlier version that participated at the 2007 AquaVIT (**Aqua Validation and Instrument Tests**) measurement campaign [Saathoff *et al.*, 2008]. This campaign was carried out at the AIDA (**Aerosol Interaction and Dynamics in the Atmosphere**) aerosol chamber at the Research Center Karlsruhe, where 17 groups from seven countries participated with 22 instruments. As the present instrument was finalized just prior to the campaign, the well defined conditions at the AIDA were used to thoroughly test various aspects regarding short- and long-term performance.

Improvements that have been implemented after AquaVIT include (a) the use of a more stable optical breadboard to minimize temperature induced amplitude drifts, (b) shorter free-space optical paths to minimize vibration-induced amplitude modulation noise, (c) low-noise laser controller, and (d) sample detector with improved noise and responsivity specifications.

Even though the performance of the present isotopic ratio spectrometer after realization of the above improvements is among the best published, it would of course be desirable to improve the effectiveness of time averaging in order to reach an even better precision. All transmissive optics of the present instrument, although being slightly tilted with respect to the optical axis, are presently not anti-reflection coated. Dielectrically coated optics with a residual reflectivity of < 0.1 % will therefore be implemented in a future version of this spectrometer.

A promising approach for the reduction of etalon fringes that originate from interference within multipass absorption cells has been proposed by *Silver and Stanton* [1988]. These authors have employed a piezoelectric transducer to one of the absorption cell mirrors, and by periodic modulation of the mirror position over several times the fringe period were able to almost entirely suppress the etalon fringes. Thereby the phase of the fringes is periodically changed and the fringe signal is reduced by averaging. It is therefore scheduled to implement such an approach into the present multipass absorption cell.

Both the use of antireflection-coated optics as well as piezoelectric transducer are believed to minimize optical interference structures and ultimately lead to an improved detection limit for isotopic ratio measurements.

It is also scheduled to switch to a slightly different laser wavelength (2.66 μm), which will allow to probe H_2^{16}O , H_2^{18}O , and HDO for measurements of $\delta^{18}\text{O}$ and δD isotopic ratios. The spectral window is depicted in Fig. 2.14 showing water vapor and its isotopologues (*red* trace) as well as CO_2 (*blue* trace) and N_2O (*green* trace) as potentially interfering absorbers. The mixing ratios are typical for the dry stratosphere. CO_2 and N_2O mixing ratios are quite constant, and their contribution can therefore very well be characterized in the laboratory.

This spectral window does not allow to probe H_2^{17}O . However, the strong correlation of $\delta^{17}\text{O}$ and $\delta^{18}\text{O}$ in atmospheric water vapor (Eq. 1.22), which has been proven by *Franz and Röckmann* [2005], compensates the requirement for $\delta^{17}\text{O}$ measurements.

The integrated line strengths of the water isotopologue absorption lines in this spectral window are significantly larger than of those probed at present. Assuming a similar signal-to-noise ratio at this slightly different wavelength, a sensitivity increase of 4.4 times and 1.5 times is expected for measurements of $\delta^{18}\text{O}$ and δD , respectively. The HDO absorption line is one of the strongest accessible absorption lines for this isotopologue.

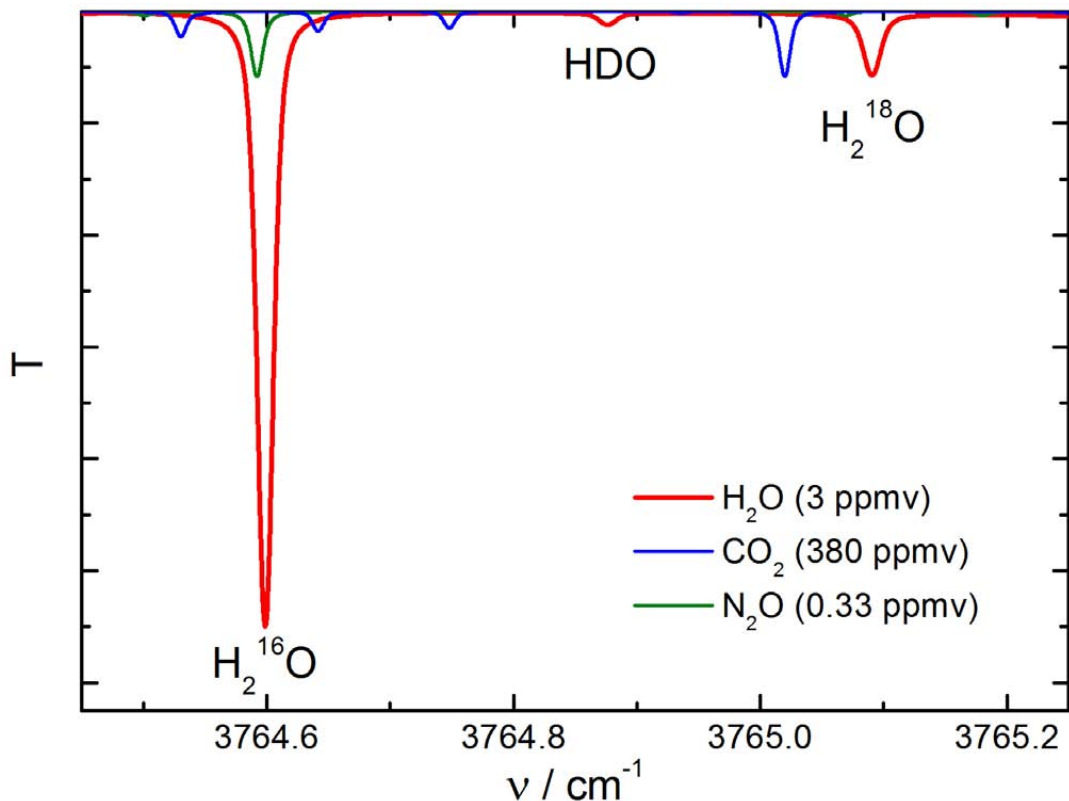


Figure 2.14: Calculated transmission spectrum of the 3765 cm^{-1} wavenumber spectral region showing absorption of 3 ppmv water vapor (red trace), 380 ppmv CO_2 (blue trace), and 0.33 ppmv N_2O (green trace) at a pressure of 50 hPa. These mixing ratios correspond to conditions present in the dry stratosphere. This spectral window offers very good possibility to probe H_2^{16}O , H_2^{18}O , and HDO absorption lines with higher integrated line strength than within the present study. Furthermore, at the wavelength presently used, the HDO absorption line can not be probed in atmospheric air as it is completely obscured by a strong CO_2 absorption line. This spectral window does not allow to probe H_2^{17}O . However, the strong correlation of $\delta^{17}\text{O}$ and $\delta^{18}\text{O}$ in atmospheric water vapor (Eq. 1.22), which has been proven by *Franz and Röckmann* [2005], compensates the requirement for $\delta^{17}\text{O}$ measurements. Assuming a similar signal-to-noise ratio at this slightly different wavelength, a sensitivity increase of 4.4 times and 1.5 times is expected for measurements of $\delta^{18}\text{O}$ and δD , respectively.

Chapter 3

A novel approach to formaldehyde measurements

The majority of the work, which is presented in the present Chapter, has previously been published in:

- (1) **C. Dyroff**, A. Zahn, W. Freude, B. Jäcker, P. Werle (2007), Multipass cell design for Stark modulation spectroscopy, *Applied Optics*, 46, 4000-4007.
- (2) **C. Dyroff**, P. Weibring, A. Fried, D. Richter, J. G. Walega, A. Zahn, W. Freude, P. Werle (2007), Stark-enhanced diode-laser spectroscopy of formaldehyde using a modified Herriott-type multipass cell, *Applied Physics B*, 88, 117-123.

Figures included in this dissertation for a more detailed description are the Figs. 3.1, 3.2, 3.9, 3.11, 3.13, as well as Fig. 3.15. Fig. 3.8 has been updated with data measured after publication of Paper 2. Also included for better overview is Tab. 3.1. Section 3.5 has been included to describe possible improvements to the Stark modulation technique, while in Section 3.6 the applicability of this technique to other gases is discussed.

The detection of ambient CH₂O in the background atmosphere requires sensitivities below 100 parts per trillion by volume (pptv). Employing a typical absorption path length of 100 m and sample pressures around 70 hPa, this translates to absorbance sensitivities in the lower 10⁻⁶ to the lower 10⁻⁷ range. To this end, the spectral data are averaged over one minute or longer. However, the averaging time is generally limited to about 30 s to 60 s on real-world airborne platforms because of instabilities of the system. Time-dependent background (etalon) structures superimposed to the spectra, which are caused by scattering from multiple optical sources, and have multiple time constants, frequencies, and phases, reduce the effectiveness of time averaging [Werle *et al.*, 1993].

To achieve high stability times, these background structures need to be captured frequently by flushing the absorption cell with zero-air, i.e., by a gas mixture without the target species for recording background spectra. The background spectra can then be subtracted from the sample spectra to achieve background free spectra of the target gas of interest [Werle *et al.*, 2004].

Many tunable diode laser absorption spectrometers rely on background subtraction. Dependent upon the design and operating environment, system stability times of several tens of seconds up to 260 s have been achieved [Kormann *et al.*, 2002; Weibring *et al.*, 2006]. However, the flushing and the resulting gas exchange times lead to a considerable degradation of the system's duty-cycle. In addition, especially on high-speed airborne platforms, relatively small spatial and short temporal atmospheric inhomogeneities are not measured when performing background measurements.

The present work investigates the possibilities and limits of a unique approach introduced by Werle and Lechner [1999]. These authors have demonstrated that a selective modulation of the absorption line of interest by means of the Stark effect can overcome the limitations induced by optical background structures. Instead of only averaging the absorption signal that is perturbed by a time-dependent background, the absorption signal itself is selectively modulated. If the absorption signal is modulated faster than the change of the background, the detected signal is free of the background.

The selective modulation of the absorption line by means of the Stark effect is based on the splitting of its rotational energy levels (i.e. ground and excited state levels) when an external electric field is applied to the sample gas [Townes and Schawlow, 1975; Werle and Lechner, 1999]. The absorption line affected by the electric field becomes distorted (broadened or shifted) by the Stark effect, thereby changing the absorption coefficient for any wavelength inside the spectral line. The background structures are not affected by the Stark effect, and it is thus possible to separate the signal of the absorption line from that of the background structure.

The present work focuses on the target gas formaldehyde (CH₂O), an important trace gas in atmospheric chemistry [Fried *et al.*, 2003; Harris *et al.*, 1989; Herndon *et al.*, 2005; Kormann *et al.*, 2002; Lancaster *et al.*, 2000; Li *et al.*, 2004; Rehle *et al.*, 2001; Werle and Popov, 1999]. This approach, however, is also applicable to other atmospheric trace constituents exhibiting an appreciable Stark effect as will be discussed in Section 3.6.

Two different data acquisition approaches are presented. In the first approach (alternate measurements of signal and background) the (static) electric field was turned ON and OFF on a scan-by-scan basis. This allowed to subtract the spectra recorded during the electric field ON from the spectra where the electric field was OFF, thus reconstructing background free spectra of the target gas. In the second approach (interleaved measurements of signal and background) the (static) electric field was modulated at a higher frequency, and the spectral data were processed by an additional lock-in amplifier referenced to the electric field modulation frequency. Both techniques extract only that part of the absorption signal which is affected by the electric field, thus removing the signal component caused by scattered and back-reflected laser radiation (etalon structures).

After briefly reviewing the theory of the Stark effect and discussing the application of it towards formaldehyde measurements in Section 3.1, a novel multipass absorption cell design is presented in Section 3.2. With the particular design presented here, an electric field can be applied to the target gas while allowing for absorption path lengths of up to 40 m. The formalisms to describe the optics of this multipass cell are described in Section 3.2.1. A detailed study of the cell's stability to various forms of misalignment is included in Section 3.2.2 and the results are compared to a classical Herriott absorption cell design. The actual cell design is described in Section 3.2.3.

Two different approaches of drift compensation by means of Stark modulation have been investigated, and these approaches are described in Section 3.3. The experimental setup that has been used to investigate the potential and the limits of the selective Stark modulation is described in Section 3.3.1. Before the two approaches are described in detail, the maximum allowable electric field for the present multipass cell design is evaluated in Section 3.3.2. The electric field plays an important role in Stark modulation experiments, as it determines the magnitude of the Stark effect and thus the signal to be measured.

The first Stark modulation approach makes use of alternate measurements of signal and background at a relatively low modulation frequency (Section 3.3.3). The second approach works with a higher modulation frequency, which is used to conduct interleaved measurements of signal and background (Section 3.3.4).

The results of the two approaches are discussed separately in Sections 3.4.1 and 3.4.2 before a more general discussion of the detection limit of the Stark modulation experiments is presented in Section 3.4.3.

A discussion of means that potentially lead to a higher sensitivity is given in Section 3.5. Finally, the applicability of the Stark modulation to other molecular species is described in Section 3.6. Of particular interest in our research group in this respect is water vapor and its stable isotopologues, and the applicability of Stark modulation to this molecule is discussed in some detail.

3.1 Stark effect

The Stark effect¹ in molecular spectra describes changes in the rotational spectrum of a molecule which has an electric dipole moment μ . Because the electric field applies torque on the molecular dipole moment and thereby changes the molecule's rotational motion [Townes and Schawlow, 1975], the spectrum is modified by a splitting of the rotational energy levels.

Formaldehyde is a slightly asymmetric (near-symmetric) prolate rotor² with a dipole moment of $\mu=2.34$ Debye (Fig. 3.1). The dipole moment is directed along the a -axis of this molecule.

For the description of the Stark effect consider two energy levels that are nearly degenerate (as is often the case for slightly asymmetric top molecules). If these levels have an energy level difference of δ , and are coupled by a dipole moment μ_{12} , these levels split into $M = 0 \dots J$ components under the influence of an external electric field E , where M is the projection of J in electric field direction. The change in energy ΔW of the M^{th} component is [Callegari, 2004; Werle and Lechner, 1999]

$$\Delta W(E) = \frac{\delta}{2} \left[\sqrt{1 + \left(\frac{2E\mu_{12}}{\delta} \right)^2} - 1 \right], \quad (3.1)$$

¹Named after Johannes Stark, German physicist, 1874–1957. Was awarded the Nobel Prize in Physics in 1919 for his *discovery of the Doppler effect in canal rays and the splitting of spectral lines in electric fields*.

²A symmetric top molecule is a molecule that has two identical moments of inertia. By historical convention a prolate rotor has $I_A < I_B = I_C$. Formaldehyde is a slightly asymmetric prolate rotor, because I_B is slightly different from I_C due to the mass distribution of this molecule [compare with Fig. 3.1 (a)].

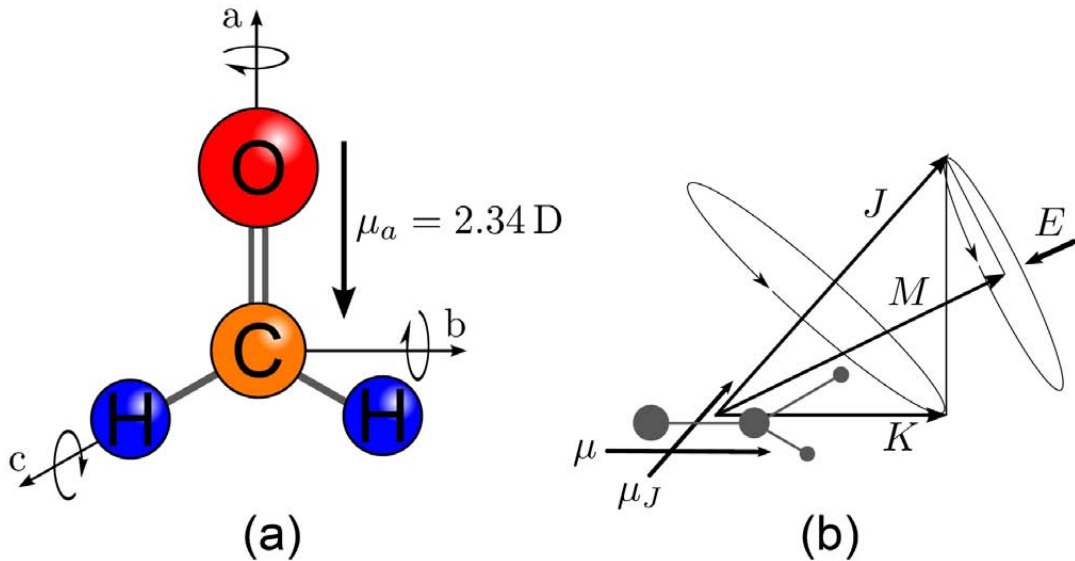


Figure 3.1: (a) Molecular structure of formaldehyde. The dipole moment μ is directed along the a axis of the molecule. The dimensions are not drawn to scale. (b) Vector model showing the influence of an external electric field E on the rotational motion of a molecule. Without external electric field the molecule precesses about the direction of total angular momentum J . When applying an external electric field E the projection of the dipole moment on J , μ_J , will interact with the electric field. The angular momentum J now precesses about the electric field E . Figure adapted from Sugden and Kenney [1965].

where the dipole matrix element μ_{12} is given by [Sakurai *et al.*, 1967]

$$\mu_{12} = \frac{\mu MK}{J(J+1)} . \quad (3.2)$$

Here K is the projection of the angular momentum J along the molecule's symmetry axis [Fig. 3.1(b)]. According to Eq. 3.2, absorption transitions with low quantum number J and high K lead to the highest energy shifts. Also, the energy level difference δ for two near degenerate levels should be rather small, and (for CH₂O) these levels must fulfill the selection rules: $\Delta J = 0$, $\Delta K_a = 0$, and $\Delta K_c = \pm 1$ (K_a and K_c represent the projection of J along the molecule's symmetry axis a and c , respectively). Depending on the polarization of the laser radiation (E-field) with respect to the (external) electric field, selection rules for the different resulting absorption transitions exist;

- (a) laser polarization parallel to the external electric field allows for $\Delta M = 0$ transitions, where an absorption line is split into J components, and
- (b) laser polarization perpendicular to the external electric field allows for $\Delta M = \pm 1$ transitions, where an absorption line is split into $2J - 1$ components. Here J is the higher of the two quantum numbers involved in the absorption transition.

Employing the Stark-MPC described in Section 3.2 one observes a Stark-spectrum that contains both $\Delta M = 0$ and $\Delta M = \pm 1$ transitions because the direction of the laser polarization will change with respect to the external radial electric field direction, thereby exciting all components equally along its path through the cell.

Table 3.1: Formaldehyde (CH_2O) absorption line parameters of the transitions shown in Fig. 3.2 (b) giving the line center frequency v_0 , integrated line strength S_{ij} , air broadening coefficient γ_{air} , ground state energy E'' , as well as the quantum numbers J , K_a and K_c for both excited state and ground state. The transitions exhibiting a Stark effect are highlighted in **bold**. Line parameters kindly provided by Peter Werle (IMK, Garmisch-Partenkirchen) [Werle, 2005].

v_0 (cm^{-1})	$S_{ij} \times 10^{-20}$ ($\frac{\text{cm}^2}{\text{cm molecule}}$)	γ_{air} ($\frac{\text{cm}^{-1}}{\text{bar}}$)	E'' (cm^{-1})	J'	K'_a	K'_c	J''	K''_a	K''_c
1 755.889 6	3.49	0.1	23.248 7	4	1	3	3	1	2
1 757.862 3	1.55	0.1	24.259 7	5	0	5	4	0	4
1 757.913 9	1.11	0.1	57.042 5	5	2	4	4	2	3
1 757.937 6	2.08	0.1	97.957 7	5	3	3	4	3	2
1 757.938 1	2.08	0.1	97.957 8	5	3	2	4	3	1
1 757.948 9	0.295	0.1	155.169 4	5	4	2	4	4	1
1 757.962 5	1.11	0.1	57.078	5	2	3	4	2	2
1 758.314 7	4.26	0.1	33.283 5	5	1	4	4	1	3

Assuming an absorption line with a line center at v_0 and a Lorentzian line shape with a HWHM Δv_L , the intensity distribution function $I(v, E)$ is the sum of the M components with their individual relative intensity S_M ,

$$I(v, E) = \sum_M \frac{S_M \Delta v_L^2}{\Delta v_L^2 + [v_0 + \Delta v_M(E) - v]^2} \quad (3.3)$$

Absorption line parameters of CH_2O (and many other gases) are listed in the HITRAN database [Rothman *et al.*, 2005]. However, the entry of CH_2O is incomplete, and for the 1757 cm^{-1} spectral region HITRAN does not list any absorption lines. Absorption line parameters of this spectral region were kindly provided by Peter Werle [Werle, 2005] and are listed in Tab. 3.1. The integrated line strength of CH_2O along with those of other relevant and potentially interfering molecules are shown in Fig. 3.2 (a).

In this study a doublet at 1757.938 cm^{-1} ($5_{32} - 4_{31}$ and $5_{33} - 4_{32}$) previously investigated by Werle and Lechner [1999] was used. For this doublet, both the ground- and the excited-state energy levels are nearly degenerate and are coupled by the selection rules mentioned above (see Tab. 3.1). The ground states have $J'' = 4$, hence they are split into five components each. The excited states have $J' = 5$ resulting in 6 components each. The integrated line strength for both transitions is $2.08 \times 10^{-20} \text{ cm/molecule}$.

A calculated absorption spectrum of 440 ppbv CH_2O at a pressure of 25 hPa is shown by the *black* trace in Fig. 3.2 (b). The nearest absorption lines are due to water (H_2O), and are around 0.35 cm^{-1} away (shown as *red* trace). The inset in Fig. 3.2 (b) shows the calculated direct absorption spectrum of the CH_2O absorption doublet (and nearby transitions) based on Eq. 3.3 without external electric field (*black* trace) and with an external electric field of 1050 Vcm^{-1} (*blue* trace).

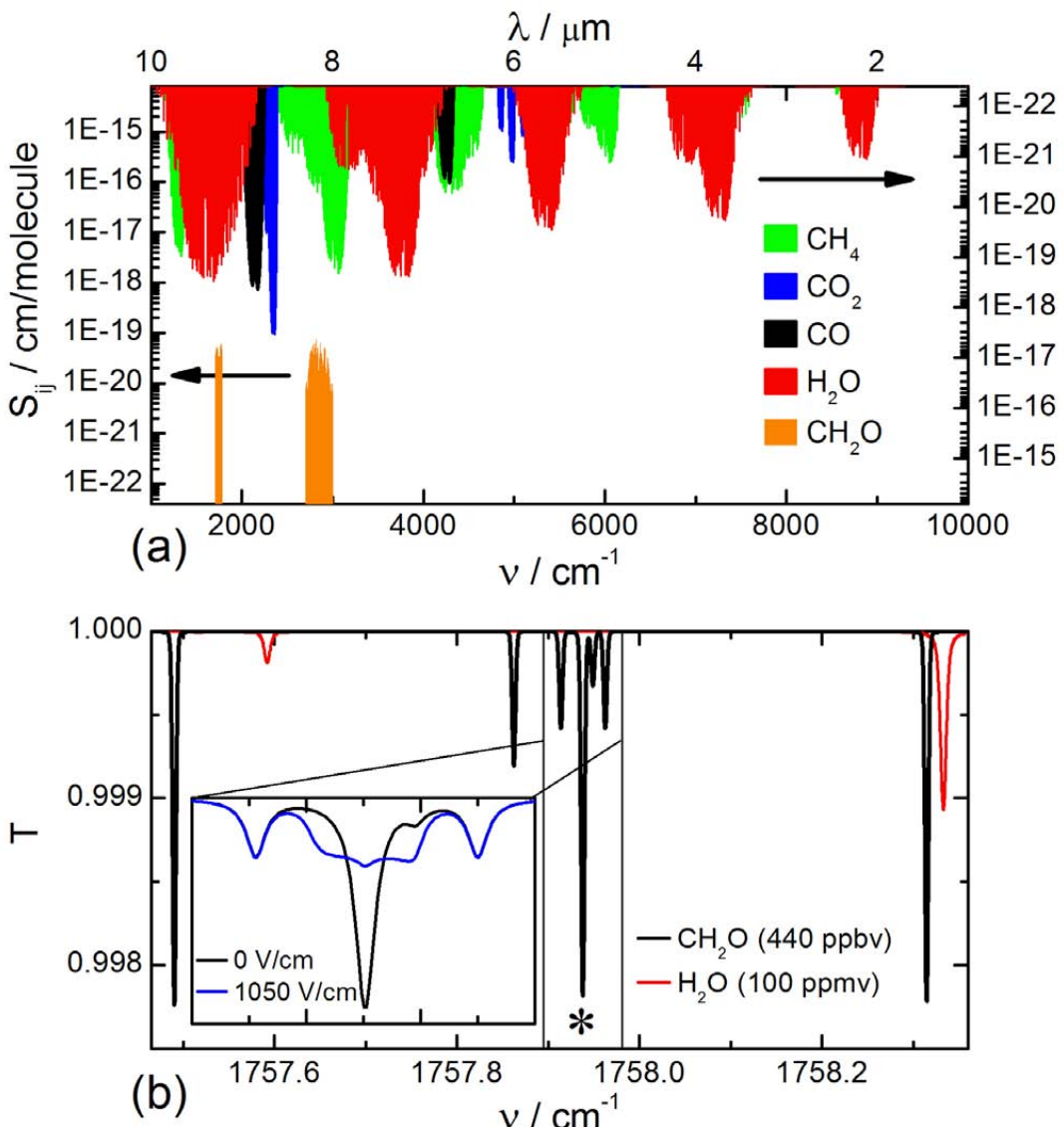


Figure 3.2: (a) Plot of the integrated line-strength versus wavenumber of CH_2O along with other important and potentially interfering atmospheric molecules. All data is found in the HITRAN database [Rothman *et al.*, 2005] except the CH_2O absorption lines near 1750 cm^{-1} . Absorption line parameters for these lines were provided by Werle [2005]. Only those absorption lines are shown that exhibit a line-strength of larger or equal to $1 \times 10^{-24} \text{ cm}^2/\text{cm}\cdot\text{molecule}$. Weaker lines are generally not suited to detect low concentration levels of these molecules. The wavenumber range of 1000 cm^{-1} to 10000 cm^{-1} corresponds to a wavelength range of $10 \mu\text{m}$ to $1 \mu\text{m}$. (b) Calculated direct transmission spectrum of 440 ppbv CH_2O (black trace) at around 1757.94 cm^{-1} for a pressure of 25 hPa and an absorption path length of 10 m. The nearest absorber is H_2O (red trace) around 0.35 cm^{-1} away. The CH_2O absorption line investigated in this study is marked by a star. (inset) Calculated direct transmission spectrum (based on Eq. 3.3) of CH_2O around 1757.94 cm^{-1} for an external electric field of $0 \text{ V}/\text{cm}^{-1}$ (black trace) and $1050 \text{ V}/\text{cm}^{-1}$ (blue trace). The pressure is 25 hPa. The absorption line in the center is observed in the present study. The neighboring lines do not show a Stark effect.

3.2 Multipass absorption cell for Stark modulation

In the present Section, a multipass absorption cell for Stark modulation spectroscopy is described. This cell is based on a modified version of the Herriott type [Herriott *et al.*, 1964]. Section 3.2.1 describes the theoretical description of the multipass cell optics as well as the finding of specific mirror radius of curvature and mirror separation in order to reach the reentrant condition. A theoretical stability analysis of the cell based on an ABCD matrix description is discussed in Section 3.2.2. The results are compared to those obtained for a hypothetical Herriott cell of same path length. Finally, the actual cell design is presented in Section 3.2.3.

The detection of trace amounts of atmospheric constituents at mixing ratio levels in the parts per billion by volume (ppbv) to the parts per trillion by volume (pptv) range, as it is required for formaldehyde (CH_2O), generally requires long absorption path lengths to increase the absorption signal. While Werle and Lechner [1999] have demonstrated that Stark modulation spectroscopy can be a means to improve the spectrometer performance, these measurements were performed employing a single pass absorption cell with only 40 cm path length.

To make use of higher absorption paths, a novel multipass absorption cell design has been employed. This design, which is based on the absorption cell principle introduced by Herriott *et al.* [1964] allows for absorption path lengths of up to 40 m, 100 \times more than what was used by Werle and Lechner [1999]. Electrodes allow for the application of an external electric field of up to 1 050 Vcm^{-1} to the target gas.

3.2.1 Reentrant condition

The laser beam propagation within the multipass cell is calculated using the equations by Herriott *et al.* [1964]. The front and rear mirrors are separated by the distance d , the radius of curvature of the cell mirrors is r , and their focal length is $f = r/2$ [Fig. 3.5 (a)]. The laser beam is coupled into the cell through the coupling hole located in the front mirror at x_0 and y_0 . After entering the cell in an appropriate off-axis direction at angles α and β , the laser beam is reflected back and forth between both mirrors. After n passes the beam hits a mirror at the position x_n , y_n . By a proper choice of the mirror distance d the beam exits the cell after a selected number of passes. Spots with even numbers n lie on the front mirror, spots with odd numbers lie on the rear mirror. Projecting the spots on a single plane leads to the radial-angular displacement θ of two consecutive spots n , $n + 1$:

$$\cos(\theta) = 1 - \frac{d}{2f} . \quad (3.4)$$

Assuming the paraxial approximation according to Herriott *et al.* [1964], one obtains

$$x_n = x_0 \cos(n\theta) + \left(\frac{d}{4f - d} \right)^{1/2} [x_0 + 2f \tan(\alpha)] \sin(n\theta) . \quad (3.5)$$

A similar equation holds for the y direction. If the laser beam leaves the cell after N passes through the cell, M concentric circles on each mirror appear. This is termed the reentrant condition:

$$N\theta = 2\pi M, \quad M = 1, 2, 3, \dots \quad (3.6)$$

As pointed out by *Durry et al.* [2002] the reentrant condition depends only on the mirror separation d and the mirror focal length f , no matter what the entrance angles α , β and the coordinates x_0 , y_0 are. The practical constraints are the size of the reflective mirror surface and the shape of the spot pattern, i.e., elliptical or circular. Combining Eqs. 3.4 and 3.6 leads to the required mirror separation for a given mirror focal length

$$d = 2f \left[1 - \cos \left(2\pi \frac{M}{N} \right) \right]. \quad (3.7)$$

There are many combinations of integers N and M that fulfill the reentrant condition in Eq. 3.6. As the laser beam has to be guided through a rather narrow gap between two cylindrical electrodes the off-axis angle of the beam and hence the angular spot displacement θ (Eq. 3.4) have to be small. This leads to a long focal length f , and consequently to a small integer M . The formalism described above has been used to specify the design parameters of the cell.

In the present work, $N = 86$ and $M = 4$ at $f = 5500$ mm was chosen to achieve an approximate optical path length of 40 m at $d = 466.4$ mm. A circular spot pattern is realized by injecting the beam at $\alpha = 1.13^\circ$ and $\beta = 0.19^\circ$, i.e., by pointing the beam onto a circle with 32.5 mm diameter on the rear mirror. The coupling hole is located at $x_0 = 0$ and $y_0 = 32.5$ mm. According to

$$L = \frac{1}{M} \sqrt{(x_n - x_{n+2})^2 + (y_n - y_{n+2})^2}, \quad (3.8)$$

the distance L between two consecutive spots on the mirror is ~ 4.6 mm for $M = 4$. Such a small spot distance requires small spot sizes, which in turn leads to the required focusing optics.

Coupling into the cell is achieved by aiming the laser beam through the coupling hole of the front mirror with a focus at half of the distance between the two mirrors. The numerical aperture (NA) of the beam is chosen such that the wavefront radius of curvature at the mirror surface matches the mirror radius of curvature. Assuming a fundamental-mode Gaussian beam at 1 575 cm⁻¹, as was used by *Werle and Lechner* [1999], one finds a spot size of $w_0 = 1.7$ mm at a numerical aperture of $NA = 1.07 \times 10^{-3}$. A comparison of the calculated beam path and the experimental results is shown in Figs. 3.3 (b) and (d).

3.2.2 Misalignment analysis

Misalignment of multipass cells, especially during field measurements due to vibrations, accelerations (shocks) and ambient temperature and pressure variations, is known to degrade the performance of TDL absorption spectrometers considerably [*Dyroff et al.*, 2004; *Roller et al.*, 2006]. Subtle alignment changes can dramatically affect the retrieved trace gas concentrations, mainly due to changing spectral background structures, but also due to changes in optical power transmitted through the system. In the following, the effect of alignment instabilities is estimated to quantify the tolerances during cell alignment. Misalignment errors that are caused by a) changes in mirror separation Δd , b) transverse mirror displacements Δx and Δy , and c) tilt of the mirrors δ_x and δ_y [Fig. 3.5 (a)] are considered. To quantify these misalignment errors an ABCD matrix description of the cell optics is used.

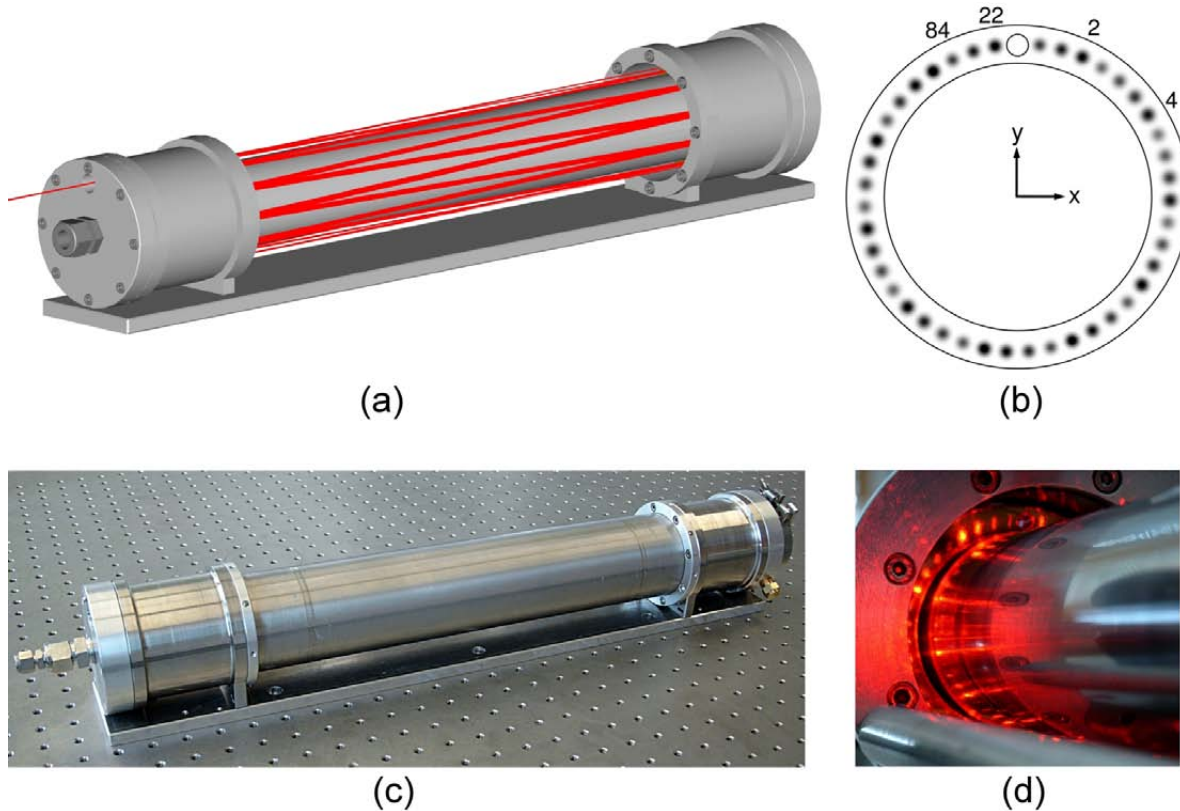


Figure 3.3: (a) Ray tracing simulation of the multipass cell for the first 22 passes. The outer electrode has been removed for clarification. (b) Spot pattern on the front mirror as observed from inside the cell as a result of a complete ray tracing simulation. (c) Photograph of the cell. (d) Photograph of the front mirror with the beam of a red trace laser aligned through the cell. The outer electrode has been removed.

In an ideal centered collinear optical system, one can use a 2×2 ray-transfer matrix to represent the transformation of a ray between two reference planes (RP) according to the matrix equation

$$\begin{bmatrix} x_1 \\ \tan(\alpha_1) \end{bmatrix} = \begin{bmatrix} A & B \\ C & D \end{bmatrix} \begin{bmatrix} x_0 \\ \tan(\alpha_0) \end{bmatrix}, \quad (3.9)$$

where x_0 and $\tan(\alpha_0)$ are the components of the incident ray vector, denoting the position of the ray and its slope with respect to the optical axis, respectively. This is illustrated in Fig. 3.4 for an arbitrary transformation matrix with elements A, B, C, and D, where both reference planes are located at the same position on the optical axis (RP).

Applying the transformation matrix to the incident ray vector yields the resulting position x_1 and slope $\tan(\alpha_1)$ after the optical element described by the transformation matrix. In an actual system the position of the optical axis in the second reference plane may be displaced slightly from its assumed position by a small distance Δx . Also, the direction in which the optical axis is pointing may deviate slightly by a small amount δ_x .

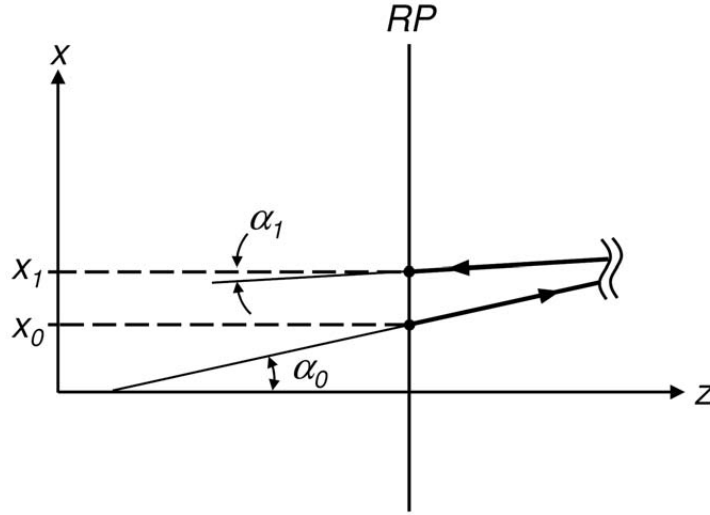


Figure 3.4: Propagation of a ray vector between two coincident reference planes.

One can represent this misalignment by adding misalignment terms to Eq. 3.9, and *Gerrard and Burch* [1994] suggest to add a third *dummy* equation,

$$\begin{aligned} x_1 &= Ax_0 + B \tan(\alpha_0) + \Delta x \\ \tan(\alpha_1) &= Cx_0 + D \tan(\alpha_0) + \delta_x . \\ 1 &= 0 + 0 + 1 \end{aligned} \quad (3.10)$$

These equations can again be written in matrix form,

$$\begin{bmatrix} x_1 \\ \tan(\alpha_1) \\ 1 \end{bmatrix} = \begin{bmatrix} A & B & \Delta x \\ C & D & \delta_x \\ 0 & 0 & 1 \end{bmatrix} \begin{bmatrix} x_0 \\ \tan(\alpha_0) \\ 1 \end{bmatrix} . \quad (3.11)$$

In the description of the multipass cell optics the 3×3 matrix in Eq. 3.11 denotes the reflection matrix \mathbf{R}_x

$$\mathbf{R}_x = \begin{bmatrix} 1 & 0 & \Delta x \\ -2/r & 1 & \delta_x \\ 0 & 0 & 1 \end{bmatrix} , \quad (3.12)$$

where r is the radius of curvature of the mirror, Δx is a small transverse displacement of the mirror axis, and δ_x is a small tilt of the mirror axis with respect to the optical axis. \mathbf{R}_x describes the reflection in the zx -plane and a similar quantity \mathbf{R}_y is valid in the yz -plane.

The actual optical system of the multipass cell contains two different matrices, the reflection matrix \mathbf{R}_x of each of the two mirrors and a matrix \mathbf{D}_x of a plane-parallel plate of air, which separates the reference planes of both mirrors,

$$\mathbf{D}_x = \begin{bmatrix} 1 & d + \Delta d & 0 \\ 0 & 1 & 0 \\ 0 & 0 & 1 \end{bmatrix} . \quad (3.13)$$

The term Δd accounts for changes in the separation of the two multipass cell mirrors. The matrix for a single pass through the cell, e.g. from the coupling hole to the rear mirror, is

calculated by $\mathbf{M}_x = \mathbf{R}_x \mathbf{D}_x$. The ray starts at the first reference plane of the front mirror. It then passes through the plane-parallel plate of air (\mathbf{D}_x) and is reflected by the rear mirror (\mathbf{R}_x). The second reference plane refers to the rear mirror. To calculate the position of the beam on the mirrors after n passes, \mathbf{M}_x is raised to the power of n and multiplied by the incident ray vector at the first reference plane $\mathbf{Z}_0 = \{x_0; \tan(\alpha_0); 1\}^T$:

$$\mathbf{Z}_n|_x = \mathbf{M}_x^n \mathbf{Z}_0 . \quad (3.14)$$

An equivalent formulation is valid for the y -direction. Together, $\mathbf{Z}_n|_x$ and $\mathbf{Z}_n|_y$ form the ray vector \mathbf{Z}_n , that contains the coordinates x_n, y_n and the slopes $\tan(\alpha_n), \tan(\beta_n)$ of the ray at the n^{th} reference plane. Here $\tan(\beta_n)$ denotes the slope of the ray in the yz -plane after n passes. Again, spots with even numbers n lie on the front mirror, spots with odd numbers n lie on the rear mirror.

Based on the formalism described above the misalignment of \mathbf{Z}_n has been calculated and compared to that of a confocal Herriott cell with approximately the same mirror separation and a circular spot pattern of equivalent diameter while introducing the three sources of misalignment listed above. It must be noted that the matrix description discussed above only describes the propagation of the center ray and does not fully describe the propagation of a practical laser beam. Furthermore, this description assumes a paraxial approximation and neglects higher order effects. The results are based on coupling into the cell in a way to obtain a circular spot pattern which is a prerequisite for the present design. Changes in the angles α and β would lead to slightly different results (compare with Eq. 3.5).

Changes of mirror distance Δd are usually related to thermal drifts of the cell or pressure changes inside or outside of the cell (e.g. for an airborne instrument during ascent/descent of the aircraft). The coefficient of thermal expansion of stainless steel is $16 \times 10^{-6} \text{ K}^{-1}$ at 20°C [Kuchling, 1984], and the base length of the present cell is $d = 466.4 \text{ mm}$. An assumed temperature increase of the cell by 2 K leads to an increase in base length of $\Delta d = 15 \mu\text{m}$. The calculations demonstrate that the ray at the coupling hole after $N = 86$ passes is displaced by only $13.5 \mu\text{m}$ along the x -direction. This corresponds to a ratio of $\Delta x / \Delta d = 0.9$. The beam pointing angle α_n changes by $\Delta \alpha_n / \Delta d = 4.5 \times 10^{-3} \text{ deg/mm}$. The beam displacement in y -direction (Δy) is negligible ($\Delta y / \Delta d < 0.02$), whereas the beam pointing angle β_n changes at a ratio of $\Delta \beta_n / \Delta d = 3.1 \times 10^{-2} \text{ deg/mm}$. With a misalignment of $\Delta d = 15 \mu\text{m}$ we find for the confocal cell that the beam is displaced in x -direction by $81 \mu\text{m}$ ($\Delta x / \Delta d = 5.4$) with $\Delta \alpha_n / \Delta d = 0.61 \text{ deg/mm}$. In y -direction one calculates a displacement of $7.2 \mu\text{m}$ ($\Delta y / \Delta d = 0.48$), whereas the beam pointing angle changes by $\Delta \beta_n = 0.66 \text{ deg/mm}$. The calculated ratios are linear approximations that are valid for small changes Δd . For a better comparison of the cell characteristics the data are summarized in Tab. 3.2.

Maximum transverse mirror displacements and mirror tilt put constraints on construction tolerances and accuracy of alignment. The calculations show that both, position and pointing angles, do not change with transverse mirror displacement and/or mirror tilt. This holds true for the confocal arrangement as well. The spot pattern becomes distorted, i.e. elliptical. The level of ellipticity is very similar for the confocal and non-confocal configuration when displacing one or both mirrors transversally. However, introducing mirror tilt reveals much less ellipticity of the pattern for the confocal arrangement. Therefore, the initial alignment of the Stark multipass cell is more demanding than that of a classical confocal Herriott cell.

Table 3.2: Comparison of beam displacement $\Delta x, \Delta y$ and beam pointing angle $\Delta\alpha_n, \Delta\beta_n$ due to changes in mirror separation d for the present Stark modulation cell and a confocal Herriott cell with a circular spot pattern of the same diameter. The ratios are linear approximations which are valid for small changes Δd .

	Stark modulation Cell	Herriott Cell
Volume	0.81	~ 21
Path length	40 m	40 m
$\Delta x/\Delta d$	0.9	5.4
$\Delta y/\Delta d$	~ 0	0.48
$\Delta\alpha_n/\Delta d$	4.5×10^{-3} deg/mm	0.61 deg/mm
$\Delta\beta_n/\Delta d$	3.1×10^{-2} deg/mm	0.66 deg/mm

3.2.3 Cell design

The Stark modulation cell contains two gold-coated spherical ring mirrors of 74 mm diameter and a focal length of $f = 500$ mm. A coupling hole of 4.5 mm diameter is located in the front mirror at a position $y_0 = 32.5$ mm from the cell axis. Each mirror is mounted by three spring-loaded screws in a stainless-steel housing. The front housing contains a CaF₂ window for beam entrance and exit. Both housings are connected by a stainless-steel cylinder. A second stainless-steel cylinder is concentrically mounted inside the cell. The nested cylindrical electrodes confine the sample gas volume and also form the electrodes for electric field application [Fig. 3.5 (c)]. Gas flow connectors are located at both housings. The spacing of the electrodes should be as small as possible (a few millimeters to 1 cm) to allow for a reasonable field strength of the order of ~ 1 kVcm⁻¹.

The inner electrode is fitted with ceramic end pieces [Fig. 3.5 (b)] to ensure electrical isolation of the mirror housings. The end pieces are designed such that the gas flow is evenly distributed into the sample volume, while the cross section area within the end pieces matches that of the sample volume, thus enabling a laminar flow. This is important for two reasons. First, turbulent motion of the sample gas leads to small local variations in temperature and pressure, which in turn produce local refractive index variations. These refractive index fluctuations may have a slightly higher or lower refractive index, and can be thought of as an eddy, which may behave the same way as a lens. While the laser beam propagates through a large number of refractive index inhomogeneities, the cumulative effect can be very significant and produce optical phase effects, which in turn lead to angle-of-arrival fluctuations or beam wander, intensity fluctuations, and beam broadening. Second, a homogeneous flow in the cell leads to a fast cell response time, because of a minimization of recirculation zones that would increase the response time of the cell. Fast cell response is important for high sampling rates, e.g. for eddy correlation flux measurements.

3.2.4 Conclusion

The design of a novel multipass cell has been described, which allows the application of a sample modulation based on the Stark effect. The multipass cell consists of two spherical ring mirrors with radius of curvature and displacement chosen such that an optical path length of

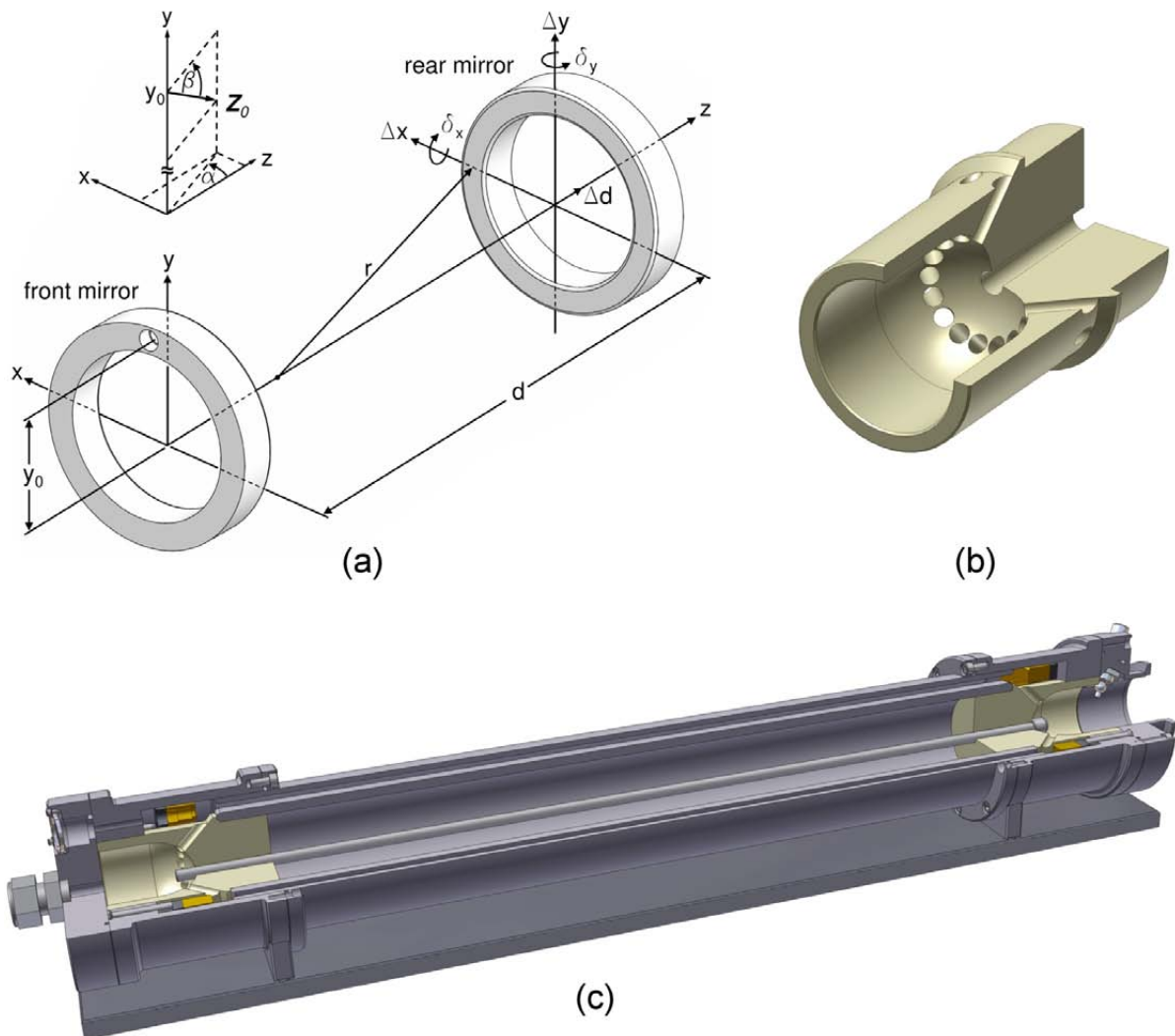


Figure 3.5: (a) Multipass cell mirrors with radius r , spaced by distance d . The coupling hole is located in the front mirror at x_0 and y_0 . The cell axis coincides with the z -axis. (b) Section view of the ceramic flow-inlet part of the cell. The ceramic also provides proper electrical isolation against the inner electrode. (c) Rendered cross-section of the cell showing the two nested cylinder electrodes.

40 m as a result of 86 passes through the cell is achieved. Two nested metal cylinders form the electrodes for the application of an electric field of up to 1 kVcm^{-1} and confine the sample gas in an overall volume of only 0.85 l, which is advantageous for fast measurements. The sensitivity of the cell towards slight misalignment has been analyzed by calculations using a ray-transfer matrix description. It could be shown that the cell is less sensitive to misalignment of the mirrors than a classical Herriott cell with similar path length and number of passes.

3.3 Drift compensation by Stark modulation

The present Section describes the spectrometer setup as well as data acquisition approaches for Stark modulation spectroscopy. First, the optical setup, which has been used for these measurements, is described in Section 3.3.1. This is followed by a description of the data acquisition setup and the procedure for concentration retrieval. The multipass cell for Stark modulation spectroscopy has been analyzed in terms of the maximum allowable electric field. This is an important measure as the Stark effect — and thus the measured signal — are proportional to this electric field. The results of this analysis are given in Section 3.3.2.

Two different data acquisition approaches are described. The first approach makes use of alternate measurements of signal and background and is described in Section 3.3.3. In this case, the Stark effect is applied at a frequency of 25 Hz to capture the spectral background superimposed on the CH₂O spectra on a spectrum-to-spectrum basis. At the second approach, a much faster modulation of the Stark effect in conjunction with lock-in detection is used for interleaved measurements of signal and background. This approach, which is described in Section 3.3.4, allows to eliminate the spectral background for each data point inside the individual spectral scan.

3.3.1 Spectrometer setup and data acquisition

The Stark-spectroscopy measurements were carried out in a laboratory environment with the setup depicted in Fig. 3.6. A double-heterostructure (DH) lead salt tunable diode laser based on PbEuTeSe semiconductor material³ in Fabry-Pérot resonator configuration was mounted inside a liquid nitrogen (LN2) dewar. The laser was fabricated by molecular beam epitaxy, and the laser injection current was restricted to a narrow stripe region by a mesa structure [Feit *et al.*, 1989; Preier, 1990]. At a device temperature of 83 K and an injection current of $I = 390$ mA the laser emitted at the desired frequency of $v_0 = 1\,757.9\text{ cm}^{-1}$.

The laser beam was collected by a 19 mm off-axis parabolic mirror (OAP). It was then focused into the multipass cell described in Section 3.2 using a $f = 750$ mm CaF₂ lens (see Fig. 3.6). The maximum path length of this cell is achieved for 82 passes through the cell at a mirror separation of 466 mm. Smaller path lengths can be achieved by changing of the mirror separation and beam pointing angles. The experiments described below have been performed with the cell aligned to 20 passes at a base length of 484 mm, resulting in an absorption path of 9.6 m.

The electrodes of the cell are used to apply a static electric field of about 1 kVcm⁻¹ to the target gas. A Teflon (PTFE) coating was applied to the electrodes to avoid adsorption of the polar formaldehyde.

Upon exiting the cell, the laser was focused onto the sample detector⁴ (SD). A fraction of the laser power was picked off with a beam-splitter (wedged CaF₂ window) and — after having passed a high concentration reference cell (RD) — focused onto the reference detector⁵ (RD). The derivative signal obtained from the RD was used for locking the diode laser frequency to

³Laser Photonics, Bedford, MA, USA

⁴LN2-cooled InSb, Cincinnati Electronics, Mason, OH, USA

⁵LN2-cooled InSb, Cincinnati Electronics, Mason, OH, USA

the observed absorption line, to compensate for slow drifts in temperature and current of the lead-salt diode-laser. A HeNe-laser was used to assist in aligning the infrared laser through the Stark-MPC.

Current and temperature of the lead-salt diode laser were controlled by analog controllers⁶. The stainless steel electrodes of the Stark-MPC were connected to a high voltage power supply⁷ which allows the generation of voltages up to 1 kV, or electric fields of up to 1290 Vcm^{-1} , respectively, based on the given 7.75 mm spacing of the electrodes of the Stark-MPC. The waveforms for both laser tuning and modulation and electric field modulation were computer generated and fed into the respective external-modulation inputs of the laser driver and high-voltage power supply.

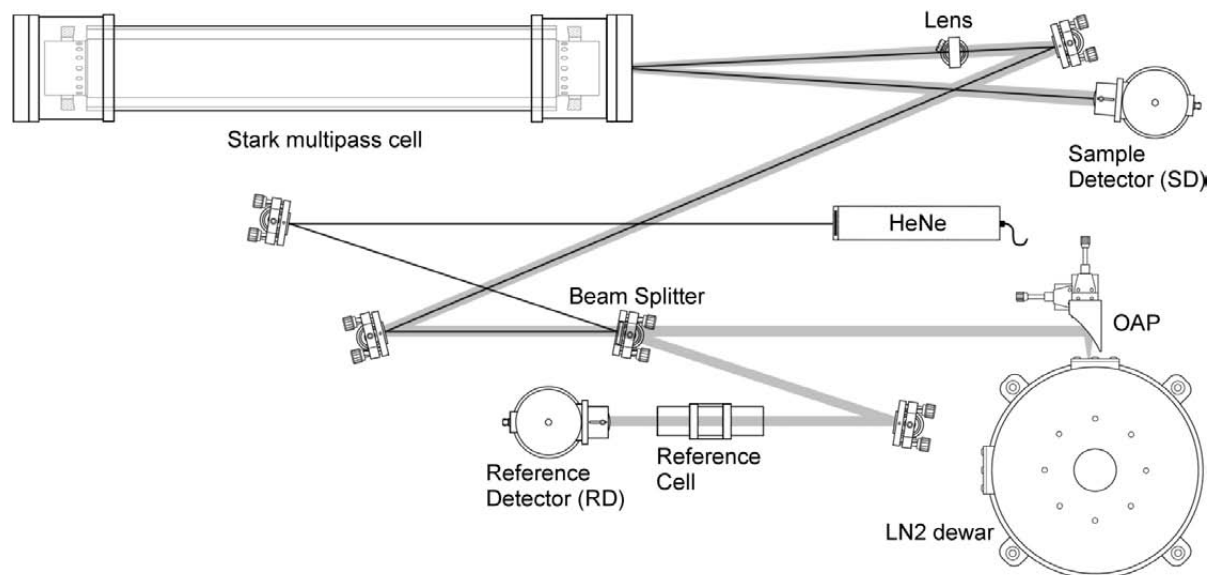


Figure 3.6: Stark spectroscopy setup. The diode laser beam was collected by a $f = 19 \text{ mm}$ off axis paraboloid (OAP) and focused into the Stark multipass cell by a $f = 750 \text{ mm}$ lens. The mirrors and high-voltage electrodes of the Stark-MPC are depicted in gray. A HeNe laser was used to align the system.

After pre-amplification the SD spectra were acquired by a 16 bit analog-digital converter card⁸ and processed by a LabVIEW program. Upon buffering in memory the spectra were demodulated at twice the modulation frequency (2f) and low-pass filtered by adjustable computer software lock-in amplifiers (see Fig. 3.7). The RD spectra were demodulated by an analog lock-in amplifier⁹ prior to being read by the PC. The second-derivative reference spectra were used by the LabVIEW program for line-locking based on a center of gravity algorithm [Weibring *et al.*, 2006].

⁶Laser Photonics, Inc., Andover, MA, USA

⁷SVR 1 000-1, Piezomechanik, München, Germany

⁸National Instruments, Austin, TX, USA

⁹Model LIA-MVD-200, Femto Messtechnik GmbH, Berlin, Germany

The Stark effect was applied with two different modulation schemes. In both schemes, the laser wavelength was slowly scanned (either 25 Hz or 5 Hz) using a triangular waveform, and at the same time it was rapidly modulated at 50 kHz using a square waveform. The spectra in the up and down ramps of the triangular scan waveform were treated independently because of hysteresis effects observed in the spectra. The up and down ramps were treated as independent samples using their own respective calibration spectra in the fitting procedure to generate a mixing ratio every 1 s for each ramp. These results were then combined to produce one averaged mixing ratio value every second.

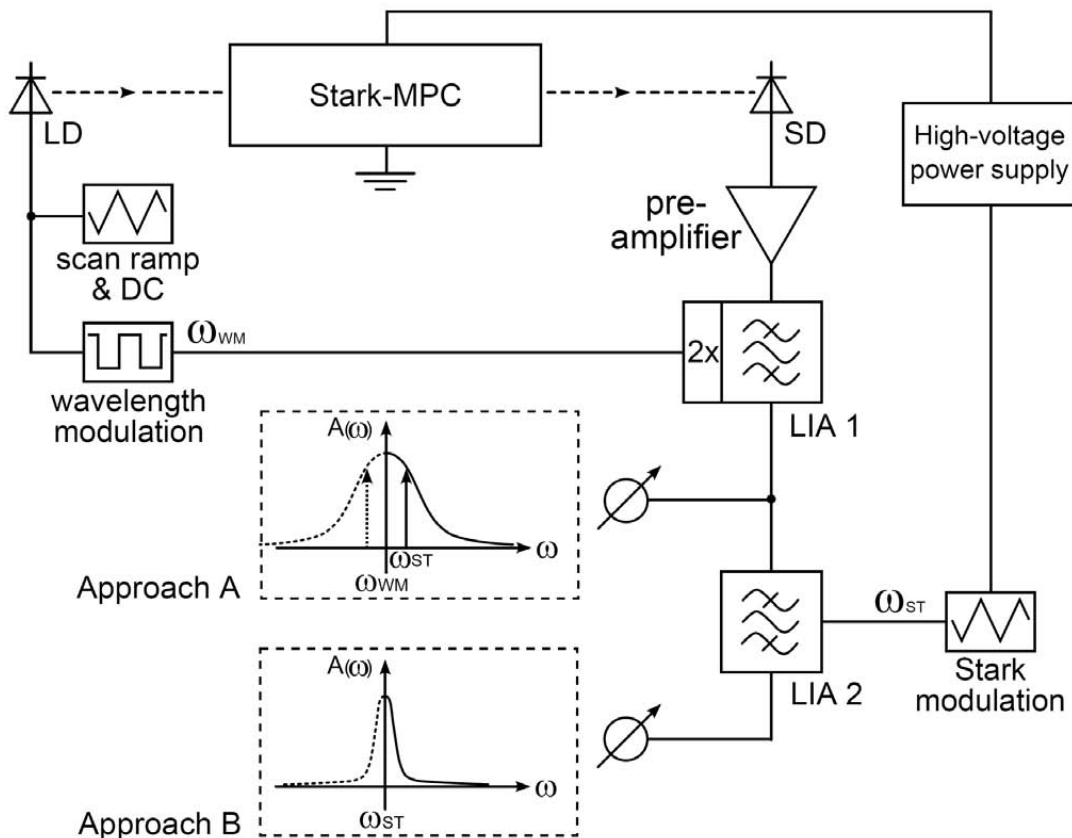


Figure 3.7: Data processing diagram of the Stark spectroscopy experiments. Approach A employs only the first lock-in amplifier (LIA 1) with a small bandwidth to record second derivative spectra. Approach B employs both lock-in amplifiers consecutively. The first LIA was used to record second derivative spectra, and its bandwidth was opened to pass the electric field modulation frequency ω_{ST} (see inset). The second LIA was referenced to the Stark modulation frequency, and low-pass filter was used to increase the signal-to-noise ratio of the spectra.

To calibrate the system, a 440 ppbv CH₂O in air gas-phase standard from a compressed gas cylinder was directed through the Stark-MPC. This standard was prepared by Dr. Eric Apel at NCAR and the CH₂O mixing ratio was determined using direct absorption employing a long path length absorption cell using FTIR spectroscopy. A 30 s calibration spectrum for both up- and down-scan was recorded and stored. In a second sequence, the cell was either flushed with the same standard or with zero-air, where the spectra were averaged over 1 s and

buffered. By least-squares fitting of the measured spectra (1 s average) of the up and the down scan to the respective calibration spectrum the sample gas mixing ratio for the up and down scan was found. The two results were then averaged to achieve a mixing ratio value for the sample spectra every 1-second. In most cases the same gas-standard used for calibration was also used for the sample gas.

For all experiments discussed in the present work, the system was set up on an optical breadboard without enclosure and thermal stabilization. No attempt was made to reduce fringes by proper system alignment since this demonstrates how effectively the Stark modulation can suppress background drifts.

3.3.2 Electric breakdown

For Stark sample modulation, the two concentrically aligned cylinders of the Stark multipass cell (Section 3.5) form the electrodes for the application of the electric field. The gap between the electrodes is 7.75 mm. The surfaces facing each other are polished and coated with a 15 μm thick layer of Teflon (PTFE) to reduce wall effects with the polar formaldehyde. The edges are rounded to avoid sparking. The inner electrode is connected to the high electric potential, while the outer electrode as well as the rest of the cell housing is connected to ground potential. The threshold electric field E_{th} , above which sparking occurs depends on the gas between the electrodes, its pressure p , and the electrode gap g . It is defined by the Paschen law [Raizer, 1991],

$$E_{\text{th}} = \frac{ag}{\ln(pg) + b}. \quad (3.15)$$

The factors a and b are tabulated values for the specific gas between the electrodes ($a = 273.8 \text{ V}/(\text{cm hPa})$ and $b = 0.891/(\text{cm hPa})$ for air [Raizer, 1991]). Fig. 3.8 shows the theoretical Paschen curve based on Eq. 3.15 along with measured values (red triangles) of the coated electrodes. The measurements reveal a lower threshold electric field E_{th} than theory predicts. This can be due to inhomogeneities of the electric field, causing sparking at electric fields lower than theory predicts. A reduction in E_{th} of around 30 % after Teflon coating of the electrodes could be assigned to the slight surface roughness of this material. The number of measurements was limited by the maximum voltage of 1 000 V ($E=1\,290 \text{ Vcm}^{-1}$) achievable by our high voltage supply.

The CH_2O doublet at $1\,757.94 \text{ cm}^{-1}$ investigated in the present work showed a maximum signal at a cell pressure of 25 hPa. At this pressure an electric field of $E = 1050 \text{ Vcm}^{-1}$ was applicable without the risk of electrical breakdown.

3.3.3 Alternate measurements of signal and background

In the conventional approach to wavelength-modulation spectroscopy the background spectrum — when applicable — is captured periodically by flushing the cell with zero-air, i.e., air where the target gas is removed. The frequency of background measurements is governed by the stability time of the system, i.e. the time-period during which the background remains stable, typically some 10–100 s. In contrast, the Stark-effect offers a background measurement on much faster time scales, ranging between a few Hz for the alternate measurements to the kHz domain for the interleaved measurements of signal and background.

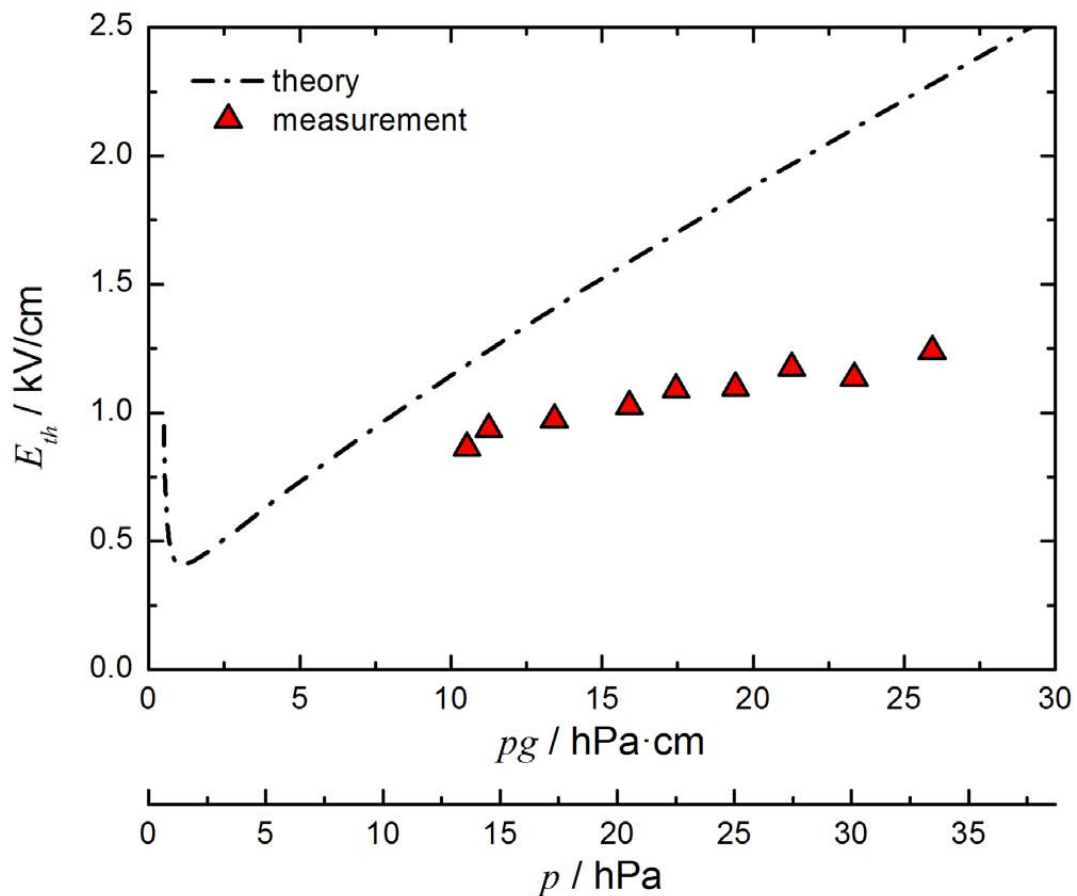


Figure 3.8: Threshold electric field E_{th} versus pressure-gap-product pg in air [Raizer, 1991]. The electrode gap for the measurement was 7.75 mm and the corresponding pressure is given on the lower x-axis. The triangles represent measured data of the actual cell. The electrodes were coated with a 15 μm thick layer of Teflon (PTFE).

At this first approach, a measurement sequence consists of two consecutive triangular scans of the laser wavelength over the absorption line of interest, i.e., a time of 80 ms at a scan frequency of 25 Hz (Fig. 3.9). During the first triangle of the sequence the static electric field was turned off to record one second-derivative sample spectrum (*red* trace in Fig. 3.9) for the up and the down scan, respectively. During the second triangle the static electric field was turned on to 1 050 Vcm⁻¹ to record one second-derivative Stark spectrum (*blue* trace in Fig. 3.9) for the up and the down scan, respectively. The Stark spectra are of reduced amplitude due to the broadening of the CH₂O absorption doublet at 1 757.9 cm⁻¹, that was used for the present study. By subtracting the Stark spectrum from the sample spectrum one calculates the processed spectrum (*black* trace in Fig. 3.10). Since the background structures (etalon structures) present in the sample and Stark spectrum are not affected by the Stark effect, the processed spectrum only contains the part of the CH₂O absorption signal affected by the Stark effect. One can think of the Stark spectrum as a background spectrum with a certain residual signal of the CH₂O absorption doublet. The different second-derivative spectra are shown in Fig. 3.10.

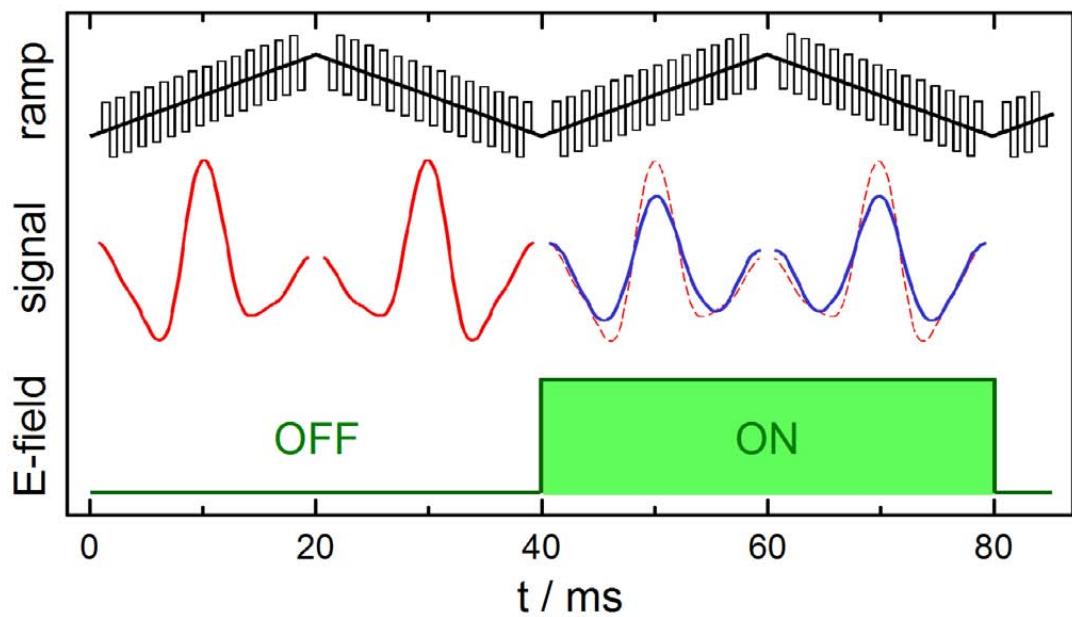


Figure 3.9: Schematic representation of the subtraction data acquisition approach. The laser wavelength is scanned over the absorption line of interest by a 25 Hz triangular ramp of the laser injection current (top trace). In addition, the laser injection current is rapidly modulated by a square wave at a frequency of 50 kHz. Demodulation of the resulting absorption signal at twice the modulation frequency results in second derivative spectra (red trace). An electric field of 1050 Vcm^{-1} (green trace) was turned on on every other scan resulting in second derivative spectra that were of reduced line center absorption (blue trace). These spectra were treated as background and subtracted from those spectra recorded when the electric field was off. The resulting spectra (black trace in Fig. 3.10) only contain the absorption signal affected by the electric field. Any spectral background structure is thus removed from the spectra.

To quantify the stability and detection limit of the system, the sample spectra and the processed spectra were measured using the 440 ppbv CH_2O standard mixture at a cell flow rate of 0.5 standard liters per minute (standard conditions of 1013 hPa and a temperature of 273.2 K) and at a cell pressure of 25 hPa. The data acquisition and calibration described above was performed for both the sample and the processed spectra to enable a direct comparison of the pure wavelength modulation technique and combined wavelength/sample-modulation technique. The results are described in Section 3.4.1.

3.3.4 Interleaved measurement of signal and background

The second modulation approach represents an even faster way to capture and to remove background fluctuations. To this end the laser scan frequency was reduced from 25 Hz to 5 Hz while the frequency of the static electric field was increased to 1.5 kHz. The 50 kHz high frequency wavelength modulation was still applied in this approach (Fig. 3.11). The electric field in this case was offset by several hundred Vcm^{-1} to produce only positive field strengths. Upon acquisition the signal of the sample detector passed two consecutive lock-in amplifiers. The first lock-in amplifier was referenced to the 50 kHz wavelength-modulation frequency, and the

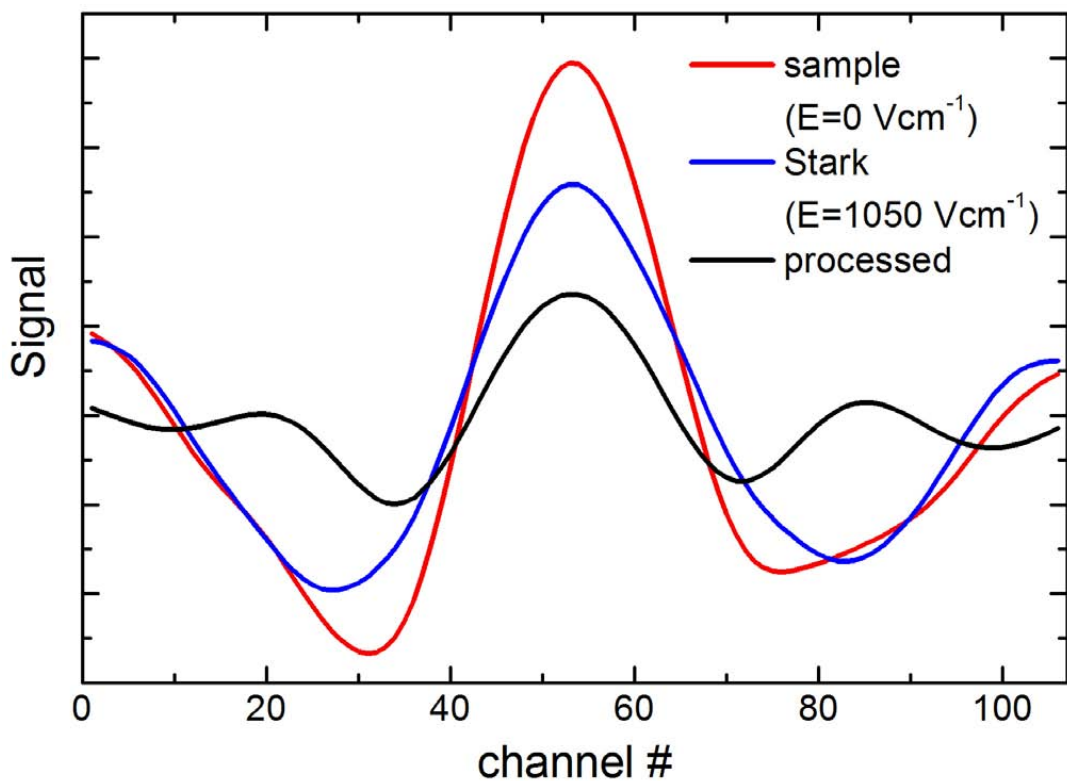


Figure 3.10: Second derivative spectra of 440 ppbv CH₂O of the 1757.9 cm⁻¹ doublet at 25 hPa without electric field (sample spectrum, *red* trace), at an electric field of 1050 Vcm⁻¹ (Stark spectrum, *blue* trace), and the spectrum gained by subtracting the Stark spectrum from the sample spectrum (processed spectrum = difference spectrum, *black* trace).

signal was demodulated at 100 kHz to obtain second derivative (2f) spectra. The bandwidth of the low-pass filter of this lock-in amplifier was set to 10 kHz, such that it passed the 1.5 kHz of the electric field modulation without decreasing the signal of this carrier frequency. The output signal of the first lock-in amplifier was then fed into a second lock-in amplifier referenced to the 1.5 kHz frequency of the electric field modulation to obtain the background-free spectra of the CH₂O line affected by the Stark effect (see Fig. 3.7). The low-pass filter of this second lock-in amplifier was set to 100 Hz to increase the signal-to-noise ratio on the spectra.

Again, 440 ppbv CH₂O was flown through the Stark-MPC at a rate of 0.5 standard liters per minute. Calibration and fitting was performed for the double-modulation second-derivative spectra only. The results of these measurements are given in Section 3.4.2.

3.3.5 Conclusion

A laboratory spectrometer for Stark modulation spectroscopy has been set up. The spectrometer contains a special multipass absorption cell with electrodes to apply an electric field of around 1000 Vcm⁻¹ to the target gas. The maximum electric field — which has been measured and compared to theoretical values — was thereby determined by sparking between the electrodes. It was determined that the maximum electric field was around 30 % lower

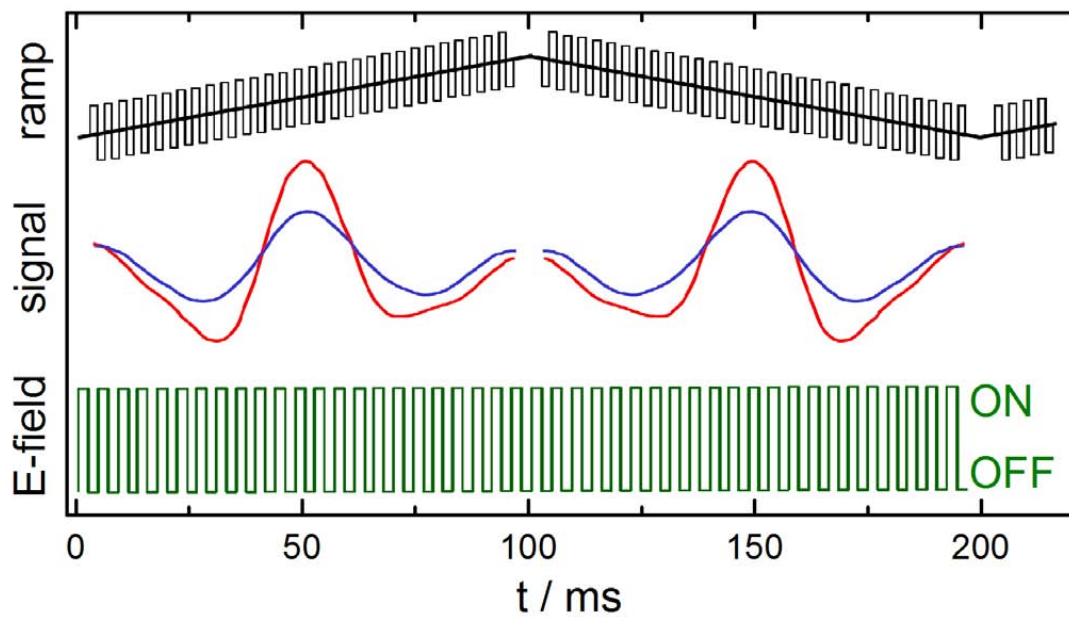


Figure 3.11: Schematic representation of the double modulation data acquisition approach. The laser wavelength is scanned over the absorption line of interest by a 5 Hz triangular ramp of the laser injection current (top trace). In addition, the laser injection current is rapidly modulated by a square wave at a frequency of 50 kHz. Demodulation of the resulting absorption signal at twice the modulation frequency results in second derivative spectra (red trace). Additionally, the electric field of 1050 Vcm^{-1} (green trace) was modulated at a frequency of 1.5 kHz. The detector signal was first demodulated at twice the laser modulation frequency ($2 \times 50 \text{ kHz}$) with a lock-in amplifier resulting in second derivative spectra. The output signal of this first lock-in amplifier was then fed into a second lock-in amplifier referenced to the 1.5 kHz electric field modulation frequency. After demodulation the resulting spectra (blue trace) only contain the absorption signal affected by the electric field. Any spectral background structure is thus removed from the spectra.

than theory predicts, which is related to the slight surface roughness of the Teflon coating of the electrodes. The spectrometer uses wavelength modulation spectroscopy with detection of second-derivative spectra. In addition, the electric field can be modulated, which leads to a selective modulation of the absorption signal due to the Stark effect.

Two data acquisition approaches have been realized. The first approach makes use of alternate measurements of signal and background. In this case, the electric field is modulated at a frequency of 25 Hz. Spectra recorded when the electric field is turned on are treated as background spectra. The background spectra are then subtracted from those spectra, where the electric field is turned off. This subtraction thus yields background-free CH_2O spectra. The second data acquisition approach uses interleaved measurements of signal and background by a high-frequency modulation of the electric field at 1.5 kHz. This second modulation signal is demodulated by an additional lock-in amplifier. As the Stark modulation does not affect the spectral background, only those signal components pass the second lock-in amplifier, which are due to the modulated Stark effect. Consequently, the resulting spectra do not contain spectral background.

3.4 System stability and detection limit

The results of both data acquisition approaches are analyzed in terms of system stability and detection limit in the present Section. The system stability is an important figure of merit as it determines the maximum allowable time in which statistically independent data may be averaged in order to reduce noise and thus improve the detection limit. The system stability is limited by systematic drift, and the Stark modulation approaches can be used to effectively compensate for this drift.

First, the results of the alternate measurements of signal and background are discussed in Section 3.4.1. These results are furthermore compared to results achieved using a classic second-harmonic detection scheme. Second, the results of the interleaved measurements of signal and background are discussed in Section 3.4.2. In Section 3.4.3 the detection limit of both Stark modulation approaches as well as the classic second-harmonic approach are compared. Concluding remarks follow in Section 3.4.4.

3.4.1 Alternate measurement of signal and background

Fig. 3.9 (a) shows the Allan plot and the underlying time-series data of the pure 2f-technique, i.e., without background subtraction, as well as for the alternate measurements of signal and background in a direct comparison. The time-series of the pure 2f-technique [Fig. 3.9 (b)] shows large periodic changes, originating from time-dependent background structures in the spectra. The degree of these changes is of the order of the absorption line itself, which can be seen by the variation of the calculated mixing ratio between around 0 ppbv and 500 ppbv. The large, low frequency changes in the time-series data are denoted as drift that limits the maximum integration time τ_{opt} to less than 10 s [Fig. 3.9 (a)]. The detection limit (1 s) of the pure 2f-technique is 32 ppbv, or in terms of optical density (αl) 3.06×10^{-5} at an absorption path length of 9.6 m. At the optimum integration time $\tau_{\text{opt}} = 10$ s the detection limit is around 22 ppbv, corresponding to an optical density of 2.1×10^{-5} .

By employing an electric field to rapidly capture the background structure within the spectra, the processed spectra only contain the fraction of the signal from the CH₂O absorption line affected by the electric field, thus removing the components responsible for drift [Fig. 3.9 (c)]. Also shown is a 50 s moving average (*blue* trace) of the time-series data to indicate how well the alternate background measurements capture low-frequency noise contributions which have degraded the system stability at the pure 2f-technique [Fig. 3.12 (b)].

The 3D-plots of Fig. 3.13 show the spectra recorded during the first 30 minutes of this experiment. The spectra have been combined to 30 s averages for reasons of a clearer presentation. In Fig. 3.13 (a) quite dramatic changes in the spectra over time are observed. These changes can clearly be attributed to time-variant background structures superimposed to the absorption signal of the CH₂O absorption line. Fig. 3.13 (b) represents the corresponding CH₂O mixing ratio deduced from the fit to the calibration spectrum, and a high correlation between background structure within the spectra and mixing ratio is observed (note for example the steep increase in deduced mixing ratio at ≈ 15 min). In contrast, the processed spectra [Fig. 3.13 (c)] do not show any contribution of background structures, indicating that these structures are very well captured and removed by this sample-modulation approach. The corresponding time series [Fig. 3.13 (d)] consequently does not show any pronounced drift behavior.

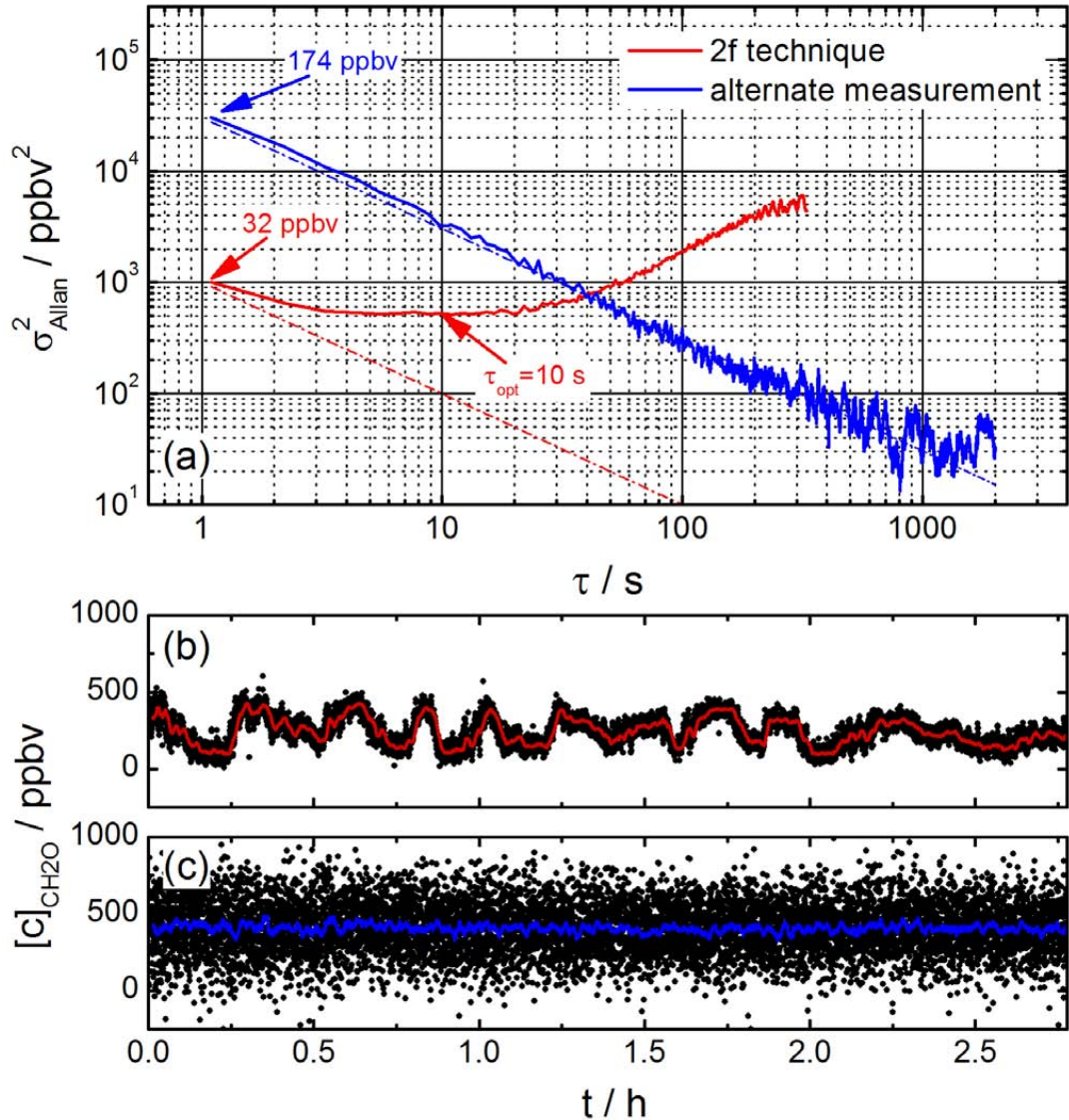


Figure 3.12: (a) Allan plot of the classic 2f-technique (red trace) and of the Stark-subtraction technique (blue trace). The dashed lines indicate the theoretical white noise behavior, where the variance (σ_{Allan}^2) is decreased proportional to the integration time (τ). (b) mixing ratio time series of the classic 2f-technique. (c) mixing ratio time series of the background subtraction approach. In the time series plots the *black dots* represent 1 s data, and the *red* and *blue* traces indicate 50 s moving average values.

It must be stressed out that the spectra shown in Fig. 3.13 originate from the same set of recorded spectra, where the spectra of Fig. 3.13 (a) were recorded in the first half of the measurement sequence, and the spectra in Fig. 3.13 (c) are the result of the subtraction of the spectra recorded during the second half from those of the first half, as described in Section 3.3.3. Therefore the strong drift observed employing the classic 2f-technique can not be due to true changes in concentration, as these changes would have also be present employing the sample modulation approach.

The Allan plot of the subtraction approach [Fig. 3.12 (a)] time-series data shows pure white-noise behavior as the Allan variance decreases linearly with integration time, exceeding stability times of 1 000 s. However, compared to the pure 2f-technique, the noise level (detection limit) is larger by a factor of about 5.4. This can be explained by the following effects: a) the noise is increased by $\sqrt{2}$ due to the subtraction of two noisy signals, and b) the signal strength after subtraction is smaller by about a factor of 2.8, leading to a lower signal-to-noise ratio. The detection limit (1 s) for this technique is 174 ppbv, corresponding to an optical density (αl) of 1.66×10^{-4} . Averaging over 100 s leads to an improved detection limit of 17 ppbv, corresponding to an optical density of 1.63×10^{-5} .

3.4.2 Interleaved measurement of signal and background

The interleaved measurements of signal and background show comparable results in terms of stability time of the system, as can be seen in the Allan plot in Fig. 3.14 (a). The system remains stable for more than 1 000 s. The detection limit (1 s) of the double-modulation approach is 361 ppbv at an absorption path length of 9.6 m, corresponding to an optical density of 3.45×10^{-4} . By averaging over 100 s the detection limit is improved to 32 ppbv, corresponding to an optical density of 3.06×10^{-5} .

The detection limit of this approach is a factor of about 2 higher when compared to the alternate measurements of signal and background (Section 3.4.1). This can be explained by the slower scan frequency of 5 Hz vs. 25 Hz used here. As the low-pass filter time constant of the second lock-in amplifier was set to 10 ms ($\Delta f = 100$ Hz), the data points in the spectrum can not be treated as independent samples. Averaging every data point 5 times longer when switching from a 25 Hz scan ramp to 5 Hz does therefore not improve the signal-to-noise ratio (SNR) of the single data points. The recorded spectra however are independent, and averaging 5 times less spectra per unit time yields a reduction in SNR of $\sqrt{5}$. The scan frequency was lowered because the lock-in amplifier of the second stage — referenced to the 1.5 kHz electric field modulation — needs a few demodulation cycles per data point in the spectrum.

Furthermore, at the 5 Hz scanning frequencies, the laser scan frequency is no longer much faster than the thermal time constant of the laser crystal. As a result, changes in laser tuning current may not only lead to changes in laser wavelength but may also lead to changes in the bulk crystal temperature, which also changes the laser wavelength. Both simultaneous tuning mechanisms can add noise to the laser scan, and this may contribute in part to the degraded performance here.

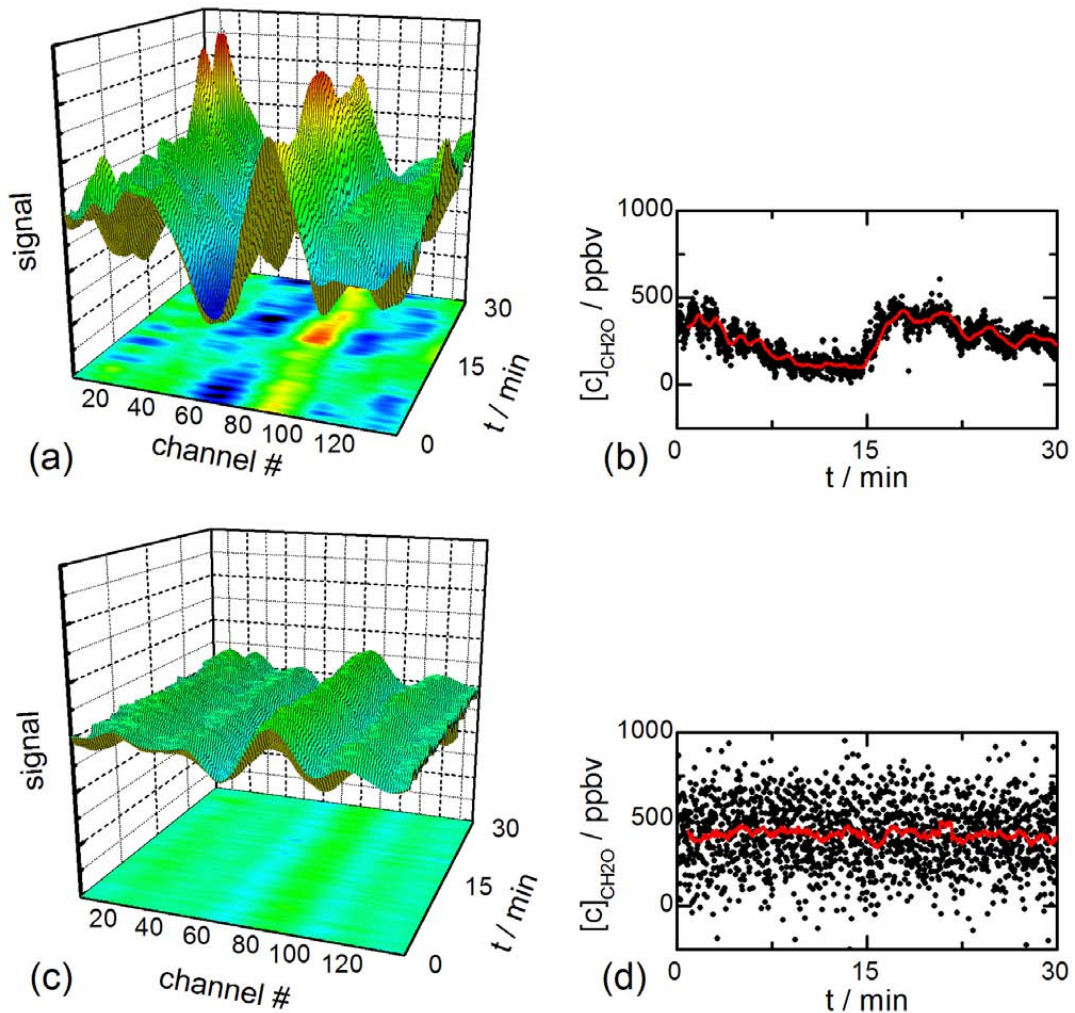


Figure 3.13: Comparison of classic 2f (upper plots) and subtraction technique (lower plots). The 3D plots show the spectra recorded during the first 30 min of the time series shown in the lower two plots of Fig. 3.12 (Spectra averaged for 30 s for clarification). Clearly visible are changes in the spectral background employing the classic 2f-technique (top plot). With the addition of an electric field and employing of the alternate measurements of signal and background, these structures are very effectively eliminated from the spectra, and averaging of the spectra over more than 1 000 s is achieved as depicted in the Allan plot of Fig. 3.12. The right hand plots show the calculated CH_2O mixing ratio. In the top plots a clear correlation between spectral background structure and mixing ratio is observed, whereas in the lower plots no such structure is evident. It is worth to note that the spectra shown in this Figure originate from the same set of recorded spectra. Fig. (a) shows the spectra recorded during the first period of the triangular wavelength scan shown in Fig. 3.9, whereas Fig. (c) shows the processed spectra resulting from the subtraction of the Stark spectra (electric field turned on) from the sample spectra (electric field turned off, top plot of this Figure).

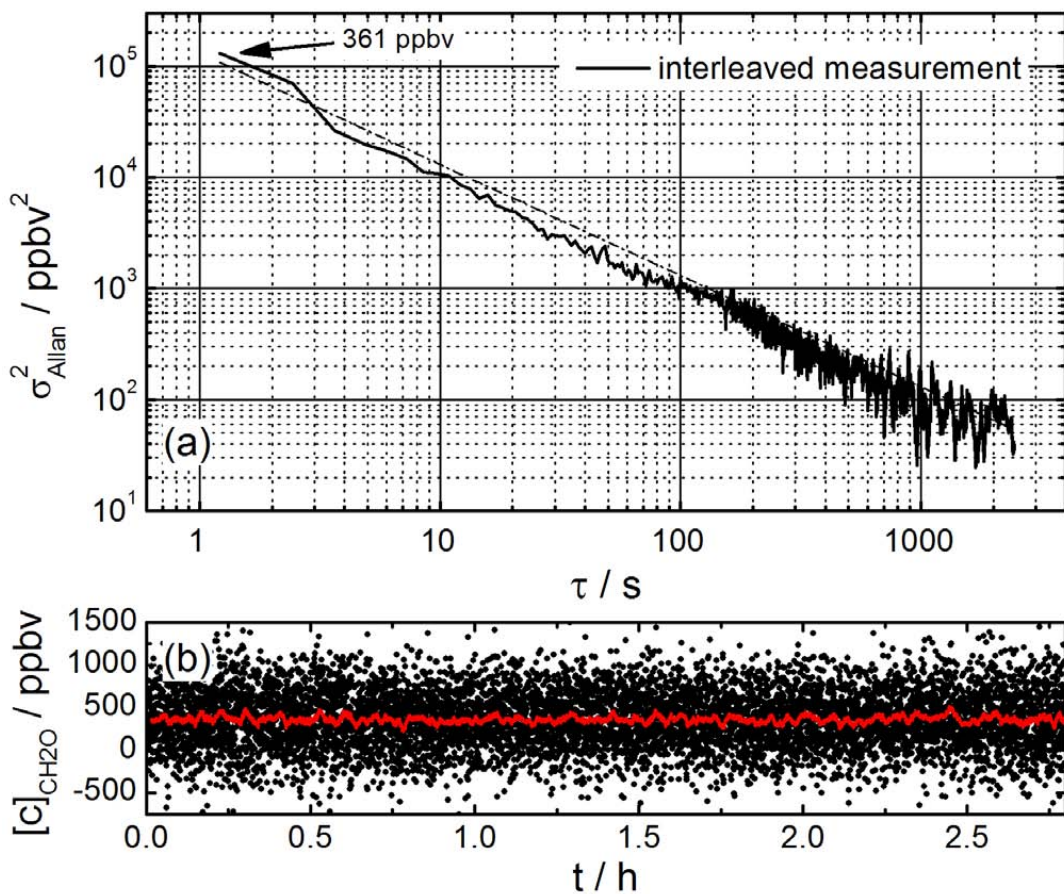


Figure 3.14: (Top plot) Allan plot of the Stark-double modulation technique. The dashed line indicates the theoretical white noise behavior, where the variance (σ^2) is decreased proportional to the integration time (τ). (Lower plot) mixing ratio time series of the Stark-double modulation technique. The *black* dots represent 1 s data, and the *red* trace indicates 50 s moving average values.

3.4.3 Detection limit

The detection limit of both Stark-enhanced techniques is generally higher than for the pure wavelength modulation technique, because the maximum contrast between absorption line within the sample spectra and residual absorption signal within the Stark spectra was limited to 37 %, as shown in Fig. 3.10. Additionally, the maximum electric field was limited by electric breakdown (sparking) between the electrodes at fields larger than approximately 1 050 Vcm $^{-1}$ at 25 hPa. Measurements revealed that the breakdown electric field E_{th} was lowered by approximately 30 % after coating of the electrodes with a 15 μm layer of Teflon (PTFE) due to the slight surface roughness of this material. This coating was chosen to reduce wall effects of the polar CH₂O with the stainless steel electrodes.

Aligning the laser beam through the Stark-MPC introduced additional noise. This was determined when comparing the noise level of the system with and without the Stark-MPC in place by bypassing the cell and comparing the signals incident on the sample detector. Even though the DC power level was higher by a factor of 8.4 when bypassing the MPC, the noise

(standard deviation) was lower by around 2.8 times. In contrast to this measurement, if shot noise was the limiting noise contribution, the noise would be higher by $\sqrt{8.4}$ when bypassing the cell. An explanation can be that the laser beam was clipped at the cell electrodes, leading to an increased amount of scattered light within the cell and potentially back to the laser.

Additional noise may originate from inter-mode competition noise. By chopping the laser beam while tuning it through a saturated H_2O -line nearby it was confirmed that about 30 % of the laser power was emitted in other longitudinal and/or spatial mode(s). Thus the increased noise could in part be due to intermode-beating within the laser. The fraction of multimode emission could not be reduced by changing the laser temperature and/or current for these measurements. Both noise sources would generate very high frequency noise, thus affecting even the 1-second results. Blocking the laser eliminates both high frequency noise effects, and the resulting 1-second Allan variance starting point fell to about 5 ppbv, which is within a factor of ≈ 1.6 of what was recently achieved by *Weibring et al.* [2006] employing a DFG spectrometer without Stark modulation. For this comparison the results of *Weibring et al.* [2006] were scaled by pressure, path length (factor 10 reduction here), the 37 % Stark modulation amplitude, and the absorption cross section ratios (a reduction of about 29 % here).

The InSb detector available for the present study was not well matched to the laser operation wavelength of $5.69\text{ }\mu\text{m}$ (1757.9 cm^{-1}), where the detector responsivity was only about 0.2 A/W. This is a factor of 15 below the maximum responsivity of this detector (Fig. 3.15). As a result, the detector signal was relatively weak, yielding a reduced signal-to-noise ratio. Unfortunately a more suitable detector for this wavelength was not available at the time of the measurements.

The sensitivity was also limited by the reduced pressure necessary for the measurement. This is because the maximum contrast of the absorption line, when applying an electric field, is achieved at around 25 hPa. A higher pressure would lead to a higher optical density at a given concentration, but would also increase the width of the absorption line. The breakdown electric field E_{th} is not sufficiently increased by an increase in pressure (see Fig. 3.8 on Page 92) and does not compensate for the additional pressure broadening of the absorption line. The optimum pressure of 25 hPa of the present experiment is governed by the parameters describing the absorption feature, i.e. the pressure broadening and the coefficient of Stark-broadening, and may be different for other absorption features showing a Stark effect.

Even though the detection limit in the present study was not determined by detector noise only (as would be desirable), the Stark-enhanced wavelength-modulation technique clearly showed its potential in terms of improving the stability of the spectrometer by eliminating time dependent background structures. Stability times routinely exceeding 1 000 s completely eliminate the need for background measurements which would require flushing of the absorption cell with zero air. To my knowledge, this is the first time such high performance was shown. This is particularly important for airborne systems, where measurement time is extremely precious. For conventional measurements, the duty cycle is typically around 55–65 % [*Roller et al.*, 2006], including ambient/calibration and background measurement sequences and flushing times in between. Applying the Stark-enhanced technique only requires recording calibration spectra about every 20 min or so, thus increasing the duty-cycle to nearly 100 %.

The Stark-enhanced technique also reduces spectral interference with most other molecules such as water vapor, because the absorption lines of these molecules generally do not show a significant Stark effect.

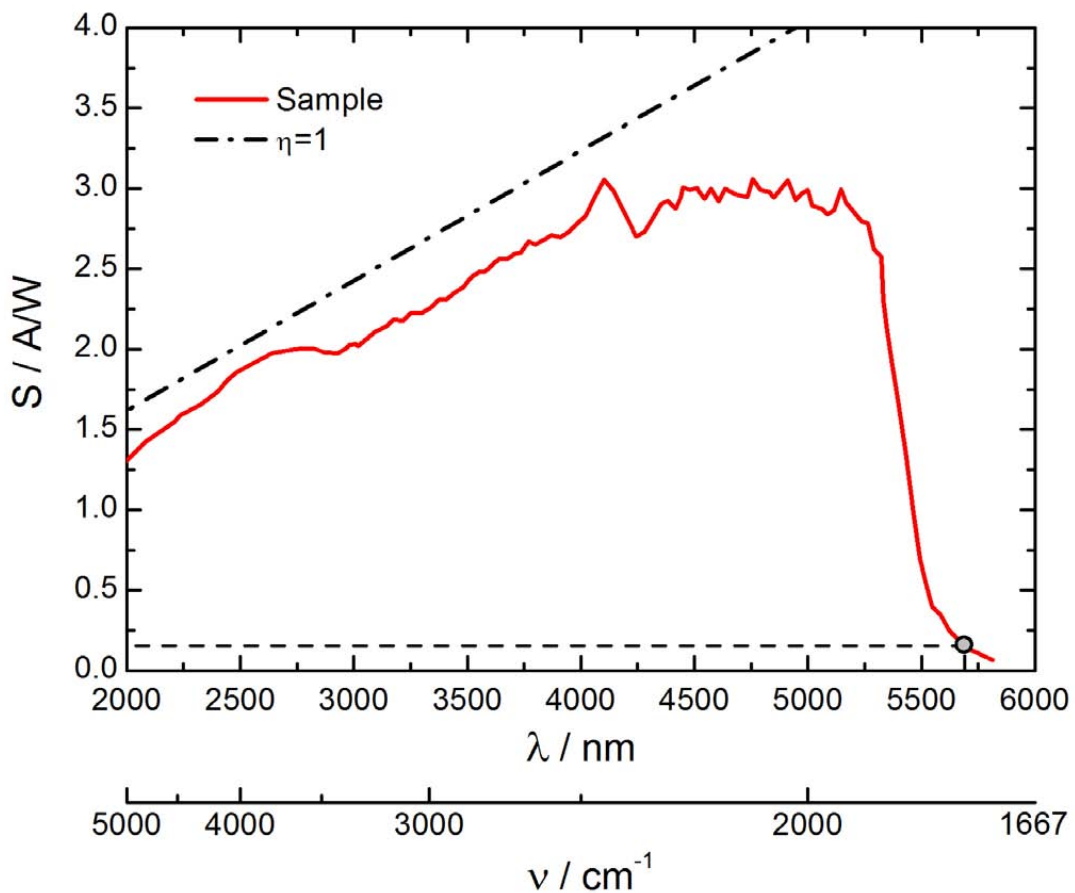


Figure 3.15: Characteristics of the InSb (sample) detector at T=80 K (reproduced from specification sheet) used for the present study. The responsivity of the detector at the laser wavelength $\lambda = 5.69 \mu\text{m}$ (1757.9 cm^{-1}) is around 0.2 A/W, and is only 7 % of the maximum responsivity of $\sim 3 \text{ A/W}$.

3.4.4 Conclusion

Two data acquisition approaches for Stark modulation spectroscopy have been studied in terms of system stability and detection limit. mixing ratio time-series have therefore been recorded, and were analyzed by means of the Allan-variance method. The first approach has made use of alternate measurements of signal and background. The electric field was thereby modulated at 25 Hz. The spectra, where the electric field was turned on, were treated as background spectra. They were subtracted from the spectra where the electric field was turned off to yield background-free absorption spectra. At the second approach, interleaved measurements of signal and background have been performed, where the electric field was modulated at 1.5 kHz. This modulation was applied in addition to the laser-wavelength modulation, and a second lock-in amplifier was used to demodulate the signal at this Stark modulation frequency.

Direct comparison with second-derivative spectroscopy without Stark modulation revealed the great potential of Stark modulation spectroscopy to compensate for systematic drift. This drift is caused by time-dependent spectral background structures that are caused by unwanted etalons within the optical setup of the spectrometer. For both Stark modulation data acquisition

approaches, stability times longer than 1 000 s have been achieved. This is around a ten times improvement over published results. Such long stability times eliminate the need to frequently record background spectra, where the absorption cell must be flushed with zero air. It was therefore possible to increase the duty-cycle of these experiments to nearly 100 %.

3.5 Future improvements

While the Stark modulation experiments described in the present work have been very successful in the improvement of spectrometer stability and thus duty-cycle, the sensitivity is to be improved to conduct atmospheric measurements.

Sensitivity is a measure of signal-to-noise ratio. The sensitivity can be increased by either increasing the signal or reducing the noise or both. One means of increasing the signal is to increase the absorption path length, as Beer-Lambert's law suggests (Section 1.1.3). A factor of 4 higher path length is feasible with the present Stark multipass cell aligned to the full 40 m path length (86 passes).

As indicated earlier, the spectral responsivity of the InSb detector used was not well matched to the laser operation wavelength. Assuming a peak responsivity of 3 A/W matched to the laser operation wavelength, the signal could be increased by a factor of 15. Assuming further, that shot noise was the dominating noise contribution, where the noise variance depends linearly on the photocurrent, one could expect an improvement of signal-to-noise ratio by a factor of $\sqrt{15} = 3.9$.

The signal could also be increased by applying higher electric fields to the target gas. Measurements of the breakdown electric field within the present cell (Section 3.3.2) indicate a theoretical margin of 30–40 % that could not be fully used due to earlier electric breakdown. This reduced electric breakdown voltage was related to the slight surface roughness of the Teflon coating of Stark electrodes, which has been applied to minimize exchange times due to adsorption and desorption of CH_2O at the electrodes. Using no coating might therefore lead to an improved sensitivity, however at the cost of increased exchange times.

In addition to increasing the signal, the noise might be reduced. The present laser showed substantial multimode behavior, as was discussed in Section 3.4.3, and replacing this laser with a single mode laser might lead to an additional improvement in sensitivity.

3.6 Applicability of Stark modulation to other gases

It has been noted that the Stark modulation techniques are not applicable for all types of molecules. The molecule must have a significant dipole moment, and the symmetry of the molecule must be such that an external electric field induces a net change in rotational energy (Stark effect). Other potential candidates for these techniques are hydrogen peroxide (H_2O_2 , $\mu = 2.26 \text{ D}$) [Bellini *et al.*, 1996], nitric acid (HNO_3 , $\mu = 2.17 \text{ D}$) [Kleiner *et al.*, 1987; Webster and May, 1985], ammonia (NH_3 , $\mu = 1.47 \text{ D}$) [Höjer *et al.*, 1991; Sasada, 1984; Verhage *et al.*, 1993], and hydrogen chloride (HCl , $\mu = 1.18 \text{ D}$) [Werle and Lechner, 1999].

Water vapor (H_2O and its isotopologues), which is another target gas of interest in the present work, has a relatively high dipole moment of $\mu = 1.84 \text{ D}$. To study the applicability of the Stark modulation technique described above, the HITRAN database [Rothman *et al.*, 2005]

has been screened for potentially suitable absorption lines. Due to the high number of water absorption lines listed in HITRAN (51 930 transitions in the 2004 edition), only transitions fulfilling the following constraints have been considered:

- integrated line strength $S_{ij} \geq 1 \times 10^{-27} \text{ cm}^2/(\text{cm molecule})$. It must be noted, though, that high sensitivity measurements require $S_{ij} > 1 \times 10^{-23} \text{ cm}^2/(\text{cm molecule})$.
- separation of neighboring energy levels $\delta \leq 1 \text{ cm}^{-1}$. The smaller the separation δ , the higher the Stark shift for a given electric field (Eq. 3.1 on Page 77).
- selection rules for two neighboring energy levels $\Delta J = 0, \pm 1$, and $\Delta K_a = \pm 1$ and $\Delta K_c = \pm 1$ (b-type) with $\mu_b \simeq 1.8 \text{ D}$ [Shostak *et al.*, 1991]. For the oxygen isotopologues, the dipole moment is directed along the b-axis of the molecule (Fig. 1.1). In HDO, the a and b-axes are somewhat tilted due to the heavier mass of the deuterium isotope, and the dipole moment has non-zero projections on both the a and b-axis. Therefore, a Stark effect may also be observed when the electric field interacts with the projection of μ on the a-axis, where $\mu_a \simeq 0.66 \text{ D}$ [Shostak *et al.*, 1991]. In this case the additional selection rules $\Delta K_a = 0$ and $\Delta K_c = \pm 1$ for HDO are valid [Callegari, 2004].

The coefficient of shift (Stark coefficient) of the highest M component of an energy level due to the Stark effect can be approximated by $C = \mu^2/\delta$ [Hz(V/cm)⁻²], where $\mu = 1.8 \text{ D}$ is the dipole moment of H₂O and δ is the separation of the two interacting energy levels [Callegari, 2004]. The highest M component of two energy levels separated by $\delta = 1 \text{ cm}^{-1}$ and fulfilling the selection rules above is thus shifted by $\approx 3.24 \text{ MHz}$ when an electric field of 1000 Vcm^{-1} is applied.

The Stark coefficients of the H₂O absorption lines that fulfill the constraints mentioned above have been calculated, and the results are tabulated in Appendix B. In order to achieve a reasonable Stark modulation of an appropriate absorption line, i.e., $\geq 100 \text{ MHz}$ for the electric field employed in the present work, the Stark coefficient would have to be $C = 100 \text{ Hz(V/cm)}^{-2}$. However, such high Stark coefficients could not be found for the three oxygen isotopologues. For HDO, large Stark coefficients could be found, but the integrated linestrengths of the corresponding absorption lines are generally too weak by one order of magnitude or more. The only suitable absorption line in this respect is the far-infrared transition at $\nu_0 = 298.741 \text{ cm}^{-1}$ (33.5 μm) with $S_{ij} = 5.75 \times 10^{-23} \text{ cm}^2/\text{cm} \cdot \text{molecule}$, for which a shift of the highest M component of $\sim 2 \text{ GHz}$ could be expected at an electric field of 1000 Vcm^{-1} . The expected shift is around 2.8 times higher than what is found for the CH₂O absorption line probed in the present work, where the highest M component is shifted by 705 MHz at a field strength of 1000 Vcm^{-1} .

As the goal in our group is to measure water vapor isotopic ratios, one would ideally want to be able to probe absorption lines of all isotopologues of interest with a large Stark coefficient. Isotopic ratio measurements require simultaneous probing of two absorption lines, one of both the major and a minor isotopologue, as discussed in Section 2.2.4. Eliminating of spectral background of just one of the absorption lines would therefore not yield an improvement as any background on the other absorption line would unavoidably yield a degradation in system performance. However, this extensive screening of the HITRAN database shows no such potential, and Stark modulation spectroscopy is therefore not applicable for high precision water isotopic ratio measurements.

Chapter 4

Summary

Laser-spectroscopic detection of atmospheric-trace gases has become a widely accepted technique, because it can offer measurements with high selectivity, and fast time response. The present work discusses techniques for the measurement of two important gases, namely water (H_2O) and its stable isotopologues, as well as formaldehyde (CH_2O). The measurement of both molecules requires very high sensitivity, which can only be achieved by low-noise instrumentation in combination with signal averaging. However, the averaging time, in which the sensitivity is improved, is generally limited by systematic drift to around 30 s to 60 s. For those measurements, where an even better sensitivity is required, means have to be found to eliminate this drift.

In addition to the high-sensitivity requirements, instrumentation for airborne operation needs to be compact and lightweight. In the particular case of the water vapor isotopic ratio spectrometer, which is described within the present dissertation, the instrument needs to fit into a 19 inch rack and must be operated fully autonomous.

Highly sensitive water isotopic-ratio measurements

For intended measurements of H_2O isotopic ratios aboard airborne research platforms, a highly compact and lightweight absorption spectrometer has been developed. The size and weight constraints were governed by the limited space and payload of the potential airborne platforms CARIBIC¹ and HALO². The final instrument has dimensions of $45 \times 56 \times 35 \text{ cm}^3$ at a mass of around 35 kg. In addition, the instrument can be operated in a fully autonomous mode to allow for unattended operation on intercontinental flights aboard CARIBIC as well as during the envisaged measurement campaigns aboard the HALO aircraft.

Wavelength-modulation spectroscopy in combination with a compact 76 m astigmatic multipass absorption cell has been applied. Isolated absorption lines of the stable H_2O isotopologues H_2^{16}O , H_2^{17}O , and H_2^{18}O have been probed using a room-temperature distributed-feedback diode laser emitting at around $3\,663 \text{ cm}^{-1}$ ($2.73 \mu\text{m}$).

By careful investigation and elimination of perturbations, a very good sensitivity was achieved, which was determined to be among the best found for H_2O isotopic-ratio measure-

¹www.caribic-atmospheric.com

²www.halo.dlr.de

ments in the literature [Hanisco *et al.*, 2007; Kerstel *et al.*, 2006; Webster and Heymsfield, 2003]. The absorbance sensitivity (OD) has routinely been in the lower 10^{-6} range for 30 s integration time. The precision for H_2O isotopic-ratio measurements was determined to be 2‰ and 6.25‰ for $\delta^{17}\text{O}$ and $\delta^{18}\text{O}$, respectively, at a water mixing ratio of 90 ppmv and a 30 s integration time.

These results mark the first and very important step towards the goal of our laboratory to perform corresponding in-situ measurements aboard airborne platforms under both tropospheric and stratospheric conditions. Atmospheric measurements using the present H_2O isotopic-ratio spectrometer aboard CARIBIC are scheduled for Jan. 2009 with regular (monthly) intercontinental flights. Furthermore, participation in several measurement campaigns aboard HALO is intended, starting with TACTS (Sep.–Oct. 2009), and followed by ML-CIRRUS (Nov.–Dec. 2009) as well as POLSTRAC (Feb.–Mar. 2010).

Drift compensation by Stark modulation

While laser-spectroscopic measurements of atmospheric formaldehyde (CH_2O) have been successfully conducted in the past [Weibring *et al.*, 2007; Wert *et al.*, 2003a,b], these measurements require extremely high sensitivity due to the very low ambient CH_2O concentrations. Even for low-noise instrumentation, the sensitivity must be improved by averaging of spectral data. On the other hand, the averaging time, in which the sensitivity is effectively improved, is often limited by systematic drift. If better sensitivity is required, new measurement approaches need to be found to overcome this limitation.

One new and promising approach to the detection of polar molecules is Stark modulation spectroscopy. This approach was investigated within the present dissertation in two different schemes in terms of its potential and its limits towards the detection of formaldehyde.

The measurements were based on wavelength modulation spectroscopy using a lead-salt tunable-diode laser and probing a CH_2O absorption feature at around $1\,757\,\text{cm}^{-1}$ ($5.69\,\mu\text{m}$). An additional highly selective modulation of the absorption coefficient by means of the Stark effect has been applied. A novel Herriott multipass absorption cell was used, which contains two cylindrical electrodes to apply an electric field to the target gas.

The study revealed an exceptional performance in eliminating systematic drift. For the first time, integration times of more than 1 000 s could be achieved, which corresponds to an improvement of approximately a factor of ten over most published results.

Appendices

A Absorption signals at wavelength modulation

In this Section the properties of second-derivative spectra due to wavelength modulation are briefly reviewed. For a more detailed discussion the reader is referred to the publications of *Wahlquist* [1961], *Arndt* [1965], *Hager, Jr. and Anderson* [1970], *Olson et al.* [1980], *Reid and Labrie* [1981]; *Reid et al.* [1980], *Iguchi* [1986], *Bomse et al.* [1992], *Uehara* [1998], and *Werle* [1998].

Gaussian and Lorentzian lineshape

The normalized Gaussian and Lorentzian lineshape functions have been introduced in Section 1.1.2. Fig. A.1 (a) displays a Gaussian (*red* trace) and a Lorentzian (*blue* trace) lineshape at equal HWHM ($\gamma = 0.05$).

At wavelength-modulation spectroscopy, the laser emission frequency ν is modulated by $\Delta\nu = a \cos(\omega_{\text{mod}}t)$. The angular modulation frequency is $\omega_{\text{mod}} = 2\pi f_{\text{mod}}$, and the modulation amplitude is a . We define the dimensionless modulation index $\beta = a/\gamma$, where γ is the HWHM of the lineshape function. With this modulation of ν , the normalized Gaussian lineshape function becomes

$$\Gamma_D(\nu, t) = \frac{1}{\gamma_D} \sqrt{\frac{\ln(2)}{\pi}} \exp \left\{ -\ln(2) \left(\frac{\nu - \nu_0 - \beta \gamma_D \cos(\omega_{\text{mod}}t)}{\gamma_D} \right)^2 \right\}, \quad (\text{A.1})$$

where the HWHM is

$$\gamma_D = \frac{\nu_0}{c} \sqrt{\frac{2 \ln(2) kT}{M}}. \quad (\text{A.2})$$

The gas temperature is T , the molecular weight is M , ν_0 is the line-center frequency, and $k_B = 1.38 \times 10^{-23}$ J/K is the Boltzmann constant.

The normalized Lorentzian lineshape function for modulation of ν is

$$\Gamma_C(\nu, t) = \frac{1}{\gamma_C \pi} \frac{\gamma_C^2}{[\nu - \nu_0 - \beta \gamma_L \cos(\omega_{\text{mod}}t)]^2 + \gamma_C^2}, \quad (\text{A.3})$$

with the HWHM

$$\gamma_C = \gamma_C^0 p \sqrt{\frac{T}{T_0}}. \quad (\text{A.4})$$

Here, γ_C^0 is the coefficient of pressure broadening ($\text{cm}^{-1}/\text{bar}$), p is the gas pressure (bar), and T is the gas temperature (K).

For arbitrary modulation index β , *Wilson* [1963] suggests to expand the lineshape function at modulation $[\Gamma(\nu, t)]$ into a cosine-Fourier series about an operating point $\bar{\nu}$

$$\Gamma(\bar{\nu}, t) = \frac{B_0}{2} + \sum_{n=1}^{\infty} B_n(\bar{\nu}) \cos(n\omega_{\text{mod}}t). \quad (\text{A.5})$$

The sine-terms of the Fourier series can be neglected because $\Gamma(\bar{\nu}, t)$ is an even function of time. Substituting $\omega_{\text{mod}}t = \phi$, the n^{th} ($n = 0 \dots \infty$) Fourier coefficient is calculated by

$$B_n(\bar{\nu}) = \frac{1}{\pi} \int_0^{2\pi} \Gamma(\bar{\nu}, t) \cos(n\phi) d\phi. \quad (\text{A.6})$$

To measure second-derivative spectra, the signal $A(\bar{v}, t)$ is demodulated by a lock-in amplifier, which is referenced to twice the angular modulation frequency ($2\omega_{\text{mod}}$), and the resulting signal is proportional to the second Fourier coefficient $B_2(\bar{v})$. This second Fourier coefficient for a Gaussian lineshape function is thus determined by calculating the integral

$$B_2^G(\bar{v}) = \frac{1}{\pi} \int_0^{2\pi} \Gamma_D(\bar{v}, t) \cos(2\phi) d\phi \quad (\text{A.7})$$

for any v of the lineshape. For a Lorentzian lineshape the integral consequently is

$$B_2^L(\bar{v}) = \frac{1}{\pi} \int_0^{2\pi} \Gamma_C(\bar{v}, t) \cos(2\phi) d\phi \quad (\text{A.8})$$

Analytical solutions of the integrals in Eqs. A.7 and A.8 have been calculated by *Reid and Labrie* [1981] and *Iguchi* [1986].

For a small modulation index $\beta \ll 1$, the signal is similar to the n^{th} derivative [Preston and Dietz, 1991]. For large modulation index $\beta \gg 1$, the resulting signal is substantially broadened. Second-derivative spectra of the lineshape functions in Fig. A.1 (a) at different modulation indices β are displayed in Fig. A.1 (b) and (c), respectively. Furthermore, Fig. A.1 (d) displays the second-derivative signal at line center (v_0) as a function of the modulation index β . It can be seen, that the maximum line-center signal is achieved at a modulation index of $\beta = 2.2$, independent of the lineshape function.

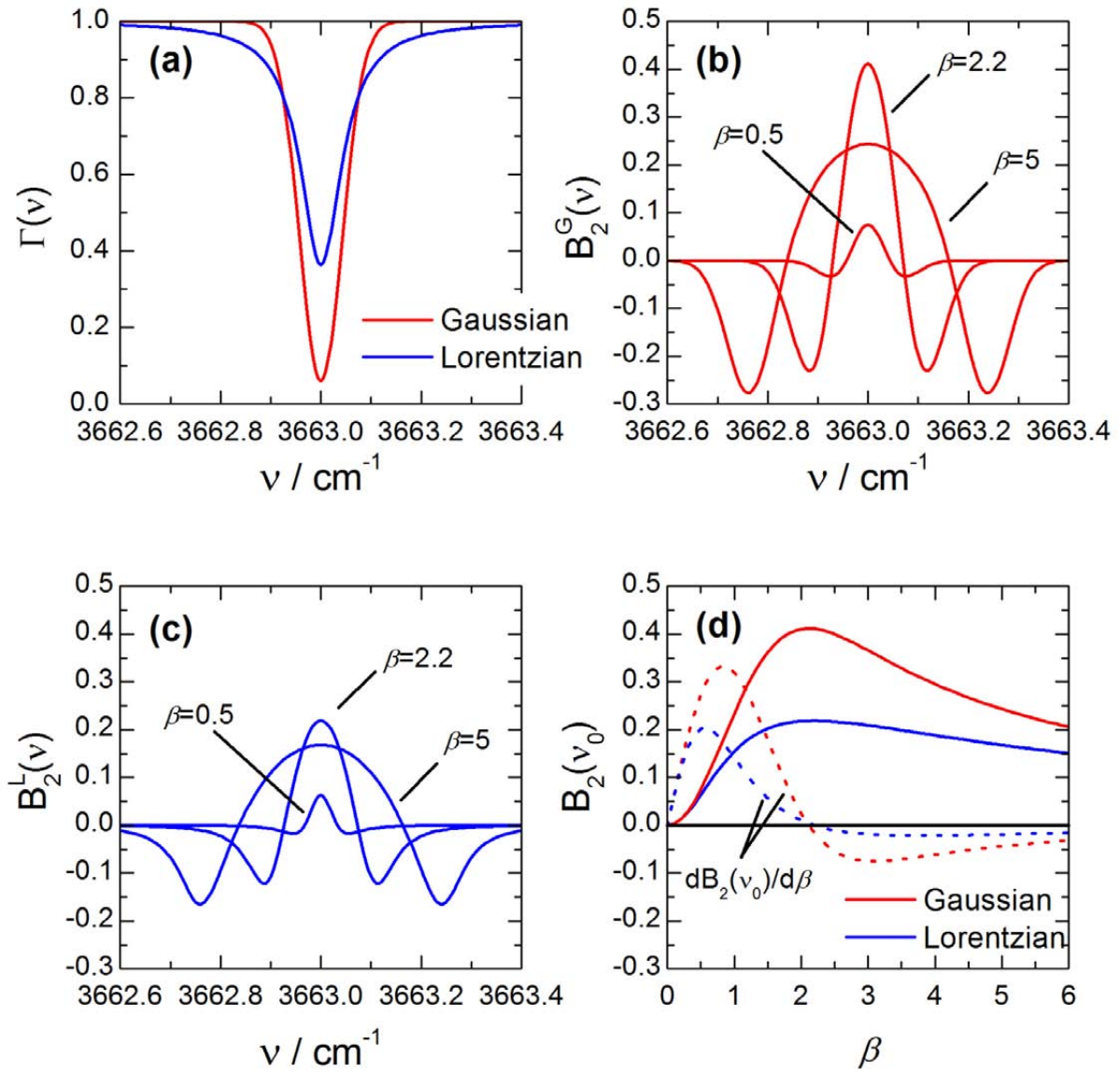


Figure A.1: (a) Gaussian (red trace) and Lorentzian (blue trace) lineshape function at equal HWHM ($\gamma = 0.05 \text{ cm}^{-1}$). (b) Second-derivative spectra of the Gaussian lineshape simulated at different modulation indices β . (c) Second-derivative spectra of the Lorentzian lineshape simulated at different modulation index β . (d) Second-derivative signal of the Gaussian (red trace) and Lorentzian (blue trace) lineshape at the line center (ν_0). The maximum second-derivative signal at the line center is achieved for both lineshapes at a modulation index of $\beta = 2.2$, which is shown by zero crossing of the derivatives $dB_2(v_0)/d\beta$ (dashed lines).

Etalon fringe

In tunable diode-laser spectroscopy one may observe spectrally periodic background signals superimposed on the absorption spectra. These background signals are due to interference of back-reflected radiation with the main laser beam, similar to the interference signal produced by a Fabry-Pérot etalon. Assume such a background (or fringe) signal with a certain free-spectral-range (FSR) to be of the form [Iguchi, 1986]

$$A_F(v) = b_0 + b \cos\left(\frac{2\pi v}{\text{FSR}}\right). \quad (\text{A.9})$$

Fig. A.2 (a) depicts such an etalon fringe signal at $\text{FSR} = 0.05 \text{ cm}^{-1}$.

Modulation of v with a modulation index $\beta = b/\text{FSR}$ at the angular modulation frequency $\omega_{\text{mod}} = 2\pi f_{\text{mod}}$ yields

$$A_F(v, t) = b_0 + b \cos\left\{\frac{2\pi}{\text{FSR}} [v - \beta \text{FSR} \cos(\omega_{\text{mod}} t)]\right\}. \quad (\text{A.10})$$

In order to calculate the second-derivative signal $B_2^F(\bar{v})$ of the etalon fringe at an operating point \bar{v} we proceed as previously for the Gaussian and Lorentzian lineshapes by solving the integral

$$B_2^F(\bar{v}) = \frac{1}{\pi} \int_0^{2\pi} A_F(\bar{v}, t) \cos(2\phi) \, d\phi. \quad (\text{A.11})$$

The resulting second-derivative signal of this etalon fringe is depicted in Fig. A.2 (b) for different modulation indices β . Fig. A.2 (c) shows the peak-to-peak etalon signal depending on the modulation index β . It can be seen that the fringe amplitude can be minimized at a modulation index of $\beta \approx 0.8, 1.35, 1.85, 2.35, \dots$. The minima result from the dependence of $B_2^F(\bar{v})$ on a Bessel function of the first kind of the order 2 with the argument $2\pi\beta$, as has been shown by Iguchi [1986].

For laser spectroscopic instrumentation, free-space optical paths that may form an etalon commonly have a length l of around 0.5 m. In this case the free-spectral-range of the fringe is $\text{FSR} = c/2l \approx 300 \text{ MHz}$, which is close to the HWHM of an absorption line at a reduced pressure of $p \approx 70 \text{ hPa}$ ($\text{FSR} \approx \gamma$). Recall, that the maximum second-derivative absorption signal is achieved at $\beta = 2.2$ [Fig. A.1 (d)]. In this case, the second-derivative etalon signal is close to one of the minima ($\beta \approx 2.35$) as shown in Fig. A.2 (c), and it can be minimized by slightly adjusting the modulation index without loosing much of the actual absorption signal [note the broad maxima of $B_2(v_0)$ in Fig. A.1 (d)].

However, as Iguchi [1986] has correctly pointed out, this minimization of second-derivative fringe signal can only be effectively applied to one fringe signal. If multiple fringe signals are present, there will generally remain a residual background, which in turn can lead to drift effects and a limited averaging time for spectral data.

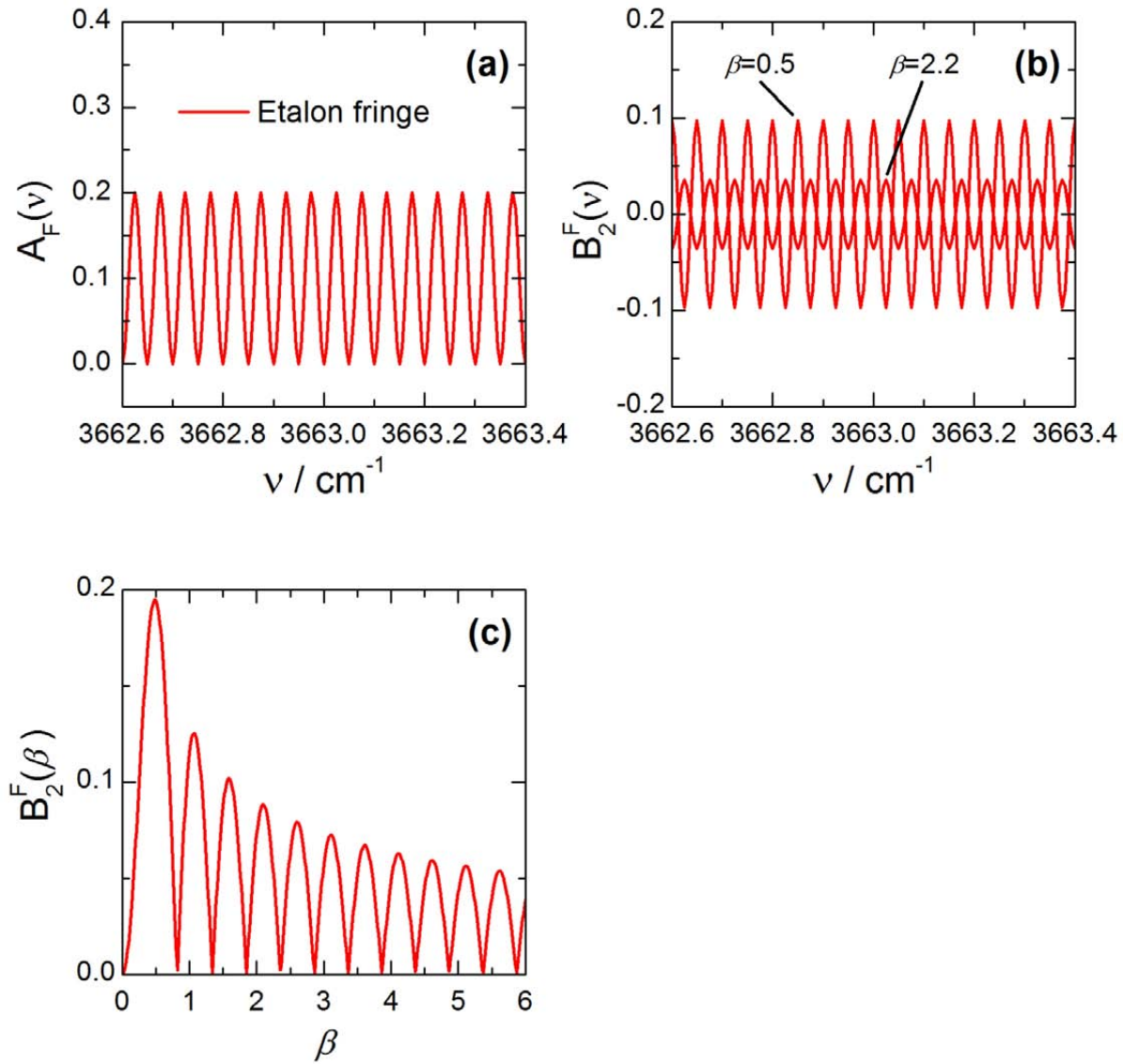


Figure A.2: (a) Etalon signal with a free spectral range (FSR) of 0.05 cm^{-1} . (b) Second-derivative spectra of the etalon signal simulated at different modulation indices β . (c) Second-derivative peak-to-peak amplitude of the etalon signal. The amplitude can be minimized at a modulation index $\beta \approx 0.8, 1.35, 1.85, 2.35, \dots$ The minima result from the dependence of $B_2^F(\bar{\nu})$ on a Bessel function of the first kind of the order 2 with the argument $2\pi\beta$ [Iguchi, 1986].

B Stark coefficients of H₂O absorption lines

Table B.1: Summary of absorption lines of H₂O and its stable isotopologues listed in the 2004 edition of the HITRAN database [Rothman *et al.*, 2005] that reveal a Stark effect. Tabulated are the line center frequency v_0 (cm⁻¹), integrated line strength S_{ij} (cm²/cm molecule), excited and ground state energy E' and E'' (cm⁻¹), vibrational quantum numbers for excited and ground state v' and v'' , rotational quantum numbers for excited and ground state J' , K'_a , K'_c , and J'' , K''_a , K''_c , and approximated Stark-coefficient C (Hz/(V/cm)²). Stark coefficient approximated by $C \approx \mu^2/\Delta E$ (μ in D, ΔE in cm⁻¹). The absorption transitions are sorted by isotopologue and by approximated Stark coefficient. It should be pointed out, that for high sensitivity isotopic ratio measurements the integrated linestrength should be $> 1 \times 10^{-23}$ cm²/(cm molecule). This requirement is quite generally not met in combination with a large Stark coefficient.

v_0	S_{ij}	E'	E''	v'	v''	J'	K'_a	K'_c	J''	K''_a	K''_c	C
H_2^{16}O												
1 888.250	5.20E-25	4 049.536 00	2 161.285 90	0 0 1	0 0 1	5	1	4	6	2	5	6.3
1 315.573	4.84E-26	4 049.536 00	2 733.962 60	0 0 1	0 0 1	5	1	4	6	6	1	6.3
1 919.937	1.48E-25	4 049.536 00	2 129.599 10	0 0 1	0 0 1	5	1	4	4	4	1	6.3
3 004.478	7.22E-25	4 049.536 10	1 045.057 90	0 0 1	0 0 0	5	1	4	6	6	1	6.3
2 128.770	1.08E-24	4 049.536 10	1 920.766 50	0 0 1	0 0 1	5	1	4	5	0	5	6.3
3 724.188	1.61E-21	4 049.536 10	325.347 90	0 0 1	0 0 0	5	1	4	5	0	5	6.3
3 561.428	5.41E-24	4 049.536 10	488.107 70	0 0 1	0 0 0	5	1	4	4	4	1	6.3
3 292.811	5.85E-23	4 049.536 10	756.724 80	0 0 1	0 0 0	5	1	4	6	4	3	6.3
3 749.174	7.83E-22	4 049.536 10	300.362 30	0 0 1	0 0 0	5	1	4	4	2	3	6.3
3 496.625	3.30E-21	4 049.536 10	552.911 40	0 0 1	0 0 0	5	1	4	6	2	5	6.3
3 603.025	3.34E-21	4 049.536 10	446.510 70	0 0 1	0 0 0	5	1	4	5	2	3	6.3
3 439.195	1.26E-23	4 049.536 10	610.341 20	0 0 1	0 0 0	5	1	4	5	4	1	6.3
2 141.520	1.05E-24	4 049.536 20	1 908.016 40	0 0 1	0 0 1	5	1	4	4	2	3	6.3
1 651.155	1.08E-26	4 049.536 20	2 398.381 60	0 0 1	0 0 1	5	1	4	6	4	3	6.3
1 995.567	1.19E-24	4 049.536 20	2 053.968 80	0 0 1	0 0 1	5	1	4	5	2	3	6.3
2 232.601	1.29E-25	4 050.052 10	1 817.451 00	0 0 1	0 0 1	4	2	3	4	0	4	6.3
2 025.900	5.41E-25	4 050.052 10	2 024.152 60	0 0 1	0 0 1	4	2	3	5	2	4	6.3
3 734.273	1.66E-20	4 050.052 10	315.779 50	0 0 1	0 0 0	4	2	3	4	2	2	6.3
3 633.843	2.95E-20	4 050.052 10	416.208 70	0 0 1	0 0 0	4	2	3	5	2	4	6.3
3 843.751	4.16E-20	4 050.052 10	206.301 40	0 0 1	0 0 0	4	2	3	3	2	2	6.3
3 439.938	3.52E-23	4 050.052 10	610.114 40	0 0 1	0 0 0	4	2	3	5	4	2	6.3
1 798.357	7.67E-27	4 050.052 20	2 251.695 30	0 0 1	0 0 1	4	2	3	5	4	2	6.3
2 127.151	2.86E-25	4 050.052 20	1 922.901 10	0 0 1	0 0 1	4	2	3	4	2	2	6.3
3 561.918	2.71E-23	4 050.052 20	488.134 20	0 0 1	0 0 0	4	2	3	4	4	0	6.3
2 236.265	2.00E-24	4 050.052 20	1 813.787 60	0 0 1	0 0 1	4	2	3	3	2	2	6.3
3 827.999	3.85E-21	4 050.052 20	222.052 80	0 0 1	0 0 0	4	2	3	4	0	4	6.3
1 920.434	7.79E-27	4 050.052 20	2 129.618 70	0 0 1	0 0 1	4	2	3	4	4	0	6.3
3 742.353	1.90E-25	5 996.637 11	2 254.283 70	0 2 0	0 0 0	9	2	9	10	8	3	6.0
3 474.372	2.31E-26	5 996.637 16	2 522.265 10	0 2 0	0 0 0	9	2	9	11	8	3	6.0
3 986.832	1.17E-25	5 996.637 24	2 009.805 10	0 2 0	0 0 0	9	2	9	9	8	1	6.0
3 023.810	8.92E-26	5 996.637 31	2 972.827 40	0 2 0	0 0 0	9	2	9	11	10	1	6.0

continued..

..continued

3 294.749	1.54E-26	5 996.637 32	2 701.888 70	0 2 0	0 0 0	9	2	9	10	10	1	6.0
2 244.221	3.88E-27	5 996.637 32	3 752.416 30	0 2 0	0 1 0	9	2	9	9	8	1	6.0
2 964.486	2.84E-26	5 997.176 17	3 032.689 70	0 2 0	0 0 0	8	3	8	12	9	4	6.0
3 942.831	7.71E-26	5 997.176 23	2 054.345 20	0 2 0	0 0 0	8	3	8	10	7	4	6.0
3 256.756	1.19E-26	5 997.176 24	2 740.420 70	0 2 0	0 0 0	8	3	8	11	9	2	6.0
3 675.271	2.75E-27	5 997.176 34	2 321.905 80	0 2 0	0 0 0	8	3	8	11	7	4	6.0
5 357.238	8.60E-24	7 096.722 00	1 739.483 60	0 2 1	0 1 0	4	1	4	3	1	3	5.5
6 821.225	3.40E-23	7 096.722 00	275.497 00	0 2 1	0 0 0	4	1	4	4	1	3	5.5
5 173.893	4.90E-24	7 096.722 00	1 922.829 00	0 2 1	0 1 0	4	1	4	5	1	5	5.5
6 811.503	9.90E-26	7 096.722 00	285.219 30	0 2 1	0 0 0	4	1	4	3	3	1	5.5
6 712.880	2.90E-24	7 096.722 10	383.842 50	0 2 1	0 0 0	4	1	4	4	3	1	5.5
6 592.754	2.60E-24	7 096.722 10	503.968 10	0 2 1	0 0 0	4	1	4	5	3	3	5.5
4 970.314	1.30E-26	7 096.722 10	2 126.407 70	0 2 1	0 1 0	4	1	4	5	3	3	5.5
6 954.444	4.60E-22	7 096.722 10	142.278 50	0 2 1	0 0 0	4	1	4	3	1	3	5.5
6 770.097	2.30E-22	7 096.722 10	326.625 50	0 2 1	0 0 0	4	1	4	5	1	5	5.5
5 221.252	6.00E-25	7 096.722 10	1 875.469 70	0 2 1	0 1 0	4	1	4	4	1	3	5.5
5 355.764	1.10E-23	7 098.069 80	1 742.305 50	0 2 1	0 1 0	3	2	2	2	2	1	5.5
4 968.471	1.20E-26	7 098.069 90	2 129.599 10	0 2 1	0 1 0	3	2	2	4	4	1	5.5
6 963.168	6.60E-22	7 098.069 90	134.901 60	0 2 1	0 0 0	3	2	2	2	2	1	5.5
5 278.735	1.10E-23	7 098.069 90	1 819.335 10	0 2 1	0 1 0	3	2	2	3	2	1	5.5
6 609.962	4.40E-24	7 098.069 90	488.107 70	0 2 1	0 0 0	3	2	2	4	4	1	5.5
5 366.173	1.10E-24	7 098.069 90	1 731.896 70	0 2 1	0 1 0	3	2	2	3	0	3	5.5
6 797.708	5.40E-22	7 098.070 00	300.362 30	0 2 1	0 0 0	3	2	2	4	2	3	5.5
6 885.914	5.70E-22	7 098.070 00	212.156 40	0 2 1	0 0 0	3	2	2	3	2	1	5.5
6 961.308	5.50E-23	7 098.070 00	136.761 70	0 2 1	0 0 0	3	2	2	3	0	3	5.5
5 190.054	9.80E-24	7 098.070 00	1 908.016 40	0 2 1	0 1 0	3	2	2	4	2	3	5.5
3 721.650	1.21E-26	6 705.045 90	2 983.396 20	1 0 0	0 0 0	14	6	8	14	5	9	5.4
4 118.516	1.20E-25	6 705.046 00	2 586.529 80	1 0 0	0 0 0	14	6	8	13	5	9	5.4
3 435.507	1.03E-26	6 705.046 20	3 269.539 60	1 0 0	0 0 0	14	6	8	15	5	11	5.4
3 344.993	2.37E-25	6 705.593 50	3 360.600 30	1 0 0	0 0 0	14	5	9	15	5	10	5.4
4 290.870	1.88E-25	6 705.593 60	2 414.723 40	1 0 0	0 0 0	14	5	9	13	3	10	5.4
4 076.259	2.29E-24	6 705.593 60	2 629.334 50	1 0 0	0 0 0	14	5	9	13	5	8	5.4
3 787.349	1.53E-25	6 705.593 70	2 918.245 10	1 0 0	0 0 0	14	5	9	14	5	10	5.4
8 665.869	5.20E-25	9 423.649 00	757.780 00	2 1 0	0 0 0	6	3	3	6	4	2	4.5
9 099.022	7.80E-26	9 424.369 60	325.348 00	1 1 1	0 0 0	5	4	2	5	0	5	4.5
7 294.771	7.20E-25	9 424.369 80	2 129.599 10	1 1 1	0 1 0	5	4	2	4	4	1	4.5
8 814.029	1.90E-22	9 424.369 90	610.341 00	1 1 1	0 0 0	5	4	2	5	4	1	4.5
7 172.507	8.80E-25	9 424.369 90	2 251.862 50	1 1 1	0 1 0	5	4	2	5	4	1	4.5
9 124.008	4.60E-24	9 424.370 20	300.362 00	1 1 1	0 0 0	5	4	2	4	2	3	4.5
8 936.263	1.00E-22	9 424.370 50	488.108 00	1 1 1	0 0 0	5	4	2	4	4	1	4.5
8 667.646	5.20E-23	9 424.370 60	756.725 00	1 1 1	0 0 0	5	4	2	6	4	3	4.5
8 977.860	1.80E-24	9 424.371 10	446.511 00	1 1 1	0 0 0	5	4	2	5	2	3	4.5
8 871.489	8.10E-26	9 424.400 60	552.912 00	1 1 1	0 0 0	5	4	2	6	2	5	4.5
3 815.941	7.71E-25	5 633.391 61	1 817.451 00	0 1 1	0 1 0	2	3	2	4	0	4	4.4
3 609.239	6.01E-24	5 633.391 67	2 024.152 60	0 1 1	0 1 0	2	3	2	5	2	4	4.4
5 217.183	1.43E-21	5 633.391 68	416.208 70	0 1 1	0 0 0	2	3	2	5	2	4	4.4
5 317.612	6.66E-22	5 633.391 68	315.779 50	0 1 1	0 0 0	2	3	2	4	2	2	4.4
5 023.277	3.49E-23	5 633.391 69	610.114 40	0 1 1	0 0 0	2	3	2	5	4	2	4.4
5 427.090	3.12E-21	5 633.391 69	206.301 40	0 1 1	0 0 0	2	3	2	3	2	2	4.4

continued..

..continued

3 710.491	2.77E-24	5 633.391 73	1922.901 10	0 1 1	0 1 0	2	3	2	4	2	2	4.4
3 381.696	2.94E-25	5 633.391 73	2 251.695 30	0 1 1	0 1 0	2	3	2	5	4	2	4.4
5 145.258	1.26E-23	5 633.391 75	488.134 20	0 1 1	0 0 0	2	3	2	4	4	0	4.4
3 819.604	1.17E-23	5 633.391 75	1 813.787 60	0 1 1	0 1 0	2	3	2	3	2	2	4.4
5 411.339	2.46E-22	5 633.391 76	222.052 80	0 1 1	0 0 0	2	3	2	4	0	4	4.4
3 503.773	7.95E-26	5 633.391 80	2 129.618 70	0 1 1	0 1 0	2	3	2	4	4	0	4.4
3 472.835	1.17E-24	5 634.120 97	2 161.285 90	1 1 0	0 1 0	1	4	1	6	2	5	4.4
3 713.355	3.89E-25	5 634.121 07	1 920.766 50	1 1 0	0 1 0	1	4	1	5	0	5	4.4
5 308.773	5.69E-23	5 634.121 08	325.347 90	1 1 0	0 0 0	1	4	1	5	0	5	4.4
5 146.013	2.61E-26	5 634.121 09	488.107 70	1 1 0	0 0 0	1	4	1	4	4	1	4.4
5 333.759	1.06E-22	5 634.121 10	300.362 30	1 1 0	0 0 0	1	4	1	4	2	3	4.4
5 081.210	4.88E-23	5 634.121 10	552.911 40	1 1 0	0 0 0	1	4	1	6	2	5	4.4
4 877.396	9.56E-25	5 634.121 10	756.724 80	1 1 0	0 0 0	1	4	1	6	4	3	4.4
5 187.610	1.73E-22	5 634.121 11	446.510 70	1 1 0	0 0 0	1	4	1	5	2	3	4.4
5 023.780	4.28E-25	5 634.121 12	610.341 20	1 1 0	0 0 0	1	4	1	5	4	1	4.4
3 726.105	1.82E-25	5 634.121 18	1 908.016 40	1 1 0	0 1 0	1	4	1	4	2	3	4.4
3 235.740	7.71E-27	5 634.121 22	2 398.381 60	1 1 0	0 1 0	1	4	1	6	4	3	4.4
3 580.152	9.88E-25	5 634.121 22	2 053.968 80	1 1 0	0 1 0	1	4	1	5	2	3	4.4
5 575.246	6.90E-26	6 655.631 30	1 080.385 40	0 3 0	0 0 0	10	5	5	9	2	8	4.3
5 130.495	6.30E-27	6 655.631 30	1 525.136 00	0 3 0	0 0 0	10	5	5	11	2	10	4.3
5 118.246	3.30E-26	6 656.395 20	1 538.149 50	0 3 0	0 0 0	9	6	4	10	3	7	4.3
5 181.414	3.00E-26	6 656.395 20	1 474.980 80	0 3 0	0 0 0	9	6	4	9	5	5	4.3
5 606.238	2.70E-25	6 656.395 20	1 050.157 70	0 3 0	0 0 0	9	6	4	8	3	5	4.3
5 440.164	2.40E-26	6 656.395 20	1 216.231 30	0 3 0	0 0 0	9	6	4	9	3	7	4.3
8 617.477	9.80E-25	8 902.696 10	285.219 00	2 1 0	0 0 0	2	2	0	3	3	1	4.1
7 209.047	1.60E-25	8 902.697 20	1 693.649 90	2 1 0	0 1 0	2	2	0	2	1	1	4.1
6 995.246	9.90E-26	8 902.697 20	1 907.451 40	2 1 0	0 1 0	2	2	0	3	3	1	4.1
8 760.420	4.60E-24	8 902.699 10	142.279 00	2 1 0	0 0 0	2	2	0	3	1	3	4.1
8 807.523	5.00E-24	8 902.699 20	95.176 00	2 1 0	0 0 0	2	2	0	2	1	1	4.1
8 865.566	1.70E-25	8 902.703 30	37.137 00	2 1 0	0 0 0	2	2	0	1	1	1	4.1
8 618.059	2.90E-24	8 903.477 70	285.419 00	1 1 1	0 0 0	2	1	1	3	3	0	4.1
6 995.881	1.00E-25	8 903.496 40	1 907.615 70	1 1 1	0 1 0	2	1	1	3	3	0	4.1
7 226.435	2.20E-24	8 903.496 40	1 677.061 40	1 1 1	0 1 0	2	1	1	2	1	2	4.1
7 262.991	1.70E-24	8 903.496 50	1 640.505 90	1 1 1	0 1 0	2	1	1	1	1	0	4.1
7 131.083	3.70E-24	8 903.496 50	1 772.413 50	1 1 1	0 1 0	2	1	1	3	1	2	4.1
8 730.132	4.50E-22	8 903.496 80	173.365 00	1 1 1	0 0 0	2	1	1	3	1	2	4.1
8 824.001	2.40E-22	8 903.496 90	79.496 00	1 1 1	0 0 0	2	1	1	2	1	2	4.1
8 861.126	3.80E-22	8 903.497 90	42.372 00	1 1 1	0 0 0	2	1	1	1	1	0	4.1
3 087.709	8.47E-26	3 976.308 00	888.598 70	1 0 0	0 0 0	5	0	5	6	5	2	3.4
3 576.851	2.26E-21	3 976.308 10	399.457 50	1 0 0	0 0 0	5	0	5	5	1	4	3.4
1 704.596	1.51E-26	3 976.308 10	2 271.712 20	1 0 0	0 0 1	5	0	5	6	3	4	3.4
1 975.445	7.10E-25	3 976.308 10	2 000.863 00	1 0 0	0 0 1	5	0	5	5	1	4	3.4
2 154.711	3.43E-24	3 976.308 10	1 821.596 80	1 0 0	0 0 1	5	0	5	4	1	4	3.4
1 933.555	1.49E-24	3 976.308 10	2 042.753 30	1 0 0	0 0 1	5	0	5	6	1	6	3.4
3 327.329	1.58E-22	3 976.308 10	648.978 70	1 0 0	0 0 0	5	0	5	6	3	4	3.4
3 234.232	1.39E-26	3 976.308 10	742.076 30	1 0 0	0 0 0	5	0	5	5	5	0	3.4
3 593.791	5.33E-24	3 976.308 10	382.516 90	1 0 0	0 0 0	5	0	5	4	3	2	3.4
3 751.470	3.28E-21	3 976.308 10	224.838 40	1 0 0	0 0 0	5	0	5	4	1	4	3.4
1 971.492	8.67E-27	3 976.308 10	2 004.815 70	1 0 0	0 0 1	5	0	5	4	3	2	3.4

continued..

..continued

3 529.056	7.22E-21	3 976.308 10	447.252 40	1 0 0	0 0 0	5	0	5	6	1	6	3.4
3 467.496	5.85E-23	3 976.308 10	508.812 10	1 0 0	0 0 0	5	0	5	5	3	2	3.4
1 845.814	2.68E-26	3 976.308 20	2 130.494 40	1 0 0	0 0 1	5	0	5	5	3	2	3.4
2 237.778	3.17E-24	3 977.261 40	1 739.483 60	0 0 1	0 0 1	4	1	4	3	1	3	3.4
3 692.042	1.57E-23	3 977.261 40	285.219 30	0 0 1	0 0 0	4	1	4	3	3	1	3.4
2 054.432	1.06E-24	3 977.261 40	1 922.829 00	0 0 1	0 0 1	4	1	4	5	1	5	3.4
3 701.764	7.87E-21	3 977.261 40	275.497 00	0 0 1	0 0 0	4	1	4	4	1	3	3.4
3 235.188	3.41E-26	3 977.261 40	742.073 00	0 0 1	0 0 0	4	1	4	5	5	1	3.4
3 593.419	7.18E-23	3 977.261 40	383.842 50	0 0 1	0 0 0	4	1	4	4	3	1	3.4
1 971.344	2.60E-26	3 977.261 50	2 005.917 00	0 0 1	0 0 1	4	1	4	4	3	1	3.4
3 473.293	6.37E-23	3 977.261 50	503.968 10	0 0 1	0 0 0	4	1	4	5	3	3	3.4
3 834.983	7.42E-20	3 977.261 50	142.278 50	0 0 1	0 0 0	4	1	4	3	1	3	3.4
2 069.810	4.96E-27	3 977.261 50	1 907.451 40	0 0 1	0 0 1	4	1	4	3	3	1	3.4
1 850.854	1.05E-26	3 977.261 50	2 126.407 70	0 0 1	0 0 1	4	1	4	5	3	3	3.4
3 650.636	5.04E-20	3 977.261 50	326.625 50	0 0 1	0 0 0	4	1	4	5	1	5	3.4
2 101.792	5.41E-26	3 977.261 50	1 875.469 70	0 0 1	0 0 1	4	1	4	4	1	3	3.4

H₂¹⁸O

421.225	3.47E-26	3 502.425 88	3 081.200 90	0 1 0	0 1 0	9	7	2	8	6	3	18.7
1 302.202	1.68E-25	3 502.607 33	2 200.405 00	0 1 0	0 0 0	8	8	1	9	9	0	18.7
9 079.500	6.48E-27	9 961.417 00	881.917 00	0 1 2	0 0 0	8	3	6	8	2	7	15.1
8 528.610	3.50E-27	9 961.642 00	1 433.032 00	1 1 1	0 0 0	9	2	7	10	2	8	15.0
9 010.480	2.14E-26	9 455.641 00	445.161 00	0 1 2	0 0 0	5	3	2	5	2	3	14.5
8 722.190	3.18E-27	9 455.874 00	733.684 00	0 1 2	0 0 0	4	4	1	5	5	0	14.5
6 681.128	2.42E-26	6 979.747 79	298.620 10	1 2 0	0 0 0	4	1	4	4	2	3	9.1
6 665.659	1.40E-26	6 980.118 64	314.459 40	0 2 1	0 0 0	3	0	3	4	2	2	9.1
7 198.388	2.53E-26	7 681.031 96	482.643 50	0 0 2	0 0 0	3	3	0	4	4	1	5.4
7 198.989	4.24E-24	7 681.661 20	482.672 50	1 0 1	0 0 0	4	4	1	4	4	0	5.4
7 340.100	7.10E-24	7 614.903 06	274.803 20	1 0 1	0 0 0	5	1	4	4	1	3	4.1
7 236.431	4.12E-26	7 615.722 22	379.291 50	2 0 0	0 0 0	5	2	3	4	3	2	4.1
5 122.198	4.12E-27	6 002.312 46	880.114 50	1 1 0	0 0 0	6	4	2	6	5	1	3.9
5 398.647	2.26E-26	6 003.191 29	604.544 10	1 1 0	0 0 0	5	5	1	5	4	2	3.9
5 556.819	9.92E-27	6 369.580 78	812.761 60	1 1 0	0 0 0	8	4	4	7	3	5	3.7
5 295.746	5.93E-27	6 370.509 15	1 074.762 90	0 1 1	0 0 0	8	3	5	9	1	8	3.6

H₂¹⁷O

3 894.588	2.65E-26	4 479.529 13	584.940 90	1 0 0	0 0 0	7	3	4	7	0	7	10.8
4 064.714	1.04E-25	4 479.841 64	415.128 00	0 0 1	0 0 0	6	4	3	5	2	4	10.8
7 482.508	7.75E-27	7 693.943 56	211.435 80	1 0 1	0 0 0	4	4	0	3	2	1	8.9
7 558.894	9.80E-27	7 694.325 10	135.431 20	0 0 2	0 0 0	3	3	1	2	2	0	8.9

HDO

1 450.335	3.53E-24	2 066.304 04	615.968 80	0 1 0	0 0 0	5	5	1	5	5	0	43 560.0
1 193.514	1.91E-24	2 066.304 05	872.790 50	0 1 0	0 0 0	5	5	0	6	6	1	43 560.0
7 413.940	2.20E-25	7 816.271 22	402.331 00	0 0 2	0 0 0	5	5	1	4	4	0	21 780.0
7 200.302	3.51E-25	7 816.271 24	615.968 80	0 0 2	0 0 0	5	5	0	5	5	1	21 780.0
1 724.804	9.16E-25	2 340.772 71	615.968 80	0 1 0	0 0 0	6	6	1	5	5	0	14 520.0
1 724.804	9.16E-25	2 340.772 74	615.968 80	0 1 0	0 0 0	6	6	0	5	5	1	14 520.0
3 817.772	2.01E-25	4 298.014 70	480.242 70	0 0 1	0 0 0	5	5	1	5	4	2	5 445.0

continued..

..continued

3 425.224	4.40E-25	4 298.014 78	872.790 50	0 0 1	0 0 0	5	5	0	6	6	1	5 445.0
7 178.195	6.29E-26	8 159.323 07	981.128 00	0 0 2	0 0 0	7	6	1	7	6	2	4 356.0
1 178.673	1.11E-24	2 159.801 18	981.128 10	0 1 0	0 0 0	6	5	2	7	6	1	4 356.0
298.741	5.75E-23	1 171.531 72	872.790 30	0 0 0	0 0 0	7	7	0	6	6	1	2 178.0
1 193.514	1.91E-24	2 066.304 01	872.790 50	0 1 0	0 0 0	5	5	1	6	6	0	2 178.0
2 853.467	3.45E-27	3 333.709 93	480.242 70	1 0 0	0 0 0	5	5	1	5	4	2	1 210.0
2 624.542	3.28E-25	3 333.710 29	709.167 80	1 0 0	0 0 0	5	5	0	6	5	1	1 210.0
2 809.152	3.20E-25	3 425.121 23	615.968 80	1 0 0	0 0 0	6	5	2	5	5	1	1 037.1
2 715.955	1.10E-24	3 425.121 65	709.166 60	1 0 0	0 0 0	6	5	1	6	5	2	1 037.1
1 178.673	1.11E-24	2 159.801 18	981.128 10	0 1 0	0 0 0	6	5	2	7	6	1	435.6
1 450.636	1.89E-24	2 159.802 18	709.166 60	0 1 0	0 0 0	6	5	1	6	5	2	435.6
7 450.156	5.33E-26	8 159.323 06	709.166 60	0 0 2	0 0 0	7	6	1	6	5	2	435.6
108.846	1.91E-24	818.013 44	709.167 60	0 0 0	0 0 0	7	5	2	6	5	1	435.6
7 295.282	9.96E-26	7 697.611 16	402.329 20	0 0 2	0 0 0	5	4	2	4	4	1	272.3
77.928	2.44E-24	480.258 70	402.330 80	0 0 0	0 0 0	5	4	1	4	4	0	272.3
1 356.774	1.61E-24	1 837.016 35	480.242 70	0 1 0	0 0 0	4	4	1	5	4	2	262.4
1 603.994	6.70E-24	1 837.018 01	233.023 70	0 1 0	0 0 0	4	4	0	3	3	1	262.4
3 409.696	2.70E-25	4 390.823 97	981.128 10	0 0 1	0 0 0	6	5	2	7	6	1	250.3
3 681.659	1.63E-24	4 390.825 71	709.166 60	0 0 1	0 0 0	6	5	1	6	5	2	250.3
3 613.105	1.27E-24	4 093.347 28	480.242 70	0 0 1	0 0 0	4	4	1	5	4	2	183.0
3 860.326	1.88E-24	4 093.349 66	233.023 70	0 0 1	0 0 0	4	4	0	3	3	1	183.0
2 713.863	5.57E-25	3 531.876 35	818.013 70	1 0 0	0 0 0	7	5	3	7	5	2	73.3
2 822.714	3.62E-25	3 531.882 29	709.167 80	1 0 0	0 0 0	7	5	2	6	5	1	73.3
4 328.580	3.81E-27	5 728.040 36	1 399.460 70	1 1 0	0 0 0	11	6	5	10	6	4	46.8
357.911	5.38E-24	1 757.381 01	1 399.470 00	0 0 0	0 0 0	11	7	4	10	6	5	46.8
7 494.719	4.16E-27	8 739.158 60	1 244.439 90	0 0 2	0 0 0	10	7	4	9	6	3	43.1
343.321	1.08E-23	1 587.771 01	1 244.450 00	0 0 0	0 0 0	10	7	3	9	6	4	43.1
240.550	1.54E-25	1 889.497 18	1 648.947 50	0 0 0	0 0 0	9	9	0	9	8	1	21.2
393.181	2.38E-24	2 042.149 00	1 648.968 00	0 0 0	0 0 0	10	9	1	9	8	2	21.2
3 416.291	1.42E-25	4 499.076 60	1 082.785 20	0 0 1	0 0 0	8	4	4	9	5	5	19.5
3 556.700	3.63E-25	4 499.232 13	942.532 40	0 0 1	0 0 0	7	5	3	8	5	4	19.5
5 295.841	1.39E-25	5 591.328 63	295.487 30	2 0 0	0 0 0	3	3	1	4	3	2	18.2
5 358.329	5.24E-25	5 591.352 58	233.023 70	2 0 0	0 0 0	3	3	0	3	3	1	18.2
1 311.120	3.47E-25	2 393.904 73	1 082.785 20	0 1 0	0 0 0	8	5	4	9	5	5	16.6
1 451.399	4.56E-25	2 393.930 93	942.532 40	0 1 0	0 0 0	8	5	3	8	5	4	16.6
7 387.333	1.97E-25	7 620.356 35	233.023 70	0 0 2	0 0 0	4	4	0	3	3	1	15.8
62.626	3.62E-24	295.677 42	233.051 20	0 0 0	0 0 0	4	3	1	3	3	0	15.8
4 026.422	2.95E-27	5 614.162 23	1 587.740 50	0 0 1	0 0 0	11	8	4	10	7	3	14.8
383.325	2.72E-24	1 971.095 01	1 587.770 00	0 0 0	0 0 0	11	8	3	10	7	4	14.8
3 635.652	3.09E-24	3 931.139 49	295.487 30	0 0 1	0 0 0	3	3	1	4	3	2	12.9
3 822.247	2.90E-24	3 931.173 28	108.926 20	0 0 1	0 0 0	3	3	0	2	2	1	12.9
3 656.686	1.03E-26	5 414.027 66	1 757.342 00	0 0 1	0 0 0	11	7	5	11	7	4	11.5
397.705	1.26E-24	2 155.084 99	1 757.380 00	0 0 0	0 0 0	12	8	4	11	7	5	11.5
3 540.506	2.38E-25	4 623.290 86	1 082.785 20	0 0 1	0 0 0	8	5	4	9	5	5	10.0
3 680.802	4.01E-25	4 623.334 46	942.532 40	0 0 1	0 0 0	8	5	3	8	5	4	10.0
1 528.120	5.97E-27	3 570.225 33	2 042.105 20	0 1 0	0 0 0	10	9	2	10	9	1	9.9
430.892	4.44E-25	2 473.041 00	2 042.149 00	0 0 0	0 0 0	11	10	1	10	9	2	9.9
3 811.827	6.46E-27	5 614.162 17	1 802.335 30	0 0 1	0 0 0	11	8	4	10	8	3	8.9
407.631	1.18E-24	2 210.015 01	1 802.384 00	0 0 0	0 0 0	11	9	3	10	8	2	8.9

continued..

..continued

1 692.771	2.29E-27	3 663.801 44	1 971.030 30	0 1 0	0 0 0	12	8	5	11	8	4	6.7
421.924	5.43E-25	2 393.019 01	1 971.095 00	0 0 0	0 0 0	12	9	4	11	8	3	6.7
7 402.153	1.39E-25	7 697.640 60	295.487 30	0 0 2	0 0 0	5	4	1	4	3	2	2.3
78.732	7.43E-24	374.409 87	295.677 40	0 0 0	0 0 0	5	3	2	4	3	1	2.3
2 799.433	5.49E-26	2 831.929 58	32.496 40	1 0 0	0 0 0	2	2	1	1	1	0	1.3
2 723.334	8.55E-24	2 832.259 72	108.926 20	1 0 0	0 0 0	2	2	0	2	2	1	1.3
4 245.604	1.82E-26	4 278.100 68	32.496 40	0 3 0	0 0 0	2	2	1	1	1	0	1.3
4 169.506	3.56E-25	4 278.432 60	108.926 20	0 3 0	0 0 0	2	2	0	2	2	1	1.3
4 192.277	3.02E-26	4 224.773 60	32.496 40	1 1 0	0 0 0	2	2	1	1	1	0	1.3
4 116.191	8.19E-25	4 225.117 54	108.926 20	1 1 0	0 0 0	2	2	0	2	2	1	1.3
1 488.194	1.21E-23	1 520.690 11	32.496 40	0 1 0	0 0 0	2	2	1	1	1	0	1.2
1 412.116	1.44E-23	1 521.042 20	108.926 20	0 1 0	0 0 0	2	2	0	2	2	1	1.2
3 779.677	3.06E-24	3 812.173 26	32.496 40	0 0 1	0 0 0	2	2	1	1	1	0	1.1
3 703.632	1.40E-23	3 812.557 70	108.926 20	0 0 1	0 0 0	2	2	0	2	2	1	1.1
7 318.608	2.72E-25	7 351.104 65	32.496 40	0 0 2	0 0 0	2	2	1	1	1	0	1.0
7 242.610	7.58E-25	7 351.536 46	108.926 20	0 0 2	0 0 0	2	2	0	2	2	1	1.0

List of Figures

1.1	Fundamental vibration and rotation of H_2O	4
1.2	Pressure dependence of absorption line width	7
1.3	Allan variance	14
1.4	Multiple pass absorption cell for signal enhancement	16
1.5	Theory of wavelength modulation spectroscopy	19
1.6	Principle of lock-in amplifier	23
1.7	Fundamentals of atmospheric transport processes	27
1.8	The CARIBIC passenger aircraft	30
1.9	The new HALO aircraft	32
2.1	Optics of H_2O isotopic ratio spectrometer	39
2.2	Overview of H_2O absorption lines	41
2.3	Laser characteristics	46
2.4	Detector characteristics	47
2.5	H_2O calibration source	49
2.6	Gas flow system	50
2.7	Schematic of data acquisition	52
2.8	Second-derivative spectrum of water isotopologues	53
2.9	Noise measurements of detection system	60
2.10	Signal-to-noise ratio of detection system	62
2.11	Allan plot of H_2O isotopic ratio measurements	64
2.12	Switching between two isotopic standards	70
2.13	Photograph of the isotopic ratio spectrometer	72
2.14	H_2O transmission spectrum near 3765 cm^{-1}	74
3.1	Molecular structure of formaldehyde	78
3.2	Overview of CH_2O absorption lines	80
3.3	Ray tracing of Stark multipass cell	83
3.4	Ray transfer matrix	84
3.5	Multipass cell for Stark modulation	87
3.6	Stark modulation spectrometer setup	89
3.7	Data processing of Stark modulation experiments	90
3.8	Electric breakdown within Stark cell	92
3.9	Schematic of alternate measurements	93
3.10	Second derivative spectra of CH_2O	94

3.11	Schematic of interleaved measurements	95
3.12	Allan plot of 2f- and alternate measurements	97
3.13	Comparison of 2f and alternate measurements	99
3.14	Allan plot of interleaved measurement	100
3.15	Detector characteristics	102
A.1	Second derivative spectra at wavelength modulation	111
A.2	Second derivative etalon spectra at wavelength modulation	113

List of Tables

1.1	H ₂ O isotopic reference materials	26
2.1	H ₂ O absorption line parameters for isotopic ratio measurements	44
2.2	Comparison of detection limit	65
2.3	Instrument specifications of the isotopic ratio spectrometer.	72
3.1	CH ₂ O absorption line parameters	79
3.2	Results of misalignment analysis	86
B.1	Stark coefficients of H ₂ O absorption lines	114

Bibliography

- Allan, D. W. (1966), Statistics of atomic frequency standards, *Proc. IEEE*, **54**, 222–230.
- Arndt, R. (1965), Analytical line shapes for lorentzian signals broadened by modulation, *J. Appl. Phys.*, **36**, 2522–2524.
- Barkan, E., and B. Luz (2005), High precision measurements of $^{17}\text{O}/^{16}\text{O}$ and $^{18}\text{O}/^{16}\text{O}$ ratios in H_2O , *Rapid Commun. Mass Spectrom.*, **19**, 3737–3742.
- Bellini, M., E. Catacchini, P. D. Natale, G. D. Lonardo, L. Fusina, M. Inguscio, and E. Venuti (1996), Stark and frequency measurements in the FIR spectrum of H_2O_2 , *J. Mol. Spectrosc.*, **177**, 115–123.
- Bomse, D. S., and D. J. Kane (2006), An adaptive singular value decomposition (SVD) algorithm for analysis of wavelength modulation spectra, *Appl. Phys. B*, **85**, 461–466.
- Bomse, D. S., A. C. Stanton, and J. A. Silver (1992), Frequency modulation and wavelength modulation spectroscopies: comparison of experimental methods using a lead-salt diode laser, *Appl. Opt.*, **31**, 718–731.
- Brenninkmeijer, C. A. M., C. Janssen, J. Kaiser, T. Röckmann, T. S. Rhee, and S. S. Assonov (2003), Isotope effects in the chemistry of atmospheric trace compounds, *Chem. Rev.*, **103**, 5125–5161.
- Brenninkmeijer, C. A. M., P. Crutzen, F. Boumard, T. Dauer, B. Dix, R. Ebinghaus, D. Filippi, H. Fischer, H. Franke, U. Frieß, J. Heintzenberg, F. Helleis, M. Hermann, H. H. Kock, C. Koeppel, J. Lelieveld, M. Leuenberger, B. G. Martinsson, S. Miemczyk, H. P. Moret, H. N. Nguyen, P. Nyfeler, D. Ora, D. O’Sullivan, S. Penkett, U. Platt, M. Pupek, M. Ramonet, B. Randa, M. Reichelt, T. S. Rhee, J. Rohwer, K. Rosenfeld, D. Scharffe, H. Schlager, U. Schumann, F. Slemr, D. Sprung, P. Stock, R. Thaler, F. Valentino, P. van Velthoven, A. Waibel, A. Wandel, K. Waschitschek, A. Wiedensohler, I. Xueref-Remy, A. Zahn, U. Zech, and H. Ziereis (2007), Civil Aircraft for the regular investigation of the atmosphere based on an instrumented container: The new CARIBIC system, *Atmos. Chem. Phys.*, **7**, 4953–4976.
- Budde, W. (1983), Physical Detectors of Optical Radiation, in *Optical Radiation Measurements*, vol. 4, edited by F. Grum and C. J. Bartleson, Academic Press, Inc., New York, NY, USA.
- Callegari, A. (2004), personal communication.

- Carlisle, C. B., and D. E. Cooper (1990), Tunable diode laser frequency modulation spectroscopy through an optical fiber: High-sensitivity detection of water vapor, *Appl. Phys. Lett.*, **56**, 805–807.
- Craig, H. (1961), Isotopic variations in meteoric waters, *Science*, **133**, 1702–1703.
- Demtröder, W. (1992), Electronic Photoabsorption Laser Spectroscopy, in *Applied Laser Spectroscopy: Techniques, Instrumentation, and Applications*, edited by D. L. Andrews, VCH Publishers, Inc., New York, NY, USA.
- Demtröder, W. (1996), *Laser Spectroscopy: Basic Concepts and Instrumentation*, Springer Verlag, Berlin, Germany.
- Dereniak, E. L., and G. D. Boreman (1996), *Infrared Detectors and Systems*, John Wiley & Sons, Inc., New York, NY, USA.
- Dinelli, B. M., B. Carli, and M. Carlotti (1991), Measurement of stratospheric distributions of H_2^{16}O , H_2^{18}O , H_2^{17}O , and HD^{16}O from far infrared spectra, *J. Geophys. Res.*, **96**, 509–7514.
- Durry, G., T. Danguy, and I. Pouchet (2002), Open multipass absorption cell for in situ monitoring of stratospheric trace gas with telecommunication laser diodes, *Appl. Opt.*, **41**, 424–433.
- Dyroff, C. (2003), Performance assessment and design improvement of a Herriott-type multipass absorption cell for highly sensitive trace-gas measurements, Diploma thesis, University of Applied Sciences Oldenburg / Ostfriesland / Wilhelmshaven, Emden, Germany.
- Dyroff, C., A. Fried, D. Richter, J. G. Walega, M. S. Zahnizer, and B. McManus (2004), Design and performance assessment of a stable astigmatic Herriott cell for trace gas measurements on airborne platforms, in *Laser Applications to Chemical and Environmental Analysis (LACEA)*, Annapolis, MD, USA.
- Feit, Z., R. Woods, D. Kostyk, and W. Jalenak (1989), Low-threshold PbEuSeTe double-heterostructure lasers grown by molecular beam epitaxy, *Appl. Phys. Lett.*, **55**(1), 16–18.
- Finlayson-Pitts, B. J., and J. N. Pitts, Jr. (2000), *Chemistry of the Upper and Lower Atmosphere: Theory, Experiments, and Applications*, Academic Press, San Diego, CA, USA.
- Franz, P., and T. Röckmann (2005), High-precision isotope measurements of H_2^{16}O , H_2^{17}O , H_2^{18}O , and the $\Delta^{17}\text{O}$ -anomaly of water vapor in the southern lowermost stratosphere, *Atmos. Chem. Phys.*, **5**, 2949–2959.
- Fried, A., B. Henry, and J. R. Drummond (1993), Tunable diode laser ratio measurements of atmospheric constituents by employing dual fitting analysis and jump scanning, *Appl. Opt.*, **32**, 821–827.
- Fried, A., B. P. Wert, B. Henry, and J. R. Drummond (1999), Airborne tunable diode laser measurements of formaldehyde, *Spectrochim. Acta, Part A*, **55**, 2097–2110.

- Fried, A., J. Crawford, J. Olson, J. Walega, W. Potter, B. Wert, C. Jordan, B. Anderson, R. Shetter, B. Lefer, D. Blake, N. Blake, S. Meinardi, B. Heikes, D. O'Sullivan, J. Snow, H. Fuelberg, C. M. Kiley, S. Sandholm, D. Tan, G. Sachse, H. Singh, I. Faloona, C. N. Harward, and G. R. Carmichael (2003), Airborne tunable diode laser measurements of formaldehyde during TRACE-P: Distributions and box model comparisons, *J. Geophys. Res., D 20*, 8798–8820.
- Fukuda, M., S. Ooyama, A. Utsumi, Y. Kondo, T. Kurosaki, and T. Masuda (2008), Effect of optical feedback noise on tunable diode laser spectroscopy, *Appl. Phys. B*, *90*, 269–272.
- Gao, R. S., P. J. Popp, D. W. Fahey, T. P. Marcy, R. L. Herman, E. M. Weinstock, D. G. Baumgardner, T. J. Garrett, K. H. Rosenlof, T. L. Thompson, P. T. Bui, B. A. Ridley, S. C. Wofsy, O. B. Toon, M. A. Tolbert, B. Kärcher, T. Peter, P. K. Hudson, A. J. Weinheimer, and A. J. Heymsfield (2004), Evidence that nitric acid increases relative humidity in low-temperature cirrus clouds, *Science*, *303*, 516–520.
- Gerbig, C., S. Schmitgen, D. Kley, A. Volz-Thomas, K. Dewey, and D. Haaks (1999), An improved fast-response vacuum-UV resonance fluorescence CO instrument, *J. Geophys. Res.*, *104*, 1699–1704.
- Gerrard, A., and J. M. Burch (1994), *Introduction to matrix methods in optics*, Dover Publications, Inc., New York, NY, USA.
- Gianfrani, L., G. Gagliardi, M. van Burgel, and E. R. T. Kerstel (2003), Isotope analysis of water by means of near-infrared dual-wavelength diode laser spectroscopy, *Opt. Express*, *11*, 1566–1576.
- Goldstein, N., S. Adler-Golden, J. Lee, and F. Bien (1992), Measurement of molecular concentrations and line parameters using line-locked second harmonic spectroscopy with an AlGaAs diode laser, *Appl. Opt.*, *31*, 3409–3415.
- Golub, G. H., and C. F. Van Loan (1996), *Matrix computations*, 3 ed., Johns Hopkins Univ Press, Baltimore, MD, USA.
- Gonfiantini, R. (1978), Standards for stable isotope measurements in natural compounds, *Nature*, *271*, 534–536.
- Grau, G. (1969), Rauschen und Kohärenz im optischen Spektralbereich, in *Laser*, edited by W. Kleen and R. Müller, Springer Verlag, Berlin, Germany.
- Grau, G., and W. Freude (1991), *Optische Nachrichtentechnik: Eine Einführung*, 3 ed., Springer Verlag, Berlin, Germany.
- Graybeal, J. D. (1988), *Molecular Spectroscopy*, McGraw-Hill Book Company, New York, NY, USA.
- Güsten, H., G. Heinrich, E. Mönnich, M. Nolle, and J. Weppner (2002), Two automated ozone analyzers for use on civil aircraft operating in the tropopause region, *J. Atmos. Oceanic Technol.*, *20*, 292–300.

- Hager, Jr., R. N., and R. C. Anderson (1970), Theory of the derivative spectrometer, *J. Opt. Soc. Am.*, **60**, 1444–1449.
- Hak, C., I. Pundt, S. Trick, C. Kern, U. Platt, J. Dommen, C. Ordóñez, A. S. H. Prévôt, W. Junkermann, C. Astorga-Lloréns, B. R. Larsen, J. Mellqvist, A. Strandberg, Y. Yu, B. Galle, J. Kleffmann, J. C. Lörzer, G. O. Braathen, and R. Volkamer (2005), Intercomparison of four different in-situ techniques for ambient formaldehyde measurements in urban air, *Atmos. Chem. Phys.*, **5**(11), 2881–2900.
- Hanisco, T. F., E. J. Moyer, E. M. Weinstock, J. M. S. Clair, D. S. Sayres, J. B. Smith, R. Lockwood, J. G. Anderson, A. E. Dessler, F. N. Keutsch, J. R. Spackman, W. G. Read, , and T. P. Bui (2007), Observations of deep convective influence on stratospheric water vapor and its isotopic composition, *Geophys. Res. Lett.*, **34**, 4814–4818.
- Hanson, R. K. (2002), *Introduction to spectroscopic diagnosis for gases*, Lecture Notes, Department of Mechanical Engineering, Stanford University, Mountain View, CA, USA.
- Harris, G. W., G. I. MacKay, T. Iguchi, L. K. Mayne, and H. I. Schiff (1989), Measurements of formaldehyde in the troposphere by tunable diode laser absorption spectroscopy, *J. Atmos. Chem.*, **8**, 119–137.
- Hase, F. (2004), personal communication.
- Häckel, H. (2005), *Meteorologie*, Verlag Eugen Ulmer, Stuttgart, Germany.
- Herbin, H., D. Hurtmans, S. Turquety, C. Wespes, B. Barret, J. Hadji-Lazaro, C. Clerbaux, and P.-F. Coheur (2007), Global distributions of water vapour isotopologues retrieved from IMG/ADEOS data, *Atmos. Chem. Phys.*, **7**, 3957–3968.
- Herndon, S. C., J. Shorter, M. Zahniser, J. Wormhoudt, D. D. Nelson, K. L. Demerjian, and C. E. Kolb (2005), Real-time measurements of SO_2 , H_2CO , and CH_4 emissions from in-use curbside passenger buses in new york city using a chase vehicle, *Environ. Sci. Technol.*, **39**, 7984–7990.
- Herriott, D., H. Kogelnik, and R. Kompfner (1964), Off-axis paths in spherical mirror interferometers, *Opt. Lett.*, **3**, 523–526.
- Höjer, S., H. Ahlberg, and A. Rosén (1991), Infrared laser Stark shift spectroscopy in ammonia: Theoretical and experimental analysis for sensing electric field-strength, *Appl. Phys. B*, **52**, 200–210.
- Houghton, J. T., Y. Ding, D. J. Griggs, M. Noguer, P. J. van der Linden, X. Dai, K. Maskell, and C. A. Johnson (Eds.) (2001), *Climate Change 2001: The Scientific Basis. Contribution of Working Group I to the Third Assessment Report of the Intergovernmental Panel on Climate Change (IPCC)*, Cambridge University Press, Cambridge, United Kingdom and New York, NY, USA.
- Huang, X., and Y. L. Yung (2004), A common misunderstanding about the Voigt line profile, *J. Atmos. Sci.*, **61**, 1630–1632.

- Humlcek, J. (1982), Optimized computation of the Voigt and complex probability functions, *J. Quant. Spectrosc. Radiat. Transfer*, 27, 437–444.
- Iguchi, T. (1986), Modulation waveforms for second-harmonic detection with tunable diode lasers, *J. Opt. Soc. Am.*, 3, 419–423.
- Jensen, E., D. Starr, and O. Toon (2004), Mission investigates tropical cirrus clouds, *Eos Trans. AGU*, 85, 45.
- Johnson, D. G., K. W. Jucks, W. A. Traub, and K. V. Chance (2001), Isotopic composition of stratospheric water vapor: Implications for transport, *J. Geophys. Res.*, 106, 12 219–12 226.
- Kerstel, E., R. Iannone, M. Chenevier, S. Kassi, H.-J. Jost, and D. Romanini (2006), A water isotope (^2H , ^{17}O , and ^{18}O) spectrometer based on optical feedback cavity-enhanced absorption for in situ airborne applications, *Appl. Phys. B*, 85, 397–406.
- Kerstel, E. R. T. (2007), Advances and challenges in stable isotope infrared spectrometry, in *Field Laser Applications in Industry and Research (FLAIR)*, Florence, Italy.
- Kerstel, E. R. T., R. van Trigt, N. Dam, J. Reuss, and H. A. J. Meijer (1999), Simultaneous determination of the $^2\text{H}/^1\text{H}$, $^{17}\text{O}/^{16}\text{O}$, and $^{18}\text{O}/^{16}\text{O}$ isotope abundance ratios in water by means of laser spectrometry, *Anal. Chem.*, 71, 5297–5303.
- Kerstel, E. R. T., G. Gagliardi, L. Gianfrani, H. A. J. Meijer, R. van Trigt, and R. Ramaker (2002), Determination of the $^2\text{H}/^1\text{H}$, $^{17}\text{O}/^{16}\text{O}$, and $^{18}\text{O}/^{16}\text{O}$ isotope ratios in water by means of tunable diode laser spectroscopy at 1.39 μm , *Spectrochim. Acta, Part A*, 55, 1941–1955.
- Kleiner, I., M. Godefroid, M. Herman, and A. R. W. McKellar (1987), Infrared laser Stark spectrum of HNO_3 at 6 μm , *J. Opt. Soc. Am. B*, 4, 1159–1164.
- Kormann, R., H. Fischer, C. Gurk, F. Helleis, T. Klüpfel, K. Kowalski, R. Königstedt, U. Parchatka, and V. Wagner (2002), Application of a multi-laser tunable diode laser absorption spectrometer for atmospheric trace gas measurements at sub-ppbv levels, *Spectrochim. Acta, Part A*, 58, 2489–2498.
- Kormann, R., H. Fischer, M. de Reus, M. Lawrence, C. Brühl, R. von Kuhlmann, R. Holzinger, J. Williams, J. Lelieveld, C. Warneke, J. de Gouw, J. Heland, H. Ziereis, and H. Schlager (2003), Formaldehyde over the eastern mediterranean during minos: Comparison of airborne in-situ measurements with 3d-model results, *Atmos. Chem. Phys.*, 3(3), 851–861.
- Kormann, R., R. Königstedt, U. Parchatka, J. Lelieveld, and H. Fischer (2005), QUALITAS A mid-infrared spectrometer for sensitive trace gas measurements based on quantum cascade lasers in CW operation, *Rev. Sci. Instrum.*, 76, 75,102–75,110.
- Kuchling, H. (1984), *Taschenbuch der Physik*, Verlag Harri Deutsch, Frankfurt am Main, Germany.
- Kurosaki, T., T. Hirono, and M. Fukuda (1994), Suppression of external cavity modes in DFB lasers with a high endurance against optical feedback, *IEEE Photonic. Tech. L.*, 6(8), 900–902.

- Lancaster, D. G., A. Fried, B. Wert, B. Henry, and F. K. Tittel (2000), Difference-frequency-based tunable absorption spectrometer for detection of atmospheric formaldehyde, *Appl. Opt.*, 39, 4436–4443.
- Lübken, F.-J., F. Dingler, H. von Lucke, J. Anders, W. J. Riedel, and H. Wolf (1999), Maserati: a rocketborne tunable diode laser absorption spectrometer, *Appl. Opt.*, 38, 5338–5349.
- Li, Y. Q., K. L. Demerjian, M. S. Zahniser, D. D. Nelson, J. B. McManus, and S. C. Herndon (2004), Measurement of formaldehyde, nitrogen dioxide, and sulfur dioxide at whiteface mountain using a dual tunable diode laser system, *J. Geophys. Res.*, 109, 148–227.
- Marsden, D., and F. P. J. Valero (2004), Observation of water vapor greenhouse absorption over the gulf of mexico using aircraft and satellite data, *J. Atmos. Sci.*, 61, 745–753.
- McManus, J. B., P. L. Kebabian, and M. S. Zahniser (1995), Astigmatic mirror multipass absorption cells for long-path-length spectroscopy, *Appl. Opt.*, 34, 3336–3348.
- McManus, J. B., M. S. Zahniser, D. D. Nelson, L. R. Williams, and C. E. Kolb (2002), Infrared laser spectrometer with balanced absorption for measurement of isotopic ratios of carbon gases, *Spectrochim. Acta, Part A*, 58, 2465–2479.
- Meade, M. L. (1983), *Lock-in amplifiers: principles and applications*, Peter Peregrinus Ltd., London, UK.
- Meijer, H. A. J., and W. J. Li (1998), The use of electrolysis for accurate $\delta^{17}\text{O}$ and $\delta^{18}\text{O}$ isotope measurements in water, *Isot. Environ. Health Stud.*, 34, 349–369.
- Moreau, G., C. Robert, V. Catoire, M. Chartier, C. Camy-Peyret, N. Huret, M. Pirre, L. Pommathiod, and G. Chalumeau (2005), Spirale: a multispecies in situ balloonborne instrument with six tunable diode laser spectrometers, *Appl. Opt.*, 44(28), 5972–5989.
- Morville, J., S. Kassi, M. Chenevier, and D. Romanini (2005), Fast, low-noise, mode-by-mode, cavity-enhanced absorption spectroscopy by diode-laser self-locking, *Appl. Phys. B*, 80, 1027–1038.
- Moyer, E. J., F. W. Irion, Y. L. Yung, and M. R. Gunson (1996), ATMOS stratospheric deuterated water and implications for troposphere-stratosphere transport, *Geophys. Res. Lett.*, 23, 2385–2388.
- Moyer, E. J., T. F. Hanisco, D. S. Sayres, J. StClair, F. N. Keutsch, N. T. Allen, L. R. Lapson, E. M. Weinstock, J. S. Smith, J. B. Paul, and J. G. Anderson (2007), The Harvard integrated cavity output spectroscopy ICOS isotope instrument, in *Field Laser Applications in Industry and Research (FLAIR)*, Florence, Italy.
- nanoplus GmbH (2008), *DFB laser diodes for 2740 nm applications*.
- Nassar, R., P. F. Bernath, C. D. Boone, A. Gettelman, S. D. McLeod, and C. P. Rinsland (2007), Variability in HDO/H₂O abundance ratios in the tropical tropopause layer, *J. Geophys. Res.*, 112, D21,305.

- Olivero, J. J., and R. L. Longbothum (1977), Empirical fits to the Voigt line width: A brief review, *J. Quant. Spectrosc. Radiat. Transfer*, *17*, 233–236.
- Olson, M. L., D. L. Grieble, and P. R. Griffiths (1980), Second derivative tunable diode laser spectrometry for line profile determination I. Theory, *Appl. Spectrosc.*, *34*, 50–56.
- Oltmans, S. J., H. Vömel, D. J. Hofmann, K. H. Rosenlof, and D. Kley (2000), The increase in stratospheric water vapor from balloonborne, frostpoint hygrometer measurements at Washington, D.C., and Boulder, Colorado, *Geophys. Res. Lett.*, *27*, 3453–3456.
- Payne, V. H., D. Noone, A. Duhia, C. Piccolo, and R. G. Grainger (2007), Global satellite measurements of HDO and implications for understanding the transport of water vapour into the stratosphere, *Q. J. R. Meteorol. Soc.*, *133*, 1459–1471.
- Preier, H. (1990), Physics and applications of IV-VI compound semiconductor lasers, *Semicond. Sci. Technol.*, *5*(3S), S12–S20.
- Preston, D. W., and E. R. Dietz (1991), *The Art of Experimental Physics*, John Wiley & Sons, New York, NY, USA.
- Profos, P., and T. Pfeifer (1997), *Grundlagen der Messtechnik*, 5 ed., R. Oldenbourg Verlag, München, Germany.
- Raizer, Y. P. (1991), *Gas Discharge Physics*, Springer Verlag, Berlin, Germany.
- Rehle, D., D. Leleux, M. Erdelyi, F. K. Tittel, M. Fraser, and S. Friedfeld (2001), Ambient formaldehyde detection with a laser spectrometer based on difference frequency generation in PPLN, *Appl. Phys. B*, *72*, 947–952.
- Reid, J., and D. Labrie (1981), Second-harmonic detection with tunable diode lasers—comparison of experiment and theory, *Appl. Phys. B*, *26*, 203–210.
- Reid, J., M. El-Sherbiny, B. K. Garside, and E. A. Ballik (1980), Sensitivity limits of a tunable diode laser spectrometer, with application to the detection of NO₂ at the 100-ppt level, *Appl. Opt.*, *19*, 3349–3354.
- Richard, E. C., K. K. Kelly, R. H. Winkler, R. Wilson, T. L. Thompson, R. J. McLaughlin, A. L. Schmeltekopf, and A. F. Tuck (2002), A fast-response near-infrared tunable diode laser absorption spectrometer for in situ measurements of CH₄ in the upper troposphere and lower stratosphere, *Appl. Phys. B*, *75*, 183–194.
- Rinsland, C. P., A. Goldman, V. M. Devi, B. Fridovich, D. G. S. Snyder, G. D. Jones, F. J. Murcray, D. G. Murcray, M. A. H. Smith, R. K. Seals, M. T. Coffey, and W. G. Mankin (1984), Simultaneous stratospheric measurements of H₂O, HDO, and CH₄ from balloon-borne and aircraft infrared solar absorption spectra and tunable diode laser laboratory spectra of HDO, *J. Geophys. Res.*, *89*, 7259–7266.
- Rinsland, C. P., M. R. Gunson, J. C. Foster, R. A. Toth, C. B. Farmer, and R. Zander (1991), Stratospheric profiles of heavy water vapor isotopes and CH₃D from analysis of the ATMOS Spacelab 3 infrared solar spectra, *J. Geophys. Res.*, *96*, 1057–1068.

- Rößner, K., M. Hücker, A. Benkert, and A. Forchel (2005), Long-wavelength GaInAsSb/AlGaAsSb DFB lasers emitting near $2.6\text{ }\mu\text{m}$, *Physica E*, **30**, 159–163.
- Roedel, W. (1992), *Physik unserer Umwelt: Die Atmosphäre*, Springer Verlag, Berlin, Germany.
- Roller, C., A. Fried, J. Walega, P. Weibring, and F. Tittel (2006), Advances in hardware, system diagnostics software, and acquisition procedures for high performance airborne tunable diode laser measurements of formaldehyde, *Appl. Phys. B*, **82**, 247–264.
- Rosenlof, K. H. (2003), How water enters the stratosphere, *Science*, **302**, 1691–1692.
- Rosenlof, K. H., E.-W. Chiou, W. P. Chu, D. G. Johnson, K. K. Kelly, H. A. Michelsen, G. E. Nedoluha, E. E. Remsberg, G. C. Toon, and M. P. McCormick (2001), Stratospheric water vapor increases over the past half-century, *Geophys. Res. Lett.*, **28**, 1195–1198.
- Rothman, L. S., D. Jacquemart, A. Barbe, D. C. Benner, M. Birk, L. R. Brown, M. R. Carleer, J. C. Chackerian, and K. C. et al. (2005), The HITRAN 2004 molecular spectroscopic database, *J. Quant. Spectrosc. Radiat. Transfer*, **96**, 139–204.
- Saathoff, H., C. Schiller, V. Ebert, D. W. Fahey, R.-S. Gao, O. Möhler, and the AQUAVIT Team (2008), The AQUAVIT formal intercomparison of atmospheric water measurement methods, *Geoph. Res. Abs.*, **10**, EGU2008-A-10,485.
- Sakurai, K., K. Uehara, M. Takami, and K. Shimoda (1967), Stark effect of vibration-rotation lines of formaldehyde observed by a $3.5\text{ }\mu\text{m}$ laser, *J. Phys. Soc. Jpn.*, **23**, 103–109.
- Sasada, H. (1984), Stark-modulation spectroscopy of NH_3 with a $1.23\text{ }\mu\text{m}$ semiconductor laser, *Opt. Lett.*, **9**, 448–450.
- Sayres, D. S. (2006), New techniques for accurate measurement of water and water isotopes: Insight into the mechanisms that control the humidity of the upper troposphere and lower stratosphere, Ph.D. thesis, Harvard University, Cambridge, MA, USA.
- Shostak, S. L., W. L. Ebenstein, and J. S. Muenter (1991), The dipole moment of water. I. Dipole moments and hyperfine properties of H_2O and HDO in the ground and excited vibrational states, *J. Chem. Phys.*, **94**, 5875–5882.
- Silver, J. A., and A. C. Stanton (1988), Optical interference fringe reduction in laser absorption experiments, *Appl. Opt.*, **27**, 1914–1916.
- St.Clair, J. M., T. F. Hanisco, E. M. Weinstock, E. J. Moyer, D. S. Sayres, J. B. Smith, R. Lockwood, and J. G. Anderson (2006), A new photolysis laser-induced fluorescence technique for the detection of HDO and H_2O in the lower stratosphere, unpublished.
- Steinwagner, J., M. Milz, T. von Clarmann, N. Glatthor, U. Grabowski, M. Höpfner, G. P. Stiller, and T. Röckmann (2007), HDO measurements with MIPAS, *Atmos. Chem. Phys.*, **7**, 2601–2615.

- Sugden, T. M., and C. N. Kenney (1965), *Microwave Spectroscopy of Gases*, D. Van Nostrand Company Ltd., London, GB.
- Tittel, F. K., D. Richter, and A. Fried (2003), Solid-state mid-infrared laser sources, in *Mid-Infrared Laser Applications in Spectroscopy*, edited by I. T. Sorokina and K. L. Vodopyanov, Springer Verlag, Berlin, Germany.
- Townes, C. H., and A. L. Schawlow (1975), *Microwave Spectroscopy*, Dover Publications, Inc., New York, NY, USA.
- Uehara, K. (1998), Dependence of harmonic signals on sample-gas parameters in wavelength-modulation spectroscopy for precise absorption measurements, *Appl. Phys. B*, **67**, 517–523.
- Urban, J., N. Lautie, D. Murtagh, P. Eriksson, Y. Kasai, S. LoXow, E. Dupuy, J. de La Noe, U. Frisk, M. Olberg, E. L. Flochmoen, and P. Ricaud (2007), Global observations of middle atmospheric water vapour by the Odin satellite: An overview, *Planet. Space Sci.*, **55**, 1093–1102.
- Verhage, A. J. L., R. A. Rooth, and L. W. Wouters (1993), Laser Stark spectrometer for the measurement of ammonia in flue gas, *Appl. Opt.*, **32**, 5856–5866.
- Viciani, S., F. D'Amato, P. Mazzinghi, F. Castagnoli, G. Toci, and P. Werle (2008), A cryogenically operated laser diode spectrometer for airborne measurement of stratospheric trace gases, *Appl. Phys. B*, **90**, 581–592.
- Vogelsang, R. (2004), Lecture Notes: Lock-In Amplifier Theory.
- Waechter, H., and M. W. Sigrist (2007), Mid-infrared laser spectroscopic determination of isotope ratios of N₂O at trace levels using wavelength modulation and balanced path length detection, *Appl. Phys. B*.
- Waewsak, J. (2004), The spectral transmittance due to water vapor, ozone and aerosol of cloudless atmosphere over the central part of Thailand, *Thammasat Int. J. Sc. Tech.*, **9**, 7–18.
- Wagenbach, D. (2008), personal communication.
- Wahlquist, H. (1961), Modulation broadening of unsaturated lorentzian lines, *J. Chem. Phys.*, **35**, 1708–1710.
- Webster, C. R., and A. J. Heymsfield (2003), Water isotope ratios D/H, ¹⁸O/¹⁶O, ¹⁷O/¹⁶O in and out of clouds map dehydration pathways, *Science*, **302**, 1742–1745.
- Webster, C. R., and R. D. May (1985), Tunable diode laser Stark modulation spectroscopy for rotational assignment of the HNO₃ 7.5μm band, *Chem. Phys. Lett.*, **121**, 429–436.
- Webster, C. R., R. D. May, C. A. Trimble, R. G. Chave, and J. Kendall (1994), Aircraft (ER-2) laser infrared absorption spectrometer (ALIAS) for in-situ stratospheric measurements of HCl, N₂O, CH₄, NO₂, and HNO₃, *Appl. Opt.*, **33**, 454–472.

- Webster, C. R., G. J. Flesch, D. C. Scott, J. E. Swanson, R. D. May, W. S. Woodward, C. Gmachl, F. Capasso, D. L. Sivco, J. N. Baillargeon, A. L. Hutchinson, and A. Y. Cho (2001), Quantum-cascade laser measurements of stratospheric methane and nitrous oxide, *Appl. Opt.*, **40**, 321–326.
- Weibring, P., D. Richter, A. Fried, J. Walega, and C. Dyroff (2006), Ultra-high-precision mid-IR spectrometer II: system description and spectroscopic performance, *Appl. Phys. B*, **85**, 207–218.
- Weibring, P., D. Richter, J. G. Walega, and A. Fried (2007), First demonstration of a high performance difference frequency spectrometer on airborne platforms, *Opt. Express*, **15**(21), 13,476–13,495.
- Weidmann, D., G. Wysocki, C. Oppenheimer, and F. K. Tittel (2005), Development of a compact quantum cascade laser spectrometer for field measurements of CO₂ isotopes, *Appl. Phys. B*, **80**, 255–260.
- Werle, P. (1998), A review of recent advances in semiconductor laser based gas monitors, *Spectrochim. Acta, Part A*, **54**, 197–236.
- Werle, P. (2005), personal communication.
- Werle, P., and B. Jänker (1996), High-frequency-modulation spectroscopy: Phase noise and refractive index fluctuations in optical multipass cells, *Opt. Eng.*, **35**, 2051–2057.
- Werle, P., and S. Lechner (1999), Stark-modulation-enhanced FM-spectroscopy, *Spectrochim. Acta, Part A*, **55**, 1941–1955.
- Werle, P., and A. Popov (1999), Application of antimonide lasers for gas sensing in the 3-4-μm range, *Appl. Opt.*, **38**, 1494–1501.
- Werle, P., R. Mücke, and F. Slemr (1993), The limits of signal averaging in atmospheric trace gas monitoring by tunable diode-laser absorption spectroscopy, *Appl. Phys. B*, **57**, 131–139.
- Werle, P., P. Mazzinghi, F. D'Amato, M. D. Rosa, K. Maurer, and F. Slemr (2004), Signal processing and calibration procedures for in situ diode-laser absorption spectroscopy, *Spectrochim. Acta, Part A*, **60**, 1685–1705.
- Werner, R. (2008), personal communication.
- Wert, B. P. (2002), Development, validation, and application of a high performance tunable diode laser absorption spectrometer for airborne formaldehyde measurements, Ph.D. thesis, University of Colorado, Boulder, CO, USA.
- Wert, B. P., A. Fried, S. Rauenbuehler, J. Walega, and B. Henry (2003a), Design and performance of a tunable diode laser absorption spectrometer for airborne formaldehyde measurements, *J. Geophys. Res.*, **108**, 4350–4364.

- Wert, B. P., M. Trainer, A. Fried, T. B. Ryerson, B. Henry, W. Potter, W. M. Angevine, E. Atlas, S. G. Donnelly, F. C. Fehsenfeld, G. J. Frost, P. D. Goldan, A. Hansel, J. S. Holloway, G. Hubler, W. C. Kuster, J. D. K. Nicks, J. A. Neuman, D. D. Parrish, S. Schauffler, J. Stutz, D. T. Sueper, C. Wiedinmyer, and A. Wisthaler (2003b), Signatures of terminal alkene oxidation in airborne formaldehyde measurements during TexAQS 2000, *J. Geophys. Res.*, *108*, 4104–4117.
- White, J. U. (1942), Long optical paths of large aperture, *J. Opt. Soc. Am.*, *32*, 285–288.
- Wienhold, F., H. Fischer, P. Hoor, V. Wagner, R. Königstedt, G. Harris, J. Anders, R. Grisar, M. Knothe, W. Riedel, F.-J. Lübken, and T. Schilling (1998), TRISTAR - a tracer in situ TDLAS for atmospheric research, *Appl. Phys. B*, *67*, 411–417.
- Wilson, G. V. H. (1963), Modulation broadening of NMR and ESR line shapes, *J. Appl. Phys.*, *34*, 3276–3285.
- Wise, S. A., and R. L. Watters Jr. (2005), Report of investigation: Reference materials 8535, 8536, 8537, *Tech. rep.*, National Institute of Standards and Technology, Gaithersburg, MD, USA.
- Worden, J., K. Bowman, D. Noone, R. Beer, S. Clough, A. Eldering, B. Fisher, A. Goldman, M. Gunson, R. Herman, S. S. Kulawik, M. Lampel, M. Luo, G. Osterman, C. Rinsland, C. Rodgers, S. Sander, M. Shephard, and H. Worden (2006), Tropospheric emission spectrometer observations of the tropospheric HDO/H₂O ratio: Estimation approach and characterization, *J. Geophys. Res.*, *111*, D16,309.
- Zahn, A. (2001), Constraints on 2-way transport across the arctic tropopause based on O₃, stratospheric tracer (SF₆) ages, and water vapor isotope (D, T) tracers, *J. Atmos. Chem.*, *39*, 303–325.
- Zahn, A. (2008), personal communication.
- Zahn, A., P. Franz, C. Bechtel, T. Röckmann, and J. U. Groß (2006), Modelling the budget of middle atmospheric water vapour isotopes, *Atmos. Chem. Phys.*, *6*, 2073–2090.

Acknowledgments

The research presented in this dissertation has been conducted mainly at the Research Center Karlsruhe, Germany, and in part at the National Center for Atmospheric Research in Boulder, CO, USA.

I would like to thank my supervisor Prof. Wolfgang Freude (Institute of High-Frequency and Quantum Electronics, University Karlsruhe) for the many valuable discussions as well as for introducing me to the field of noise measurements. His helpful suggestions for writing publications and the present dissertation are much appreciated.

Many thanks go also to Prof. Herbert Fischer (Institute of Meteorology and Climate Research, Research Center Karlsruhe) for proposing this exciting research project and for his co-supervision.

I gratefully acknowledge the co-supervision by Prof. Jürg Leuthold (Institute of High-Frequency and Quantum Electronics, University Karlsruhe). His introduction to the top-down approach has largely improved my presentation skills.

Dr. Peter Werle brought my present research position to my attention. I thank him for sharing his expert knowledge and wide experience in the field of laser spectroscopy and trace-gas detection that helped making this project successful.

I gratefully acknowledge the many helpful discussions with Dr. Andreas Zahn. Working in his group was a great experience in any respect. I could not have asked for more creative freedom.

I further appreciate the help of and the many valuable discussions with colleagues at the IMK, namely Joel Brito, Daniel Fütterer, Frank Hase, Detlev Sprung, Josef Weppner, and many more.

I'm very grateful to Frank Helleis, MPI-CH, Mainz, for the many helpful discussions and suggestions about the housekeeping and DSP electronics and software.

The design of various mechanical parts of the water vapor isotopic-ratio spectrometer was nicely done by Harald Franke of Enviscope GmbH.

I also acknowledge the helpful discussions with and suggestions by Dr. Barry McManus and Dr. Mark Zahnizer of Aerodyne Research, Inc.

Alexander Streili and co-workers at the IMK workshop are thanked for accurately machining many parts that have been used within the present spectrometers.

The Stark modulation experiments have been carried out during my visit at the National Center for Atmospheric Research, in Boulder, CO, USA.

I would like to thank the members of the Analytical Photonics and Optoelectronics Laboratory, namely Drs. Alan Fried, Petter Weibring, Dirk Richter, as well as Jim Walega for their interest in my work and for their contribution to the experiments. Dr. John Orlando has provided FTIR measurements of the CH₂O gas-standard, which is gratefully acknowledged.

I would further like to acknowledge the introduction to the Stark effect by Dr. Andrea Callegari, Laboratory of Ultrafast Laser Spectroscopy, École Polytechnique Federale de Lausanne, Switzerland.

Many thanks to Tammy McMinn and Nima Gharavi for making my spare time in Boulder very enjoyable.

Finally, and most importantly, I thank Kerstin for her love and support.

List of own Publications

Journal Papers

C. Dyroff, P. Weibring, A. Fried, D. Richter, J. G. Walega, A. Zahn, W. Freude, P. Werle (2007), Stark-enhanced diode-laser spectroscopy of formaldehyde using a modified Herriott-type multipass cell, *Applied Physics B*, 88, 117-123.

C. Dyroff, A. Zahn, W. Freude, B. Jänker, P. Werle (2007), Multipass cell design for Stark-modulation spectroscopy, *Applied Optics*, 46, 4000-4007.

P. Weibring, D. Richter, A. Fried, J. G. Walega, **C. Dyroff** (2006), Ultra-high precision mid-IR spectrometer II: system description and performance characteristics, *Applied Physics B*, 85, 207-218.

P. Werle, **C. Dyroff**, A. Zahn, P. Mazzinghi, F. D'Amato (2005), A new concept for sensitive in-situ stable isotope ratio infrared spectroscopy based on sample modulation, *Isotopes in Environmental and Health Studies*, 41, 323-333.

Conference presentations

C. Dyroff, A. Zahn, P. Werle, P. Weibing, A. Fried, D. Richter, G. J. Walega, W. Freude (2007), Stark-enhanced diode-laser spectroscopy of formaldehyde using a modified Herriott-type multipass cell”, *Field Laser Applications in Industry and Research (FLAIR)*, Florence, Italy, September 03.

C. Dyroff, A. Zahn, P. Werle, W. Freude (2006), On the in situ measurement of H₂O isotopic ratios in the UT/LS by means of diode laser spectroscopy, *Spring-Meeting of the German Physical Society*, Heidelberg, Germany, March 13-16.

C. Dyroff, A. Zahn, P. Werle, W. Freude, and A. Callegari (2005), A new concept for the in situ measurement of atmospheric trace gases and stable isotope ratios based on a sample modulation multipass cell, *5th International Tunable Diode Laser Spectroscopy Conference*, Florence, Italy, July 15.

Contributed presentations

A. Zahn, **C. Dyroff**, J. Keller (2007), Airborne atmospheric research in Europe: CARIBIC and HALO, *Field Laser Applications in Industry and Research (FLAIR)*, Florence, Italy, September 06.

A. Fried, D. Richter, P. Weibring, J. G. Walega, C. Roller, F. Tittel, **C. Dyroff** (2005), Lead-salt and difference frequency generation IR spectrometers: performance comparisons and common requirements for ultra sensitive airborne measurements, *5th International Tunable Diode Laser Spectroscopy Conference*, Florence, Italy, July 15.

P. Werle, P. Mazzinghi, F. D'Amato, A. Zahn, **C. Dyroff** (2004), Principles, performances & perspectives of diode-laser sensors: A spectroscopic approach to atmospheric measurement challenges, *ESF-IAEA International Workshop on Stable Isotope Ratio Infrared Spectrometry (SIRIS)*, Vienna, Austria, September 7.

Curriculum Vitae

Christoph Dyroff

Born December 10th, 1976
in Geislingen an der Steige
Citizenship: German

Education

- 04/2003–09/2003 Visiting Scientist at the National Center for Atmospheric Research, Analytical Photonics and Optoelectronics Laboratory, Boulder, CO, USA
- 02/2002–06/2002 International CAD/CAE Program with major in Aerospace Engineering at École Supérieure des Techniques Aéronautiques et de Construction Automobile (ESTACA) in Paris, France
- 08/2001–12/2001 Visiting Scientist at the University of Canterbury, Department of Physics and Astronomy, Christchurch, New Zealand
- 09/1999–11/2003 Studies at University of Applied Sciences Oldenburg/Ostfriesland/Wilhelmshaven, Emden, Germany
Major: Applied Laser Technology
Degree: Dipl.-Ing. (FH)
(best diploma award)
- 08/1997–06/1998 Technical College in Gütersloh, Germany
- 08/1993–01/1997 Apprenticeship as Electronics Installer (Energieelektroniker) at Elektro Beckhoff GmbH in Verl, Germany
(best transcript award)
- 08/1987–06/1993 Realschule (secondary school) in Verl, Germany

Work Experience

- 01/2004–02/2004 Assistant at the University of Applied Sciences Oldenburg/Ostfriesland/Wilhelmshaven, Department of Technology, Laser Analytics group, Emden, Germany

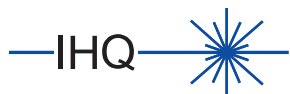
- 10/2002 Student assistant at the University of Applied Sciences Oldenburg/Ostfriesland/Wilhelmshaven, Department of Technology, Laser Analytics group, Emden, Germany
- 08/2000 Student assistant at the Institute of Lasertechnology Ostfriesland (ILO), Emden, Germany
- 02/1997–07/1997 Technician at Elektro Beckhoff GmbH in Verl, Germany

Karlsruhe Series in Photonics & Communications, Vol. 5

Edited by Prof. J. Leuthold and Prof. W. Freude

Universität Karlsruhe (TH)

Institute of High-Frequency and Quantum Electronics (IHQ)
Germany



In-situ investigation of trace gases furthers the understanding of many important physical and chemical processes of the earth's atmosphere. Due to the low concentration of many atmospheric gases, highly sensitive measurement equipment is needed. In addition, stringent space and weight restrictions apply for airborne operation. Compact tunable diode-laser spectrometers with low-noise system components and advanced signal processing meet these requirements.

This book discusses the mechanical and opto-electronic design of laser spectrometers for measuring two very important atmospheric gases, namely water vapor and its isotopic ratios, and formaldehyde. For measuring water vapor, shot-noise limited sensitivity has been achieved by a careful choice of system components and data processing. For measuring formaldehyde, even higher sensitivity is required. In this case a selective sample modulation exploiting the Stark effect has been used to effectively compensate systematic drift. Thus, with much longer averaging times, the sensitivity was greatly improved.

About the Author

Christoph Dyroff was born in 1976 in Geislingen a. d. Steige, Germany. In 1997 he completed an apprenticeship as an electrician. In 2003 he was awarded the Dipl.-Ing. (FH) degree in Applied Laser Technology from the University of Applied Sciences in Emden, Germany. As a visiting student in New Zealand, France, and in the USA he was educated in laser spectroscopy and in mechanical and optical engineering. In 2008 he received the Dr.-Ing. (PhD) degree in Electrical Engineering from the University of Karlsruhe, Germany. His research is focused on the design and application of highly-sensitive laser spectrometers for measuring atmospheric trace gases.

ISSN: 1865-1100

ISBN: 978-3-86644-328-0

www.uvka.de